Synthesis, Modification and Application of Metal Organic Frameworks and their Derivatives

by

Xueliang Mu *BEng*

Thesis submitted to University of Nottingham

for the degree of Doctor of Philosophy

March 2019

Abstract

To date, metal-organic frameworks (MOFs) have been developed significantly into numerous applications. This success is primarily attributed to the diversified complete networks created by different synthesis methods. On this basis, a considerable number of modification and transformation strategies are explored to overcome the known limitations of MOFs and to stabilize the active sites, as well as, to add multi-functional species for improving the intrinsic properties of MOFs. In this thesis, several studies, including MOFs preparation, MOFs modification and its possible application are performed to interpret the nature of this material and to identify the suitable material structures for modern industrial process.

The first part of this thesis focuses on the preparation of HKUST-1, one of the copper-based MOFs. This preparation adopted a conventional solvothermal method in a reflux unit. In addition, different reaction periods and temperatures have been implicated in the operation of the reflux unit. After pristine HKUST-1 preparation, it is accompanied by an activation process and different temperature of the air dryer for degas purpose. Considering the activation process, it is possible to adjust the textural properties, morphology and size of HKUST-1 crystals through changing the states of HKUST-1 before activation and the types of activation solvents. The focus of this study was to design an optimized method for the synthesis of nano-scale HKUST-1 with high output, large surface area and good CO_2 uptake. It was found that the nano-scale HKUST-1 (T85-3-Pm4-120) was successfully synthesized at a yield of 87 % under low temperature of 85 ^{o}C using a molar ratio of 6:3:2 for triethylamine(TEA), Cu^{2+} and trimesic acid (TMA). The highest porosity

was achieved after pristine HKUST-1 was activated (powder activation) at 120 °C for four times using methanol. The result showed the optimal HKUST-1 (T85-3-Pm4-120) had a CO_2 uptake of 2.5 mmol/g. It is therefore demonstrated that this new approach is a reliable and effective way to synthesize highly porous HKUST-1 MOFs under a mild condition, which is comparable with conventional HKUST-1 by others.

The second part of this thesis illustrates the modification of pristine HKUST-1, regarded as post-synthetic modification. In the modification, two distinct strategies were proposed and were adopted. One of them is to incorporate MoS_2 quantum dots as a core with a shell of HKUST-1. In this study, a 'one-pot' synthesis method was utilized for the growth of HKUST-1 on MoS_2 quantum dots to form MoS_2/HKUST-1 core-shell hybrid. Before verifying the structure of this hybrid by characterization, a detailed DFT calculation was conducted to assess the possibility of success. Moreover, it proved that the formation of the core-shell composite starts from the adsorption of a Cu^{2+} cation on a MoS_2 quantum dot. This configuration would be followed with the appearance of an intermediate (MoS_2+Cu)-TMA structure, which was a configuration of the lowest energy among all possible configurations at this stage. It was also found that MoS_2+Cu not only accelerates the deprotonation of trimesic acid, but also stabilizes the structure of HKUST-1 on MoS_2. After that, the as-synthesis hybrid was tested on the CO_2 adsorption capacity and indicated a good CO_2 uptake (4.75 mmol/g) owing to a high surface area (1638.9 m^2/g for MH-2). To account for these interactions among them, the secondary building unit (SBU) was modeled to study the mechanism of the adsorption of CO_2 on the MoS_2/HKUST-1 hybrid.

The second strategy of modification is the phase transformation of MOFs utilizing HKUST-1 as a self-sacrificial templet via carbonization/pyrolysis. The annealing process was

employed to understand the carbonization process of MOFs. At a fixed heating rate up to 430 °C and an inert atmosphere, the pre-treated HKUST-1 exhibited an expectedly structural stability before 280 ^{o}C with noticeable change of pore property. When the temperature continued to rise to 330 ^{o}C, the graphitization of the structure led to the formation of Cu nanoparticles. Characterized by the In-situ technology, the acceleration of framework collapse was caused by the presence of local vacancy (unsaturated Cu sites or incomplete protoned carboxylic groups), which is attributed to the break of bridging organic linker. Besides, size and morphology of the resulting materials were influenced by different temperature and prolonged isotherm step under a harsh condition. Thus, this research not only demonstrated the thermal behaviour of HKUST-1 in different temperatures, but also provided an optimized solution for the preparation of CuNP/GO sample.

Based on the above-mentioned carbonization mechanism, a series of CuNP/GO catalysts was testified in CO oxidation. The results suggested that CuNP/GO sample (330C-3H), prepared under 330 ^{o}C for 3 h, demonstrated a better catalyst performance, and reached a maximum reaction rate at 180 ^{o}C (T_{93} = 180 ^{o}C) with an apparent activation energy of 57.17 kJ/mol. To gain a better understanding of the reaction mechanism, the formation of intermediates was monitored using In-situ techniques. The result illustrated that CO molecules preferably bind to the surface of the unstable Cu_4O_3 phase, in which Cu^+ and Cu^{2+} active sites co-exist. This unique surface property leads to the adsorption of CO and O_2 on different positions. Induced by the strong chemical interaction, dissociated oxygen atoms bond to adjacent CO molecule as CO_3^{2-}.

To summarize, in this thesis, HKUST-1 is taken as an example to illustrate in great depth the complete process from the preparation of MOFs, to their modification and applications, covering a wide range of theoretical study and experimental work. In addition, based on the results of the research to date, recommendations for future work were also made at the end of this thesis.

Key words:

MOFs, HKUST-1, synthesis, modification, application, DFT calculation and In-situ characterization

Publication during candidature

1. **Xueliang Mu**, Yipei Chen, Edward Lester, Tao Wu, Optimized synthesis of nano-scale HKUST-1 under mild conditions and its application in CO_2 capture. **Microporous and Mesoporous Materials**, 2018, p.249-257.
2. **Xueliang Mu**, Xiang Gao, Haitao Zhao, Michael George, Tao Wu, DFT study of the adsorption of elementary mercury on the 1T-MoS_2 monolayer. **Journal of Zhejiang University-SCIENCE A (Applied Physics & Engineering)**, 2018, 19(1), p. 60-67.
3. Haitao Zhao, **Xueliang Mu**, Xiang Gao, Tao Wu, Structural defects in 2D MoS_2 nanosheets and their roles in the adsorption of airborne elemental mercury. **Journal of Hazardous Materials,** 2019, 366, p. 240-249 (Author 1 and Author 2 have the same contribution).
4. Shuai Liu, Chen Lin, **Xueliang Mu**, Mengxia Xu, Jiahui Yu, Gang Yang, Xiang Luo, Haitao Zhao, Wu Tao, Development of Pd_n / g-C_3N_4 adsorbent for Hg^0 removal - DFT study of the influences of support and Pd cluster size. **Fuel** 2019 [accepted].
5. Haitao Zhao, **Xueliang Mu**, Gang Yang, Mike George, Pengfei Cao, Billy Fanady, Siyu Rong, Xiang Gao, Tao Wu, Graphene-like MoS_2 containing adsorbents for Hg^0 capture at coal-fired power plants. **Applied Energy,** 2017, 207, p. 254-264.
6. Haitao Zhao**, Xueliang Mu**, Gang Yang, Chengheng Zheng, Chenggong Sun, Xiang Gao, Tao Wu, Microwave-induced activation of additional active edge sites on the MoS_2 surface for enhanced Hg^0 capture. **Applied Surface Science**, 2017. 420: p. 439-445.

7. Yipei Chen, **Xueliang Mu**, Edward Lester, Tao Wu, High efficiency synthesis of HKUST-1 under mild conditions with high BET surface area and CO_2 uptake capacity. **Progress in Natural Science: Materials International**, 2018, p. 584-589.

8. Haitao Zhao, Gang Yang, **Xueliang Mu**, Kaiqi Shi, Xiang Gao, Tao Wu, Recovery of elemental mercury from coal-derived flue gas using a mos_2-based material, **Energy Procedia**, 2017, p. 3584-3589.

9. Haitao Zhao, Gang Yang, **Xueliang Mu**, Pengfei Cao, Xiang Gao, Tao Wu, Hg^0 capture over MoS_2 nanosheets containing adsorbent: effects of temperature, space velocity, and other gas species, **Energy Procedia**, 2017, p. 4408-4413.

10. **Xueliang Mu**, Shuai Liu, Yipei Chen, Xiang Luo, Tao Wu, Self-assembling MoS_2/HKUST-1 composite - theoretical and experimental study [under preparation].

11. **Xueliang Mu**, Shuai Liu, Yipei Chen, Xiang Luo, Tao Wu, Self-assembly composites of HKUST-1 MOFs with MoS_2 for gas adsorption [under preparation].

Acknowledgements

First of all, I am especially grateful to my supervisors, Prof. Tao Wu and Prof. Michael George, who provided me the opportunity and generous financial support to develop my research career in UNNC. I deeply appreciate their mentorship that guided me to become proficient technically. Furthermore, I would like to thank Dr. Haitao Zhao for his valuable advice to my PhD study.

I would like to thank all the members, past and present, of the Nottingham New Material Institute and friends from the University of Nottingham Ningbo China. They have made my three-year PhD life genuinely enjoyable. I would like to thank my co-workers Dr. Yipei Chen and Dr. Xiang Luo for their valuable discussions and inputs to this work. I would also like to acknowledge Mrs. Shiying Tao, Mr. Gang Yang, Mr. Liangliang Zhu, Mrs. Shanshan Xu for the technical advice and setting the lab standard for constantly making the lab a better, more efficient place for everyone. Many conversations with Mr. Shuai Liu, Mr. Peng Jiang, Ms. Luyao Tang, Dr. Shu Liu, Dr. Huayang Li in general scientific problems were valuable in helping me to clarify systematic thoughts.

I would also like to acknowledge the Ministry of Science and Technology, China and the University of Nottingham Ningbo China (UNNC) for the financial support during the three years of this project.

Finally, I would like to dedicate this work to my parents whose dreams for me have resulted in this achievement with their loving upbringing and nurturing.

Thank all of you.

Table of Contents

Table of Figures

List of Tables

List of Abbreviation

A

AR = Analytical Grade

B

BET = Brunauer Emett Teller

BTC = Bezenetricarboxylate

C

Charact. = Characterization

CP = Chemically Pure

CO_2 = Carbon Dioxide

CO = Carbon Monoxide

Cu = Copper

Cu_4O_3 = Paramelaconite

COFs = Covalent Organic Frameworks

CUS = Coordinatively Unsaturated Sites

D

DFT = Density Function Theory

1D, 2D, 3D = One, Two, Three Dimension

DMF = Dimethylformamide

DMSO = Dimethylsufoxide

DES = Deep Eutectic Solvents

DEF = Diethylformamide

E

EDS = Energy Dispersive X-Ray Spectrometer

EtOH = Ethanol

ERC = Electrochemical reduction of carbon dioxide

F

FTIR = Fourier Transform Infrared Spectroscope

H

H_2 = Hydrogen

H_2O = Water

HRTEM = High-Resolution Transmission Electron Microscope

HINA = Isonicotinic acid

Mater. = Material

MeOH = Methanol

I

IRMOFS = Iso-Reticular MOFs

G

GO = Graphene Oxide

GDE = Gas Diffusion Electrode

L

LAG = Liquid-Assisted Grinding

M

MEOH = Methanol

MF = Micro Filtration

MW = Microwave

MOFs = Metal Organic Frameworks

MoS_2 = Molybdenum Disulphide

MTBS = Tributylmethylammonium Methyl Sulphate

MAS NMR = Magic Angle Spinning Nuclear Magnetic Resonance

N

N_2 = Nitrogen

NPs = Nano Particles

O

O_2 = Oxygen

P

PFR = Plug Flow Reactor

PCPs = Porous Coordination Polymers

POPs = Porous Organic Polymers

PSM = Post Synthetic Method

Q

QDs = Quantum Dots

S

SEM = Scanning Electron Microscope

SBU = Secondary Building Unit

SSA = Specific Surface Area

$scCO_2$ = Supercritical CO_2

T

TMA = Trimesic Acid

TEA = Triethylamine

TEM = Transmission Electron Microscope

TGA = Thermo Gravimetric Analysis

TOF = Turnover Frequency

TON = Turnover Number

THT = Tetrahydrothiophene

TMDCs = Transition Metal Dichalcogenides

U

UF = Ultra filtration

X

XPS = X-Ray Photoelectron Spectroscopy

XRD = X-Ray Diffraction

Z

ZIF = Zeolitic Imidazolate Frameworks

ZMOFs = Zeolite like MOFs

Chapter 1 Introduction

1.1 Background

Currently, the expansion of human population and industrial footprint is leading the energy consumption increasing [1-3]. The 83% of the global energy consumption is sourced from conventional energy (coal, natural gas and oil) in 2020 as shown in Figure 1-1 [4]. However, the complete and incomplete combustion of carbon-based energy would yield large amount of CO2 and CO gas, which would be a main cause of climate change and numerous environmental problems [5]. When improving the climate change and environmental issues, the efforts of potential porous materials will be a substantial benefit to renewable and environmentally friendly remediation, storage systems and catalytic experiment.

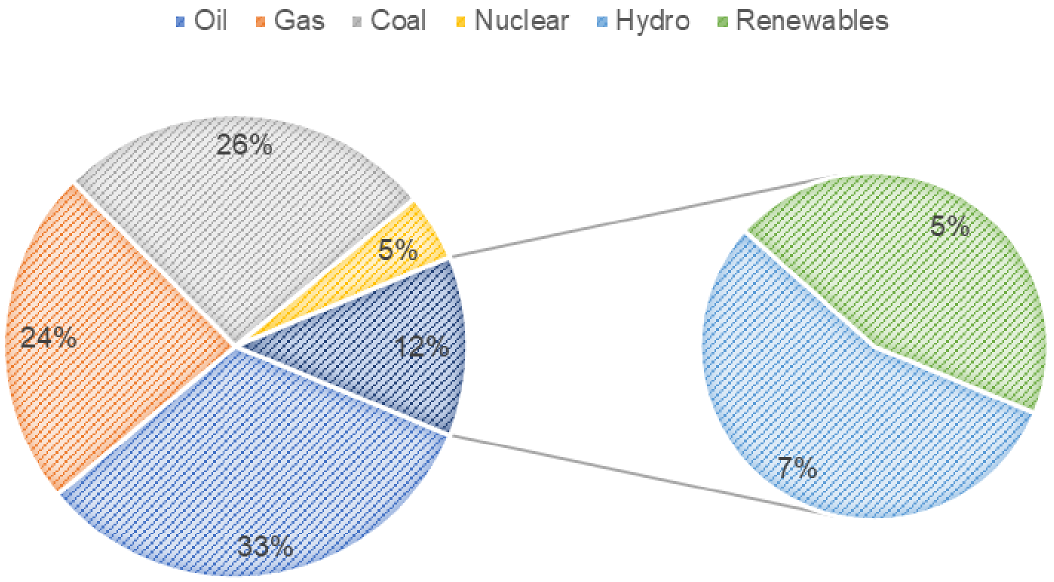

Figure 1-1 Shares of primary energy [4]

One famous porous material is zeolites, which are widely used in various applications, including water treatment [6], VOC adsorption and catalysis [7], oil refinery [8], etc. Similarly, metal-organic frameworks (MOFs) become an emerging class of crystalline inorganic-organic porous composites, comprised of organic linkers and metal nodes. The tunable pore size and topologies of MOFs ensures its versatile architecture and a great advantage over conventional porous materials. Nowadays, MOFs are also considered as promising porous materials for gas storage/separation, catalysis, drug delivery and sensing, etc.

Various approaches applied to MOFs family afford to enrich them with a high level of complexity and functionality. To enrich the diversity of MOFs family, the synthesis method of MOFs was developed into solvothermal method [9], electrochemical preparation [10], microwave heating method [11] and sonochemical method [12], etc. Although these approaches have made important discoveries and will continue to bring achievements, it is urgently required to control materials on the molecular level for the product of materials on demand [13, 14]. Consequently, the downstream like activation and post-synthetic modification are utilized for suiting the SBU strategy [15] towards the certain MOF and its correspondent application. Based on the diversity of SUB, the rich structure and application of MOFs were found as shown in Figure 1-2.

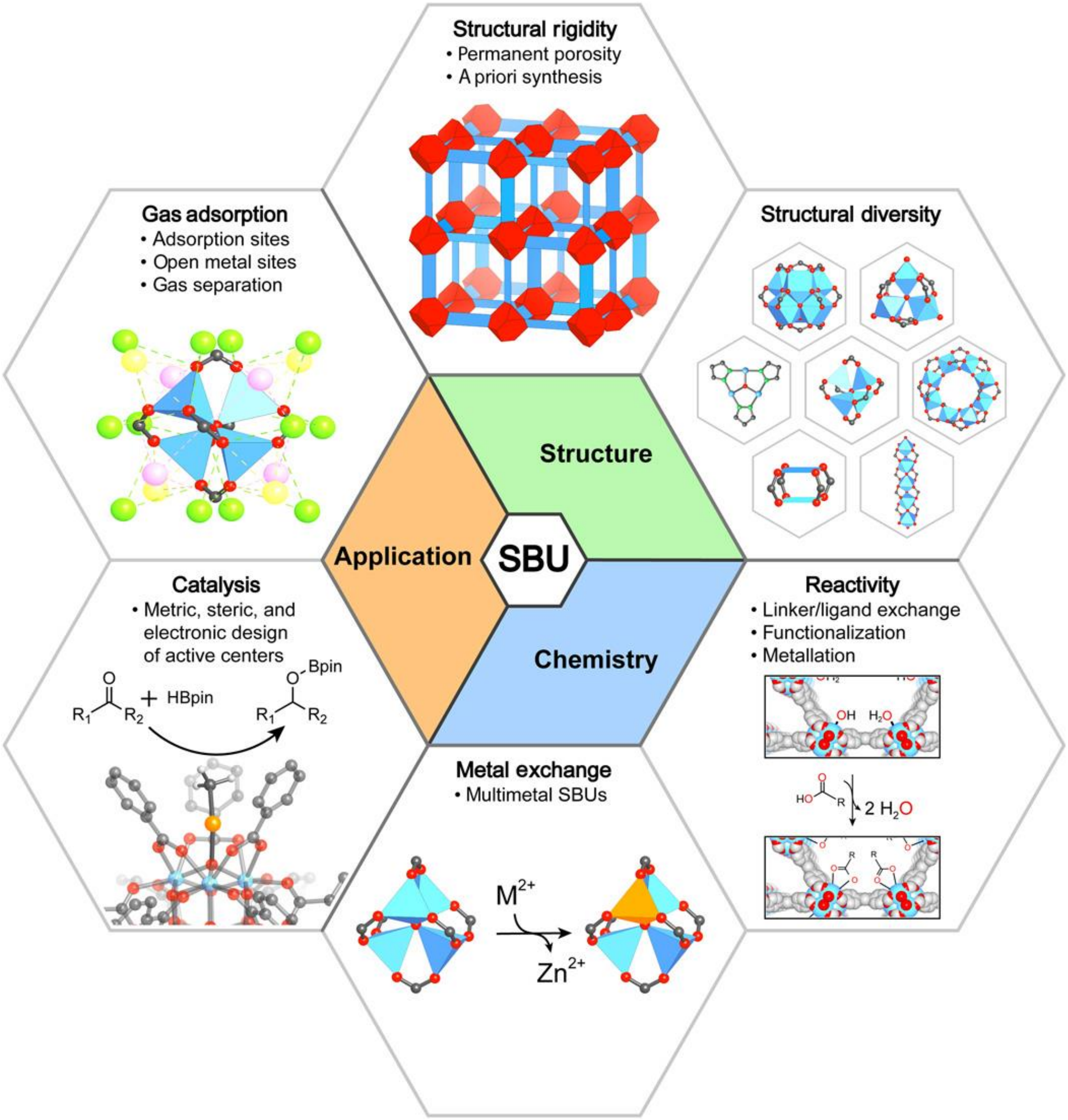

Figure$_{2}$ 1-2 Impact of the SBU on the structure, chemistry, and applications of MOFs [15].

For these purposes, catalytic active metals/metal oxides embedded by MOFs (core-shell) blazes up a new trail to prepare size selective incorporation catalyst for heterogeneous reaction. Yaghi et al. reported Pt @ MOF nanoparticles performed unusual product selectivity [16]. Furthermore, Tsung et al. illustrated that a MOF shell provides exceptional molecular size selectivity [17]. Thus, this uncommon method is worth attempting. The direct pyrolysis/carbonization of material is a common treatment in numerous applications, but in the field of MOFs, this approach brings an unusual effect from carbonized derivatives. As an initial research, Radek et al. successfully prepared high surface area of Fe_2O_3 (200-400 m^2/g) via thermally treating $Fe_4[Fe(CN)_6]_3$. However, there has been slow progress in the MOFs-derived porous metal oxides. Until recently, a novel idea was adopted in 2012 using a two-step thermolysis method, including carbonization in a N_2 environment and oxidation in air [18]. The obtained Fe_2O_3, where MIL-88(Fe) serves as the sacrifice, has a surface area of 75 m^2/g and uniform nanoparticles size of 20 nm. These different trials effectively pave the road for the specific morphology of derivatives via carbonization of MOFs.

Hence, increased complexity and functionals can be achieved by the adjustment of synthesis condition and the introduction of additive, which could bring more open metal sites and unique structure of MOFs based hybrid. The latter manner of MOFs modification can create additional functionals beyond the intrinsic properties of the parent MOFs. Especially, it is favourable in the aspects of increased sorption capacity and improved catalytic activity. Apart from those, the direct carbonization of MOFs, creating small clusters or even single atom catalyst, has been another way to expand and broaden the functions of MOFs material in the potential application.

Among the MOFs, HKUST-1 is one of the well and extensively studied MOFs. It exhibits sufficient chemical and thermal stability, as well as is composed of Cu open sites that can provide rich adsorption and redox chemistry. In this thesis, HKUST-1 has been therefore chosen as a candidate to study the screening synthesis of MOFs, MOFs modification and its application in adsorption and redox catalysis.

1.2 Objectives

i) To improve MOFs textural properties by screening synthesis conditions and activation process, and to exploit the effect of synthetic parameters on the size, porosity and morphology of MOFs particles.

ii) To explore the formation of HKUST-1 on MoS_2 nanosheet and to examine the adsorption behaviour of CO_2 on MoS_2/HKUST-1 hybrid by experimental and computational study.

iii) To analyse the thermal behaviour of pure HKUST-1 around its transition temperature range, and to study the relationship between temperature and the formation of CuNP/GO, and to learn the physical properties of different CuNP/GO under a range of temperature.

iv) To obtain controllable and effective structure of new catalyst, and to test its efficiency in CO catalytic oxidation.

Prompted by the research objectives, the strategy of this work is concisely described as follows:

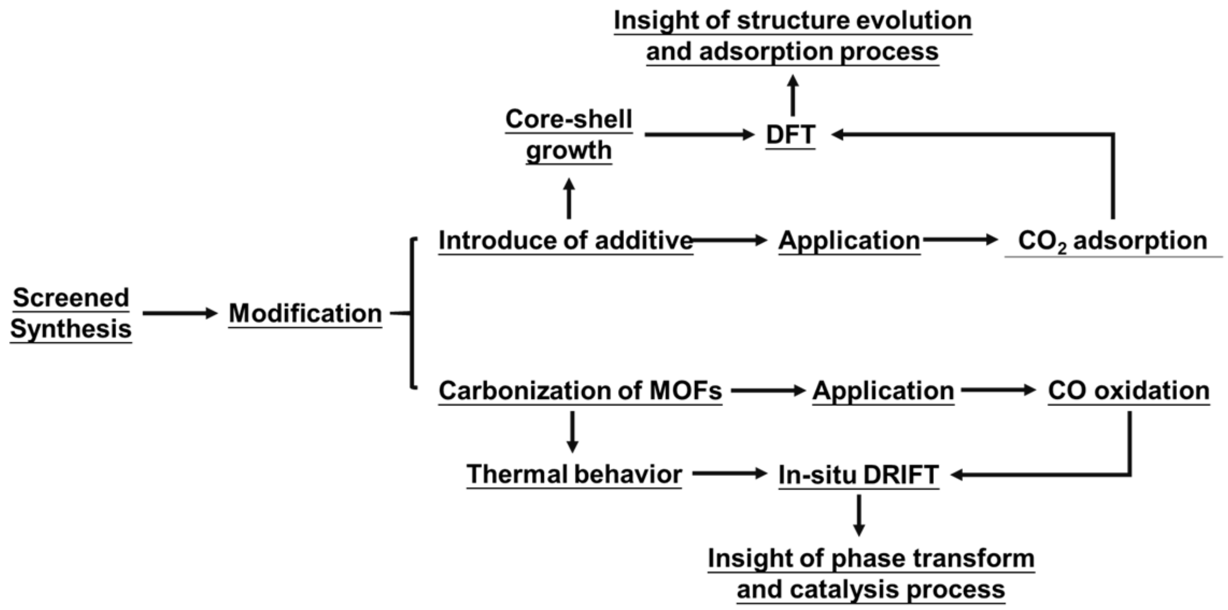

Figure 1-3 Research Plan

To develop MOFs with improved affinity for gas adsorption and its potential in certain catalytic reaction, this thesis consists of a synthesized HKUST-1 with high textural properties, a novel core-shell structured MoS_2/HKUST-1 hybrid, and a layered structured CuNP/GO via methodical carbonization. From the research plan in Figure 1-3, the synthesized HKUST-1 with high textural properties needs rigorous screening under various synthesis conditions. The variables of condition include reaction period, temperature, selection of activation combination and degas condition. After these screenings, precise control of MOFs crystals in morphology, size and textural properties can be obtained and can become a guidance for the larger-scale application. Before direct application of the lab-scale MOFs, there are two accessible approaches to optimize and transform the structure of HKUST-1, so as to making it easier to withstand a harsh condition. Firstly, the additive effect has been widely used for post-synthetic modification of MOFs. Here, MoS_2 quantum was chosen as a participant and led HKUST-1 to grow on their outside as a coat. Besides, computational and experimental methods repeatedly verified the possibility of the formation of the structure. As for the second method, the transformation of HKUST-1 into graphitic carbon would be a facile and simple method to stabilize its new physiochemical properties and endure harsh conditions. The process of carbonization has been investigated by the In-situ DRIFT to explain its evolution of graphitization. After that, the optimal CuNP/GO product was tested in fundamental catalytic reaction, i.e., CO oxidation. The catalysis process will combine In-situ technology with conventional experiment to explain the effect of CuNP/GO on CO and O_2 molecules. The entire thesis is revealed by In-situ techniques or DFT calculations to account for the observation during the reaction from the atomic level.

1.3 Structure of the thesis

Chapter 1. Introduction

This chapter provides a general background of MOFs development related to the thesis and a scheduled technical route, as well as an overview of objectives.

Chapter 2. Literature Review

This chapter introduces a detailed lifecycle of HKUST-1 as an example of MOFs, in terms of preparation, modification and its industrial application.

Chapter 3. Experimental Details

This chapter presents experimental rigs and steps involved in the research. The synthesis approach of original MOFs, MoS_2/HKUST-1 hybrid, and CuNP/GO are provided. All characterization means are described from their mechanisms and operation processes. The catalytic reaction process and gas adsorption test are briefly summarized. The calculation procedure is mentioned, as well.

Chapter 4. Nano-scale HKUST-1 under and its application in CO_2 capture

This chapter examines the effect of synthetic condition (reaction temperature, period, activation condition, degas condition) on the textural properties, morphology and size of HKUST-1 crystals. The relationship between these variables and HKUST-1 physical features is explained in detail. The CO_2 adsorption capacity is tested via static and dynamic adsorption, where the larger surface owns higher CO_2 uptake. The optimal product is T85-3-Pm4-120, which is reacted at 85 ^{o}C and activated with methanol in the solid phase, finally degassed under 120 ^{o}C by air dryer. This chapter was published in

Microporous and Mesoporous Materials, Volume 270, 2018, Pages 249-257.

Chapter 5. MoS_2/HKUST-1 core-shell composite and its application of CO_2 capture

This chapter adopts a ‘one-pot’ synthesis method for the growth of HKUST-1 on MoS_2 quantum dots to prepare MoS_2/HKUST-1 core-shell composites. A series of such composites was prepared with different MoS_2 quantum dots and HKUST-1 molar ratios. Image characterization and physical properties tested all verify the formation of core-shell structure with a large surface area (1638.9 m^2/g for MH-2) and a high CO_2 uptake (4.75 mmol/g). In addition, the growth of HKUST-1 on MoS_2 quantum dots and the interaction among the composite and CO_2 were revealed via DFT calculation. The details will be considered within this chapter.

Chapter 6. The thermal behaviour of HKUST-1 structure in different temperatures

This chapter reveals the thermal behaviour of HKUST-1 in a temperature range of structural failure. Through a facile and effective method of pyrolysis, the treated HKUST-1 exhibited various structure as a function of temperature. After 330 ^oC, the graphitic carbon appeared, loading large amount of Cu nanoparticles. Through In-situ and conventional characterization, the results revealed that decomposition of HKUST-1 was promoted with local vacancy sites (unsaturated Cu site or incomplete deprotoned carboxylic group). The results also showed different temperature and different prolonged isotherm step both influenced the size of CuNP on the graphene oxide sheet.

Chapter 7. Construction of CuNP/GO catalyst and its application in CO catalytic oxidation

This chapter studied the CO oxidation on CuNP/GO catalyst surface via In-situ DRIFT.

The indispensable characterizations were employed to determine the effect of Cu content and metal particle size distribution on the catalyst activity and define the structure-performance relationship. The detailed catalytic eigenvalues were measured through catalytic temperature gradient. In-situ technique exhibits CO would bind to the surface of Cu(I) or Cu(II) of Cu_4O_3 and then combines with the surrounding dissociated oxygen atoms or lattice oxygen atoms to form CO_3^{2-} followed with the presence of formate on the surface at 180 ^{o}C.

Chapter 8. Conclusions and recommendation for future work

This chapter contains the overall conclusions of the thesis and gives some suggestion for future work.

Chapter 2 Literature review

2.1 Introduction

Metal organic frameworks (MOFs), a group of porous coordination polymers (PCPs) [19], are an emerging class of crystalline porous materials self-assembled by metal-containing nodes and organic linkers, which are regarded as the secondary building units (SBUs) [20]. Towards further understanding the structure of SBU in MOFs, it is necessary to have a brief overview on the evolution of metal-organic compounds. When MOFs have not yet been developed, the coordinated networks including single-metal nodes connected with organic linkers [i.e., $NC(CH_2)_4CN$] were prepared in 1959, which is considered as “former MOFs” [21]. Many studies devoted to the preparation of various coordinated networks [22-25]. However, these coordinated structure was limited by the mode of single-metal nodes linking. Until 1998 [26], a true MOFs, termed as MOF-2 was synthesized, which was the formation of two-dimensional porous layers stacked by SBUs. Afterwards, characteristics and potentials of MOFs received extensive attention and recognition with efforts of numerous chemists like Yaghi et al. [27].

The unique characteristics of porous materials include easily adjustable pore size and rich multilevel pore, comprised of micropore and mesopore. The formation of the simple unit and complex structural material only requires modulating the connectivity of the inorganic moiety and the nature of the organic linkers [28]. These feasible means can obtain the coordination material with (1D, 2D and 3D) different dimensional frameworks, and 2D and 3D framework contain a large number of uniform pores or open channels [29] as shown in Figure 2-1. Over the past thirty years, the term of MOF was familiar with

Yaghi et al. [30] concerning a 3D MOF. Unlike zeolites [31], this crystalline material is not pure inorganic compounds but is a member of organic-inorganic hybrid polymers [32]. Normally, MOFs can be classified into iso-reticular MOFs (IRMOFs) [33], Zeolitic Imidazolate frameworks (ZIFs) [34], and zeolite like MOFs (ZMOFs) [35], covalent organic frameworks (COFs) [36] and porous organic polymers (POPs) [37]. Due to the unique textural structure and excellent physiochemical properties, MOFs have been applied to various fields, such as energy storage [38], CO_2 adsorption [39], toxic gas storage and separation [40], catalysis [41], etc.

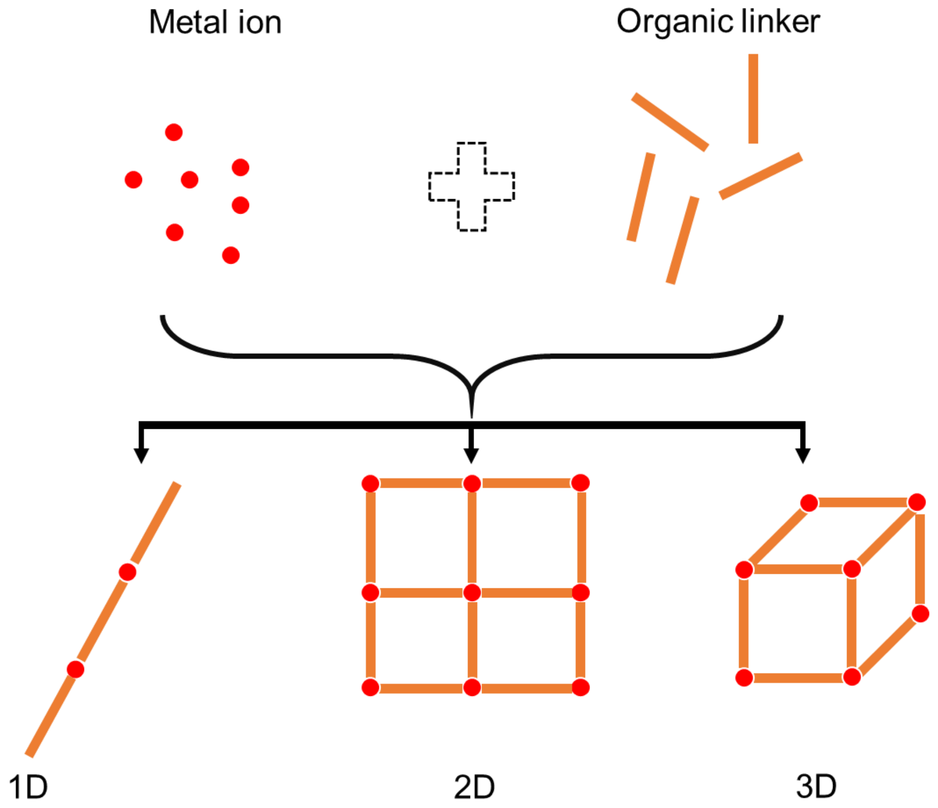

Figure 2-1 Schematic representation of the formation of MOFs with different dimensionalities (1D, 2D and 3D)

As one of the most widely used Cu-based MOF, HKUST-1 (i.e. MOF-199 or $Cu_3(BTC)_2$), consists of 1,3,5-benzenetricarboxylate (BTC) and a di-nuclear $Cu_2(CO_2)_4$ paddlewheel cluster [42]. The 3D-structure of HKUST-1 reveals the small pore in the octahedral cage of HKUST-1 has an aperture of 10 Å and the two large pores in the cub-octahedral cages are aperture of 14 Å [43] in Figure 2-2. The coordinatively unsaturated copper sites (CUSs) easily adsorb guest molecule that can be evacuated via an activation process. Once the Cu Lewis acid sites are opened, the sites can be occupied with target molecules for further application of molecule capture and catalysis. Based on the development and design of HKUST-1, the scope of this review presents the fundamental information of MOF in terms of preparation and its tunable parameters. Likewise, the modification of MOFs would be described to overcome the inherent shortcomings of MOFs for further applications. Furthermore, the utilization of pristine HKUST-1 and modified HKUST-1 based materials were discussed in industrial application. The comprehensive review gives a deeper insight of specific MOF (HKUST-1) development, and also suggests the extension of MOFs area in preparation, modification and application.

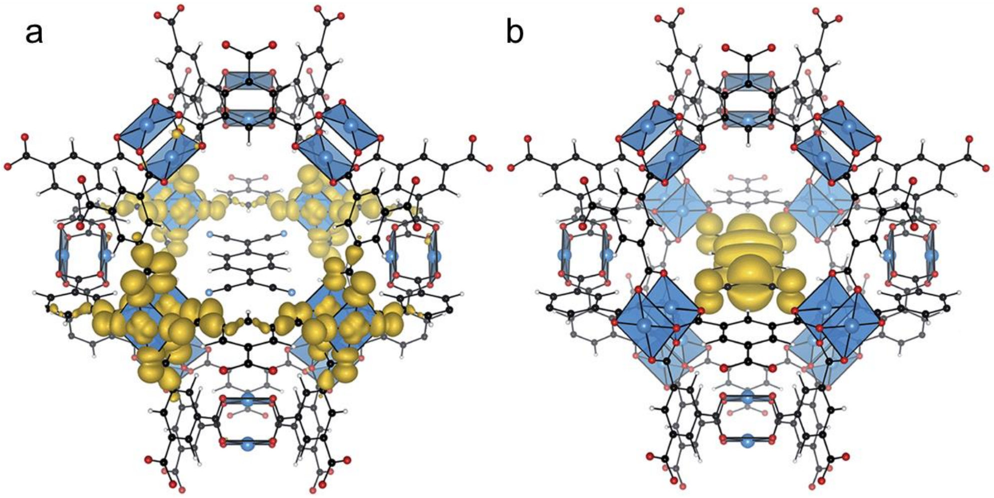

Figure 2-2 Three distinct internal pores in HKUST-1 [43]

2.2 Preparation

The different textural features of MOFs can be derived through the control of various parameters. The main parameter for the preparation of a MOF is the structural components, such as the **ligands** and **metal ions**. Geometry (bond angle, length, volume) and chirality of the ligands play an important role in MOF preparation. Similarly, the size, oxidation state and charge-accepting ability (from ligands) of the metal ions determine the formation of MOF texture (porosity, geometries and sizes). Thus, distinct choices of ligands and metal ions diversify the types of SBUs through the precise synthesis regulation of predictable framework.

MOFs can be prepared via various methods starting from conventional solvothermal synthesis, microwave-assisted synthesis, electrochemical synthesis and sonochemical synthesis to mechanochemical method. In a solvo-condition, a polar solvent, such as DMF, MEOH, EtOH, etc., is introduced into the reaction system that contains the ligands and metal ions. The modulator is another parameter for the controlled formation of MOFs, which determines the nucleation rate, particle size of MOFs. The removal of solvent impurity trapped in MOFs interior pores is a challenging task, which may affect the possible application in some fields, such as gas storage and catalysis. This process activates MOFs to uncover their permanent porosity and removes guest molecules (solvent or other substances involved in reaction) in the interior of MOFs without imperilling its structural integrity and porosity.

2.2.1 Synthesis methods

As a milestone, Nalco Chemical Company and Yaghi jointly declared a MOF synthesis under solvothermal condition [44, 45]. Encouraged by the tremendous success, numerous studies have been devoted to exploring and designing the novel and commercially practicable approaches in order to prepare different MOFs, pursuing the aspect of efficiency, reproducibility and economic benefit [46]. Electrochemical synthesis of MOFs was earliest commercialized by BASF [47] and their strategy adopted exclusion of anions using an electrode as metal ion sources. Microwave-assisted synthesis [48], and sonochemical synthesis [49] lead to the faster crystallization rate with smaller crystals. The use of mechanochemical synthesis [50] enables the preparation of MOF with free solvent and without heating, as well as, the production of MOF can lessen the activation labour after the mechanochemical synthesis. In addition, the preparation of HKUST-1 is also described throughout the history of MOFs synthesis, and the synthesis methods of HKUST-1 have been evolved into the current five main methods, such as conventional solvothermal, microwave-assisted, electrochemical, sonochemical and mechanochemical synthesis.

2.3.1.1 Conventional solvothermal (hydrothermal) synthesis

Conventional solvothermal synthesis is implemented in a closed vessel under autogenous pressure or in reflux unit under ambient pressure. When the synthetic solution only contains H_2O/EtOH, the synthesis method would be named as hydrothermal synthesis. Usually, the MOFs prepared in closed vessels would own more regular grain structure and a higher initial specific surface area before activation, than one prepared in reflux unit. Since the first HKUST-1 was successfully synthesized in 1999 [42], there have been plentiful synthesis studies focusing on the choice of synthetic conditions (solvent category, synthesis temperature, period, and other parameters) to optimize the HKUST-1 texture. Some HKUST-1 related studies are presented in Table 2-1.

Table 2-1 Textural properties of HKUST-1 prepared via solvothermal (hydrothermal) synthesis

Method	Solvent	Temp. °C	Period h	S_{BET} m^2/g	V_{Pore} cm^3/g	Activation Agent
Solvothermal [51]	DMF, EtOH, H_2O	85	8	1482	0.83	MeOH
Solvothermal [51]	DMF, EtOH, H_2O	85	20	698	0.39	CH_2Cl_2
Solvothermal [52]	DMF, EtOH, H_2O	85	24	921	0.49	CH_2Cl_2-DMF
Solvothermal [53]	DMF, EtOH, H_2O	85	20	1507	0.75	DMF-CH_2Cl_2
Solvothermal [54]	DMF	75	24	1261	0.70	DMF-NH_4NO_3 EtOH/H_2O-EtOH/H_2O
Solvothermal [55]	DMF, EtOH, H_2O	100	10	1482	0.75	MeOH
Hydrothermal [55]	EtOH, H_2O	140	48	857	0.43	H_2O
Hydrothermal [56]	EtOH	120	14	1510	0.57	H_2O-EtOH
Hydrothermal [56]	EtOH, H_2O	120	14	1253	0.47	H_2O-EtOH
Hydrothermal [57]	EtOH, H_2O	100	13	1218	0.53	EtOH/H_2O
Hydrothermal [42]	EtOH, H_2O	180	12	692	0.33	CH_2Cl_2
Hydrothermal [58]	EtOH, H_2O	120	12	-	0.41	
Reflux [56]	EtOH	Bp	48	1624	0.62	H_2O-EtOH
Reflux [59]	DMF	Bp	12	1239	0.62	DMF-H_2O

The order of chemicals in the activation agent column is written in the order of activation steps in the corresponding research. Bp is the boiling point of solution. DMF is N, N-Dimethylformamide, EtOH is ethanol, MeOH is methanol.

Regarding the synthesis of HKUST-1 via solvothermal condition, it is always accompanied by the formation of the impurities. Most of them are derived from the incompletely reacted ligands and metal ions, and the other is metal oxide (i.e. Cu_2O) derived from metal ions. When HKUST-1 synthesized in EtOH/DI H_2O at 180 °C, the product can be detected to contain few Cu_2O impurity and its pore volume was blocked by these impurities with low value of 0.33 cm^3/g [60]. To eliminate this issue, several syntheses [52, 55, 57, 61] by adjusting temperature range (100 to 150 °C) and period (12 to 48 h) successfully prepared HKUST-1 without Cu_2O. Though Cu_2O-free HKUST-1 [58] was synthesized at 120 °C for 12 h, textural properties (0.41 cm^3/g) was not improved. To achieve free Cu_2O with high texture, some researchers started to try low temperature synthesis (reflux synthesis in ambient pressure) [56] [59], such the synthesized product without any Cu_2O impurities possessed the excellent specific surface area (SSA) by Brunauer, Emmett and Teller (BET) theory of 1624 (EtOH) and 1239 (DMF) m^2/g, respectively.

2.3.1.2 Microwave-assisted synthesis

Microwave(MW) synthesis represents a fast synthesis practice for the MOFs preparation compared with conventional solvothermal one [62]. In MW-assisted synthesis, a reactant mixture with an appropriate solvent is transported into a closed vessel and put in classical oven type-reactors for a suitable irradiation period at the proper microwave dielectric heating. In the MW unit, microwave irradiation triggers heating of the overall system by ionic conduction and dipolar polarization, accompanied with a rapid heating of the liquid phase [61, 63]. EtOH and EtOH/DI H_2O are often used as solvent for HKUST-1 preparation in MW [61, 64], also, butanol has been attempted [65]. The SSA of product remained similar [61]. Notably, a MW-assisted synthesis at an ambient pressure was recently suggested to synthesize HKUST-1 [66]. Several parameters (concentration of reactant, solvent type, temperature, reaction period, and MW power) would influence textural properties and yields of the as-synthesis HKUST-1. For instance, the increase of the reactant concentration improved BET SSA but decreased product yield. Solvents in presence of EtOH/H_2O or DMF reduced SSA drastically. The optimal product was prepared under the screened condition (630 W, 70 °C, and 10 min) with a solvent combination including EtOH, H_2O, and DMF (1:1:1, vol.%) and its BET SSA of and pore volume were 1863 m^2/g and 0.8 cm^3/g, respectively.

2.3.1.3 Electrochemical synthesis

Electrochemical synthesis is to exclude anions, like nitrate or chloride, resulting in prompt coordination of metal ions with ligand molecules for MOFs preparation. As a milestone of continuous production, the company BASF patented MOFs synthesis based on electrosynthesis in 2005 [47]. The method included an immersed Cu plate electrode in BTC ligand solution as an electrolyte. With a certain current or voltage for 150 min, the copper electrode releases Cu(II) ions into the solution and these free copper ions can be reacted with the dissolved BTC. The synthesized octahedral crystals of HKUST-1 has BET SSA of 1820 m^2/g. The other research also attempted to synthesize lab-scale HKUST-1 electrochemically [56]. The electrolyte using a mixture of BTC ligand and additive (methyl-tributyl-ammonium methyl sulphate, MTBS, to increase conductivity) was dissolved in different solvents, and the electrode was two copper strips. As a comparison of solvents, EtOH offered a better conductive environment than EtOH/DI H_2O [56]. Moreover, such produced HKUST-1 possesses 1309 m^2/g (BET SSA) and 0.5 cm^3/g (pore volume). Electrochemical synthesis lowers the requirement of high temperature and long reaction period. Besides, its product is quite pure with excellent textural properties.

2.3.1.4 Sonochemical synthesis

Sonochemical synthesis can make homogeneous nucleation through reducing crystallization time and particle size in contrast with solvothermal one [67, 68]. The substrate mixture is fed into a horn-type Pyrex reactor in an inert atmosphere, which is mounted in a sonicator unit equipped with an adjustable power output and no external cooling. The acoustic cavitation causes the formation and collapse of micro bubbles in solution and accelerates the reaction rate in the sonochemical synthesis, where local formation of high temperature and pressure renders rapid temperature ramp rate [69]. Furthermore, it was reported that the HKUST-1 yield for 1h via sonochemical synthesis is equivalent to HKUST-1 yield via solvothermal synthesis more than 10 h [70]. To create cavitation easily under low vapor pressure, HKUST-1 was also tried to prepare using deep eutectic solvents (DESs) including the mixture of choline chloride and dimethylurea [71] at a relatively high temperature, where DESs can act as a solvent and ligand. The final product had SSA of 1822 m^2/g and pore volume of 0.76 cm^3/g.

2.3.1.5 Mechanochemical synthesis

Although MW-assisted and sonochemical synthesis decreases time for MOFs preparation, they are always an extension of conventional solvothermal synthesis and cannot get rid of the solvent effect. In contrast, solvent-free advantages of mechanochemical synthesis must be considered. The mechanochemical synthesis of HKUST-1 requires no solvent containing powders of metal salts and ligands or accessibly uses a little MeOH for liquid-assisted grinding (LAG) mode, in a conventional batch ball mill [72, 73]. About the LAG mode, 4,4′,4″-benzene-tribenzoic acid (H_3BTB) as an additive was applied in reaction of H_3BTC and $Cu(OAc)_2 \cdot H_2O$, the HKUST-1 synthesized via the LAG would have higher crystallinity, the addition of liquid may improve the extent of liquid-phase crystallization without much different crystal formation rate [74, 75]. Though the decrease of particle size is generally operated with grinding, the long-term grinding could result in destruction of crystals [76, 77].

Of great practical importance, the microwave-assistant, electrochemical, sonochemical and mechanochemical can reduce the synthesis duration and enhance the reaction rate. For the microwave-assistant treatment, it can provide a large amount of energy to the molecules than others. However, the vessel walls are the coldest part in microwave heating, as well as, this limits the nucleation of bubbles only generated at the contact of the solvent with vapor, where effective reaction area is limited. The sonochemical approach can cause more serious changes on thermal impact and pressure differences, which can improve the contact area of precursor. Nevertheless, noteworthy should be thought that the volatile solvent is not favourable in this system, because the high solvent vapor pressure can affect the accompanied bubble implosion and decrease the final quality of the product. Different from these two methods, electrochemical and mechanochemical syntheses are comparatively popular to prepare MOFs. Electrochemical synthesis earliest initiates the continuous production of MOFs and produces relatively large output of MOFs industrially. However, the method requires lots of energy to support progress of reaction. Regarding mechanochemical method, it has become a future popular technology, and it allows reaction to proceed rapidly with a small amount of solvent or even without solvent. However, there is no systematic theory to explain the process when mechanochemical reaction occurs. Compared with these four methods, the conventional solvothermal synthesis requires a special equipment (autoclaves) which can withstand high pressure and extended duration up to several weeks or even months. In spite of those, the conventional solvothermal synthesis is able to gain higher yields and better crystallinity for MOFs, as well as controllable synthetic condition allows MOFs to develop reproducible solutions, due to the long period of synthesis. In addition, the presence of elevated pressure can result in temperature of solvent above its boiling point, which affords higher solubility of the precursors in the solution and enhances the reaction. Therefore, conventional solvothermal synthesis is still a competitive means to synthesize MOFs.

2.2.2 Reaction solvent media

Prior to the preparation of MOFs, a specific choice of reaction solvents becomes a focal issue, since different solvent media in MOFs synthesis have dissimilar effects on the formation of the coordination environment and bring about slightly distinctive characteristics of the same framework, i.e., connectivity and dimensionality. Solvents could be involved in coordination with metal ions or can also be a guest molecule in the structure of molded crystal. That is, the ligand deprotonation can be tailored by selected solvent media like DMF or by adding the basic solvent media [78]. These solvents can be transformed into correspondent amines at higher temperatures and thus deprotonate carboxylates.

Usually, some MOFs synthesis would rely on a dual-solvents system in conventional solvothermal synthesis, which generates various coordination modes of ligands. Some researcher studied the formation of HKUST-1 in H_2O/EtOH solvent systems [79]. The result indicated HKUST-1 cannot form in the absence of EtOH or the presence of a little EtOH in H_2O. While the content of EtOH reaches up to 30 vol.%, the HKUST-1 appears at an ambient temperature. Besides, the crystal size of as-synthesized HKUST-1 can be affected by the content of the mixed solvent, ascribed to the strength of hydrogen bonds between the solvent molecules and ligands.

The effect of a mixed solvent system was further studied in electrochemical synthesis. A preliminary study [80] to optimize electrochemical synthesis of HKUST-1, has been undertaken by modifying the electrochemical synthetic conditions including solvent combination of EtOH, H_2O, MeOH and DMF. Those results presented that the optimal synthesis condition of HKUST-1 should be in a solvent combination of H_2O : EtOH (1:1). Compared with synthesis in H_2O and EtOH, the formation of HKUST-1 in DMF or mixture of DMF and H_2O required additional activation, and DMF would easily occupy in the pore and act as a coordinated solvent like H_2O coordinated. The XRD patterns further proved the crystallinity of HKUST-1 in the absence of DMF or few DMF would be preferable to one in absolute DMF solvent. Similarly, another research announced solvent media also influenced the crystallization of HKUST-1 [78, 81, 82]. It was observed that larger crystals formed when the H_2O percentage (from 10 to 50%, vol.%) was increased in the electrolyte H_2O/EtOH solvent, because the hydration of the Cu^{2+} cations from H_2O slowed down the reaction. In addition, H_2O content in the electrode was observed over 50% when detaching HKUST-1 crystals. In the case, a secondary phase in the product was detected as the presence of a catena–triaqua-m-(1,3,5-benzenetricarboxylate)-copper(II) compound [83]. Later, the solvent effect was investigated on the formation of HKUST-1 in different solvents (e.g., MeOH, EtOH, 2-propanol, acetonitrile, N,N-dimethylformamide (DMF), and dimethylsulfoxide (DMSO)) [84]. The results indicated that the increase of crystal size was caused by the increase of H_2O percentage in MeOH and EtOH but the use of H_2O in DMSO has no effect on the synthesis of HKUST-1. For morphology, HKUST-1 crystal morphology in DMF and acetonitrile is different from MeOH or EtOH. Besides, 2-propanol can induce the formation of uniform and less dense HKUST-1 layers. Tributylmethylammonium methyl sulphate (MTBS) is also used into HKUST-1 synthesis. However, it was found that MTBS used in HKUST-1 thin film formation could damage the Cu mesh and non-adhesive HKUST-1 crystals appeared at the anode under lower current density [82]. Another disadvantage of using MTBS could decrease the SSA of HKUST-1 due to the electrolyte salt blocked in its pores [56].

Therefore, no matter what kind of solvent media combination was applied into the synthesis of MOFs. It is essential whether the solvent used is easily removed from the unsaturated coordinated site or the pore/channel of MOF after synthesis, and does not affect the crystallization of MOF. Considering all potential solvents, the main four solvents can be listed as H_2O, EtOH, MEOH and DMF, however, H_2O has the highest affinity to coordinate with the metal centres, followed by DMF. While solvents such as MeOH and EtOH tend not to be coordinated with the metal centre in the presence of the H_2O and DMF, respectively. From the view of environmental benign and economy, the combination of MeOH/EtOH/H_2O would be a favourable choice for most of MOFs synthesis. It is not only polarity of theirs, but also owns smaller molecule size easier removed from as-synthesized MOFs through activation, compared with other solvent. These observations deserve further promotion to the design strategy for other MOFs.

2.2.3 Modulator

In MOF synthesis, the organic ligands used as linkers for metal ions usually are bidentate or tridentate carboxylic acids. The presence of high concentration ligand (i.e. high ligand-to-metal ratio) in MOF synthesis solution can limit the connectivity of metal ions and wrap the entire crystal seed, where crystal growth is restrained by excess ligand and causes smaller crystals [85, 86], but such case can decrease the efficiency of the deprotonation. Thus, an extra method to regulate the particle size of MOFs involves the addition of deprotonation agent (i.e., modulating agent or surface capping agent). The novel synthetic system with modulator becomes a buffer for the ligand deprotonation and relieves the interaction between metal ions and ligands. As a result, intermediate metal-ligand interaction leads to smaller crystals [83, 87, 88].

As modulators, triethyl amine (TEA) [89, 90] and hexadecyl-trimethyl ammonium bromide (CTAB) [91] have been extensively utilized with good compatibility in different MOFs synthesis [92-94]. The morphology and size of HKUST-1 crystals were investigated using various modulators whose properties are comparable during the synthesis procedure [95]. The sodium acetate and sodium formate as the modulator were also studied to direct the size and morphology of HKUST-1 [87]. Distinctively, the hierarchical octahedral-shape of crystals was synthesized from densely packed sub-micrometre crystals using TEA as the modulator. Despite that, an improper ratio of these modulators could produce unexpected crystalline structures [96].

2.2.4 Metal salt

For obtaining certain physiochemical properties of MOFs, the affirming particularity of the precursor plays a significant part in a synthesis process. Accordingly, it is necessary to optimize precursors for specific MOF preparation. Regarding HKUST-1 itself, BTC ligands is used as organic linker for copper ion sourced from different soluble copper salt in order to construct a framework. Commonly, copper salt, including $Cu(NO_3)_2$, $CuCl_2$, $Cu(SO_4)_2$, or $Cu(OAc)_2$, acts as the copper precursor. The different HKUST-1 MOFs were prepared with mentioned metal salts in a relatively eco-friendly media, e.g., near the ambient temperature with DI H_2O or temperature around the boiling point of EtOH [97]. That showed $Cu(SO_4)_2$ and $CuCl_2$ do not provide an appropriate copper source for BTC in EtOH solution with low yields, and even copper chloride does not form any HKUST-1 precipitate in EtOH solution, which was in good agreement with other literatures [96]. Thus, copper acetate and copper nitrate have become two alternatives for the preparation of HKUST-1 [98]. Despite that, it is reasonable to consider that the presence of SBUs already exists in $Cu(OAc)_2$ before HKUST-1 formation by metal-ligand exchange, but $Cu(NO_3)_2$ initially needs In-situ formation of SBUs before assembling of HKUST-1 component. Obviously, it is found that HKUST-1 precipitation settles down faster in $Cu(OAc)_2$, but a certain period of induction is detected before precipitation occurs in $Cu(NO_3)_2$. The different molar ratios of $Cu(NO_3)_2/Cu(OAc)_2$ and an analogous experiment with $Cu(NO_3)_2/Na(OAc)$ both show the formation of HKUST-1. Interestingly, the increase of the acetate ions results in the formation of an unknown by-product for both systems. Therefore, it is essential for a suitable choice of inorganic precursor to control over predictable network topologies, also, $Cu(NO_3)_2$ substitutes $Cu(OAc)_2$ as a metal source should be a rational choice [99] in HKUST-1 synthesis engineering.

2.2.5 Activation process

In numerous cases, the experimental observations of SSA and pore volumes in MOFs are seriously less than those theoretical values predicated on single-crystal structures, and inappropriate activation is regarded as a reason for the low-value observations. It was said “despite Nature's abhorrence of a vacuum it may be possible to devise rods (linkers) with sufficient rigidity to support the existence of solids with relatively huge empty cavities” [23]. The “abhorrence of a vacuum” is worsened, that is, the pores or channels are occupied by high boiling point solvents (e.g. DMF, DMSO, or N,N-diethylformamide (DEF)) that would become a necessary step for MOF synthesis process. To remove these impurities left in cavities, it would be required the significant capillary forces should be created during activation. On the contrary, concomitant surface tension can cause fully or partially destruction of frameworks. Therefore, there are five strategies to activate MOFs as followed, (i) conventional heating and vacuum; (ii) freeze-drying; (iii) chemical treatment; (iv) solvent-exchange; and (v) supercritical CO_2 ($scCO_2$) processing.

As an initial trial in the field, **conventional activation** is the removal of solvent and other guest molecules by direct heating and vacuum pumping. However, the kind of activation would provide poor efficiency to open the complete porosity of many MOFs and can result in partial or even full loss of porosity upon the activation [100]. Recently, the activation by benzene **freeze-drying** has been reported. This activation requires the MOFs to be immersed in and exchanged with benzene. The freeze-drying technique is subjected to a conventional step. After freeze-drying, the treated HKUST-1 is warmed at a low pressure, and then the benzene starts the transition of direct solid-to-gas phase, which limits the transition of liquid-to-gas phase and minimizes related capillary forces. In some cases, a

chemical treatment is desired to clean MOFs for exclusion of ionic species. When the removal of impurities cannot rely on evaporation, it is simply evacuated by heating or vacuum. This is due to non-volatility of isolated ions. Thus, when molecules like benzoic acid are utilized in MOFs preparation and are ligated as ions, chemical treatment, here must be a right strategy for MOFs. The extent of generality of these two approaches is unknown and limited by the features of benzene species in most of MOFs.

As extensively and successfully utilized activation strategy, **solvent-exchange** is to replace the high-boiling point solvent (e.g., DMF) or the lower boiling point solvent (e.g., $CHCl_3$) used in the synthesis, and then removing these solvents under relatively mild conditions. Compared with them, the use of **$scCO_2$** is a relatively new activation for MOFs that has proved to be widely applied. The $scCO_2$ is marked with a series of terms such as green, cost competitive and scalable. Activation by $scCO_2$ is developed based on the conventional solvent-exchange process and required solvents like EtOH (dissolved in liquid CO_2 and compatible with the rig) are exchanged with $scCO_2$ at high pressure (i.e., >73 atm) for several hours.

HKUST-1 possesses a large amount of micropore and high SSA. The published BET SSA range is from 692 to 2042 m^2/g (N_2 adsorption) [42, 101, 102]. The SSA of samples activated by flowing $scCO_2$ and conventional heating under evacuation from various solvents differs considerably in Table 2-2. The SSA of sample processed by only $scCO_2$ activation in absolute solvent is closed to that of material treated by conventional heating and vacuum. In addition of heating after $scCO_2$ activation, the samples present higher textural properties than before, and under 170 ^{o}C treatment had higher value than other comparable experimental ones [103], but the HKUST-1 activated from absolute EtOH was only five percent higher than conventional one. About the conventional heating under evacuation with different solvent, it can be found that the SSA of these samples increased in the order of HKUST-1 (DMF) < HKUST-1 (CH_2Cl_2) < HKUST-1 ($CHCl_3$) < HKUST-1 (EtOH) < HKUST-1 (MeOH), whose polarity increases in the following order: $CHCl_3$ < CH_2Cl_2 < EtOH < MeOH < DMF. Except for DMF, MeOH and EtOH are higher polar and favour hydrogen bonds. The other two solvents ($CHCl_3$ and CH_2Cl_2) are non-polar and polar aprotic solvents, respectively. The boiling points of these solvents vary from 40 to 100 °C. The factors to be considered in solvent selection are the change in boiling point of the solvent and coordinative interaction capacity for the HKUST-1 construction. Generally, samples using high polar solvents have high textural properties in the solvent activation [102]. Therefore, no matter what route is applicable to the activation of MOFs, it is also crucial to choose an exact activation solvent.

Table 2-2 BET surface areas (m^2/g) of HKUST-1 activated by flowing $scCO_2$ and conventional heating under evacuation.

Solvent	Flowing $scCO_2$ activation	Heating after flowing $scCO_2$ activation	Conventional heating under evacuation
N/A			1100 [102]
DMF	830 [103]	1737 [103]	1072 [102]
CH_2Cl_2	1098 [103]	1751 [103]	1168 [102]
$CHCl_3$	1394 [103]	1713 [103]	1245 [102]
EtOH	1610 [103]	1770 [103]	1718 [102]
MeOH			2042 [102]

Both pristine HKUST-1 synthesis methods were the same.

The activation process, which removes un-reacted metal salts, ligands, or solvents in MOFs interior, has been an important step for obtaining high SSA samples. Five primary strategies have been discussed as mentioned and there are usually multiple strategies to screen conditions for optimal activation. Besides, different strategies responding to different MOFs should have dissimilar effect. Each of the strategies has its advantage on certain class of MOF activation. Though utilization of $scCO_2$ activation for MOFs has promoted the textural properties of evacuated MOFs to a higher level, conventional heating under evacuation with proper activation solvent indeed is able to meet the almost of the product quality and application requirement currently. For HKUST-1, it is recommended at low temperature (85 ^oC) and vacuum condition to the remove guest molecules from the MOFs interior for replacing the synthesis solvent with a low boiling point, such as EtOH, MeOH, and CH_2Cl_2. In particular, HKUST-1 exchanged via MeOH presented considerably enhanced textural properties compared with that exchanged via CH_2Cl_2 [51].

2.3 Modification

Mostly, MOFs adopting the abovementioned synthesis routes consist of CUSs and mono- or bi-functionalized ligands. However, materials suffer from a list of structural problems such as their fragility to acidity, complex and long-term activation processes, and restriction in various applications (e.g., the framework collapse with moisture) [104]. A feasible method of escape from the weakness is the chemical modification of MOFs after the already formation of crystals. Supposing the MOFs is very robust and porous to enable post-transformations with framework integrity, plenty of available chemical modification approaches are supposed to adjust the framework components. Therefore, tuning MOFs based on the target application would perhaps improve their performance.

2.3.1 Post synthetically modified MOFs

In a broad sense, MOFs modified in a post-synthetic scheme is identified as chemical derivatization of MOFs; in a narrow sense, it may only involve the covalent bond formation with the MOFs. In general, the post-synthetic modification (PSM) method [104] can be branched as: (i) addition of dual ligands with diverse functionality during the pre-synthesis process, (ii) the tandem graft of various groups onto the monofunctional ligand by PSM, and (iii) the bifunctional ligand through separate reactions by PSM. Thus far, PSM has expanded the horizon of MOFs applications. In 1999, lab-scale HKUST-1 appeared in the world [42]. In its published study, it was referred the instability of axial ligands on SBUs allows them replaced by other molecules. To confirm the point, HKUST-1 treated by pure pyridine generate a new different formulation in intact MOFs, coordinated with pyridine as the new axial ligands. Remarkably, it was found that the direct addition of pyridine in the pre-synthesis of MOFs cannot produce the form of pyridine-decorated HKUST-1. With the aid of pre-synthesis modification, the modification of HKUST-1 entered a new era. Subsequently, another researcher attempted the growth of HKUST-1 on the MCF-NH_2 surface [105]. The grafted functionalities directed synergetic effect between two components, which generated extra porous structures at the interface and thus improved CO_2 uptake. Among the samples, the optimal sample showed the highest BET SSA (1539 m^2/g) as well as CO_2 uptake (3.89 mmol/g), and it is much better than that of pristine HKUST-1. It should be mentioned in the presence of amino groups on the surface led to considerable CO_2 uptake. Besides, to improve the multi-function of HKUST-1, as-synthesized HKUST-1 was chemically modified with ethanedithiol to add thiol groups, and then the vinyl-containing ionic liquid was fixed with thiol groups on carriers. A bifunctional material [HVIm-$(CH_2)_3SO_3H]HSO_4$@HKUST-1 (IL@HKUST-1) [106] was prepared, with both Lewis and Brønsted acid sites. The material was examined in the esterification of oleic acid with EtOH, and the conversion of oleic acid reached 92.1% without any loss after five times of recycle.

2.3.2 Core-shell structured MOF composites

Apart from direct use, MOFs can be further utilized either as a core substrate or as a coat substance to merge functional materials. Effectively, MOFs are integrated with different functional materials to form core and shell structured composites, which are an accessible route to further broaden MOFs' ability or create possible functionality for potential application [107]. Therefore, plentiful HKUST-1 based composites have been incessantly synthesized by MOFs assembled with functional species, such as graphene [108], graphene oxides [109], carbon nanotubes [110], metal nanoparticles(NPs) [111], nano-rods [112], metal oxides [113], and MOFs [114], have shown a striking performance in gas storage [109, 113], catalysis [110, 111, 113], energy storage [111], hydrogen generation [112], et al. In these hybrid materials, the integrating of the individual MOFs and functional species together not only provides multifunctionality but also brings new physiochemical properties. The incorporation of MOFs and functional materials can simultaneously broaden the application areas of both.

2.3.3 Carbonized MOF derivatives

It is approved that porous carbons, metals, metal oxides, and their multi-component compositions are prominent inorganic materials in the field of nano engineering. The porous carbon materials possess the high SSA and large pore volume as well as excellent physiochemical properties; their utilization is mostly decided by the textural and geometrical properties [115]. Likewise, MOFs have a highly ordered porous structure and abundant inorganic-organic ingredients, it was proposed as a sacrifice to generate a variety of nanostructures via carbonization, whose product could have the high SSA and narrow pore-size distribution [115]. For the conversion from MOFs to carbon with [116-118] or without [119, 120] a secondary carbon source, the heating condition (i.e. heating rate and target temperature) and the nature of MOFs (i.e. crystal-size and composition) are critical to adjust carbon materials with various functionalities and structures. To obtain porous carbons, recently, HKUST-1 was annealed from ambient temperature to 600 ^{o}C under Ar flow at the rate of 5 ^{o}C/min, and then heated to 800 ^{o}C at the rate of 3 ^{o}C/min with isothermal step of 5 h. The carbon derived from HKUST-1 exhibited SSA of 50 m^2/g after washed by HF solution [121]. However, the other research studied the metal retained on MOF residues [122]. Though tuning the temperature and isotherm period of HKUST-1 carbonization, a systematic synthesis study was exploited for a Cu NP embedded on porous carbon composite. In addition, such prepared Cu NP embedded porous carbon composite exhibited good sensitivities towards glucose (detection limit: 3.2×10^{-9} M). This is approvable for the attempt of unusual PSM method on the MTC (MOFs to carbon) of HKUST-1. More than this trial, numerous carbonization studies have participated in preparing inorganic materials of Cu [123], CuO/Cu_2O [124] derived from HKUST-1, with controllable size and morphology.

MOFs carbonization is simple and effective to obtain metals, metal oxides and their composites, which are hetero-atom doped with carbon or a graphitic carbon layer. These derivatives have tunable morphology and enhanced conductivity. This originates from the high textural properties, the distinctive crystalline framework and the orderly dispersed metal-organic component of MOF.

2.4 Applications

One intention of synthesizing MOF is modifying MOF by designing their physiochemical properties without any change of the intrinsic structure. The advantage of coordinatively unsaturated metal sites (CUSs) of MOFs and their high SSA guarantee a high adsorption capacity of different gases. Therefore, MOFs based materials are fascinating in the storage and separation of gases and catalysis.

2.4.1 Energy storage

Currently, hydrogen and methane both are seen as the two future clean energy carriers. Compared with conventional fuel (i.e., gasoline), two of them own higher gravimetric heats of combustion (120 MJ/kg for H_2, 55.7 MJ/kg for CH4 vs. 46.4 MJ/kg for gasoline) [125-127]. Besides, hydrogen has zero CO_2 emission, and methane has a relatively lower CO_2-to-energy content compared to gasoline. More importantly, it has become an urgent issue to replace the use of petroleum-based gasoline and diesel fuel. That is, high storage of H_2 and CH_4 based fuel becomes the ultimate pursuit of any fuel-cell related technologies. The physisorption of H_2 and CH_4 on high SSA materials is an effective answer towards the matter. Yaghi et al. demonstrated the potential and exceptionally high uptake of MOFs-based materials for CH_4 and H_2 storage in 2002 [100] and 2003 [128], respectively, which is the milestone of MOFs as an available energy media. Generally, H_2 tends to interact physically with the surface of MOF pores through van der Waals forces at ambient temperature and low pressure [129]. Hence, the reduced H_2 uptakes in numerous MOFs were observed at a high temperature. HKUST-1 and MOF-5 (IRMOF-1) as a comparison were tested about their H_2 adsorption properties [130, 131]. The H_2 uptake of HKUST-1 (13 mmol/g) at 1 bar and 77 K was 2-fold amount of MOF-5 (7.5 mmol/g) [130]. However, MOF-5 (25.5 mmol/g) had a significantly higher H_2 uptake than HKUST-1 (18 mmol/g) at 65 bar [131]. At low pressures, the adsorbed hydrogen is substantially dominated by the binding strength between H_2 and CUSs, while the adsorbed H_2 amount at high pressures is mostly dominated by the SSA [132]. Furthermore, it can be recommended that a completely activated HKUST-1 could improve its maximum hydrogen uptake (20 mmol/g at 26 bar and 77 K) [51]. A membrane, including HKUST-1 on a Cu-net, was used to separate H_2/N_2 mixture, where H_2/N_2 separation factor was 7 at the ambient temperature and pressure [133].

On the contrary, the non-physisorption of H_2 on HKUST-1 was also explored sine the notable irreversible hydrogenation process occurs above room temperature [129], where H_2 dissociates on the Cu(II) sites and reacts with SBUs chemically, resulting in the hydrogenation process ($Cu_3(BTC)_2 + 3H_2 \rightarrow 3Cu + 2H_3BTC$). The observation of HKUST-1 indicates that the open metal site should be highlighted during designing the MOF based hydrogen storage material, because too strong interactions between H_2 and metal site possibly destruct the CUS configuration. Also, the factor of high temperature could limit the application of such MOFs in hydrogen.

Analogy with H_2 adsorption, it was testified that the adsorption of CH_4 on HKUST-1 is mainly through two binding sites: (i) on CUSs by the enhanced Coulomb interaction and (ii) at potential pocket sites via the enhanced van der Waals interaction [134]. The methane of 160 cm^3(STP) cm^{-3} was adsorbed at the CUSs and window site of the small octahedral cage of HKUST-1 at 25 °C and 35 bar. The pelletized sample of HKUST-1 [135] keeps CH_4 adsorption capacity of 8 mmol/g at 303 K and 54 bar. Except for that, HKUST-1 membrane [133] has a CH_4/H_2 separation factor of 6.

2.4.2 Carbon dioxide storage

Currently, anthropogenic CO_2 emission to the atmosphere is a primary climate problem, as followed, it is an urgent need to lower cumulative CO_2 emission from industrial activities for the elimination of its impact on climate change [136]. Accordingly, it is an emergency action to advance a series of carbon capture storage (CCS) materials and related techniques that can effectively reduce the regeneration cost [137]. Lots of sorbents for this purpose, such as activated carbon, zeolites and porous polymers, have been assessed. Among of them, MOFs become a desirable candidate for CO_2 capture. As a representative, HKUST-1 is one of the well-known MOFs for CO_2 capturing. The adsorption of CO_2 on HKUST-1 can proceed in three different ways [138]. (i) In the low coverage condition (1:1, CO_2 per Cu^{2+} site), CO_2 molecules adsorb on the CUSs. The CO_2 molecules on the sites are tilted toward the adjacent sites, and such arrangement cannot be kept until the horizontal interactions are strong enough. (ii) At slightly higher coverages, the CO_2 molecules favourably take up the opening windows of the small cages. (iii) At even higher coverages, the CO_2 molecules occupy the sites of the small cages and large cages. The binding strengths between CO_2 molecules and different transition metals can be clarified as the relative strength of electrostatic interactions from the effective charge of the metal atom in CUSs, which is sourced from incomplete screening of 3d electrons. As a comparison, four MOFs of HKUST-1, IRMOF-1, IRMOF-3, and $Zn_2[bdc]_2[dabco]$ were investigated theoretically [139], the simulation studied the effect of

CUSs, pore size, electrostatics, and ligand functionalization on CO_2 adsorption. Among these MOFs, the results elucidated HKUST-1 has the highest uptake at low pressures. The three pores of MOFs all influence CO_2 adsorption. Interestingly, the presence of H_2O molecules [140] can increase CO_2 uptakes in HKUST-1, which is coordinated to CUSs in the framework. About the introduction of CUSs into MOFs, the study [141] presented that doping of metals in MOFs enhance CO_2 adsorption capacities. Further, the effects of different impurities in flue gas mixture (H_2O, O_2, and SO_2) on CO_2 capture of HKUST-1 were considered as a technical reference for its industrial applications [142].

In practical, commercial HKUST-1, i.e., Basolite™ C300, showed a stronger CO_2 regenerability with a CO_2 uptake of 4 mmol/g (at 35 ^oC and 1 bar) in contrast of zeolite [143]. With the CO_2 pressure increasing at 25 ^oC, the CO_2 uptake of 10.6 mmol/g at 10 bar would be decreased to 9.54 mmol/g at 42.4 bar. Analogy to other results, a combination of experimental and theoretical study also proven the valid CO_2 uptake of HKUST-1 is 10.3 mmol/g at 30 ^oC and 5 bar [138]. HKUST-1 pellets prepared without a binder have an adsorption capacity of 2.68 mmol/g at 25 ^oC and 0.8 bar [52], which is relatively lower than 2.67 mol/kg [144] and 3.53 mol/kg [135] reported at the same pressure. Over a HKUST-1 membrane, the material [133] possessed 3.25 mmol/g CO_2 uptake and a separation CO_2/H_2 factor of 6.8 at 25 ^oC and 1 bar. Meanwhile, nine different MOFs were tested about the CO_2 uptakes in a range from 0 to 42 bar at 298 K, the performance of HKUST-1 CO_2 adsorption in low pressure conditions was ranked second among all MOFs, CO_2 uptake of HKUST-1 was lower 0.8 mmol/g than that of MOF-74 and was an approximately fivefold higher than that of MOF-177 (4.9, 4.1 and 0.8 mmol/g for MOF-74, HKUST-1 and MOF-177, respectively, at 298 K and 1 bar) [144].

2.4.3 Toxic gas adsorption

The discharge of anthropogenic toxic pollutants directly into the atmosphere, severely affects the eco-environment and human life. The valid capture, separation and eventually the degradation of these toxic pollutants are imperative for the safety of the environment and human health. These pollutants comprise toxic gases (NOx, SOx, CO, NH_3), heavy metals, and organics. Remarkably, porous materials are at the forefront to lessen the adverse effects of human activity in industry process [145]. On that account, the mentioned properties of MOFs should be maximized and applied into harmful gas treatment.

The adsorption of environmentally toxic gases on HKUST-1 was widely investigated. Over the HKUST-1, NH_3 adsorption in dry conditions would distort the MOFs structure without the collapse of crystal, due to a strong chemisorption on CUSs. Besides, similar to the perturbation in the adsorption of H_2O, the case of NH_3 adsorption is more intense [146]. The corresponding practical result [147] proved NH_3 uptake is 6.76 mmol/g at 25 ^oC and ambient pressure without moisture, whereas 50 % increase of NH_3 uptake was observed under the same conditions with moisture. The NH_3 molecules interact with the CUSs in HKUST-1 and link with H_2O adsorbed on CUSs. About SO_2 uptake in HKUST-1 at high temperature [148], the SO_2 uptake of HKUST-1 increased with rising temperature from 200 to 300 ^oC. A continuous heating (up to 400 ^oC) results in the adsorption of a little SO_2. Generally, it is found the maximum SO_2 uptake is 0.7×10^6 mol/mg in the temperature range between 200 and 500 ^oC. The adsorption behaviours of H_2S and NO_2 with/without moisture conditions were also studied, the results showed that the occurrence of adsorption is related to the existence of CUSs, which attracts H_2S and NO_2 gas molecules.

These sites induce both adsorbed species to react further with these unsaturated Cu and form the sulphate and nitrate of copper. In the contrary of SO_2, CO_2 and NH_3, the uptakes of H_2S and NO_2 on the adsorbents decreased with moisture compared to those without moisture [149]. The other research also indicated HKUST-1 has a certain adsorption capacity for sulphur hexafluoride (6.38 mmol/g at 295 K and 4 bar) [55] [45].

In addition of the NO and O_2 storage [150, 151], The adsorption behaviour of Ar, CO, and N_2 over the HKUST-1 have been investigated [55]. For hydrocarbon adsorption and separation, small aromatic compounds [152], high-molecular weight hydrocarbons [153], methane and n-butane mixture [154], propane and ethane [155], n-butane (nC4), iso-butane (iC4), 2-methylbutane (2MB), and 2,2-dimethylpropane (neoP) [156] were tested by HKUST-1 based materials. In the aspect of purification, removal of tetrahydrothiophene (THT) in methane [157], and pressure swing separation of rare gases (krypton and xenon) [157] were also attempted, and the efficiency of purification was high using HKUST-1. As for the removal of heavy metal ion (Hg^{2+}) from aqueous solution [158], the pristine HKUST-1 did not have the adsorption ability for Hg^{2+} ions, but the thiol-functionalized HKUST-1 showed a high affinity to Hg^{2+} ions and the removal efficiency reached 99% after 24 h at an ambient temperature (3.57 mmol/g of maximum Hg^{2+} adsorption capacity).

2.4.4 Catalysis

Labelled with high porosity, tunable functional surface, and isolated metal sites, MOFs are supposed as an emerging catalytic material [159]. Due to great amounts of CUSs, MOFs can inherently act as Lewis acid catalysts [160]. A class of MOFs exemplified by HKUST-1 owns a large amount of inherent Lewis acid site, which is mainly donated by CUSs. The type of MOFs shows strong interactions with polar guest molecules on CUSs, whose isosteric heats of adsorption were high [53]. However, for the existence of dissociation-association mechanisms, the structural rearrangement of MOFs is undesired, which results in the potential collapse of the network. In the aspect, various post-synthetic modifications become an effective method by importing extra catalytic functionalities to the surface of MOFs interior [58]. As known, MOFs cannot stand above 330 ^{o}C and become unstable in moisture or polar solvents, where the metals or ligands could leach out [161-163]. Thus, poor stability has been a crucial problem towards MOFs and narrows application range of MOFs in heterogeneous catalysis [58]. With the rescue of MOF treatment, modified HKUST-1 has been tested in different catalytic reaction, i.e. addition, redox, cyclization, substitution, and hydrogenation.

As a common addition reaction, **cyanosilylation** allows the addition of nitrile groups and silyl groups via double bonds or triple bonds catalysed on Lewis acid sites. The meso-HKUST-1 as Lewis acid catalysts was used for cyanosilylation reaction of benzaldehyde [164]. The result indicated the introduced mesopores of meso-HKUST-1 could improve mass transfer and make reactant highly accessible to Lewis acid Cu sites.

In the field of redox reaction, **electrochemical reduction of carbon dioxide (ERC)** using different electrodes in electrolytes has been broadly investigated. However, the observation was found the hydrocarbons intermediates can only be effectively formed on Cu-based electrodes [165]. As known, the problems of Cu-based electrodes are the low reaction area of electrodes and low current density in conventional ERC technology. To solve the problem, gas diffusion electrode (GDE) adopted a strategy of HKUST-1 loaded on carbon paper. The faradaic efficiencies (FEs) of CH_4 on HKUST-1 based GDE are 2~3 fold higher than that of conventional GDE under negative potentials (-2.3 to -2.5 vs SCE), and the FE of the side reaction (hydrogen evolution reaction) was dropped down to 30% [166].

The **oxidation of C-H bonds** is one of the essential and primary reactions in organic synthesis [167]. As an example, the benzylic oxidation of C-H bonds is an efficient route to prepare high value chemical feedstock from low cost raw materials like alkyl aromatics. In this sense, core-shell structure HKUST-1@Fe_3O_4 NPs have been attempted through the growth of HKUST-1 shell of carboxyl groups attached onto the core of Fe_3O_4 chemically. Such structured MOF performs excellent catalytic activity for the benzylic oxidation of C-H bonds (up to 99% conv. and 99% sel.) and excellent recovery and re-use without loss of activity after magnetic separation [168].

Besides CO_2 reduction, it is another feasible strategy to turn CO_2 into other cyclic carbonates via the **cyclization reactions** between CO_2 and epoxides to remediate the greenhouse effect. As mentioned, the constructed HKSUT-1 is definitely qualified as a preeminent catalyst for chemical fixation of CO_2. A CO_2 cyclization reaction was investigated for 48 h through the catalysis of HKUST-1, where the condition was under CO_2 pressure of 1 atm and at the ambient temperature. The reaction yields, using HKUST-1 catalysed epoxidation, were 65% for 2-methyloxirane, 54% for 2-ethyloxirane, 56% for 2-

(chloromethyl)oxirane, and 57% for 2-(bromomethyl)oxirane with correspondent turnover frequency (TOF) values of 135.4, 112.5, 116.7, and 118.8 h^{-1} per Cu_2 cluster [169].

One category of **Friedel-Crafts substitution reactions**, alkylation reactions, proceeds by substitution of electrophilic aromatic on Lewis acid catalysts. HKUST-1 was used for the sono-synthesis of bioactive compounds and bis(indolyl)methanes, through a Friedel-Crafts substitution reaction. The high catalytic activity of commercial HKUST-1 was evidenced by the high yield of bis(indolyl)methanes (up to 85%) [170].

Hydrogenation involves the reaction of H_2 and another compound to synthesize saturated hydrocarbons, aldehydes, and alcohols [171]. In this reaction, the unsaturated hydrocarbon molecules require arriving at the Lewis acid site of catalysts, which activates the alkenes and splits hydrogen atoms [172]. One of the reported strategies through incorporating functional species into MOFs was to obtain Pd/Fe_3O_4@HKUST-1. The modified HKUST-1 can be used for hydrogenation of 1-octene in solution with conversion 100% and yield 99% [173].

2.5 Summary

MOFs are a class of emerging porous metal organic hybrids with exceptional textural properties and physiochemical properties that are controllable. This type of materials can potentially be used in adsorption and heterogeneous catalysis. In this review, many efforts have been made on the development of HKUST-1, a typical example of MOFs about its preparation, modification and industrial application.

In the section of its preparation, HKUST-1 with different texture properties can be produced by using conventional solvothermal, microwave, sonochemical, electrochemical or mechanochemical methods. Except for the conventional solvothermal methods, the other methods are more complicated involving the use of more synthetic ingredients, as well as, required synthesis conditions are critical. In contrast, the conventional solvothermal approach still is the optimal selection for its operability and accessibility. However, the current HKUST-1 preparation via conventional solvothermal synthesis requires long period and high synthetic temperature to obtain the final product. Therefore, this thesis would focus on the screen of synthetic condition to optimize synthetic step and reduce synthetic period and temperature. Briefly, $Cu(NO_3)_2$ as a metal precursor is dissolved in the solvent of EtOH/H_2O or EtOH in reflux unit, which would be an optimal strategy for the preparation of pristine HKUST-1. After that, the activation process is conducted in the solvent MeOH or MeOH/H_2O to exchange guest molecules in as-synthesis HKUST-1, and then the dehydrated HKUST-1 is degassed at 80-180 ^{o}C overnight. The general procedure of HKUST-1 preparation can obtain a high SSA and large pore volume. Meanwhile, the pre-synthetic and post-synthetic variables in HKUST-1 preparations are also discussed.

Before talking about its application, post-synthesis modification must be referred as a means to create diverse, active sites for adsorption and catalysis in MOFs, which mostly functionalizes the ligands of the material using various organic reactions as tools. Among a variety of methods, the strategies of core-shell structured MOFs and carbonization are remarkable, not only they provide novel structures, but they certainly solve the liability and lack of specific functionality in a potential application. Therefore, further post-synthetic modification should pay more attention to the development of these two.

Finally, the issues regarding the application must be discussed after the synthesis. Because of the presence of CUSs in HKUST-1, it promotes the MOF as a promising material for adsorption and catalysis. As a storage media, HKUST-1 has been explored about its capacity for fuel gas, CO_2, some toxic gas and even heavy metal ions. As a multi-level porous material, the different kinds of gas separation also have been examined. As a Lewis acid catalyst, various organic reactions that may involve copper-based CUSs have been tried and show good catalytic activity during the reaction. Noteworthy is that, the water or products could also have a competitive interaction on CUSs and prevent the continuous catalytic process. Sometimes, H_2 adsorbed at high temperatures can induce hydrogenation with unsaturated metals to destruct structure. It is possible that reaction conversions could be overestimated in case of reactant still adsorbed in MOFs. Therefore, the post-synthetic modification should further focus on the stabilization of active structure.

Chapter 3 Methodologies

3.1 Introduction

This chapter details experimental and theoretical methodologies with the purpose to study HKUST-1 synthesis and original/modified HKUST-1 as the adsorbent and catalyst. The chemicals and equipment used during the experiments were provided in the section 3.2 and 3.3. The processes for preparation of samples and general screening of candidate materials were then described in the section 3.4. Following that, experimental system and procedures were introduced. In the final section, the principles of different techniques for the characterization and analysis were described.

3.2 Chemicals

In this research, all chemicals were utilized without further purification and purchased from commercial sources. The following materials were used for all sample preparations in Table 3-1. To eliminate the influence of other elements, all chemicals used are analytical grade.

Table 3-1 The chemical reagents used in the experiment

No.	Chemicals	Grade	Supplier
1	$Cu(NO_3)_2$•$3H_2O$	Analytical Grade	Sigma Aldrich
2	MoS_2 powder	Analytical Grade	Sigma Aldrich
3	Ethanol	≥99.8%	Sigma Aldrich
4	Methanol	≥99.8%	Sigma Aldrich
5	Trimesic Acid	95%	Sigma Aldrich
6	Ultra-pure water	18.2 MΩ cm resistivity	Mille-Q integral 5 purification unit

3.3 Equipment

The details of equipment used in this study are provided in Table 3-2. One HKUST-1 preparation rig, which included a heating jacket, a refrigerated/heated bath circulator, and a reflux unit, was used to synthesize HKUST-1 MOFs. Online Mass Spectrometer was applied to analyse gas components in the exhausted gas from a catalytic reaction rig. A tube furnace was adopted to anneal HKUST-1 MOFs. Several furnaces and oven were employed for preparing samples.

Table 3-2 The equipment used in the experiment

Equipment	Model
Air Dryer Oven	BPG-9156 (Shanghai Yiheng Co., Ltd., China)
FTIR Spectrometer	Nicolet IS10（Thermo Scientific, USA）
Electronic Precision & Analytical Balance	MSE2.7S-000-DF (Sartorius, USA)
Electronic Balance	FA2104 (Shanghai Shunyu Hengping Co., Ltd.)
Temperature-Programmed Chemisorption Analyzer	FINESORB-3010 (Zhejiang Fantai Co., Ltd., China)
Scanning Electron Microscopy	FEI Nova NanoSEM 450 (FEI Technologies Inc, USA)
Energy Dispersive X-Ray Spectrometer	FEI Nova NanoSEM 450 (FEI Technologies Inc, USA)
Elemental Analyser	PE 2400 Series II CHNS/O (PE, USA)
X-Ray Diffraction	Bruker D8 A25 (Bruker, Germany)
Surface Area & Porosimetry System	Micromeritics ASAP 2020 Plus Physisorption (Micromeritics Instrument Corp., USA)
Transmission Electron Microscopy	FEI Tecnai F30 (FEI Technologies Inc, USA)
Heating Jacket	JK-ESS-100B (JKI Co. Shanghai)
Tube Furnace	SG-GL1200K (Shanghai Optics and Fine Mechanics Instillation, Chinese of sciences)
Refrigerated/Heated Bath Circulators	Thermo A40 (Thermo Fisher Scientific, USA)
Online Mass Spectrometer	OmniStar ThermoStar GSD320 (Pfeiffer Co., Ltd., Germany)

3.4 Experimental system and procedure

3.4.1 Preparation of samples

Batch synthesis for MOFs samples was considered in this project. The main experimental instruments were displayed in Figure 3-1. The temperature of the heating jacket and the temperature of the chemicals can be both monitored by the thermocouple of the heating jacket. The magnetic stirrer would be placed in the round-bottom flask, and the agitation speed of the stirrer can be altered by a digital display controller. The temperature and the agitation speed are presented on the electronic display. The activation process was also performed by heating via the heating jacket, while a condenser was connected to the round-bottom flask. The condenser was supplied with cooling water. The schematic shows the flow direction of the chilling water. Usually, the counter-current chilling water flow in contrast with steam direction to achieve a highly efficient heat exchange.

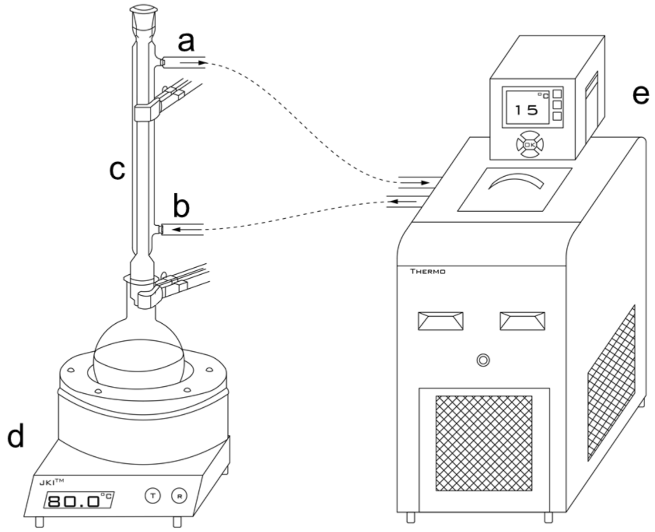

Figure 3-1 The equipment for HKUST-1 MOFs preparation. a, water out; b, water in; c, reflux unit; d, heating jacket; e, refrigerated circulators. The relative height of the instrument in the picture is consistent with the actual instruments.

3.4.2 Screening preparation of HKUST-1

The preparation of HKUST-1 MOFs consists of an activation step following by initiation at an increased temperature. Firstly, 0.03 mole of copper nitrate trihydrate (Sigma Aldrich, 98%) was dissolved in a 250 ml of deionized water to form solution A, while 0.02 mol of trimesic acid (TMA) (Sigma Aldrich, 95%) and 0.06 mol of Triethylamine (TEA) (Sigma Aldrich, 99.8%, anhydrous) were added in a 250 ml of ethanol (Sigma Aldrich, 99%) to form Solution B. These two solutions were then mixed and heated under constant stirring to the pre-set temperature level, i.e., 25, 50, 75, 80, 85 °C, and kept isothermal for a period of time (3, 6 or 9 h). The solution was subsequently cooled down to room temperature in an ice bath and centrifuged to produce pristine HKUST-1, which was activated using slurry state activation, powder state activation or slurry-powder state activation to remove internal impurities. The slurry state activation referred to the activation of the centrifuged HKUST-1 after synthesis; the powder state activation referred to activation of the dried centrifuged HKUST-1; while the slurry-powder state activation referred to the slurry state activation followed by drying and further activation of the HKUST-1 powder. In this research, the activation agents used were ethanol and methanol. The activation process was carried out in a reflux condenser. The amount of ethanol or methanol used was kept at the same level as 62.5 ml per gram of pristine HKUST-1. The activation process was conducted for 3 h. After that, the activated solution was centrifuged to obtain precipitation and dried into the powder state to obtain final HKUST-1 under 120 ^{o}C. The sample being activated by slurry/powder state activation method using ethanol/methanol as the agent was denoted as Se/Pe or Sm/Pm (‘S and P’ stands for slurry state and powder state, while ‘e and m’ stands for ethanol and methanol). A suite of samples was screened under different conditions, such as the reaction period (3, 6, and 9 h), reaction temperature (25, 50, 75, 80, 85 ^{o}C), activation methods, and drying temperature (120, 180 ^{o}C) and were named as based on preparation conditions. For example, T85-3-Sm1Pm1-120 stands for the HKUST-1 prepared under 85 ^{o}C for 3 hours, and dry at 120 ^{o}C in the air dryer, i.e., firstly slurry state activation with methanol as the agent, followed by powder activation using methanol as the agent.

3.4.3 Fabrication of MoS_2 nanosheets

The fabrication of MoS_2 nanosheets, following the method as described elsewhere [174], undergoes sonication-induced exfoliation of bulk MoS_2 within N-methylpyrrolidinone (NMP). Briefly, the bulk MoS_2 of 0.3 g was sonicated in NMP of 100 mL for 6 h. Then, the suspending liquid was centrifuged (2000 rpm, 25 min) and ~3/4 of supernatants were obtained. The collected supernatants, including MoS_2 was further centrifuged at 11500 rpm for 15 min to get rid of the left NMP and washed by ethanol 2-3 times. After drying at 100 °C overnight, the MoS_2 nanosheet of 0.02 g was obtained. This process would be repeated to collect expected mass of the sample for the next steps.

3.4.4 Preparation of MoS_2/HKUST-1

The obtained MoS_2 nanosheets were redispersed in ethanol being MoS_2/ethanol suspensions by sonicator. The variables as molar ratios of MoS_2/reactants in ethanol (EtOH) solvent were attempted to assemble HKUST-1 layer on MoS_2 nanosheets. The optimized preparation condition was found as follows: containing 11.5 mg (0.007 mmol) MoS_2/ethanol suspension was added to 16.8 mg/mL TMA/EtOH solution under sonication and the solution volume was up to 250 mL. Then, 250 mL of 30 mg/mL $Cu(NO_3)_2$/EtOH solution was added to commence the synthesis reaction under 50 °C. After 3 h, the product was cooled to 20 °C and then dried at 120 °C overnight. About 7.7 g pristine product collected was going through the activation process, the process by methanol was applied in washing the HKUST-1 to eliminate impurities, which blocked the pores of the HKUST-1. This process was operated in a reflux unit, and aliquots of identical volume (sample: MEOH, 8 g:500 ml) were taken for washing at pre-selected time intervals of 3 h. Before the final product collected, the activated product was centrifuged (7000 rpm) for 5 min and dried at 120 °C overnight. The molar ratios ($Cu(NO_3)_2$: TMA: MoS_2), e.g. 3:2:0 (MH-0), 3:2:0.007 (MH-1), 3:2:0.13 (MH-2), 3:2:0.031 (MH-4), 3:2:0.055 (MH-8), 3:2:0.078 (MH-10) always led to the formation of original HKUST-1 and modified HKUST-1 (MoS_2/HKUST-1) nanocrystal mixtures.

3.4.5 Thermal annealing of HKUST-1

The thermal annealing of HKUST-1 at various temperatures was carried out in a horizontal tube furnace under continuous N_2 flow (99.999%). Each time, about 500 mg of MOFs sample was used in a ceramic boat. Before being heated to the target temperature at 5 °C per minute, the furnace with the sample was purged with dry N_2 to make sure no air or moisture residue remained. And then the treated sample in Table 3-3 was held at this target temperature for **X** h (**X**=0, 1,3 ,6). Waiting for the annealed sample to room temperature, they were collected in a glass vial in the ambient air.

Table 3-3 The annealing parameter

Annealing Time(H)	Annealing Temperature(^{O}C)
0	220
1	220
3	220
6	220
0	250
1	250
3	250
6	250
0	280
1	280
3	280
6	280
0	330
1	330
3	330
6	330
0	380
1	380
0	430
1	430

3.4.6 Catalytic evaluation system

To achieve the aims and objectives of this research, a dedicated experimental rig was designed and built in our laboratory. The schematic diagram was shown in Figure 3-2, respectively. Generally, main four functions can be achieved by this experimental system, i.e. annealing of the sample, investigation of CO redox, and TPD, TPR, etc. The system allowed the In-situ measurement of gas concentration by the online mass spectrometer.

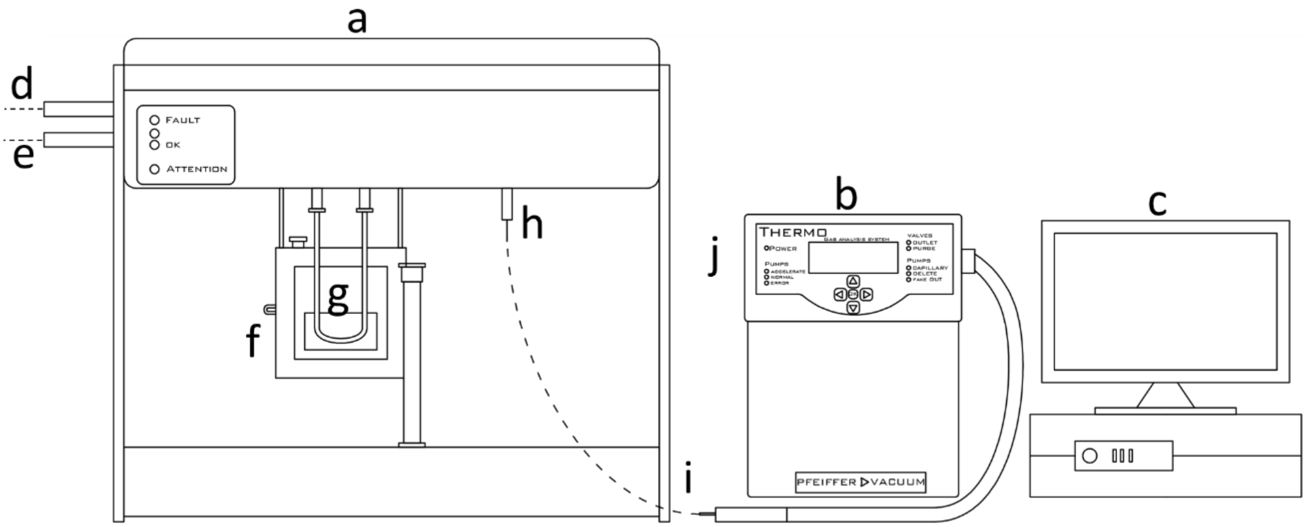

Figure 3-2 Catalytic reaction rig. a. Temperature programmed reduction instrument; b. Online mass spectrometer; c. Computer with data analysis software; d. Mixture of CO (1%), O_2 (20%), Ar (79%) in; e. Ar (99.999%) in; f. Heating jacket; g. U type reactor; h. Mixture Gas out; i. Gas detector in; j. Control panel. The relative height of the instrument in the picture is consistent with the actual rigs.

3.4.7 Catalytic activity tests - CO oxidation

CO oxidation activity over the powder was evaluated in a temperature-programmable tube furnace reactor (i.d. 4 mm) loaded with 30 mg catalyst and stabilized with quartz wool on both ends of the samples. The temperature of the sample was controlled by a thermocouple near the sample. Then, the U-type reactor filled with catalyst was preheated in an oven at 250 ^{o}C under 40 mL/min of Ar for 3h to remove moisture and adsorbed impurities. After the heating treatment, the reaction was performed in a flowing CO/O_2 mixture (1.0% CO, 20.0% O_2, Ar balanced) with a flow rate of 40 mL/min. The CO concentrations at the outlet were monitored using an online mass (OmniStar ThermoStar GSD320). CO conversion was calculated according to the following:

$$X_{CO} = \frac{[CO]_{in} - [CO]_{out}}{[CO]_{in}} \times 100\% \qquad \text{Equation 1}$$

Where $[CO]_{in}$ and $[CO]_{out}$ are the CO concentrations of inlet and outlet, respectively.

The oxidation rate of CO (in units of μmol CO/(s*gcat)) was calculated by:

$$r = \frac{\frac{X_{CO}}{100} \cdot f_{CO} \cdot 1000}{V_m \cdot 60 \cdot m_{cat}} = \frac{X_{CO} \cdot f_{CO}}{6 \cdot V_m \cdot m_{cat}} \qquad \text{Equation 2}$$

where f_{CO} is the flow rate of CO in the feed stream (in mL/min), V_m is the molar volume of CO (from the ideal gas law, $V_m = RT/p$, in mol/L) and m_{cat} is the mass of the catalyst in grams.

When the CO conversion was < 12%, the empirical Arrhenius equation of the activation energy is as following,

$$\ln r = -\frac{E_a}{RT} + C \qquad \text{Equation 3}$$

That is,

$$E_a = \frac{R \cdot ln(\frac{r_1}{r_2})}{\frac{1}{T_2} - \frac{1}{T_1}} \qquad \text{Equation 4}$$

Where R is the ideal gas constant (8.3144621 J/(K·mol)), T is the reaction temperature (in the unit of K).

3.5 Characterization techniques

The variety of techniques used to characterize the samples synthesized in the work reported are summarized as followed. Each characterization was repeated thrice, and the relative error was less than ±5%.

3.5.1 X-ray diffraction (XRD)

The X-ray diffraction is an effective means to investigate the crystallographic structure and grain size of crystalline materials. XRD is generated by the elastic scattering (Thompson scattering) of X-ray photons from atoms in a periodic lattice. Figure 3-3 explains the scattered monochromatic X-rays give constructive interference in phase and generate lattice spacings satisfying the Bragg's law ($n\lambda = 2dsin\theta$). Where n is an integer, λ is a wavelength of the radiation, d is interplanar spacing (m), $sin\theta$ is the angle of incidence of radiation. A single crystal produces only one family of Bragg peaks in the diffraction pattern. The XRD, therefore, is the fingerprint of certain crystalline phase. The intensity, position, width and shape of the diffraction patterns stretch out crystalline data from a sample. A list of diffraction results includes a record of photon intensity as a function of detector angle 2θ.

In this work, Powder XRD (PXRD) patterns were measured using a Bruker D8 diffractometer using Cu-Kα (λ=1.54 Å) radiation at 40 kV and 40 mA, in the range 5-90° (2θ), with a step size of 0.01°/2θ. Loose powder samples were placed in a diffractometer that was mounted on a sample holder. All systematic errors were eliminated through careful manipulation of a zero-point detector position.

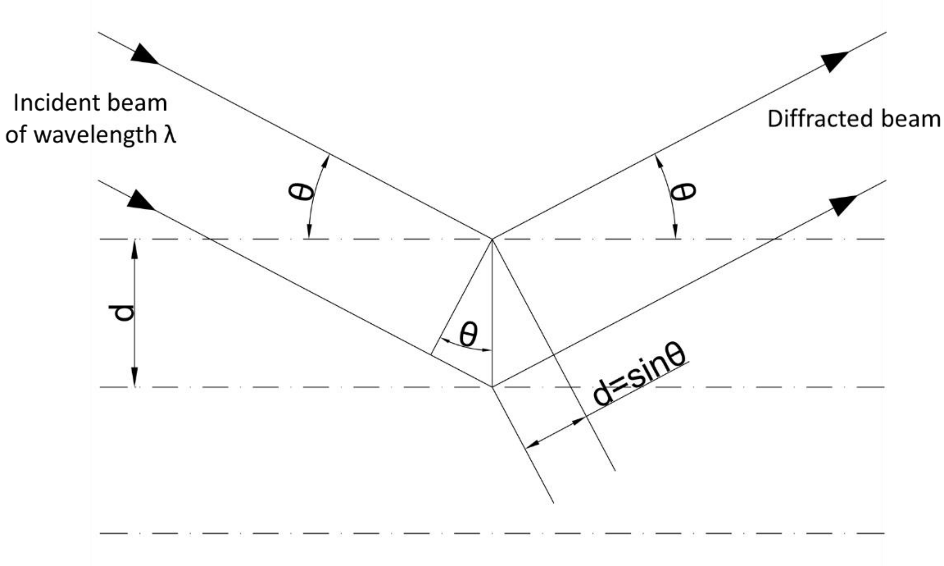

Figure 3-3 Braggs analysis for X-ray diffraction by crystal planes

The crystallinity percentage (*%C*) was defined as the ratio of the sum of the relative intensity of the five most intense peaks and can be calculated as [198].

$$\%C = \frac{\sum_{i=1}^{5} I_{relsample}}{\sum_{i=1}^{5} I_{relreference}} \times 100 \qquad \text{Equation 5}$$

In this calculation, the C300 (C300 is commercial product acquired from Sigma) was used as the reference (100% crystallinity).

The X-ray diffraction (XRD) patterns of the CuNPs/GO catalysts were obtained via a SmartLab 3KW X-ray diffractometer using a target CuKα operated at 40kV and 30mA with a scan rate of 0.02°/s (2θ). The average crystallite size of Cu (d_{XRD}) has been calculated by the X-ray broadening technique using the Debye-Scherrer's as follows:

$$\mathrm{d}_{XRD} = \frac{0.89\lambda}{FWHM \cdot cos\theta} \qquad \text{Equation 6}$$

Where is the wavelength of CuKα radiation (15.406 nm), *FWHM* (in Rad) is the full width at half maximum of the characteristic peak (111) of Cu, and the θ is the diffraction angle for the (111) plane.

3.5.2 Scanning electron microscopy (SEM)

A scanning electron microscope (SEM) is a typical study of sample's surface, which can raster an electron beam across the sample surface using magnetic fields in high vacuum in Figure 4-3. The beam of electrons imparts charge to the sample, sending out various signals that contain information on the morphology and component of the sample surface. The most common SEM mode comes from the detection of secondary electron emission of atoms excited by the electron beam in the high vacuum. Numerous secondary electrons are observed with sample topography using a secondary electron detector. After scanning the sample and collecting the secondary electrons, an image containing the morphology of a surface is generated.

SEM images were obtained using a FEI Nova NanoSEM 450 (FE-SEM) and ImageJ software. All images were obtained with a potential of 20 kV applied to a W filament electron source. To overcome beam charging problems, the specimen surface was coated with a 5-nm gold layer using a Quorum Q150T-S sputter coater/carbon coater prior to SEM analysis. Images were obtained under high-vacuum utilizing both Secondary and Backscattered Electron Detectors. All samples were prepared for SEM imaging by dispersing the material onto a double-sided adhesive conductive carbon tape that was attached to a sample holder.

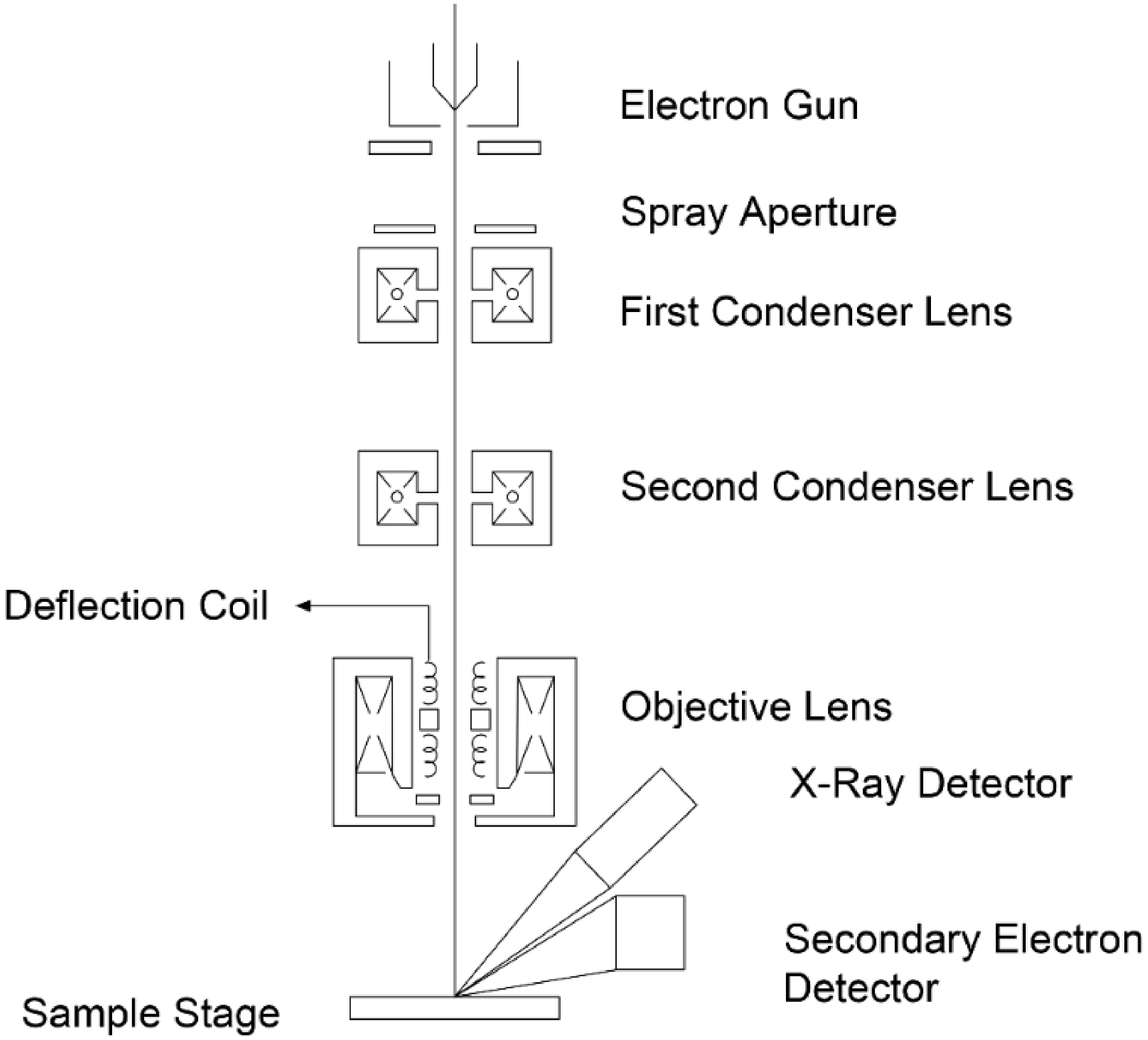

Figure 3-4 Schematic drawing of the electron and X-ray optics of SEM

3.5.3 Transmission electron microscopy (TEM)

Transmission electron microscopy (TEM) is another microscopy technique to generate a projection image of thin specimens, where an electron beam is spread through an electron transparent sample to form an image with very high spatial resolution. The schematic diagram in Figure 5-3 presents the component arrangement for a TEM. The electrons are released by an electron gun at the top and go through a vacuum the microscope column. Then, the electrons are focused by condenser lenses into a very thin beam and projected onto the sample. Afterwards, electron beam goes through the sample and the objective lenses. Finally, unscattered electrons hit the fluorescent screen at the bottom of the microscope, which offer an image of sample containing its information displayed in different parts with varied darkness. Note that the entire sampling area is illuminated by the beam at once in this configuration; the beam is not rastered over the sample as in SEM imaging, and TEM uses an electron beam at least an order of magnitude greater in energy.

In this work, TEM imaging was performed using a FEI Tecnai F30 operated at 200 kV to determine the micro-texture and microstructure of MOFs sample. Prior to imaging, the sample powder was dispersed in ethanol or methanol by ultrasonic radiation for 10 min, and a drop of the suspension was placed onto a copper grid for TEM imagining. Particle size analysis used ImageJ, with images scaled, and background corrected before thresholding.

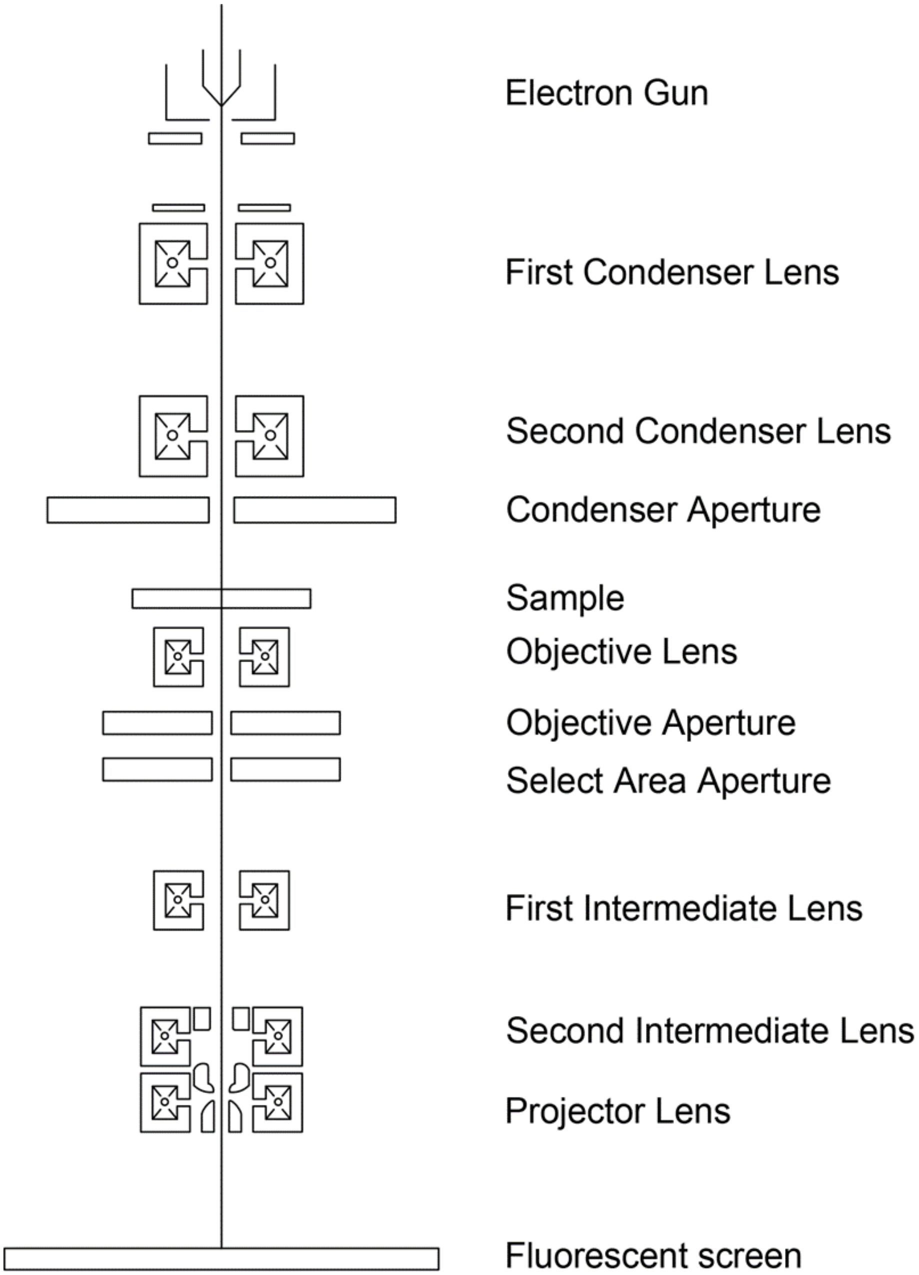

Figure 3-5 Schematic drawing of TEM

3.5.4 Energy dispersive X-ray spectroscopy (EDS)

Energy dispersive X-ray spectroscopy (EDS) analysis is a method for elemental analysis, which is based on a set of characteristic X-ray emission energies from each element. The electron gun (shown in Figure 3-4) used for SEM imaging is also capable of generating X-ray characteristic from the elemental composition of the imaged sample. These X-rays in the electron gun are generated sufficiently high energy electrons to excite electrons (Backscattered electrons) in the sample and cause them to be ejected from the energy level occupied in the ground state. The energy of an emitted X-ray is determined by the energy difference between the shells. Each of these transitions gives rise to a distinct peak in the spectra obtained from the EDS. These peaks are labelled according to the element of the atom in which the transition occurred.

In this work, Energy dispersive X-ray spectroscopy (EDS) analysis of all samples was conducted using an EDAX Roentgen Spectrometer attached to a FEI Nova NanoSEM 450. An electron beam energy of 20 kV was used, with a 132 eV detection resolution, a spot size of around 1 μm and a 50 s collection time. Prior to analysing, all samples were dispersed onto a conductive carbon tape that was attached to a flat aluminium sample holder and were metalized using a Quorum Q150T-S sputter with a gold layer of 5 nm thickness.

3.5.5 N_2 gas isotherm

A N_2 gas isotherm is usually a volume of gas adsorbed as function of relative pressure to analyse surface area and pore properties of materials. Adsorption of an adsorptive species onto an adsorbent surface can be driven by either chemical or physical mechanisms depending upon the identities of the solids being analysed and the gases seen as probes. However, for a variety of reasons, including low heats of adsorption, no activation energy for adsorption, full reversibility and no site specificity, only gases that are physisorbed onto surfaces are used to study surface areas. Non-polar $N_2(g)$ is frequently used as a probe gas molecule due to its low interaction potential when compared to polar gas molecules and low cost. The adsorption potential due to van der Waals interactions is monitored by the such gas molecule near a planar surface, in a mesopore and in a micropore.

To obtain surface areas from adsorption isotherm kinetic theories, this was proposed originally by Langmuir, and the Type I isotherm was defined as a monolayer of molecules covering the adsorbent. However, multilayer adsorption is perfectly possible in cases of physisorption and indeed in micropores it happens rapidly at low partial pressures due to “micropore filling”. Brunauer, Emmet and Teller (BET) were able to modify Langmuir’s original model to account for this and due to this ability to account for multilayer adsorption the BET theory more accurately calculates the surface area of microporous materials.

In this work, the specific surface area, pore volume, and pore size of the MOFs samples were measured by N_2 adsorption at 77 K using Micromeritics ASAP 3020 Volumetric Adsorption Analyser. Samples with weight (35-50 mg) were loaded into a sample tube and evacuated under 10^{-5} torr dynamic vacuum at 150 ^{o}C for 12 h prior to the surface area measurements. After pre-treatment, the sample and tube were precisely weighed again to obtain the evacuated sample weight. The specific surface areas of the samples were obtained using a Brunauer-Emmett-Teller (BET) model, while the pore volume and pore width were measured using Horvath-Kawazoe (original H-K, seen as the slit) procedures.

3.5.6 CO_2 Gas adsorption

CO_2 gas adsorption is a gas adsorption technique to test a CO_2 sorption capacity of materials. Equilibrium CO_2 capacity is a good parameter in comparing the effect of different conditions for the performance of the sorbent material. The equilibrium capacities referred here are the maximum capacities but are not necessarily equal to the maximum capacity. The equilibrium capacities mostly are influenced by physical factors.

The adsorption isotherm of CO_2 on samples evacuated by Micromeritics ASAP 2020 Volumetric Adsorption Analyser was measured volumetrically at 25 ^{o}C, up to ambient pressure. Before each measurement, the sample was placed in the sample tube at 180 ^{o}C under vacuum overnight. CO_2 was dosed into the system incrementally, and equilibrium state reached with no further change in pressure (within 0.01 kPa). The excess adsorbed amounts per unit adsorbent mass were calculated by a mass balance for the injected pure CO_2 and sample using the generalized virial-coefficient equation of state.

3.5.7 Temperature-programmed desorption (TPD)

Temperature-programmed desorption determines the number, type, and strength of active sites on a catalyst surface by measuring the amount of gas desorbed at different temperatures. After the analysis gas dosed on the sample until saturation, the gas desorption is run with a linear temperature ramp while an inert gas flowed through the sample. At a certain temperature, the heat overcomes the bond energy between adsorbed gas and active site, hence the pre-adsorbed gases desorb from the sample. The amount of desorbed species with temperature yields the number and strength of active sites. The number of desorption peaks can indicate the surface sites with the different bond energies, and the peak area represents the quantity of adsorbed species on a given active site.

The active sites of the original/modified HKUST-1 composites were determined by CO_2 TPD, to evaluate desorption rate of adsorbed molecules as a function of temperature and the basic site distribution. 100 mg of composite was put in a quartz microreactor (shown in Figure 3-6) and pre-treated by argon flow of 40 mL/min at 200 ^{o}C for 1 h, and then cooled to 25 ºC. The composite was injected with CO_2 (10% CO_2 / N_2) for 30 min at 25 ºC. Afterwards, Ar flow was purged into the pre-treated composite for 60 min to eliminate the physisorbed CO_2, and the temperature of a sample chamber was subsequently increased to 400 ^{o}C with a heating rate of 10 ^{o}C/min. The amount and quantitatively calibration of CO_2 in the effluent was recorded by the online mass spectrometer (OmniStar ThermoStar GSD320).

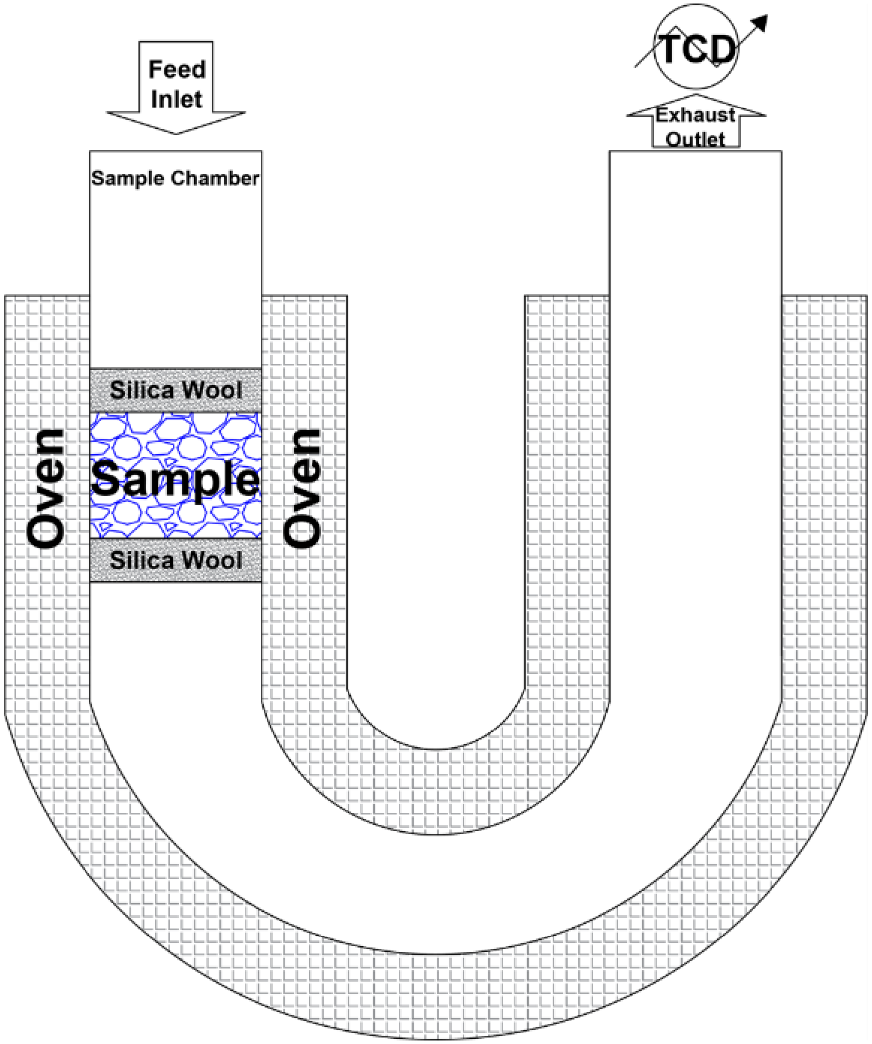

Measurable Variables

Gas (Feed inlet)
- types/composition
- space velocity
- pressure

Sample
- sample state (powder/pellets)
- mass

TCD (Thermal conductivity detector)
- signal intensity
- integration of peak area (based on calibration of adsorbate)

Oven
- temperature rate
- catalytic temperature

Figure 3-6 Schematic drawing of TPD

3.5.8 Thermal gravity analysis (TGA)

Thermogravimetric analysis (TGA) is an approach where the mass loss of a sample is measured as a function of temperature or time. For the dynamic measurement, the sample is heated at a constant heating rate. For the static measurement, the sample is held at a constant temperature.

In this work, TGA can be applied to analyse mass loss when the sample in one heating mode within a surrounding atmosphere. These include as below:

i) Desorption and adsorption of gases (regenerability in multiple cycles)

ii) Volatile substances and moisture

iii) Loss of H_2O

iv) Oxidation of MOFs in air

v) Thermal decomposition in a N_2 atmosphere

The temperature range of a typical TGA instrument (NETZSCH TG instrument) is around 25 to 600 ^{o}C. A variety of gas atmospheres, including N_2, and air can be introduced into the samples. Normally, MOFs sample weights of around 10 mg in an alumina crucible in N_2 flow (40 mL/min). For thermogravimetric analysis, samples would be in the form of loose powders to keep a uniform temperature for the sample, as well as, to ensure that the sample temperature is as close to the set gas temperature as possible. The accuracy of the weight change is 0.01 mg.

3.5.9 Regenerability in multiple cycles

The regenerability of adsorbents are among the most important properties when exploiting efficient CO_2 adsorbents. It is essential that the adsorbent uptake does not change after multiple adsorption-desorption cycles, where adsorbent is able to keep its structure and properties. The stability is the significant characteristic for an adsorbent, since it determines the lifespan of the sample and the frequency of its replacement in an adsorption unit. The adsorption-desorption cycling would select the change test of temperature and/or pressure according to the structural and chemical properties of the adsorbent. Therefore, the most appropriate adsorbent is to be tested in individual adsorption processes (TSA, PSA, VSA, PTSA) [175].

To assess the regenerability of MOFs, multistage CO_2 adsorption-desorption cycles were conducted on a TGA system (NETZSCH STA49 F3). Prior to the cyclic adsorption-desorption test, around 15 mg MOFs samples were conducted at 150°C for 2 h in a nitrogen gassing system. Until the chamber cooling down to 25°C, the pure CO_2 (99.999%, 60 mL/min) flowed at 25 °C for a period of 10 min. According to the mass increment during this stage, the CO_2 uptake at a certain temperature was measured. After completion of the CO_2 adsorption process, a desorption process was conducted by introducing nitrogen flow (99.999%, 40 mL/min) as the regeneration of the adsorbent. The adsorption-desorption cycles were repeated ten times in a continuous manner. The duration of a single sorption/desorption cycle for MOFs was 20 min.

3.5.10 Fourier Transform Infrared Spectroscopy (FTIR)

Fourier transform infrared spectroscopy is especially useful for identification of the fundamental vibrations and associated rotational-vibrational structure presented from a sample. FTIR depends on the fact that most molecules absorb light in the infra-red region of the electromagnetic spectrum. This absorption corresponds specifically to the bonds presented in the molecule. Collected raw data of FTIR use Fourier transform methodology to determine the signals. Distinct peaks corresponding to the stretching or bonding of chemical bonds can therefore be identified.

In this project, FTIR spectra was recorded in a Bruker vertex 70 FTIR spectrophotometer to determine the existence of functional groups in the MOFs samples. Prior to measurement, a fitting pressure was put on the MOFs samples and appropriate KBr powder to achieve optimal mixing. The dried KBr pellets containing MOFs samples were scanned over the spectral region of 400 to 4000 cm^{-1} at 0.5 cm^{-1} nominal resolution. Every spectrum was background corrected for water and CO_2.

In-situ diffusion reflectance infrared Fourier transform spectroscopy (In-situ DRIFTS) was conducted to study the adsorption-desorption of CO over the catalysts. DRIFTS needed to be measured in the mid-infrared region (4000-1000 cm^{-1}) using a Bruker Vertex 70 FTIR spectrophotometer including, a Praying Mantis DRIFTS cell (Harrick model HVC-DRP) and a high-temperature environmental chamber with KBr windows. The detector was loaded with a mercury-cadmium-telluride (MCT) detector cooled by liquid nitrogen. Approximately 100 mg of the CuNP/GO catalysts (330C-3H) powder was put into the test chamber and was heated to the 180 ^{o}C under an Ar flow of 100 mL/min. After 30mins, background spectrum was collected by 100 scans, and this spectrum was then subtracted from the sample spectra for each measurement.

3.5.11 X-ray photoelectron spectroscopy (XPS)

The XPS was performed to observe the chemical component, especially the valence state of the elements in samples. In this work, The XPS was carried out using a an ESCALAB 250Xi Electron Spectrometer. Before sample introduction, the base pressure in the XPS analysis chamber was 2×10^{-9} Torr, and the pressure was kept $\leq 2 \times 10^{-8}$ Torr within tests. The XPS data were internally calibrated, fixing the binding energy of C1s at 284.6 eV. The experimental curves were generated using the CasaXPS software (Version 2.2.73).

3.5.12 Temperature-Programmed Reduction (TPR)

TPR is a powerful tool to measure the number of reducible species (usually metal oxides) in the catalyst. TPR analysis is performed with a linear temperature ramp using a reducing gas, usually H_2 in an inert gas such as argon. If a reduction takes place at a certain temperature, the change of H_2 concentrations is recorded, giving the integrated H_2 consumption. In addition, TPR analysis can reveal the effect of the support and promoters on the reducibility of the catalyst.

In this study, the MOFs samples were placed in the quartz U-type reactor. The sample was heated from 25 ^{o}C to 800 ^{o}C at a constant ramp rate of 10 ^{o}C/min while the reducing gas, 5% H_2 in Ar, of 40 cm^3/min flowed through the sample. The concentration of hydrogen was recorded over the entire temperature range by a mass spectrometer.

3.6 Computational Method

HKUST-1 is a well-studied MOF initially reported by Chui et al, whose structure was illustrated in Figure 3-7(a) [176]. The first structure model was also reported that has repeated paddlewheel type Cu corners connected to the oxygen of four organic linkers (benzene-1,3,5-tricarboxylate). In calculations, the structure of HKUST-1 has always been simulated by considering models of decreasing size. As the model, a dicopper-carboxylate cluster was considered, where the distant carbon atoms were saturated with protons to maintain the charge neutrality (Figure 1(b)). Full geometry optimizations have been performed on the adsorption of the guest molecules on this paddlewheel model by using DFT methods. With keeping the confidence of the calculation results, the cost of calculation would be reduced in this model.

The periodic spin-polarized DFT calculations of the interaction of original HKUST-1 synthetic solution (Cu^{2+}, TMA, H_2O, ethanol) on MoS_2 nanosheet, interaction of the CO_2 molecule with HKUST-1, and the interaction of CO_2 molecule with MoS_2/HKUST-1 system, were modeled using the primitive cell of MoS_2 nanosheet (4×4). The primitive cell lattice parameters ($a = b= 12.6415$ Å, $c = 18.10810$ Å, $\alpha = \beta = 90^o$, $\gamma = 120^o$, and $V = 2506.1138$ Å^3) were optimized by calculation. The analyses of the formation process of one complete HKUST-1 were modeled using a larger primitive. Such the primitive cell lattice parameters ($a = b = 20$ Å, $c = 30$ Å, $\alpha = \beta = 90^o$, $\gamma = 120^o$, and $V = 10392.3048$ Å^3) were optimized by calculation to prevent the periodic interaction. During geometry optimization, the interacting molecule and entire adsorbent were allowed to relax. The projector augmented wave approximation (PAW) [177], and the plane wave basis set with an energy cutoff of 400 eV were used. Monkhorst-pack 3 x 3 x 1 k-point grid was employed to try out the

Brillouin zone while 6 × 6 × 1 k-point was used to calculate the density of state (DOS). Generalized gradient approximation with Perdew Burke Ernzerhof (GGA-PBE) exchange correlation functional [178, 179] was employed. The empirical dispersion correction (D3) was added to amend the long-range effects [180]. The correction of dispersion corrections with DFT would be more reliable for the estimation of MOF structures, predicting changes in structure, and determining the interaction of adsorbent with adsorbate [181-184]. Charge transfer were listed using the Bader analysis [185]. The total population density of the empty versus the occupied site used the same basis set and framework coordinates. All calculations were performed with VASP 5.3 [186] program suites. Adsorption energy from the formula was calculated as,

$$E_{ads} = (E_{total} - E_{adsorbent} - nE_{adsorbate})/n \qquad \text{Equation 7}$$

E_{ads} is the adsorption energy of the adsorbate to the adsorbent. $E_{adsorbent}$ is the total energy of the entire adsorbent and $E_{adsorbate}$ is the total energy as an isolated adsorbate. A negative value of E_{ads} means that the adsorption is exothermic, which is favourable for more negative.

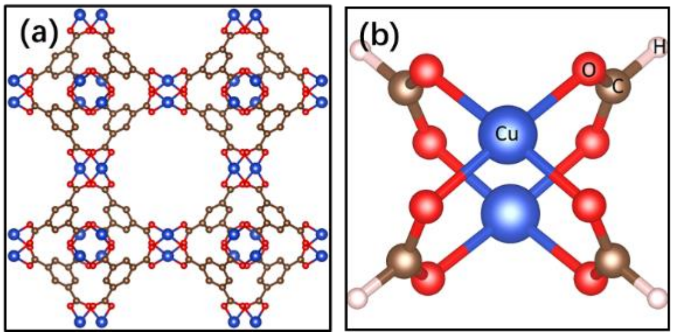

Figure 3-7 Structure of HKUST-1 framework [176]. (a) complete structure of HKUST-1 framework; (b) simplified structure of HKUST-1. Blue ball is Copper atom, Red ball is Oxygen atom, Pink-white ball is Hydrogen atom, Brown ball is Carbon atom.

3.6.1 Density Functional Theory (DFT)

DFT is a non-interacting theory and an electronic structure method to study many-body systems through the density alone [187-189], where the approximation is necessary. In an interacting many-electron system, all the physics can be given by a complete Hamiltonian [190, 191],

$$\hat{\mathrm{H}}_{el} = -\frac{\hbar}{2m_e}\sum_i \nabla_i^2 + \sum_i V_{ext}(r_i) + \frac{1}{2}\sum_{i\neq j}\frac{e^2}{|r_i - r_j|} \qquad \text{Equation 8}$$

where *i* is the total electrons in the system. The first term is the kinetic energy of independent electrons. The second term is the external potential of independent electrons, and the last term is the Coulomb interaction between all pairs of electrons. The term of V_{ext} includes the electron-ion interaction within a crystal and the effect of an external electric field.

To solve the correlated N-body wavefunction yielded by Hamiltonian and simplify the many-electron problem, the DFT was emerged and started with Hohenberg-Kohn theorem and Kohn-Sham equation on the total electron density in a many electron system.

The Hohenberg-Kohn theorem [192] states that the external potential $V_{ext}(r)$ is individually decided by the corresponding ground-state charge density n(r). Regarding a given system in the external potential $v(r)$, consisted of moving particles by Coulomb-interaction, the exact ground-state electronic energy is expressed by the energy functional [193].

$$E_v[n] = T[n] + \int d^3r\, v(r)\, n(r) + W_{coul}[n] \qquad \text{Equation 9}$$

where $T[n]$ (kinetic contribution) and $W_{coul}[n]$ (Coulomb energy) are universal functionals of the charge density, that is, these functionals are independent of the external potential

$v(r)$ in the system. The theorem provides reasonable results and significant insight without much effort. Meanwhile, the number of DOF (degree of freedom) on density functional approach is reduced to a minimum.

To find the value of $n(r)$, Kohn and Sham[194] assumed the many-electron system can be mapped onto an auxiliary system of (many) non-interacting electron with corresponding orthogonal Kohn-Sham orbital. The auxiliary system owns the same number of valence orbits as the system without electron interaction. Therefore, the $W_{coul}[n]$ can be separated into three distinct parts, and the energy functional becomes,

$$E_v[n] = T[n] + \int d^3r\, v(r)\, n(r) + E_{Hartree} + E_{II} + E_{xc}[n] \qquad \text{Equation 10}$$

where $E_{Hartree}$ is a Hartree term, E_{xc} is an exchange-correlation term and E_{II} is the ion-ion interactions. The E_{xc} is determined by the charge density of each point in space and requires some approximation to be calculated, as given by,

$$E_{xc}[n] = \int n(r)\, \varepsilon_{xc}\, (n(r))dr \qquad \text{Equation 11}$$

which is from the local density approximation (LDA). In an auxiliary electron system, a Schrodinger-like equation (Kohn-Sham equation) can be obtained by the minimization of energy functional using LDA, as followed,

$$\{-\frac{1}{2}\nabla^2 + [V(r) + \mu_{xc}(n(r))]\}\varphi_{nk}(r) = \varepsilon_{nk}\varphi_{nk}(r) \qquad \text{Equation 12}$$

where $V(r)$ includes the Hartree energy and the external (ionic) potential. Also, the exchange correlation potential (μ_{xc}) depends on charge density. This equation can be resolved by a self-consistent scheme and give accurate results of ground state properties

[195-198], like total energies, equilibrium crystal structures, atomic forces, and charge density distribution that are in good agreement with related experiments.

Chapter 4 Nano-scale HKUST-1 and its application in CO_2 capture

4.1 Introduction

Metal-organic frameworks (MOFs) are hybrid crystalline compounds consisting of organic ligands bridging inorganic moieties. MOFs exhibit unique structure and outstanding properties in porosity, pore size and surface area and have been used in various fields such as gas storage, adsorption, separation, and catalysis [199]. Recently, more and more effort has been made to explore the application of nano-scale MOFs in areas, such as liquid phase catalysis [200, 201], adsorption [202] and drug delivery [203], etc.

HKUST-1, a copper-based MOF, is one of the earliest reported MOFs [204] whose structure is based on Cu^{2+} ions linked with 1,3,5-benzenetricarboxylate struts. The conventional solvothermal method for the preparation of HKUST-1 involves heating the solution up to 180 °C to form crystalline Cu_3 $(BTC)_2$ [205]. The Cu_3 $(BTC)_2$, synthesized at 75-120 °C, has to be kept in an autoclave for a long period, varying from 1 day up to a few weeks, to remove impurities that are trapped in the pores [206]. Although slow diffusion techniques require significantly long time for the synthesis of MOFs, it is still the preferred method for the synthesis of MOFs due to its tunable reaction conditions, such as, the control of the rate of nucleation and crystal growth by the control of concentration gradient (temperature gradient) [207-211]. Normally, the synthesis of MOFs with good thermal stability has to be conducted under hydro/solvothermal conditions. To date, commonly adopted methods for the rapid preparation of HKUST-1 include microwave heating, ultrasound irradiation, mechanochemistry, and solvothermal synthesis, which are summarized in Table 4-1. Normally, conventional solvothermal and electrochemical methods require long time to synthesize HKUST-1 with high surface area. Although mechanochemical, microwave heating and ultrasound irradiation methods can be used to produce HKUST-1 in much shorter time, the surface area of the MOFs prepared is not high enough (<1500 m^2/g). In addition, the size of HKUST-1 particles prepared via these methods is in micron scale and cannot meet some of the special requirements in catalysis when nano particles are preferred to enable higher mass transfer rate or to achieve higher thermal resistance [212, 213]. Because of this, there has been numerous work being carried out on the synthesis of nanoscale MOFs [214-216]. However, there is still a need to develop cost-effective techniques for the preparation of nanoscale HKUST-1 MOFs under mild conditions, which are able to produce MOFs with high surface area (> 1500 m^2/g).

Table 4-1 MOFs prepared under Different Methods

Method	Microwave heating[217]	Ultrasound irradiation[217]	Mechano-chemical[218]	Conventional solvothermal[219]	Electro-chemical[220]
Surface area (m^2/g)	1080	1156 [217]	1421	1000-1800	1500-2100 *
Particle Size (μm)	10	0.2-0.4	>50 [a]	1.5-3.5	15.9 *
Temperature (°C)	140	25-40	-	100-180	-
Synthesis Time (min)	60	1	20	720-4320	150

* Basolite C300, Sigma-Aldrich. [a] from SEM image [218]

In this study, the effort was made to develop and optimize a new method for the preparation of HKUST-1 MOFs in a fast and efficient manner. Attempts were also made to control the synthesis of the MOFs in nanoscale with high surface area and high yield. A series of characterization techniques was applied to the characterization of the products prepared under different conditions. The synthesis conditions were therefore optimized and used to prepare nanoscale HKUST-1, which was further studied to explore its potential in CO_2 capture.

4.2 Results and Discussion

4.2.1 Screening synthesis of HKUST-1

It is generally believed that the alkaline TEA could accelerate the deprotonation of H_3BTC and promote the nucleation of particles into nanoscale [222], which is accordance with the distribution of particle size in this research. In this study, the effect of synthesis temperature, time, pre-treatment temperature and activation methods on the synthesis of HKSUT-1 MOFs was investigated. The first attempt was made to find out an optimal reaction duration and temperature for the synthesis of MOFs. From Figure 4-1, it can be seen that the variation in reaction time from 3 h to 9 h showed no significant impact on the specific surface area for samples in Region I. That means 3 hours provide sufficient time to allow the synthesis reaction to complete, which is shorter than the time required for conventional HKUST-1 synthesis (≥ 24 h) [219]. This is due to the addition of the alkaline TEA, which accelerates the synthesis reaction. Furthermore, in Region II, the pristine HKUST-1 went through the pre-treatment in an air dryer under two different temperatures, 120 and 180 ^{o}C. The results indicated that 120 ^{o}C did not have a negative effect on the pores in the HKUST-1.

It can be seen from Figure 4-1 that in Region III, the two samples prepared at 50 and 85 ^{o}C showed significantly different BET surface areas. It is obvious that the temperature of 85 ^{o}C favours the formation of HKUST-1 with large BET surface area. This low temperature (85 °C) is much lower than the temperature (180 °C) adopted for the synthesis of HKUST-1 MOFs for the first time. The low-temperature level can inhibit the formation of the by-product (Cu_2O) and therefore contribute to a high selectivity and yield.

After synthesis, the pristine HKUST-1 has to be activated to remove the impurities (unconverted reactant or by-product) that are trapped in the pores. The activation can also activate the metal sites, which are always surrounded by water and other gas molecules. As shown in Region IV, pristine HKUST-1 was activated via either slurry state or powder state activation by ethanol or methanol. The BET surface area of T85-3-Se1-120 and T85-3-Pe1-120 was lower than that of T85-3-Sm1-120 and T85-3-Pm1-120. It is reported that methanol is a better activation agent and can remove more impurities than ethanol [227]. It is clear that the BET surface area of T85-3-Pe1-120 and T85-3-Pm1-120 was higher than that of T85-3-Sm1-120 and T85-3-Pe1-120, which suggests that powder state activation is more efficient in the removal of impurities from pores.

In Region V, it shows that repeated slurry activation resulted in lower BET surface area, which might be due to the destruction of micropores to form larger pores and subsequently result in lower BET surface area. However, repeated powder state activation shows different impacts on BET surface area, as shown in Region VI. Four times of powder state activation result in the highest surface area around 1542.4 m^2/g.

The combination of slurry-powder state activation was applied to activate pristine HKUST-1 and the BET surface area of individual samples is shown in Region VII in Figure 4-1. It is found that the BET surface area of T85-3-Sm1Pm1-120, T85-3-Se1Pm1-120 and T85-3-Sm1Pe1 was higher than that of the sample being activated once via slurry state activation. Furthermore, the BET surface area of T85-3-Sm1Pm1-120 was higher than that of T85-3-Sm1Pe1, which again prove the powder state activation using methanol as the activation agent is a reliable and efficient method. However, the BET surface area of one more times of powder activation by methanol (T85-3-Sm1Pm2-120) was reduced. Therefore, it can be concluded that slurry state activation removes the impurities in the pores but does not significantly contribute to the formation of higher BET surface area.

Among the 17 samples prepared, the highest BET was found for T85-3-Pm4-120, which is 1542.4 m^2/g. There are also other five samples, i.e., T85-3-Pm1-120, T85-3-Pm2-120, T85-3-Pm3-120, T85-3-Pm5-120, and T85-3-Sm1Pm1-120, that have BET surface area greater than 1100 m^2/g. The highest BET surface area is attributed to the cleaning of pores, which is associated with a final HKUST-1 yield of 87%.

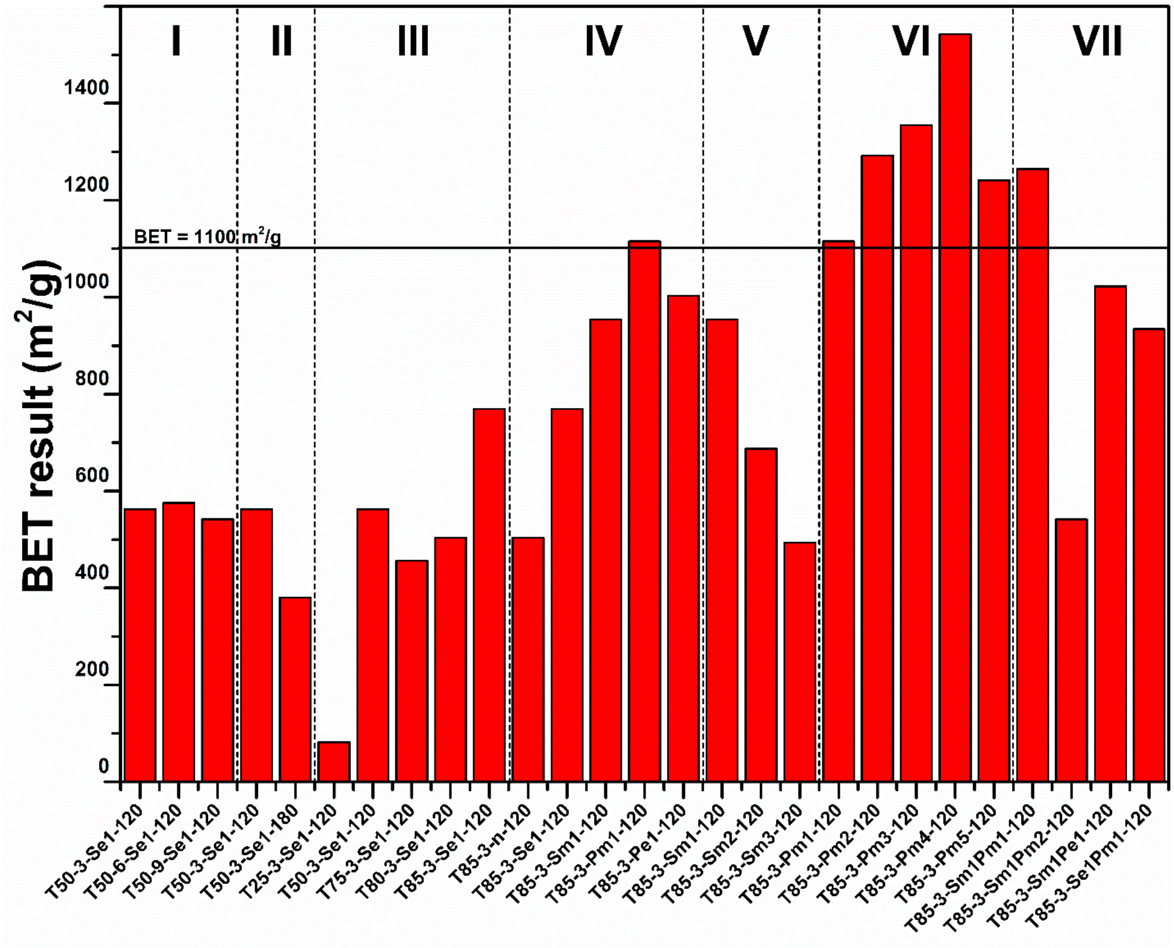

Figure 4-1 Screening of HKUST-1 with large specific surface area. I, reaction period; II, drying temperature; III, synthesis temperature; IV, slurry/powder state activation using methanol/ethanol as the activation agent; V, repeated slurry state activation using methanol as the activation agent; VI, repeated power state activation using methanol as the activation agent; VII combination of slurry and powder activation. (T25, T50, T75, T80, T85-A stand for reaction temperature at 25, 50, 75, 80, 85 °C. T50-3, T50-6, T50-9 stand for reaction duration of 3, 6, and 9 h at 50 °C, respectively. T50-3-Se1-180 indicate the pristine HKUST-1 yielded at 50 °C with a duration of 3 h was activated once using slurry state activation method and dried at 180 °C. Sm1 means slurry state HKUST-1 was washed by using methanol. Pe1 means powder state HKUST-1 was washed by using ethanol once. Sm1Pm1 means slurry state washing firstly, and then followed by powder state washing.)

4.2.2 The nano HKUST-1 formation and its morphological features

To understand how the morphology of HKUST-1 is affected by synthesis conditions and powder activation process, SEM analysis was conducted with morphological features of different samples shown in Figure 4-2 (I) - (IV). It is evident that all samples are of nano-particle size (<100 nm) but form agglomerates. In the Region I of Figure 4-2 and Figure 4-3, the samples synthesized under 50 ^{o}C for 3/6/9 h were similar in morphology, but particle size of the samples decreased with the increase in the synthesis period. That means longer synthesis period would favour the formation of smaller nanoscale particle. There is some possibility for the reason of the presence of smaller nanoscale particles. In most batch processes, the precursors of solvothermal reaction form the structure of MOFs over a long time, due to the slow heating rates. As a result, the instant concentration of precursor should be constant above the critical nucleation threshold if the period is extended and the continuous nucleation would be concurrently followed with growth. When the long reaction period was extended sufficiently, the particle size range would be changed from broad distribution to the focused one. In addition of the deprotoned agent, the nuclei in synthetic solution would be more dispersed widely over a course of reaction when the agent and reactant are mixed completely, and the particle size distribution would be narrow and tend to smaller size.

Regarding the influence of synthesis temperature on the morphology of HKUST-1, as shown in Region II of Figure 4-2 and Figure 4-3, the samples synthesized from 25 to 85 ^{o}C after 3 h demonstrated differences in particle size distribution and average particle size. The SEM image (Figure 4-2(II)) shows similar morphology which is featured with different small spherical particles. Under low temperature (25 ^{o}C), it shows crystal structure with blocky shape and obvious sharp edges with the highest average particle size of 93.6 nm, whereas samples prepared under higher temperatures (50 ,75 ,85 °C) are more spherical and are of smaller particle size. In addition, the synthesis temperature of 50 and 85 °C leads to the formation of the smaller average particle size of around 72 nm in the Region II of Figure 4-3(b). However, the bar (53.8-67.5 nm) of T85-3-Se1-120 is higher than the bar (67.5-87.2 nm) of T50-3-Se1-120 in the Region II of Figure 4-3(a). Therefore, further investigation was conducted to understand the influence of powder activation and slurry activation process on the morphology of the samples prepared under the optimal synthesis temperature of 85 °C. In the powder state activation by methanol, the second time of powder state activation led to the formation of the smallest average particle size of 76.0 nm and peak of particle distribution is in the range of 67.50-81.25 nm. However, the particle size increased in the third, fourth and fifth time of powder state activation, which could be attributed to the crystal regrowth of primary particle during multiple activation process in methanol solution. In addition, these three samples showed different morphology but similar average particle size around 90 nm. For comparison purpose, the slurry state activation by using methanol was also conducted. The samples, T85-3-Sm**X**-120 (X=1, 2, 3), were prepared and are shown in Figure 4-2(III). These samples showed different morphology and demonstrated that particle size can be reduced followed by the additional times of slurry state activation, which is shown in the Figure 4-3(III). Combined with Figure 4-3(IV), the results indicated the size of particles by slurry state activation was lower than the size of particles undergoing powder state activation. Clearly, slurry state activation shows similar trend in washing times, which is the particle size reduced with the times (≤2) of activation process. Therefore, although slurry activation process can lead to the formation of smaller size nano particles, it cannot form HKUST-1 with nano-particle with BET surface area greater than 1100 m^2/g (as shown in Region V of Figure 4-1). Despite the particle size expansion after 3 times of powder state activation, the specific surface area of T85-3-Pm**X**-120 (X=1, 2, 3, 4) increased from 1115.3 to 1542.4 m^2/g when the sample was activated via powder state activation for a few times. Therefore, it can be concluded that to form nanoscale sample with large surface area, the sample shall be prepared under 85 ^oC and activated via powder state activation for at least two times.

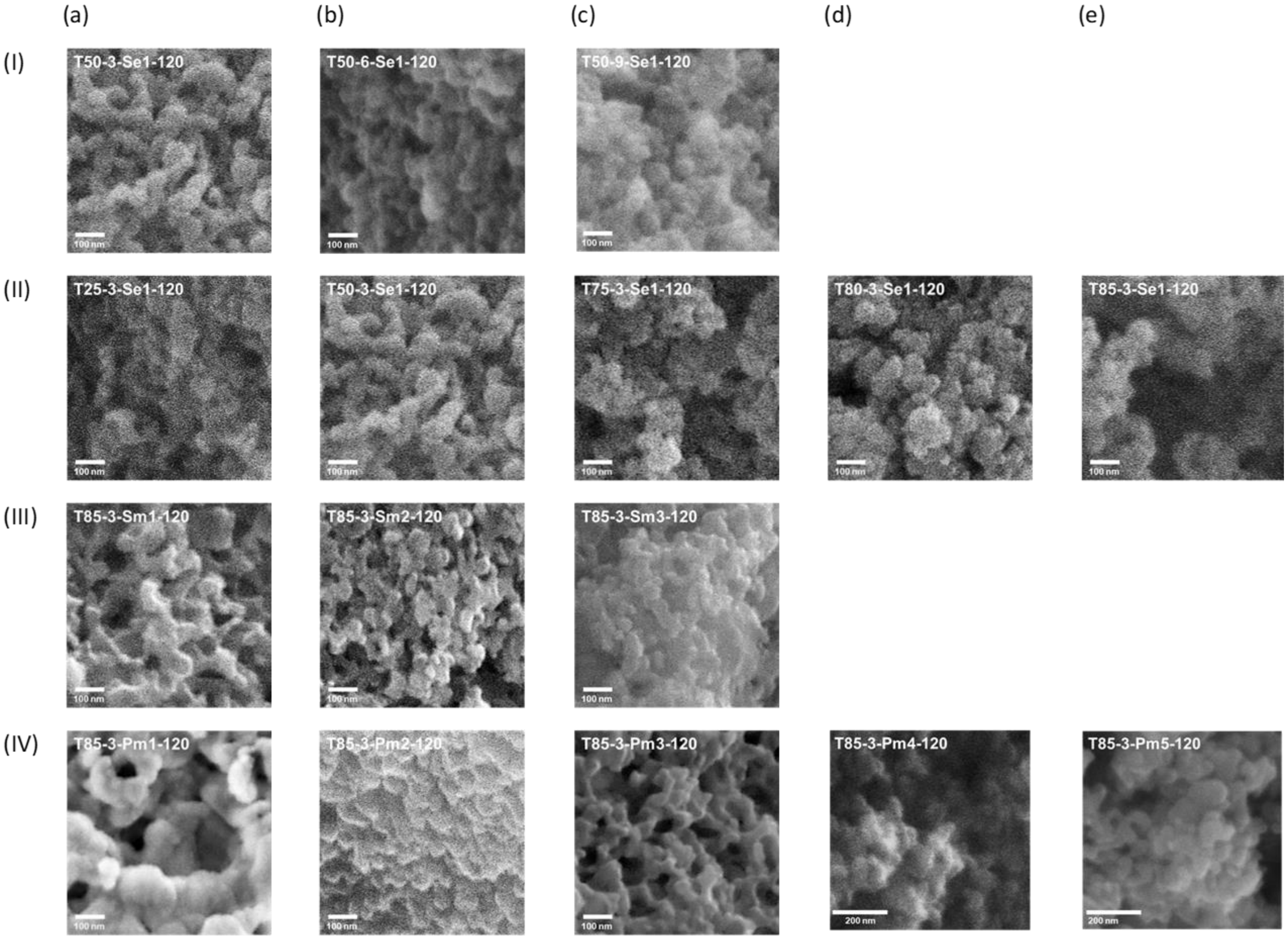

Figure 4-2 Morphology of HKUST-1 MOFs prepared under different preparation conditions. I, reaction time. II, synthesis temperature. III, slurry state activation. IV, powder state activation.

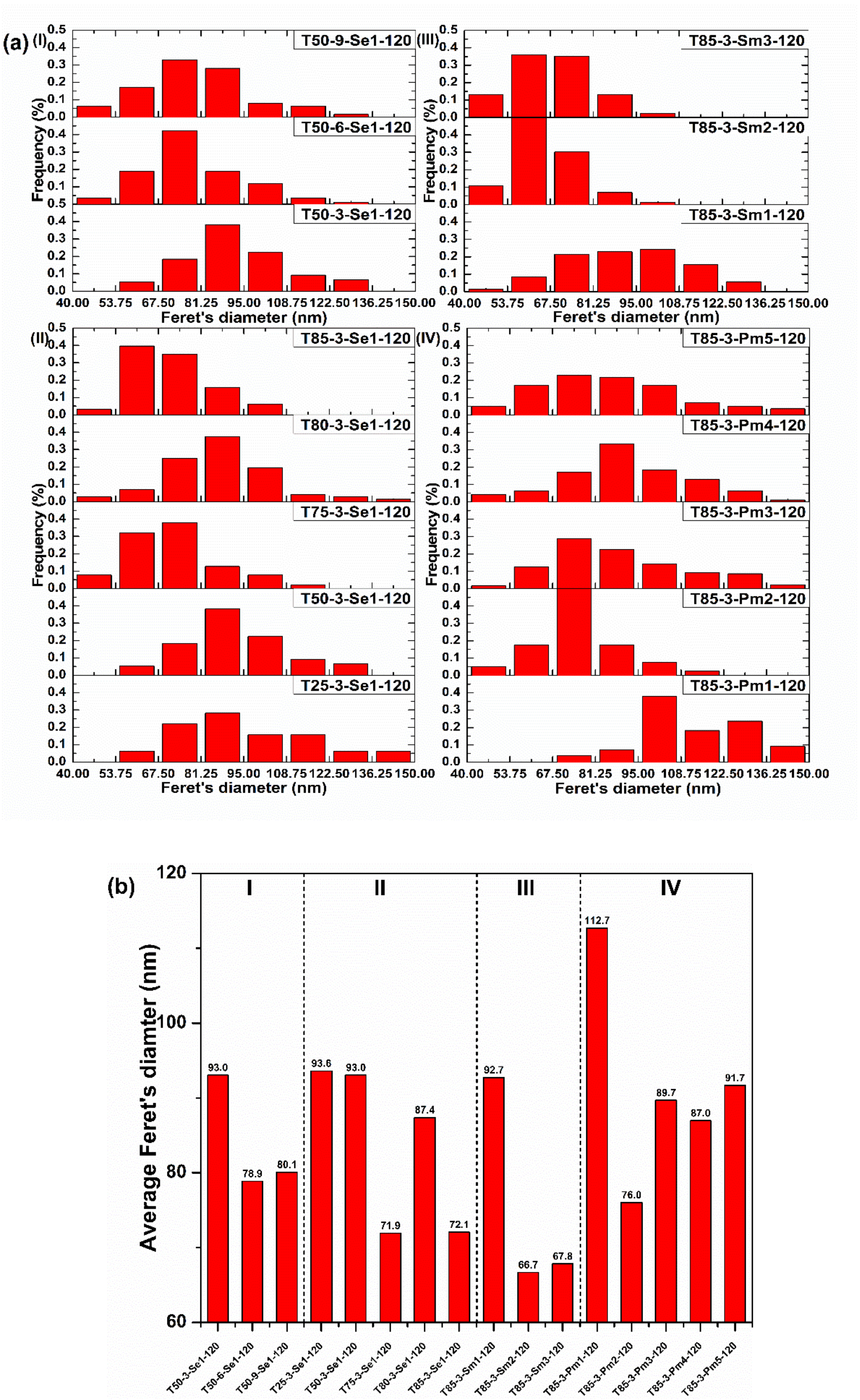

Figure 4-3 Particle size (based on Feret's diameter) of each synthesized sample vs different preparation method (results obtained from ImageJ). a, particle size distribution. b, average particle size (average Feret's diameter). I, reaction time. II, synthesis temperature. III, slurry state activation process. IV, powder state activation.

Table 4-2 BET results of different activation process

Preparation Method	S_{BET}[1] (m^2/g)	$S_{Langmuir}$[2] (m^2/g)	$V_{Total\ Pore}$[3] (cm^3/g)	$V_{Micro\text{-}Pore}$[4] (cm^3/g)	%$V_{Micro\text{-}pore}$[5] (cm^3/g)	PH*
T85-3-N-120	503.5	580.1	0.31	0.2	0.65	3.63
T85-3-SE1-120	769.6	904.7	0.58	0.29	0.5	3.6
T85-3-SM1-120	954.4	1197.7	0.49	0.4	0.82	3.86
T85-3-PM1-120	1032.3	1235.4	0.55	0.45	0.82	7.01
T85-3-PE1-120	1003	1161.1	0.47	0.38	0.81	6.07
T85-3-SM2-120	687.5	719.7	0.49	0.23	0.47	4.78
T85-3-SM3-120	493.5	516.4	0.36	0.16	0.44	5.63
T85-3-PM2-120	1292.3	1452.4	0.56	0.47	0.84	7.7
T85-3-PM3-120	1354.6	1579.3	0.63	0.54	0.86	7.87
T85-3-PM4-120	1542.4	1647.9	0.65	0.57	0.88	8.17
T85-3-PM5-120	1241	1358.2	0.53	0.46	0.87	8.2
T85-3-SM1PM1-120	1264.6	1437.8	0.57	0.49	0.86	6.22
T85-3-SM1PM2-120	541.6	731.2	0.45	0.24	0.53	6.88
T85-3-SM1PE1-120	1022.7	1184.5	0.48	0.4	0.83	6.18

Note:1. Specific surface area by BET. 2. Specific surface area by Langmuir. 3. Total pore volume by original Horvath-Kawazoe. 4. Micro pore volume by t-plot. 5. Micro pore volume percentage in total volume. * pH values of solution were measured after the activation.

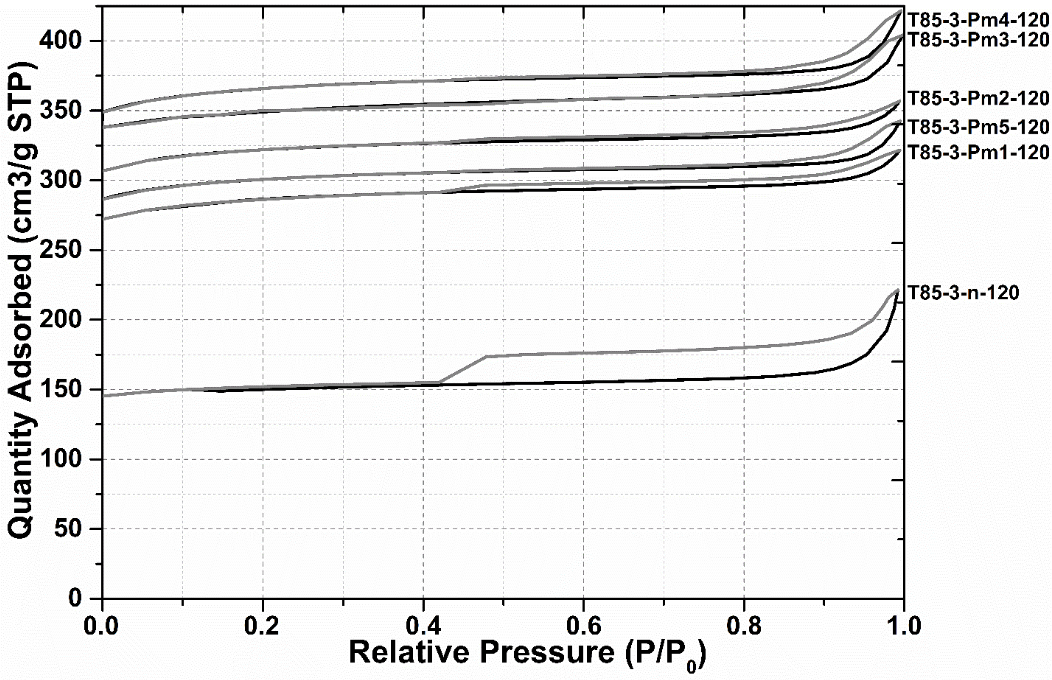

Figure 4-4 Nitrogen adsorption and desorption isotherms of the synthesized HKUST-1. Grey line is the adsorption isotherm; black line is the desorption isotherm.

4.2.3 Nitrogen isotherm analyses

To explore the pore distribution and pore properties, the nitrogen isotherm analyses were investigated. It is found that N_2 adsorption rate increases at a low relative pressure ($0.0 < P/P_0 < 0.1$) (as shown in Figure 4-4), the shape of each line indicates that they are Type I isotherm according to the IUPAC (International Centre for Theoretical and Applied Chemistry) classification [221, 223]. Samples with Type I isotherm are of microporous (< 2 nm) structure [224]. The hysteresis loop at a higher relative pressure ($P/P_0 > 0.4$) indicates capillary condensation of mesopores for N_2, which contributes to the stacking combination of large particle of HKUST-1 [225] or the creation of defects under such synthesis method [226]. That is, the hysteresis loop for

T85-3-n-120 and T85-3-Pm1-120 would be due to the defects, because this loop was the cavitation phenomenon [227] that occurs when the pore size is less than 6 nm. Besides, the hysteresis loop for T85-3-Pm**X**-120 (X=2,3,4,5) at P/P0 > 0.8 appeared due to larger pores over 10 nm [228]. This loop is caused by the inter-particle pores of nanoparticle agglomerate [229].

The influence of the activation process on the surface properties of HKUST-1 was also investigated. As shown in Table 4-2, BET surface area after the activation is in the range of 503-1542 m^2/g, which is very close to the values reported by Diring [230] and Ameloot [231], but much higher than those obtained by Chui [205]. In addition, the total pore volume was reported as in the range of 0.21 - 0.79 cm^3/g [232], whereas the effective pore volume was reported as 0.82 cm^3/g [233]. In this study, the as-synthesized samples exhibited a total pore volume of 0.31 - 0.65 cm^3/g, which is comparable with reported data. The relatively low N_2 adsorption capacity of the raw material (T85-3-N-120) is attributed to some micropores in the MOFs being blocked by TEA and/or its derivatives. The high N_2 adsorption capacity indicates that the modulator is absent from the pores after the activation. The percentage of micropore volume shown in Table 4-2 suggests that these samples are comprised of plenty of micropores. After the activation process (powder, slurry and combination activation), there are less or more effects on the pore properties (BET, Langmuir, Total pore volume, Micropore volume, and Microporosity) of these samples listed in Table 4-2. As for slurry activation, the methanol or ethanol as solvent exchange agent both can clean the interior of pore and improve the N_2 adsorption capacity, but methanol can provide more efficient solvent exchange effect than ethanol's, in spite of that, more times (>2) of slurry activation by methanol would have a negative influence on pore properties of samples. This is attributed to the decrease in percentage of micropores, which means excessive times of slurry state activation might damage micropores of HKUST-1 and form more mesopores. In addition to the improvement of powder activation (namely combination activation), such the combination activation process would provide better pore properties based on the sample activated once in the slurry state. That is, appropriate number (<2) of powder activation should have a positive effect on the removal of impurities in pores and maintaining a stable pore structure, also, the methanol participation (T85-3-SM1PM1-120) is still better than ethanol (T85-3-SM1PE1-120). As to the alone powder activation, the BET specific areas of samples activated just once by ethanol or methanol have been up to 1000 m^2/g. As the times of powder activation by the methanol increase later, it has been improving in pore properties until the fifth activation starts. Hence, compared with the slurry state activation process, powder state activation with appropriate times has an advantage in the removal of impurities trapped in pores.

Meanwhile, the pH value of the solution after activation was monitored by using a pH meter, the results of which are shown in Table 4-2. It is clear that pH value generally increased with BET specific surface area, which is associated with the removal of impurities and TEA derivatives. It is speculated that powder state activation retained the high BET surface area and did not damage the pore structure of HKUST-1. Therefore, the powder state activation by methanol is considered as an appropriate method for the treatment of the pristine HKUST-1.

4.2.4 Crystallinity analyses

XRD analysis was conducted to show the crystalline phases of the porous HKUST-1. It can be seen that all the diffraction peaks in the Figure 4-5 (a) &(b) match well with the pattern of C300 and simulation, indicating that these samples are pure phase of HKUST-1. From Figure 4-5, it is evident that the XRD peak positions and relative intensities of the synthesized MOFs also agree well with those of the simulated HKUST-1 (red spikes labelled by star at the bottom of Figure 4-5) [234]. Due to the low-temperature condition adopted for the synthesis of HKUST-1, the diffraction peaks of Cu_2O (36.7°, PDF #04-003-6433) do not show in the XRD spectrum, which means that (Cu_2O) was not formed.

It can be seen from Table 4-3 that the synthesis temperature has significant impacts on the crystallinity of the samples. In the samples of T**X**-3-Se1-120 (X=25, 50, 75, 80, 85), the crystallinity percentage of T85-3-Se1-120 is very close to that of the C300 (%Crystallinity = 95.4%), which demonstrates that the low synthesis temperature (85 °C) can lead to the formation of HKUST-1 with appropriate crystal structure. After the samples were further processed via powder state activation, the crystallinity percentage of each sample did not vary significantly compared with the variation in temperature. After more times of powder state activation, the crystallinity percentage is improved until 5 times of powder state activation. However, further powder state activation does not show much influence on crystallinity percentage. Therefore, to obtain the highest crystallinity percentage of HKUST-1, the sample shall be prepared under 85 °C with the four times of powder activation process.

In addition, the hydration degree of the HKUST-1 could be determined by the I_{200}/I_{220} ratio [235], where higher I_{200}/I_{220} ratio indicates a smaller hydration degree. Normally, a smaller hydration degree indicates that more copper coordination sites are accessible for other molecules, such as CO_2. The T85-3-Pm4-120 shows the highest value of I_{200}/I_{220}, which suggests that it can capture more CO_2 than any other samples. This result suggests that the proper condition (T85-3-Pm4-120) lead to the formation of HKUST-1 with desired properties in CO_2 adsorption.

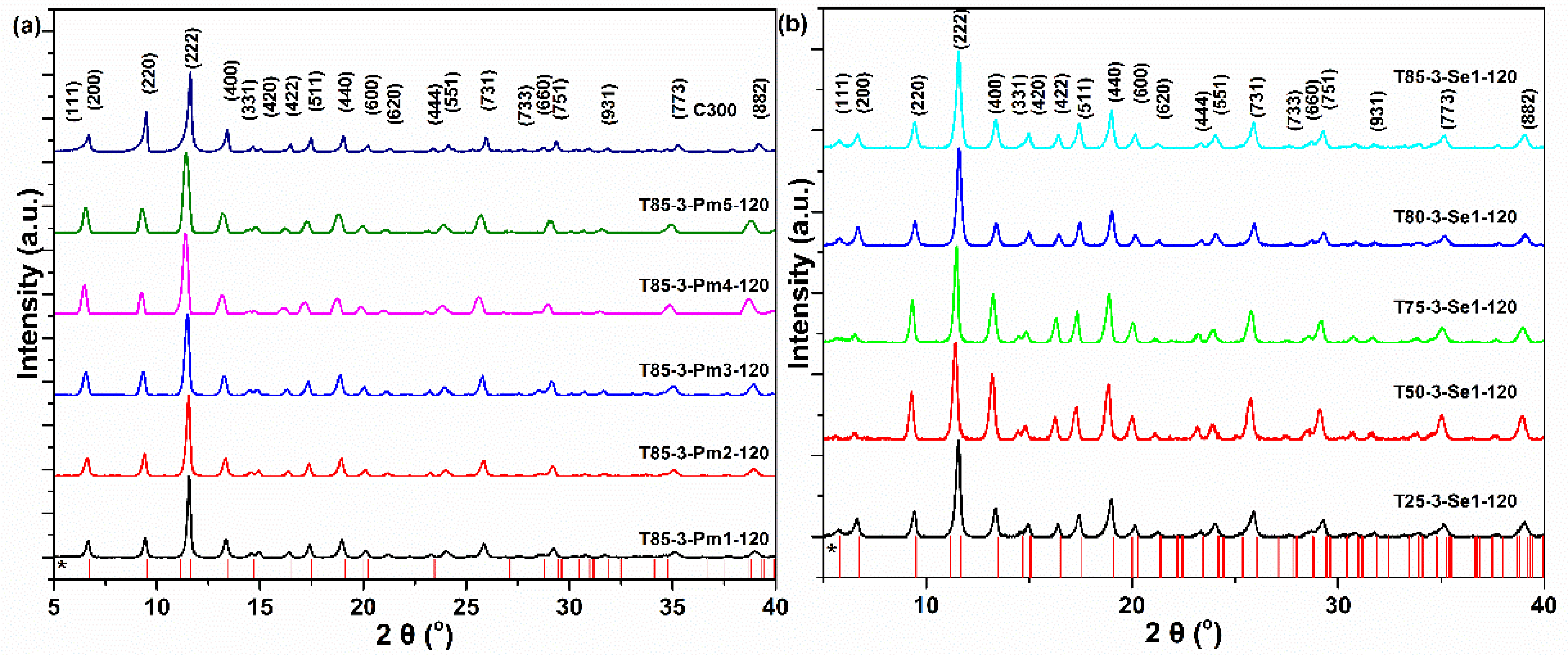

Figure 4-5 XRD spectrum of each sample. (a) HKUST-1 activated by repeated powder state activation. (b) HKUST-1 synthesized under different reaction temperatures. * indicates simulated PXRD data from single crystal data.

Table 4-3 XRD patterns of relative peak intensity based on the HKUST-1 peak intensity of (222)

	$I_{(200)}$ %	$I_{(220)}$ %	$I_{(222)}$ %	$I_{(400)}$ %	$I_{(420)}$ %	%Crystallinity	$I_{(200)}/I_{(220)}$
T85-3-PM5-120	30.2	30	100	24	7.4	98.3	1.01
T85-3-PM4-120	38.5	28.7	100	18.8	6.7	98.9	1.34
T85-3-PM3-120	27.5	28.1	100	23.2	6.1	94.9	0.98
T85-3-PM2-120	22.8	27.3	100	19.2	6.1	90	0.84
T85-3-PM1-120	20.2	24.2	100	20.4	6.5	87.9	0.83
T85-3-SE1-120	14.3	27.2	100	29.3	15.1	95.4	0.53
T80-3-SE1-120	17.3	25.4	100	21.7	13.9	91.5	0.68
T75-3-SE1-120	7.8	43.7	100	48.6	10.6	108.2	0.18
T50-3-SE1-120	5.2	47.7	100	63	13.3	117.7	0.11
T25-3-SE1-120	17.1	26.8	100	26.2	13.6	94.3	0.64
C300	16	47.6	100	27.4	3.8	100	0.34

Note: %Crystallinity was based on Equation 1.

4.2.5 Thermal-stability analyses

The HKUST-1 ($Cu_3(BTC)_2(H_2O)_3\cdot xH_2O$, x=3) prepared in this study was tested in TGA to show its thermal stability. As shown in Figure 4-6, these samples have similar TG curves from 35 to 900 °C. At temperatures below 120 °C, the weight loss is due to the desorption of physisorbed water or gases. This was followed by the release of water trapped in the pores when the temperature was raised up to 180 °C. The HKUST-1 was then heated up to 350 °C and exhibited modest loss of weight, as shown in DTG curve of the Figure 4-6. However, the weight loss increased significantly when temperature was raised above 350 °C. Due to temperature rising, metal ions of some ligands were reduced, and MOFs were pyrolyzed to form carbon. The weight loss levelled off at a higher temperature when MOFs were completely transformed into CO_2, CO, Cu, Cu_2O, and CuO. This finding is consistent with what has been reported by others, the MOFs retained its molecular formula but lost the microporous nature after being heated to 350 to 427 °C [236]. In the end, the final product of XRD spectrum was in Figure 4-7. The diffraction indicated the residue was in the presence of Cu_2O phase with a little CuO and Cu.

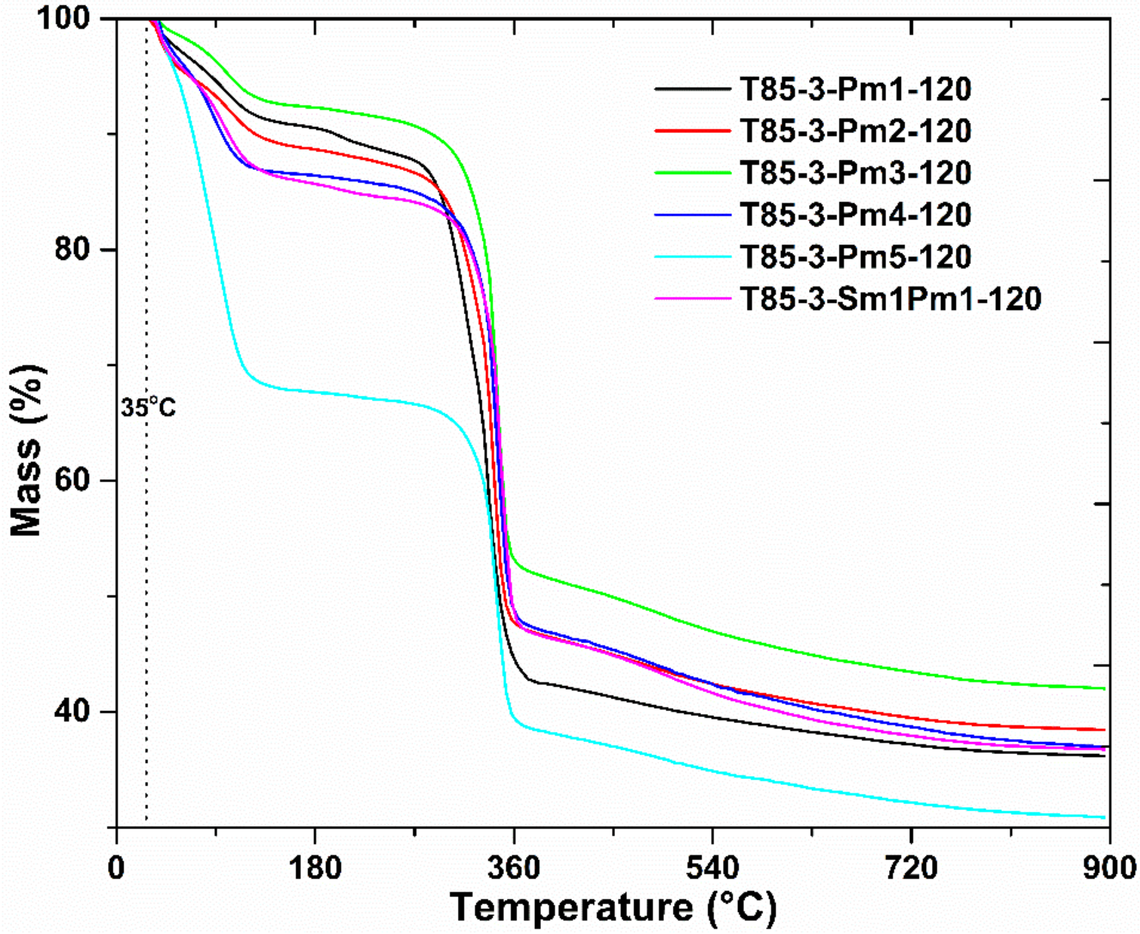

Figure 4-6 TGA analysis of T85-3A-Pm1, Pm2, Pm3, Pm4, Pm5 and Sm1Pm1-120 from 35 °C to 900 °C within N_2 atmosphere.

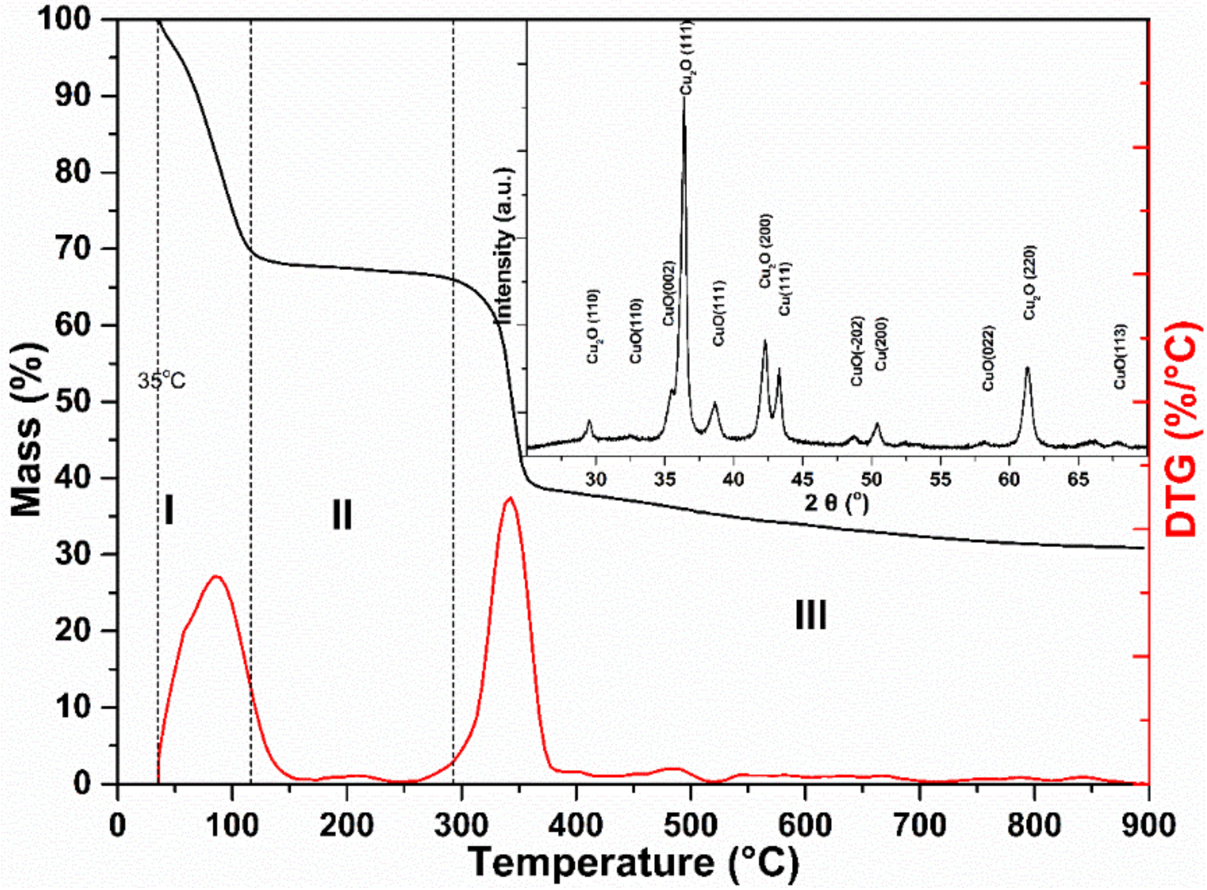

Figure 4-7 Temperature vs Mass or DTG of T85-3-Pm4-120 in N_2 atmosphere, inset graph is XRD spectrum of T85-3-PM4-120 residue after being heated to 900 °C. I, desorption of physisorbed water and guest gas. II, thermal resistance. III, destruction of HKUST-1.

4.2.6 CO_2 adsorption analyses

It was found that the presence of divalent metals significantly increased CO_2 binding strength and resulted in higher selectivity toward CO_2 adsorption [237]. Due to the highly crystalline structure and the existence of Cu^{2+} metal ions, HKUST-1 is expected to have high affinity toward CO_2. Normally, CO_2 adsorption can be evaluated by two methods, i.e., static and dynamic adsorption. In this study, the static adsorption test was carried out at 27 °C with pressure from 0-1 bar. In the dynamic test, a thermogravimetry study with pure CO_2 flow at 27 °C was carried out.

The CO_2 uptake of T85-3-Pm**X**-120 (X=1,2,3,4,5) and T85-3-Sm1Pm1-120 is shown in Figure 4-8. The CO_2 uptake capacity of T85-3-Pm4-120 sample exhibited a steep rise in a short time, and reached a maximum of 8.12% wt. (1.84 mmol/g), at 27 °C and 1 bar. It is generally believed that CO_2 adsorption capacity is dependent on pore volume of the adsorbent [238]. The larger the microporosity (< 2 nm), the higher the CO_2 adsorption capacity (< 2 nm). Besides, the I_{200}/I_{220} ratio of each sample can also be used as an indicator for CO_2 adsorption capacity. To reveal the CO_2 adsorption property of T85-3-Pm4-120, CO_2 adsorption isotherm was obtained and is shown in Figure 4-9. The CO_2 recycle of T85-3-Pm4-120 were measured at 27 °C under 1 bar in Figure 4-9. The result illustrated that the desorption process finished rapidly by N_2 purging under the same condition and the adsorption capacity remains almost unchanged after ten adsorption/desorption cycles, which revealed the good adsorption stability of

T85-3-Pm4-120. It is clear that the adsorption capacity of T85-3-Pm4-120 increased with pressure, and such the sample could have CO_2 uptake of 11%wt (2.5 mmol/g) under static adsorption, which is higher than reported data under similar experimental conditions as shown in Table 4-4.

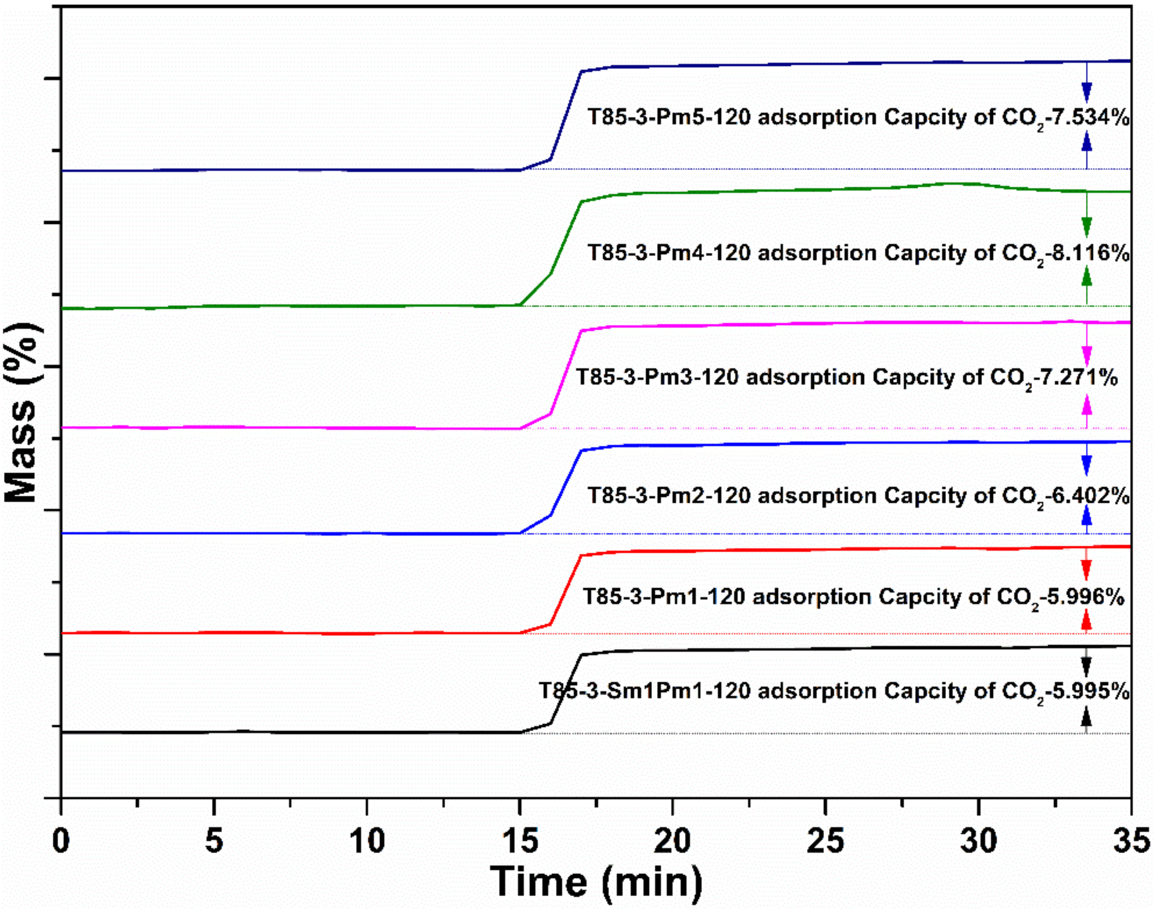

Figure 4-8 Adsorption capacity of CO_2 at 27°C for HKUST-1 samples (TGA data). In the range of 0-15 min, all samples were in N_2 atmosphere with N_2 flow of 40ml/min before CO_2 gas flowed in.

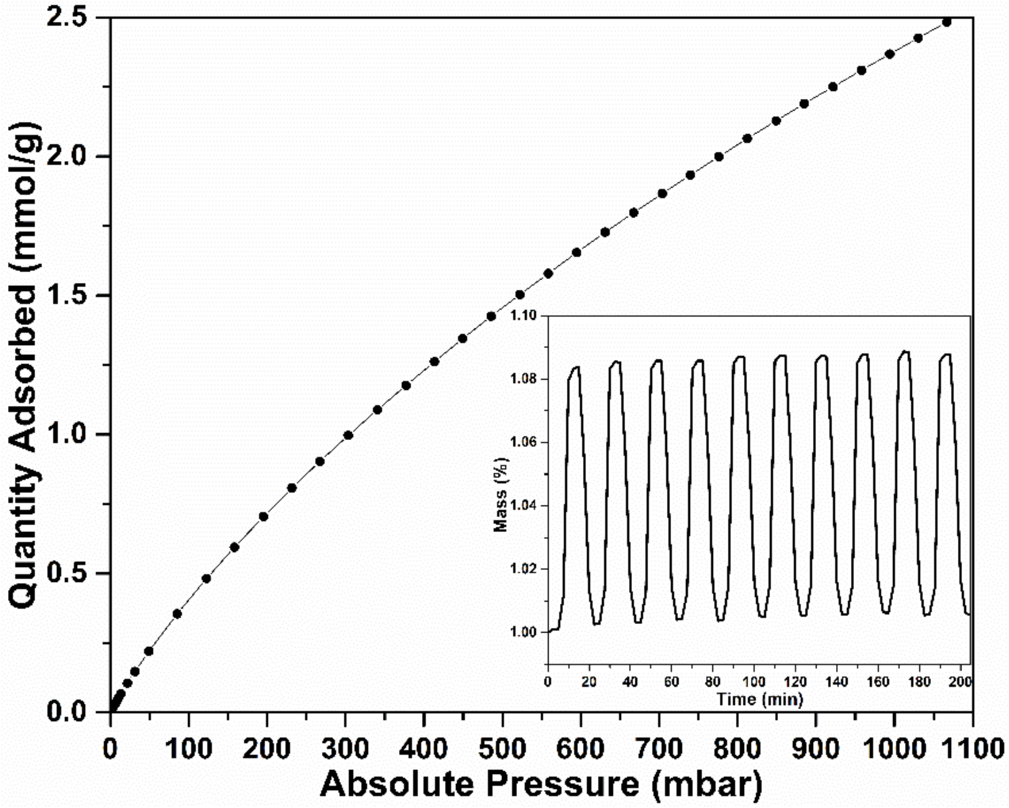

Figure 4-9 CO_2 isotherm of T85-3-Pm4-120 at 27 °C, inset graph is CO_2 recycle of T85-3-Pm4-120

Table 4-4 Comparison of CO_2 adsorption capacity for others' HKUST-1

Literature	Adsorption manner	Adsorption capacity mmol/g	temperature ^{o}C
Sheng et al. [239]	Dynamic adsorption	1.82	30
Chugh et al. [240]	Dynamic adsorption	1.45	30
Shen et al. [241]	Static adsorption	0.15	20 (0.75 bar)
Yunxia et al. [242]	Dynamic adsorption	1.80	32 (5 bar)
This research	Dynamic adsorption	1.84	27 (1 bar)
This research	Static adsorption	1.95	27 (0.75 bar)
This research	Static adsorption	2.50	27 (1 bar)

4.3 Summary

a) The optimized hydro/solvo-thermal approach developed in this research is a cheap and efficient method for the synthesis of nanoscale HKUST-1 MOFs with a BET surface area of 1542.4 m^2/g.

b) The activation methods for HKUST-1 MOFs shows two different features, i.e., the improvement of the specific surface area and the increased micropore volume and smaller mesopore size.

c) It was also found that the HKUST-1 prepared in this study showed a high CO_2 uptake around 11% wt. (2.50 mmol/g) at 27 ^{o}C and 1 bar.

Acknowledgement

Published in Microporous and Mesoporous Materials 270 (2018): 249-257. The title of paper is "Optimized synthesis of nano-scale high quality HKUST-1 under mild conditions and its application in CO_2 capture." All the copyright belongs to Microporous and Mesoporous Materials.

Chapter 5 MoS_2/HKUST-1 core-shell composite and its application in CO_2 capture

5.1 Introduction

Metal organic frameworks (MOFs) demonstrate high capacity in the small molecule (CO_2) uptake owing to its high surface area and tunable porous structure [243-245]. However, the huge void space cannot be fully utilized for gas capture or storage due to the weak interactions between the prime sites of MOFs and the gas molecules [246, 247]. To improve the capacity of the adsorption of small molecules, such as CO_2, the addition of basic species to MOFs has become one of the most popular modification methods [248]. However, this approach normally results in a decrease in both surface area and pore volumes [249]. Therefore, most recent research was mostly focused on the assembly of composites based on MOFs and other functional materials such as graphite oxides, polymers, metal nano-particles and mesoporous silica, etc. [250-256].

In the past two decades, owing to their graphene-like structure and novel properties, 2D transition-metal dichalcogenides (TMDCs) have attracted significant attention [257-260]. Of these TMDCs, molybdenum disulphide (MoS_2) is a typical graphene-like material with a Mo atom layer sandwiched by two layers of S atoms [261], which has fascinating properties leading to its applications in many fields, such as energy storage [262], catalysis [263], adsorption [264]. In addition, HKUST-1 keeps a higher density of Cu(II) open sites than most of the known MOFs [265]. These exposed metal sites provide a high metal-to-unit cell ratio, making HKUST-1 a promising material for gas uptake [266], separation [267], and etc. To date, little research has been carried out on the MoS_2/HKUST-1 core-shell composite and its application in gas capture/storage, needless to say the research to understand the mechanism of the growth of such composites.

Although it has been reported recently that Co, Ni, Cu-containing MOFs cross-linked with graphene or graphene oxide exhibit enhanced CO_2 uptake [268, 269] because of their adjustable surface areas and metal nodes [270], the effective preparation of MoS_2/HKUST-1 composites for enhanced CO_2 uptake still faces huge challenges. To date, no work has been reported on the ‘one-pot’ synthesis of MoS_2/HKUST-1 composite that is of core-shell structure.

In this study, we focused on the development of a new strategy for the one-pot synthesis of MoS_2/HKUST-1 core-shell composites. The first principles calculations were carried out to reveal the mechanism of the growth of HKUST-1 alone and the growth of HKUST-1 on the MoS_2 (001) quantum dots to form core-shell composites. In addition, molecular dynamic computational study was conducted to show the interactions between MOF and MoS_2 and between CO_2 and the MOF+MoS_2 composites. Lastly, CO_2 adsorption testing was also performed to examine the CO_2 uptake capacity of such the MoS_2/HKUST-1.

5.2 Results and discussion

5.2.1 HKUST-1 formation

In the self-assembly of MOFs, the two sub-reactants (organic ligands and metal precursors) are combined spontaneously. It is difficult to directly investigate the influence of individual reactants on the growth of MOFs since the growth of MOFs starts from a mixture, including multitudinous species (reactants and intermediates) including SBUs (secondary building units) and other larger units. Besides, the ion state of organic ligands can be supplied directly as a reactant or be induced by the mixture of reactants, likewise, the inorganic coupling units could be fabricated in the metal precursors or during the course of the synthesis process. For these reasons, the formation of SBU is crucial to understand the growth of MOFs as well as to demonstrate the formation of a complete unit of HKUST-1, i.e. the possible reaction pathways for the growth of a complete HKUST-1 unit.

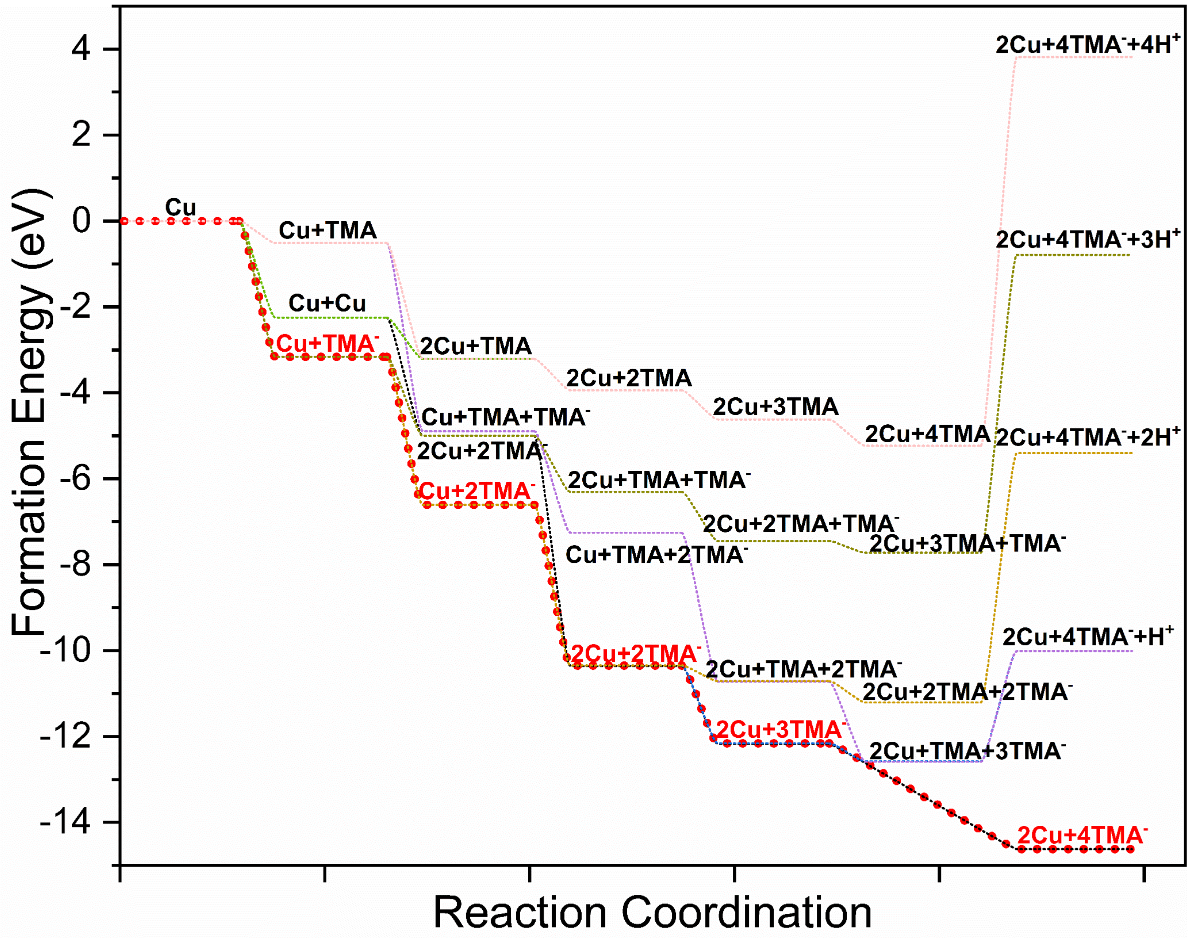

Figure 5-1 Possible pristine HKUST-1 formation processes (red dotted path is the most possible reaction pathway).

To study the formation of an entire HKUST-1 unit, effort was made to understand how possible reactant participants (Cu, TMA, TMA^-, H^+) [271] participate in the formation of a MOF SBU. The actual units of growth are more likely to be simpler fragments, such as individual solvated trimesic species or Cu^{2+} ions, a trimesate anion with Cu^{2+} cations coordinated to one or more COO-$^-$ groups of the trimesate moiety or perhaps a copper dimer type unit. Based on 75 possible reaction pathways investigated in this study and the results of the refinements, as shown in Figure 5-1, it can be concluded that the most possible reaction pathway is the pathway that is highlighted into red. The formation of HKUST-1 starts from a Cu^{2+} cation coordinating fully with a trimesate anion to form a HKUST-1 SBU ($Cu+TMA^-$) (as shown in Figure 5-2(a)), followed by the coordinating with anther trimesate anion to form ($Cu+2TMA^-$) (as shown in Figure 5-2(b)), which increases the structural stability of the Cu^{2+} cation and the COO^- groups of the trimesate moiety. It is clear in Figure 5-2(a) and (b) that two oxygen atoms on the carboxyl group of trimesate anion are bound to the Cu^{2+} cation, which ensure the saturation of the O atoms. However, further growth of a HKUST-1 unit is the two trimesate anions together with the original Cu^{2+} cation to bound to another Cu^{2+} cation (as shown in Figure 5-2(d)). After the Cu^{2+} dimer bridges assembled completely to form a ($2Cu+2TMA^-$) structure, two more trimesate anions bound to the unsaturated Cu-Cu bridge, and form a complete SBU packaging, which is consistent with the finding of study using an atomic force microscopy (AFM) [272].

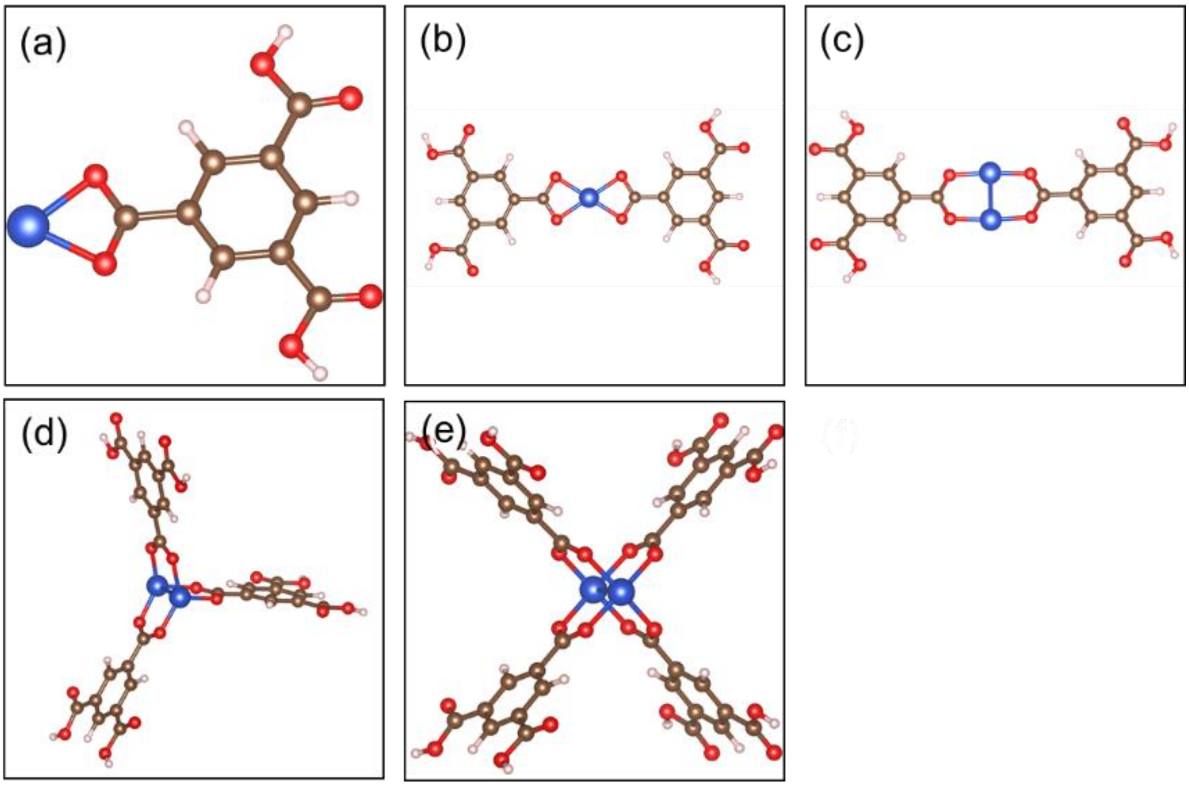

Figure 5-2 most possible HKUST-1 Formation process. (a) Cu+TMA^- (b) Cu+2TMA^- (c) 2Cu+2TMA^- (d) 2Cu+3TMA^- (e) 2Cu+4TMA^-

5.2.2 HKUST-1 growth on MoS_2 quantum dots

In this study, the energetic properties of molecules adsorbed on the MoS_2 (001) quantum dots were studied. Table 5-1 summarized the calculated energy of the adsorption of molecules on the MoS_2 (001) monolayer. The bold values for each adsorbate are corresponding to its favourable adsorption configuration. All the models used in the calculation are presented in Appendix and most stable adsorption configurations were exhibited in Figure 5-3. Firstly, The adsorption of individual Cu atoms and TMA molecules was considered on the 2D MoS_2 monolayer. A 4 × 4 supercell of a MoS_2 monolayer was selected as the computational unit. The optimized lattice constant of monolayer MoS_2 is 3.12 Å, while the corresponding vacuum slab is larger than 15 Å. To determine the favourable adsorption configuration of a single Cu atom on the MoS_2(001), three adsorption sites were considered, namely, on top of a hexagon (H), on top of a Mo atom (T_{Mo}), on top of a S atom (T_S) as shown in Figure 9S-1 (Chapter 9 Appendix). Furthermore, in terms of the favourable adsorption configuration of a single TMA molecule or TMA^- anion, seven adsorption sites have been studied as illustrated in Figure 9S-2. After finding the more stable configuration of Cu atoms on MoS_2 and TMA/TMA^- on MoS_2, the behaviour of Cu cluster and single Cu atoms on MoS_2 monolayer was studied. The stable structure of the Cu_3 cluster on the MoS_2 monolayer was chosen along the surrounding of the Cu_2 cluster, and the most stable structure of the Cu_3 cluster is shown in Figure 9S-3(c). In addition, the Cu_4 metastable structure on the MoS_2 monolayer was based on Cu_3 cluster in Figure 9S-3(d). By analogy, the structures of the Cu_n (n = 5-7) clusters are identified as shown in Figure 9S-3 (e-j). To confirm the possibility of single atom distribution on the MoS_2 monolayer, single Cu atoms were placed in the adjacent T_{Mo} site without forming Cu-Cu bond, which is shown in Figure 9S-4. The adsorption of TMA, TMA^-, Cu, nH_2O and nEtOH(n=1,2,3) on the most stable configuration of MoS_2+Cu system has also studied and is shown in Figure 9S-5, Figure 9S-6 and Figure 9S-7. To determine the most favourable adsorption configuration of TMA/TMA$^-$ on the MoS_2+Cu system, three adsorption sites have been considered, which have three different angles between the plane of TMA/TMA$^-$ benzene ring and the plane of upper monatomic S-layer, i.e. 0^o, 45^o, 90^o. As for H_2O and EtOH molecules, the molecule is initially placed with its centre of mass exactly closed to the neighbouring Cu atom. For possible adsorption sites, configurations with various molecule orientations have then been attempted. The stability of an adsorption configuration is determined by the adsorption energy.

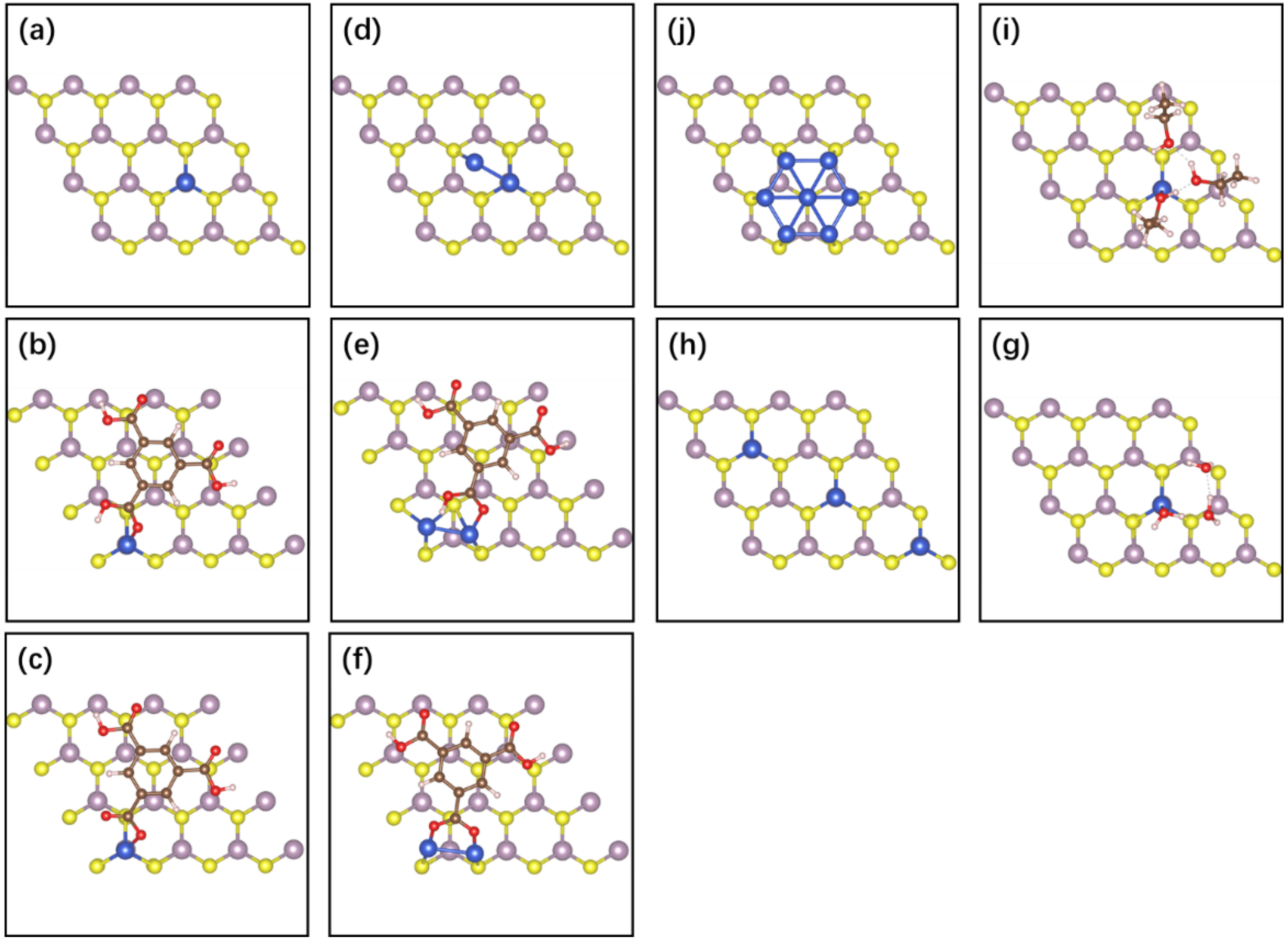

Figure 5-3 Adsorption configurations. Top views of the most favourable configurations for (a) (MoS$_2$)-Cu; (b) (MoS$_2$)-TMA; (c) (MoS$_2$)-TMA$^-$; (d) (MoS$_2$)-Cu$_2$; (e) (MoS$_2$+Cu$_2$)-TMA; (f) (MoS$_2$+Cu$_2$)-TMA$^-$; (j) (MoS$_2$)-Cu$_7$; (h) (MoS$_2$)-Cu, Cu, Cu; (i) (MoS$_2$+Cu)-nH$_2$O; (g) (MoS$_2$+Cu)-nEtOH. Violet ball: Mo atom; yellow ball: S atom; pink ball: H atom, and red ball: atom.

Table 5-1 Adsorption energy of different adsorption systems

MoS_2 Adsorption system[1]	Site	E_{ads}[2] eV	Cluster Adsorption system[1]	Site	E_{ads}[2] eV	MoS_2+Cu_n Adsorption system[1]	Site	E_{ads}[2] eV	No MoS_2 Adsorption system[1]	E_{ads}[2] eV
(MoS_2)-Cu	T_S	-1.16	(MoS_2)-Cu	T_{Mo}	-1.73	(MoS_2+Cu)-TMA	90°	-1.09	(Cu)-TMA	***-0.51***
	H	-1.61	(MoS_2)-Cu_2	T_H	-2.04		45°	-1.01		
	T_{Mo}	***-1.73***	(MoS_2)-Cu_3	T_{Cu}	-2.20		***0°***	***-1.5***		
(MoS_2)-TMA	center$_{Mo}$	-0.9	(MoS_2)-Cu_4	T_S	-2.33	(MoS_2+Cu)-TMA^-	90°	-3.63	(Cu)-TMA^-	***-3.16***
	bridge	-0.92	(MoS_2)-Cu_5	B	-2.46		45°	-3.59		
	top	-0.92	(MoS_2)-Cu_6	T_{Mo}	-2.62		***0°***	***-3.9***		
	center$_{Mo}$ cross	-0.93	(MoS_2)-Cu_7	**B**	**-2.66**	(MoS_2)-Cu_2	T_S	-2.2	(Cu)-Cu	***-2.25***
	cross	-0.93	Single atom[3] Adsorption system[1]				H	-2.35		
	center$_S$	-0.93				(MoS_2+Cu_2)-TMA	90°	-1.03		
	center$_S$ cross	***-0.99***	(MoS_2)-Cu	TMo	-1.73		45°	-1.04	(Cu_2)-TMA	***-0.96***
(MoS_2)-TMA^-	center$_{Mo}$	-0.94	(MoS_2)-Cu,Cu	TMo	-1.77		***0°***	***-1.37***		
	top	-0.95	(MoS_2)-Cu,Cu,Cu	**TMo**	**-1.80**	(MoS_2+Cu_2)-TMA^-	***0°***	***-4.3***		
	bridge	-0.96				(MoS_2+Cu)-nH_2O	$1H_2O$	*-0.64*	(Cu_2)-TMA^-	***-2.75***
	center$_S$	-0.98					$2H_2O$	-0.49		
	center$_{Mo}$ cross	-0.98					**$3H_2O$**	**-0.65**		
	cross	-0.99				(MoS_2+Cu)-nEtOH	1EtOH	***-0.88***		
	center$_S$ cross	***-1.04***					2EtOH	-0.52		
							3EtOH	**-0.76**		

Note: 1, adsorption system is named as the rule of (adsorbent)-adsorbate, which is one adsorbate being linked with the adsorbent. 2, E_{ads} is the adsorption energy of adsorbate on adsorbent. 3, single atom refers to Cu atom being adsorbed on the MoS_2 monolayer without forming of Cu-Cu bond.(The bold site name corresponds to the adsorption configuration of Figure 5-3.)

The study on the geometry and stable configurations of Cu_n clusters (n=1-7) on MoS_2 quantum dots has been studied (as shown in Figure 9S-3) shows that Cu-S bond formed at the interface of Cu cluster and MoS_2 quantum dots. As a control group, the single atoms of Cu were dispersed at the adsorption site T_{Mo} of the MoS_2 monolayer. For the system of Cu cluster deposited onto the MoS_2 surface, the adsorption energy of Cu_n Cluster (Cu_n, n=1-3) was greater than that of the dispersed single Cu atoms on the MoS_2, which indicated that Cu tends to be in the formation of clusters on MoS_2 quantum dots rather than singular atoms. The structures of Cu_n cluster ($n \leq 7$) deposited on MoS_2 quantum dots have been studied, which showed that the stability of Cu clusters deposited on MoS_2 quantum dots increased with the number of Cu atoms. The adsorption energy increases rapidly when the number of Cu atoms is no more than 3 and then levels off, which indicated that the Cu_n/MoS_2 configuration became stable. The adsorption energy changed from -1.73 eV to -2.66 eV, which fell in chemisorption region. Therefore, it can be concluded that relatively lower concentration of Cu favours the growth of metastable Cu clusters on the MoS_2 quantum dots, while higher concentration of Cu normally results in the formation of a Cu layer covering the surface of the MoS_2.

As shown in Table 5-1, MoS_2 nanosheet (001) adsorbs Cu atoms at T_{Mo} sites, TMA at $center_S$ cross and TMA^- anion at $center_S$ cross, with an adsorption of -1.73 eV, -0.99 eV and -1.04 eV, respectively, which suggests that MoS_2 quantum dots adsorb Cu more favourably than other species in the reactant solution containing MoS_2 quantum dots, Cu^{2+} cations, TMA, TMA^- anion. Also, Cu^{2+} cations can station easily on MoS_2 quantum dots and form a stable structure. When the reaction can proceed further, (MoS_2)-Cu act as the site for the growth of HKUST-1, which corresponds to the existence of Cu-S bond shown by the FTIR results. When the formation of HKUST-1 proceeds at this (MoS_2)-Cu site, it may be further bound to either a Cu^{2+}, a TMA, or a TMA^- anion. However, the calculated adsorption energy indicated that (MoS_2)-Cu system can adsorb a TMA^- anion at 0° site with an adsorption energy of -3.90 eV or bound to another Cu^{2+} cation at H site with an adsorption energy of -2.35 eV. Conversely, in the existence of TMA^- anions, it is difficult for Cu^{2+} to form a cluster on the MoS_2 quantum dots. This binding pattern also helps maintain the molar ratio of ions (Cu^{2+}:TMA^-) in the system. It is also found that with the addition of nH_2O (water) and nEtOH (ethanol), the magnitude of single molecule adsorption energy is lower than that of Cu^{2+} cation, TMA, and TMA^- anion, which indicates that water and EtOH molecules do not compete strongly with other ligands to coordinate with Cu cations and have no major influence on the growth of MoS_2/HKUST-1 composite.

Based on the pristine HKUST-1 formation mechanism, it is speculated that the (MoS_2)-Cu site adsorbs another TMA^- anion after the adsorption of the first TMA^- anion, and then the MoS_2+Cu+2TMA^- site accepts another Cu^{2+} cation to finish the growth of a complete HKUST-1 unit. In addition, compared with the growth of HKUST-1 alone, the existence of MoS_2 quantum dots enhances the formation of HKUST-1 and leads to a more stabilized structure, for example, the adsorption energy of the (MoS_2+Cu)-TMA (-1.50 eV) is three times greater than that of the (Cu)-TMA (-0.51 eV). Therefore, the use of an appropriate amount of MoS_2 nanosheets is crucial for the enhanced HKUST-1 formation and the preparation of MOF single crystal.

Table 5-2 Bond length of TMA OH group before and after adsorption on MoS_2 quantum dots

	Site	$d_{O\text{-}H}$^{1} /Å	Δ%$_{O\text{-}H}$^{2}	$d_{H\text{-}NA\ Cu}$^{3} /Å
TMA		0.980	0	
(Cu)-TMA		1.005	2.55	2.290
(Cu_2)-TMA		1.014	3.47	2.123
(MoS_2)-TMA	centers cross	0.981	0.10	
(MoS_2+Cu)-TMA	0°	0.982	0.20	2.874
(MoS_2+Cu_2)-TMA	0°	1.022	4.29	2.202

Notes: 1, $d_{O\text{-}H}$ is the bond distance of the hydroxyl (-OH group) from the -COOH group closest to Cu^{2+} cation ($d_{O\text{-}H}$). 2, Δ%O-H is the change of bond distance before and after TMA adsorption on MoS_2. 3, $d_{H\text{-}NA\ Cu}$ is the distance between H molecule from the -COOH group closest to Cu^{2+} and NA (nearest adjacent) Cu^{2+}.

The effect of MoS_2 quantum dots on particle size of the composite is attributed to the negative charge S-top layer providing stable reaction sites for Cu^{2+} (increase nucleation rate) and further stabilize the structure of HKUST-1. This dual function of MoS_2 is important to the synthesis of MoS_2/HKUST-1 composite.

The geometric properties of a single TMA molecule being adsorbed on the individual MoS_2 quantum dots and Cu^{2+} cations or MoS_2+Cu unit, have also been studied for this research. The bond length of -OH and the distance of H towards its nearest adjacent Cu atoms are listed in Table 5-2. For comparison purpose, the bond length of an optimized TMA molecule is calculated using the same approach to illustrate whether MoS_2 quantum is a strong competitor against the bond of TMA hydroxyl breaking and can displace H atom with adsorbed metal site (Cu^{2+} cation) on MoS_2. In Table 5-2, compared with (Cu)-TMA system, (2Cu)-TMA system could have a little higher adsorption for TMA (-0.91 eV in Table 5-1), and own a stronger deprotonation ability given by longer bond length of -OH (1.014 Å), that is, the increasing number of Cu^{2+} cation improves the deprotonation of TMA. With the addition of MoS_2, (MoS_2)-TMA and (MoS_2+Cu)-TMA showed the relative low deprotonation ability for TMA. However, the introduction of one more Cu, (MoS_2+2Cu)-TMA system performs the best deprotonation ability, the longest bond length of OH (1.022 Å). Also, (MoS_2+2Cu)-TMA system shows the strongest H affinity (the shortest $d_{H\text{-}NA\ Cu}$, 2.202 Å). Thus, during the deprotonation process of TMA molecules, Cu^{2+} cation plays an essential role in this reaction, and MoS_2 does not prevent the continuous reaction under a low number of Cu^{2+} cation. Moreover, more Cu^{2+} cations on MoS_2 nanosheets can facilitate the deprotonation of TMA molecules available for the coordination with Cu ions, and result in increasingly accelerated nucleation rates and meanwhile reduce crystal size as confirmed by the particle size distribution.

5.2.3 Crystallinity analyses

The XRD patterns for a series of HKUST-1 and MoS_2/HKUST-1 samples are presented in Figure 5-4. It is evident that the diffraction peak positions of the original/modified HKSUT-1 are consistent with what is reported for the simulated HKUST-1 [273], which means that the structure of the HKUST-1 in the composite is not affected by the coexistence of MoS_2. There were no obvious diffraction peaks of Cu_2O (36.7°, PDF #04-003-6433) in the XRD patterns in each sample. No extra orientation was detected in the XRD pattern, manifesting the polycrystalline attribute of the parent HKUST-1. It is noted that the XRD peak of MoS_2 (002) face at 15° was not discernible, which is attributed to the small amount of MoS_2 quantum dots used in the synthesis of MoS_2/ HKUST-1 and also to the quantum level of MoS_2. Hence, the peak of MoS_2 (002) can be easily overlapped by the peaks of HKUST-1 (331). However, with the increase in the content of MoS_2, the HKUST-1 diffraction peaks of (311) are strengthened except for MH-2, as illustrated in Table 5-3, which suggests that MoS_2 and HKUST-1 might have formed composites. Besides, the intercalation of MoS_2 was found to increase the crystallinity of HKUST-1 at the MoS_2 content of MH-X (X=1-3), which elucidates that MoS_2 plays an important role in the synthesis of HKUST-1. Therefore, it can be concluded that the introduction of MoS_2 quantum dots has no negative effects on the growth of HKUST-1 but facilitates the formation of HKUST-1 of high crystallinity, and the N_2 isotherm in Appendix (Chapter 9) was also discussed about the issue of improved crystallinity by MoS_2 quantum dots added.

Table 5-3 XRD patterns of relative peak intensity based on the peak intensity of HKUST-1 (222)

ID	I(331) /%	Crystallinity[1] /%
MH-0	10.90	94.10%
MH-1	12.80	94.97%
MH-2	10.90	95.74%
MH-3	11.00	95.71%

Notes: 1, Crystallinity% = (total area of crystalline peaks) × 100/(total area of all peaks), where the broad peaks were considered from amorphous phase, sharp peaks were from crystal phase.

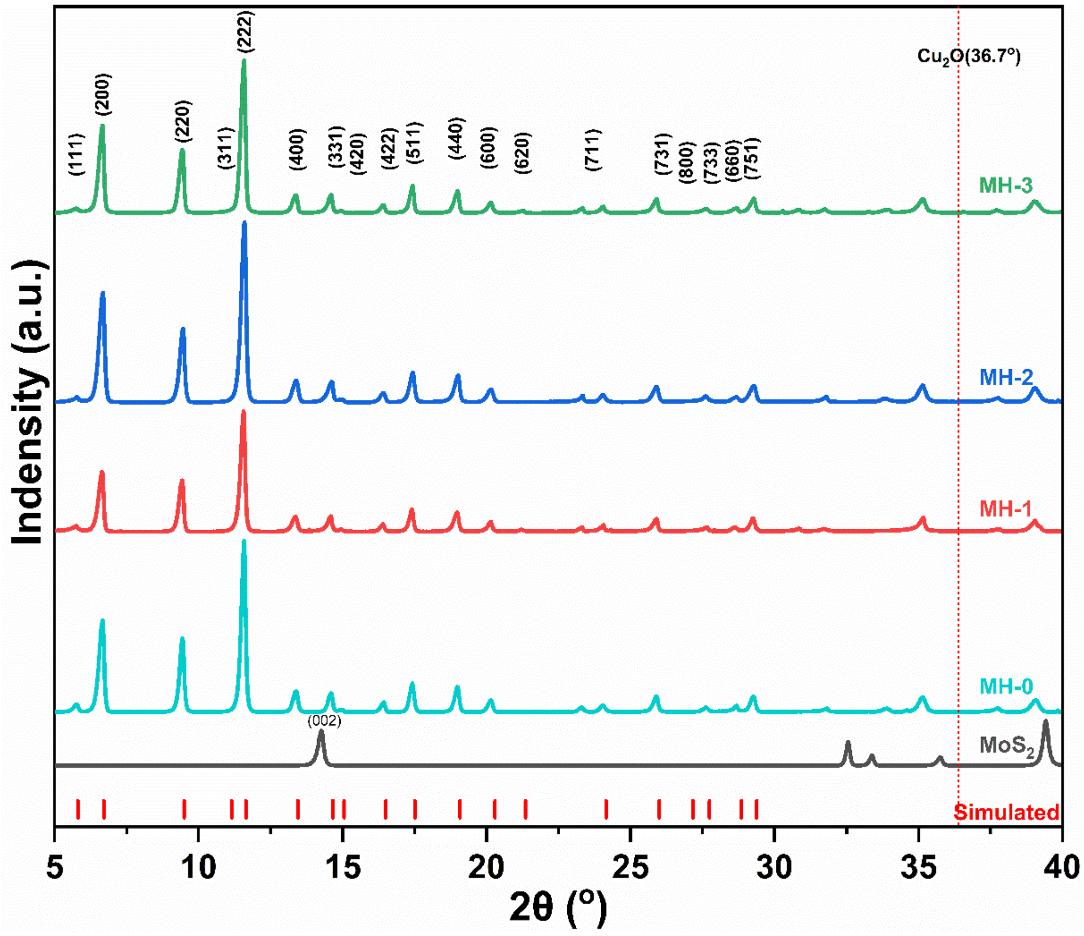

Figure 5-4 XRD patterns of pristine HKUST-1 & MoS_2/HKUST-1 composite

5.2.4 Morphology and microscopic structure

Figure 5-5 shows the TEM images of MoS_2/HKUST-1 composite. The elemental mappings of Mo, S, Cu, O and C atoms (Figure 5-5(a)) further confirmed the core and shell hierarchical structure of the MoS_2/HKUST-1 composite prepared in this study. It is also evident that the average size of dark particle (MoS_2) was around 3 nm and can be considered as quantum dot [274]. This size level is in good agreement with the characterization results reported by other researchers [275]. HRTEM images of the MoS_2/HKUS-1 composite (Figure 5-5(b)) indicate that the open space between neighbouring MoS_2 quantum is relatively large. All the MoS_2 quantum in the composites are with $d_{(100)}$ of 0.27 nm, which is in good agreement with the distance of Mo-Mo in the (001) plane of MoS_2. Thus, the MoS_2 quantum dots do not agglomerate after the formation of HKUST-1. In Figure 5-5(c), it is clearly revealed that the MoS_2 quantum dots are uniformly distributed and HKUST-1 assembled on these MoS_2 quantum dots to form core and shell structure composite.

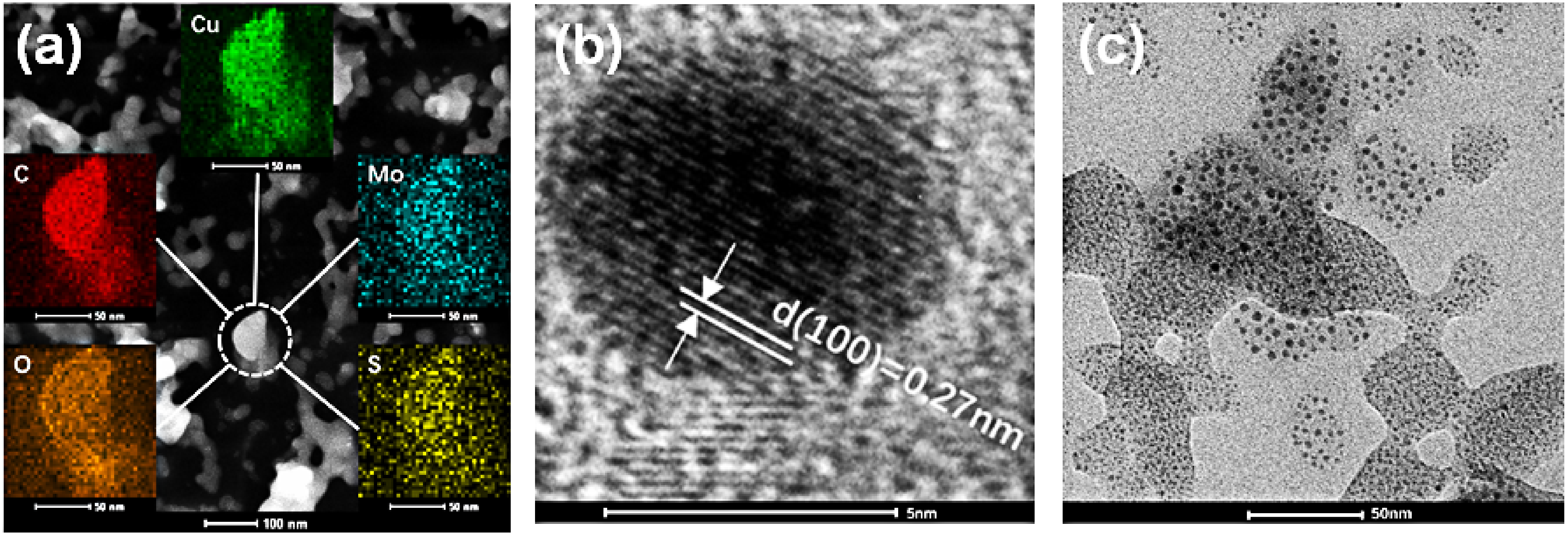

Figure 5-5 HRTEM and elemental mapping of MoS_2/HKUST-1 composite (sample MH-3). (a) elemental mapping image of MoS_2 / HKUST-1; (b) and (c) TEM image of MoS_2 / HKUST-1

5.2.5 Functional group identity

The FTIR spectra of pristine HKUST-1 and MoS_2/HKUST-1 composite is diagrammed in Figure 5-6. The IR spectrum of MH-0 show bands at 1700,1645, 1570, 1553, 1449 and 1373 cm^{-1} are consistent with the presence of the COO- moiety and such frequencies are characteristic of this bidentate coordination mode. The peaks at 1449 and 1373 cm^{-1} indicate the presence of the iso- and aniso- bidentate dicopper(II) carboxylate, a type of monomeric clusters in the $[Cu_3(BTC)_2]$ frame [276]. In the FTIR spectrum of the MoS_2/HKUST-1 composite, the weak absorption peaks at 480, 610 and 1060 cm^{-1} are tentatively assigned to γ_{as}(Mo-S) vibration [277], Cu-S stretching modes [278] and asymmetric valence S=O vibration [279]. The FTIR results proved the existence of MoS_2 within HKUST-1 and the existence of Cu-S bond, which suggest that the Cu cations are boned to MoS_2 prior to the formation of HKUST-1. This is consistent with the steps reveal by DFT calculation. Therefore, it can be concluded that HKUST-1 is formed on the Cu^{2+} cation that is initially adsorbed on MoS_2 quantum dots, based on which a composite of core and shell structure is formed.

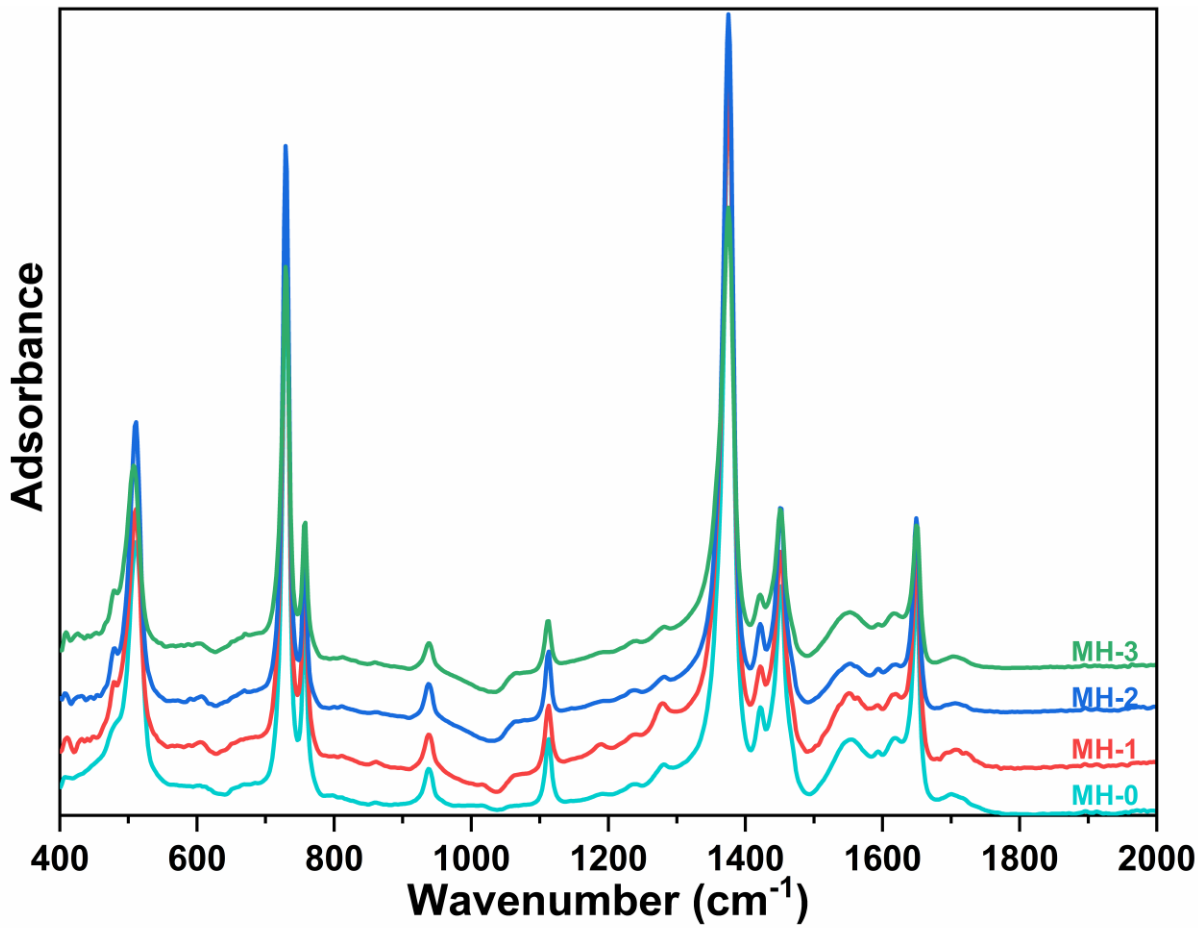

Figure 5-6 The FTIR spectra of HKUST-1 and MoS_2/HKUST-1 composite

5.2.6 Surface property

With the increase in MoS_2 content (MH-X, X=2, 3), surface area of the samples became greater than the surface area of the original HKUST-1 (MH-0,1272.48 m^2/g), as illustrated in Table 5-4, so does the total pore volume. However, for MH-1, surface area of the sample was lower than that of the original HKUST-1 (MH-0) but the total pore volume was higher. The order of micropore volume was similar. These tendencies of textural properties implied that the intercalation of MoS_2 might alter pore structure of the samples, and thus have significant influence on surface area. According to the DFT calculation, when Cu^{2+} ion content is small, Cu^{2+} ion is likely to form on MoS_2 as a monolayer. However, when Cu ion concentration is high, copper ions might combine with each other and form large metal clusters or irregular multilayers on the surface of MoS_2. Therefore, when a large amount of MoS_2 is added (MH-X, X=2, 3), the Cu concentration becomes relatively low, wherein, a regular Cu ion layer tends to form on MoS_2 quantum dots, which provides easily accessible sites for TMA ions and facilities the formation of HKUST-1. This subsequently enables the growth of HKUST-1 of high crystallinity. By contrast, a small amount of MoS_2 (MH-1) leads to a relatively high concentration of copper ions, which favours the formation of large metal clusters or irregular multilayers on the surface of MoS_2. Such irregular arrangement of Cu clusters results in the formation of HKUST-1 of lower crystallinity, therefore, a lower surface area and porosity as shown in Table 5-4.

Table 5-4 Surface properties of sample

ID	S_{BET} (m^2/g)	$S_{Langmuir}$ (m^2/g)	V_{TP} (cm^3/g)	Porosity (%)	D_p (Å)	pH	Yield (%)	A_{HL}	crystallite size (nm)
MH-0	1272.5	1478.7	0.68	0.74	5.56	1.70	90.3	8.8	51.84
MH-1	1207.7	1425.8	0.79	0.59	6.53	2.39	93.3	7.4	49.63
MH-2	1638.9	1811.2	0.84	0.72	6.99	1.12	91.2	2.3	43.37
MH-3	1521.2	1754.7	0.82	0.72	6.50	1.37	91.4	1.1	50.14

Notes: S_{BET}, specific surface area of BET. $S_{Langmuir}$, specific surface area of Langmuir. V_{TP}, the volume of total pore. Porosity, the ratio of micropore volume and total pore volume. D_p, the average diameter of pore. A_{HL} (area of hysteresis loop) is the difference of N_2 desorption curve area and N_2 adsorption curve. Crystallite size was based on the FWHM value according to XRD pattern.

5.2.7 CO_2 adsorption

5.2.7.1 CO_2 isotherm tests

For static adsorption analysis, the CO_2 uptake of the HKUST-1 and MoS_2/HKUST-1 were measured at 1 atm and 25 °C as shown in Figure 5-7, following the procedure described elsewhere [280, 281]. The uptake of MoS_2/HKUST-1 composites is higher than that of the original HKUST-1, except for MH-1. The actual uptake values of MH-X (X=1-3) are 16.3 wt.% (3.70 mmol/g), 20.4 wt.% (4.64 mmol/g), 19.3 wt.% (4.38 mmol/g) compared to 18.1 wt.% (4.12 mmol/g) of MH-0. The variation in CO_2 uptake is attributed to the additive effect of HKUST-1 and excessive MoS_2, which results in the blockage of the pores as well as reduced pore size. Generally, higher concentration of MoS_2 would provide more adsorption sites, firstly, for Cu ion, which prevents the formation of a large layer of Cu ion on MoS_2 and the growth of the individual metal cluster on MoS_2 monolayer, thus more sites for TMA. This promotes the formation of pores in MoS_2/HKUST-1 composites. In addition, the CO_2 uptake on other different MOFs was listed in Table 5-5. The CO_2 uptakes of HKUST-1 and MoS_2/HKUST-1 composites in this work are higher than almost HKUST-1 composite MOFs or other MOFs. Besides, the highest CO_2 uptake of sample (MH-2) was higher than similar core-shell composites (HKUST-1/GO, 3.37 mmol/g) [282]. Therefore, such synthesized HKUST-1 and MoS_2/HKUST-1 composite could become a promising candidate for CO_2 capture. The thermal stability and CO_2 regenerability were also discussed in Appendix, and sample (MH-2) the adsorption capacity remains almost unchanged after ten adsorption-desorption cycles, which revealed the potential of MoS_2/HKUST-1 composite as CO_2 adsorbents.

Table 5-5 CO_2 uptake on other different MOFs

Adsorbent	CO_2 uptake mmol/g	Temperature °C	Pressure bar
HKUST-1 [283]	4.18	25	1
MH-0*	4.12	25	1
MH-1*	3.70	25	1
MH-2*	4.64	25	1
MH-3*	4.38	25	1
HKUST-1/GO [282]	3.37	25	1
HKUST-1/HCM [284]	2.75	25	1
mil-101/mc [285]	2.67	25	1
UIO-66/GO [286]	3.37	25	1

*The samples prepared in this paper

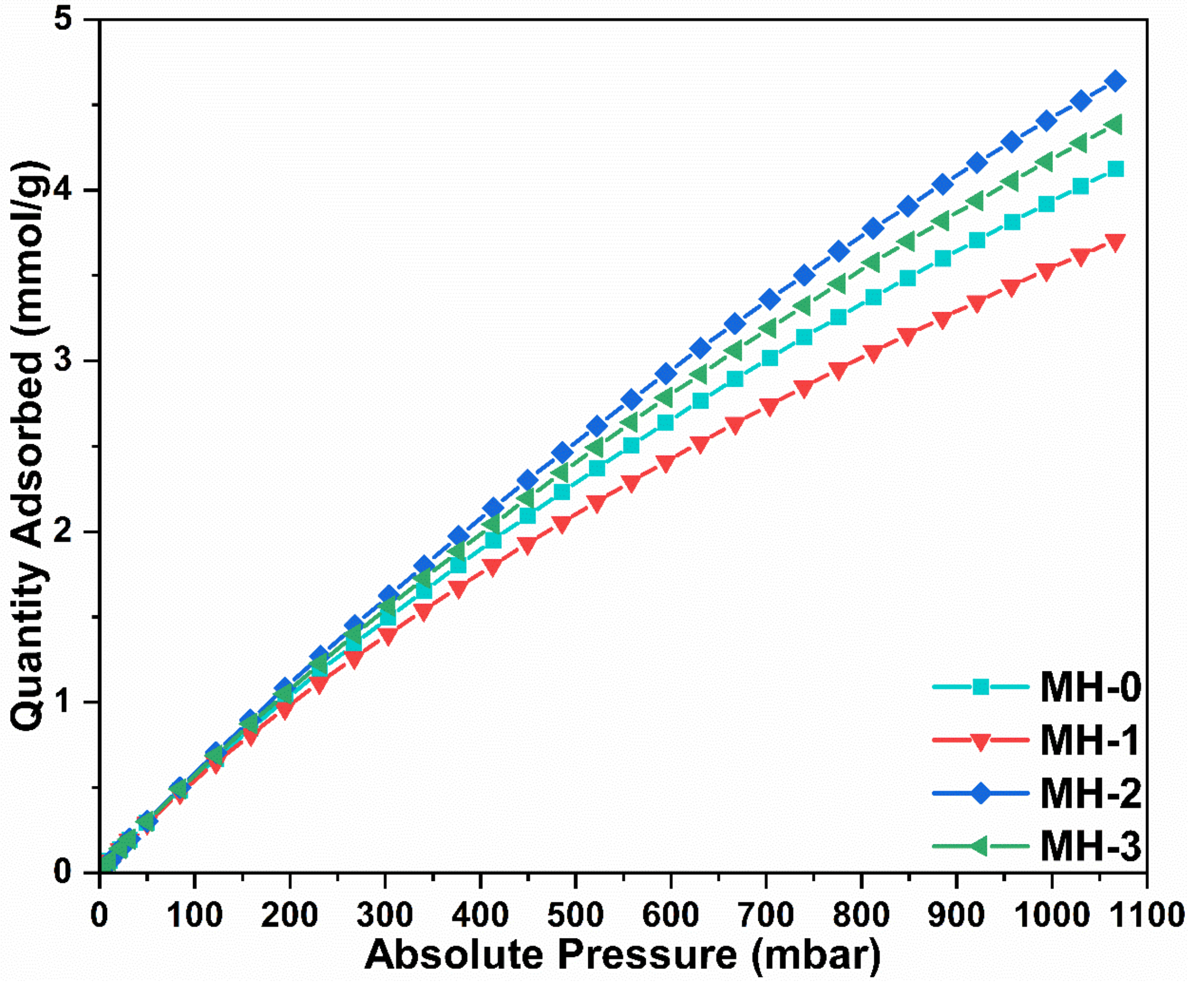

Figure 5-7 CO_2 adsorption isotherm of HKUST-1 and MoS_2/HKUST-1 (25 °C , 1 bar)

5.2.7.2 Mechanism of CO_2 adsorption on the MoS_2/HKUST-1 composite

Before searching the stable structure of CO_2 adsorption, the favourable adsorption configuration of SBU cluster should be verified., three adsorption sites are considered, namely, Cu-Cu bond (perpendicular to the MoS_2 monolayer) on top of a hexagon (H), on top of a Mo atom (T_{Mo}), on top but followed by an SBU rotation along Cu-Cu bond by 15° (cross). According to Table 5-6, the H site of (MoS_2)-SBU (0.77 eV, approximate chemical adsorption) is a favourable configuration compared with other two possible configurations and there is no obvious distortion in the structure of SBU. Combined with CO_2-TPD results, one CO_2 adsorption site on individual SBU and MoS_2+SBU has been identified as shown in Figure 5-8 (a) and (b), which is the site in the close vicinity of the coordinatively unsaturated metal site, termed as the coordinatively unsaturated site (CUS sites). Although the CO_2 molecule is of linear molecular structure, it is strongly tilted away from the Cu-Cu axis of the paddlewheel towards the Cu^{2+} ion (lying on the edge of the triangular shaped open, $\angle$ Cu-O-$C_{(SBU)}$=124.8°/ $\angle$ Cu-O-$C_{(MoS2+SBU)}$=136.6°)

Table 5-6 Optimized SBU on MoS_2 and most stable CO_2 adsorption configuration

Adsorption system	Site	E_{ads} eV	∠Cu1-O9-C5[1]	ΔQ_1[2] e	ΔQ_2[3] e
(MoS_2)-SBU	T_{Mo} cross	-0.73			
	T_{Mo}	-0.74			
	H	-0.77			
(SBU)-CO_2		-0.17	124.8°	-5.30E-05	
$(MoS_2$+SBU)-CO_2		-0.19	136.6°	-1.34E-03	-5.10E-03

Notes: 1, ∠Cu1-O9-C5 was the angle between Cu1-O9 and O9-C5; 2, (ΔQ_1) was charge transfer based on the Bader charge analysis, where the negative ΔQ_1 means charge transfer from the CO_2 molecule to adsorbent; 3, (ΔQ_2) was charge transfer based on the Bader charge analysis, where the negative ΔQ_2 means charge transfer from the CO_2 and SBU to adsorbent.

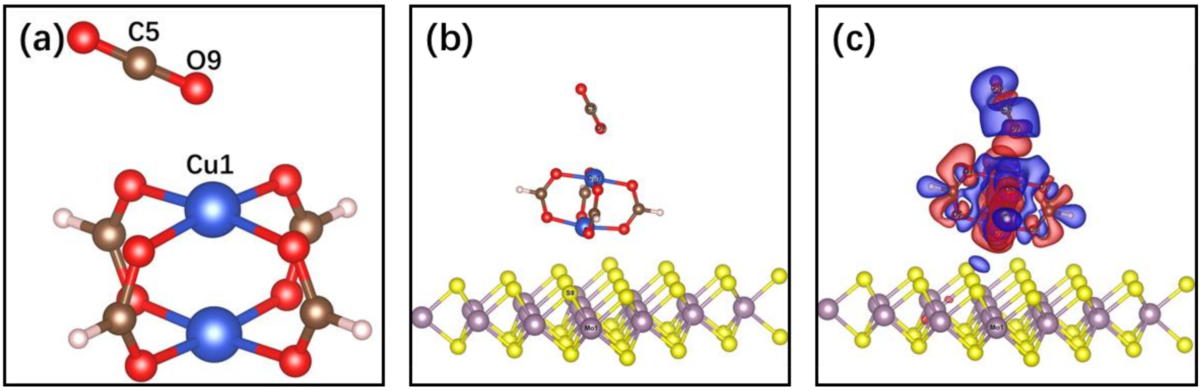

Figure 5-8 CO_2 adsorption configuration with SBU and MoS_2+SBU and plots of its charge density difference. (a) (SBU)-CO_2 adsorption configuration, (b) $(MoS_2$+SBU)-CO_2 adsorption configuration, and, (c) Charge density difference plots for $(MoS_2$+SBU)-CO_2. The red (blue) distribution corresponds to charge accumulation (depletion). The iso-surface is taken as 5.0E-03e/Å^3. The direction and value of charge transfer are also denoted. Charge density difference images calculated by the formula $\Delta\rho = \rho_{adsorption\ system} - (\rho_{adsorbent} - \rho_{CO2})$.

Moreover, the charge transfer between adsorbent and adsorbate was evaluated by Bader charge analysis. It was found that charge transfer of (MoS_2+SBU)-CO_2 was two orders of magnitude higher than that of (SBU)-CO_2, meanwhile, SBU and CO_2 molecule donate -5.10E-03 e to the surface of MoS_2 monolayer. This means that the individual SBU or original HKUST-1 can only provide weak van der Waals forces to adsorb CO_2 molecules. However, for the adsorption of CO_2 on the MoS_2/HKUST-1 core-shell composite, CO_2 acts as a charge donor in (MoS_2+SBU)-CO_2, providing -1.34E-03 e to the adsorbent, as shown in Figure 5-8(c), which is controlled by the electrostatic interaction with the top Sulphur layer of the MoS_2 monolayer and Cu^{2+} cation of the secondary paddlewheel.

Accordingly, it is hypothesized that the improved interaction is mainly from MoS_2 quantum dots due to its exposed edge sites and from the increased crystal space of HKUST-1 caused by the intercalation of MoS_2 [287]. As shown in Figure 5-7, the CO_2 uptake of the HKUST-1 is 4.12 mmol/g, which is attributed to the open Cu sites capturing CO_2 molecules via weak van der Waals forces. Based on the CO_2 uptake of MH-0, the molar ratio of CO_2 per Cu^{2+} was 0.83:1, which was almost the occupation of the CUS sites. That is, only one CO_2 molecule can interact with one CUS site, where the CO_2 molecule is tilted towards the CUS site [288]. For MH-2, the molar ratio of CO_2 per Cu^{2+} was 0.94:1. The addition of MoS_2 consequently increased the binding capacity of HKUST-1 in CO_2 adsorption, which is attributed to one Cu^{2+} bonding to one CO_2 molecule. Stronger electrostatic force induced by MoS_2 quantum dots can result in enhanced adsorption of CO_2 on HKUST-1.

5.3 Summary

a) Theoretically, it is found that the growth of the MoS_2/HKUST-1 composites of core-shell structure consists of six steps. It not only provides the possibility for MoS_2/HKUST-1 composites as the formation of core-shell structure, but also indicates that MoS_2 is an integral part of the composites and plays an important role in controlling the size and crystallinity of the MOF crystals, which is dominated by the interactions between surface Sulphur atoms and metal centres.

b) Due to the deprotonation, the growth of HKUST-1 on the MoS_2 quantum dots initiated the construction of core-shell structure, and the TMA molecule was bonded to Cu(II) ions, which was firstly adsorbed on MoS_2(001) quantum dots rather than Cu(II) cations in the solution.

c) The MoS_2/HKUST-1 composites exhibit a high efficiency for CO_2 capture and optimal composite improved adsorption efficiency by 13% compared with HKUST-1. The enhanced CO_2 adsorption is attributed to the presence of a high specific surface area together with the strong electrostatic force induced by MoS_2 quantum dots.

Chapter 6 Thermal behaviour of HKUST-1 structure in different temperatures

6.1 Introduction

Metal-organic frameworks (MOFs) [289, 290] have caught a noteworthy attention in many fields, including gas storage [291] and separation [292], catalysis [293], and sensor [294], since they own high specific surface area (SSA) and micro-porosity. The porous hybrid frameworks composed of metal-carboxylate coordination moieties and tunable organic linkers form crystalline networks, which effectively allow small gas molecule diffusing into its interior pore. Driven by the enormous requirements of its application, MOFs should be featured with the practical structural stability to avoid unnecessary structural distortion [295], framework disruption [296] and temperature/pressure-induced phase transitions [297].

One of the promising Cu based MOFs, HKUST-1, was earliest synthesized in 1999[42]. With the presence of Cu active site, it has been developed into toxic gas removal agent [298, 299], energy storage medium [300] and even catalyst component or catalyst supporter [301, 302]. However, lots of research has referred the breathing effect [303], the distortion and decomposition of HKUST-1 in many applications [304, 305]. This phenomenon “breathing” is mainly due to a reversible structural transition of MOFs driven by the external stimuli. Some research found the structure of HKUST-1 was changed or even collapsed after adsorbing water through the observation of ^{1}H and

^{13}C MAS NMR spectroscopy [306]. Then, it was reported that the presence of some polar small molecule (H_2O, EtOH, MeOH) could induce the distortion of HKUST-1 structure [307]. Furthermore, the adsorption of H_2S in HKUST-1 led to the collapse of the MOF structure [308]. Those results all imply that the inherent synthetic HKUST-1 structure is not a proper choice when the breathing effect is crucial. Talking of adsorption and desorption cycles, it would be seriously influenced from the breathing effect on cost-effective capacity in HKUST-1 for target gases under favourable conditions (temperature or pressure) [309]. To control and retain surface functionality and metal centres in MOFs, significant efforts have been committed to post-synthesis pore engineering and surface modifications, such as metal and ligand exchange [310], doping [311] and functionalization [312], and additional functional framework or polymer grafting of MOF structures [313]. Even so, there is still a necessity for a facile and highly practical approach for industrialized process without dependence of extensive chemical modifications.

The thermal annealing is an effective approach of modifying structures [314] and enhancing properties of metals [315], ceramics [316], and polymers [317]. According to the effect of temperature on the HKUST-1 framework under an inert condition, it will implement structural changes and unstable structural optimization. However, there were no elaborate designs of MOF annealing modification, especially in investigation on the mechanism of the entire HKUST-1 annealing process and the properties of the re-created structure, where re-created adsorption feature or catalytic performance could be overlooked easily.

As known, reliable thermal stability of HKUST-1 can reach 280 °C under an inert atmosphere but decomposes at higher temperatures [305]. In this work, HKUST-1 followed as the previous synthesis method [318, 319], possesses three distinct internal pores and high BET SSA value of ~1500 m^2/g. The change of surface structure following the releasing of pyrolysis product would be observed until the framework complete decomposition the phase composition. Morphology and thermal stability of these samples were examined through indispensable characterization. The key issue is the growth of Cu nanoparticles embedded on graphene oxide, which also reveals the mechanism about whole annealing process of HKUST-1. The In-situ technology, DRIFT, revealed the formation of formate intermediates after 350 °C, followed by CO_2 and CO released. Such process implied the presence of a defective structure in HKUST-1 and decomposition of bridging carboxylic linker directly causing the graphitization of HKUST-1 framework.

6.2 Results and Discussion

6.2.1 Thermal gravity analyses

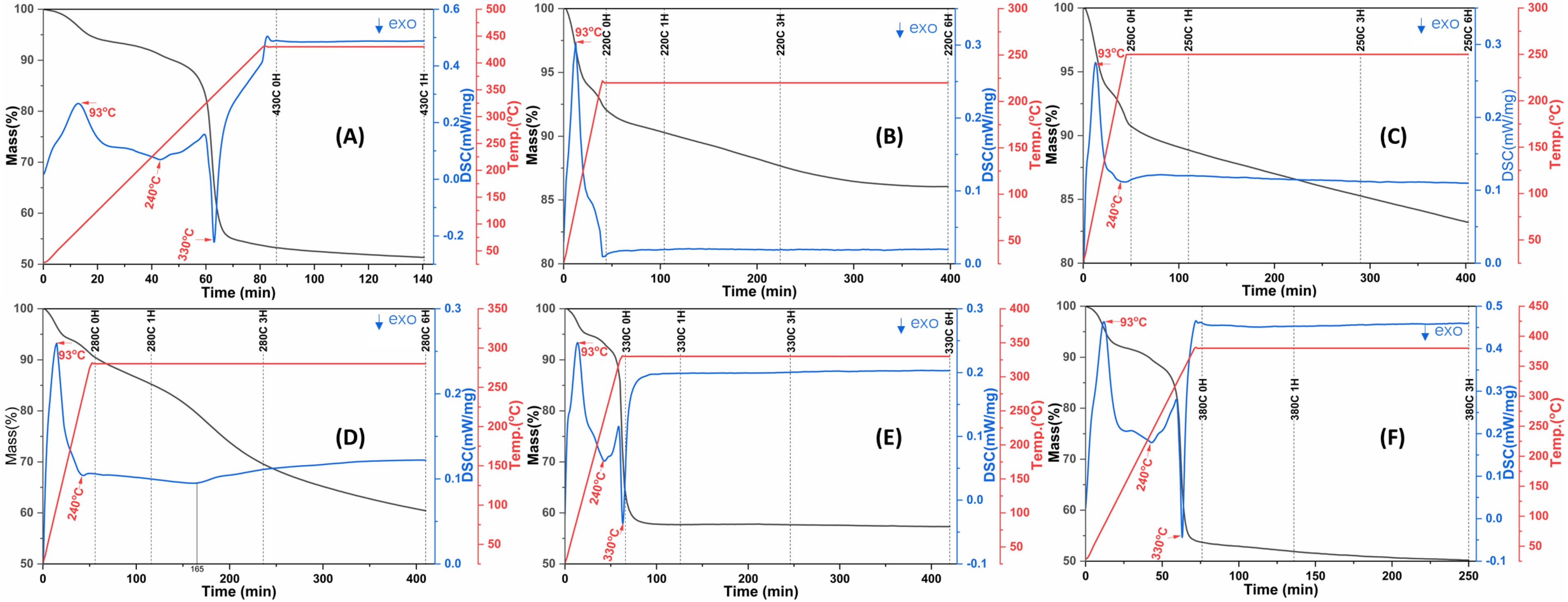

Figure 6-1 TGA plots of dry HKUST-1 with a heating rate of 5 °C/min, decomposition temperature of (A) 430 °C maintaining for 1 h; (B) 220 °C maintaining for 6 h; (C) 250 °C maintaining for 6 h; (D) 280 °C maintaining for 6 h; (E) 330 °C maintaining for 6 h; (F) 380 °C maintaining for 3 h. Red line is the temperature as function of time. Blue line is the DSC as function of time. Dark line is the mass as function of time.

In this study, the nano-scale HKUST-1 were prepared in our previous research, and the dry HKUST-1 was collected with solvent exchange followed by drying at 120 °C overnight. As shown in Figure 6-1(A), mass loss of HKUS-1 from 25 °C to 430 °C confirmed the framework decomposition started around 330 °C and complete decomposition ended before 430 °C. There was no obvious mass loss between 120 and 280 °C, also referred in other work [318, 319]. Therefore, three annealing temperatures were chosen from the temperature range of remained structure and structure decomposition, respectively. That is, 220, 250, 280 ^{o}C were chosen from stable-structure temperature range and 330, 380, 430 ^{o}C were chosen from decomposed-structure temperature range. Meanwhile, the isothermal step was extended from 0 h to 6 h after the heating temperature reached up to target temperature. As shown in Figure 1-6(B) and 1-6(C), the sample was maintained under 220 ^{o}C and 250 ^{o}C, respectively, lasting for 6 h. At these two temperatures, it was near to saturation for 220C 6H sample, but there was no sign of saturation with a constant mass loss at rates of 0.02 wt.%/min, since the mass loss part of HKUST-1 was contributed to the impurities of HKUST-1 diffused out as the vapour formation under this temperature. However, in Figure 6-1(D), the sample at 280 °C kept losing mass when isothermally continued up to 6 h and the mass loss reached 30%. When the sample temperature rose to 330 °C and 380 °C for a while, respectively, the mass-loss process ended without a long time, and there was no mass loss in the isothermal step.

6.2.2 On-line mass spectra analyses

Firstly, the possible gas emission was detected through the TPD of heating HKUST-1 combined with mass-spectroscopy (MS) analysis under the flow of Ar in Figure 6-2(A). The result revealed that CO_2, CO, CH_4 and H_2 would start to be released at around 280 ^oC and then the emission would reach the peak at around 330 ^oC in the annealing temperature range between 50 and 600^oC. The order of the potential gas release amount is CO_2>CO>CH_4>H_2 before 400 ^oC. However, CO and H_2 would be released again after 400 ^oC, that meant high-temperature inert environment promoted further cleavage of the bond in left hydrocarbon containing oxygen groups. Notably, the MS signals visibly exhibit that the mass-loss is mainly attributed to the release of these pyrolysis gases. Motivated by this observation, further isothermal step of TPD for annealing HKUST-1 solely focused on the release of CO attributed to the TGA mass-loss in Figure 2-6(B). The HKUST-1, annealed under 330 ^oC for 6H, 380 ^oC for 3H and 480 ^oC for 1H, all exhibited the CO releasing was initiated at around 280 ^oC and reached the peak at around 330 ^oC before heating up to the target temperature. When the temperature program entered the isothermal step, there was no CO releasing corresponding to smooth mass-loss curve in Figure 6-1(A), (E) and (F). Except for HKUST-1 maintained under 280 ^oC for 6 h, the CO was released after the isothermal step was remained around 5 h, which was attributed to the mass loss of around 2.3 wt.% (350 min to 410 min) in Figure 1-6(D).

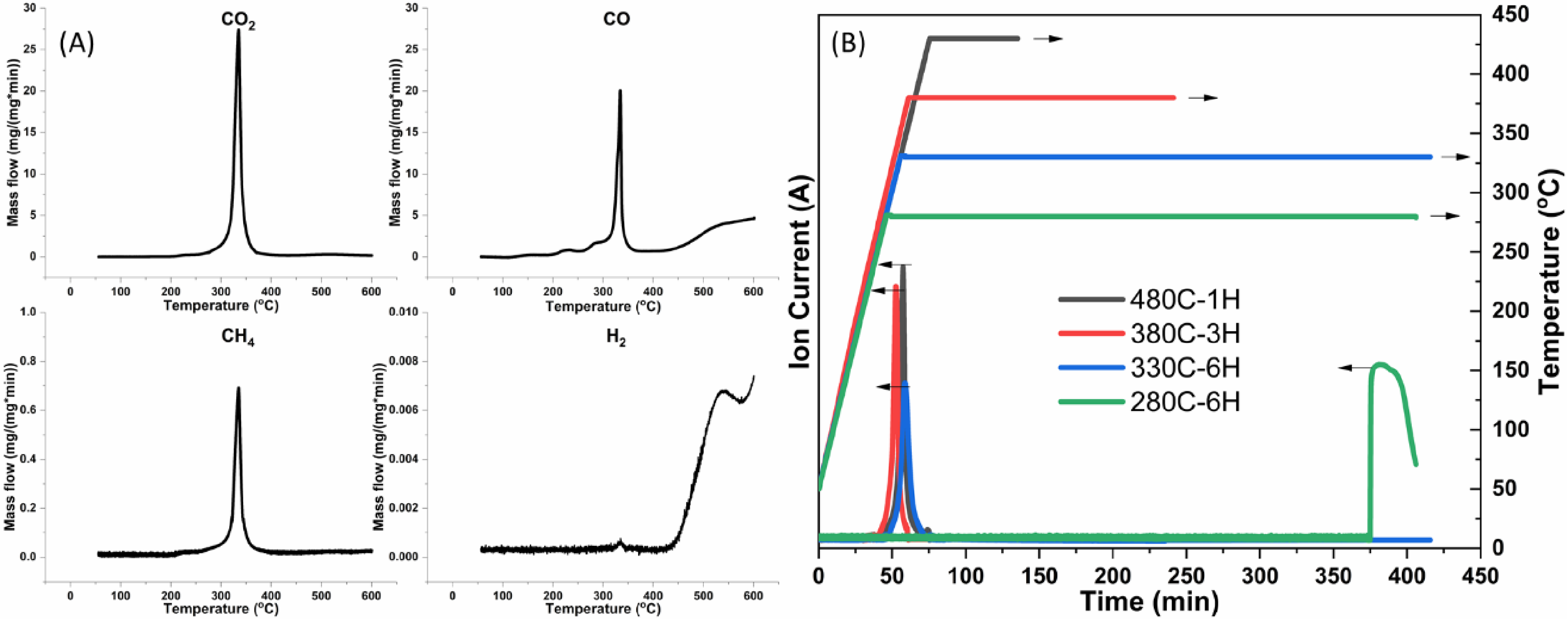

Figure 6-2 The temperature-programmed desorption (TPD) curves of pyrolysis gas released from HKUST-1 in the Ar environment under the (A) temperature range between 50-600 °C and (B) the target temperature (280 °C for 6 h, 330 °C for 6 h, 380 °C for 3 h and 480°C for 1 h). all heating process were programmed with 5 °C/min. Ion Current of CO was calibrated by the standard mixed gas of CO 1%/ Ar balanced in Figure 6-2(B).

6.2.3 Crystallinity analyses

Next, a set of annealed batch samples were prepared at predetermined temperatures (220-430 °C) with various prolonged isothermal steps. The structures of annealed samples were initially confirmed with XRD patterns in Figure 6-3. It is worth mentioned, almost of samples annealed under mild condition presented high crystallinity as evidenced by the sharp and one-to-one correspondent reflections with the simulated HKUST-1. Further, the sample annealed under the harsh condition also displayed sharp and correspondent diffraction with the reference of graphene oxide(GO) [320] and metallic Cu. The sharp XRD peaks at the whole range of angles meant that the crystals were highly ordered in the long-range without much local short-range disorder. Along the ordinate of temperature, the local short-range change starts at 380 ^{o}C. That indicated the structure of HKUST-1 maintained stable before 330 ^{o}C and benzene ring and Cu(I) in HKUST-1 started to be carbonized into layered structure graphene oxide and metallic Cu reduced by C atoms under high temperature after 380 ^{o}C, also this kind of Cu/GO structure can be kept at 430 ^{o}C without any change. Along the abscissa, the XRD patterns of annealed HKUST-1, at temperature of 220 and 250 ^{o}C for a prolonged period of 6 h, remained a long-range order of the HKUST-1 crystalline structure, which is corresponding to the low mass-loss of TGA at 220 and 250 ^{o}C. However, the local short-range disorder started to appear when the samples are annealed for the prolonged period of time (e.g., 280 ^{o}C for 3 h,) or at a relatively harsh condition (330 ^{o}C for 1 h) but before the framework decomposition (380 ^{o}C for 0 h).

Especially, the transition state of 220C 3H sample illustrated the intensity of (220) almost make it higher than that of (222) peak. Thus, this short-range disorder was related to the onset formation of cubic metal Cu and graphitization of the benzene ring in HKUST-1. The framework decomposition, graphitization, and Cu particles formation appeared in sequence when the samples were prepared at 430 °C. Note that cubic metallic Cu was observed with weak diffraction of Cu_2O and CuO.

The average lattice constant and crystallite size of each annealed HKUST-1 sample were summarized based on XRD patterns through JADE software in Table 6-1. With the temperature increasing (220C-430 ^{o}C, 0H), the lattice constant of each sample was decreased gradually, which was caused by the destruction of structure due to the rising temperature. However, in that temperature range, the crystallite size was increased before the structure destruction and then decreased in the higher temperature. For the reason, the increase in crystallite size was caused by the volume expansion and expansion of pyrolysis gas generated by structural decomposition of HKUST-1 before 330 ^{o}C. In addition of temperature increasing, the yield of GO was provided as dispersed substrate for the reduced copper particles, where the GO substrate can increase the dispersion of Cu particles and reduce these particle sizes. Regarding the prolonged isotherm step in the temperature of 220 and 250 ^{o}C, the behaviour of both treated sample was the same, where the lattice constant was firstly increased before 3 h followed with decreased and the crystallite size was increased in the whole period. The main factor was the evaporation of impurity gas physisorbed. Before the isotherm time of 3 h, the removed impurity gas or guest gas was diffused out from the pore of MOFs and bodied up the whole MOFs crystal size and volume. After 3 h, the impurity gas was emptied out, thus, the structure of MOFs was recovered to the original stable state in 220 and 250 ^{o}C, respectively. Despite crystallite size, the generated macropore cannot be restored and kept in the prolonged isothermal step. For the isotherm process at 250 - 330 ^{o}C, the crystal lattice and grain changes were consistent with direct heating without isothermal step. Finally, due to the formation of Cu NP embedded on GO at a high temperature (380 – 430 ^{o}C), the isotherm process would not influence the structure of long-period annealed sample.

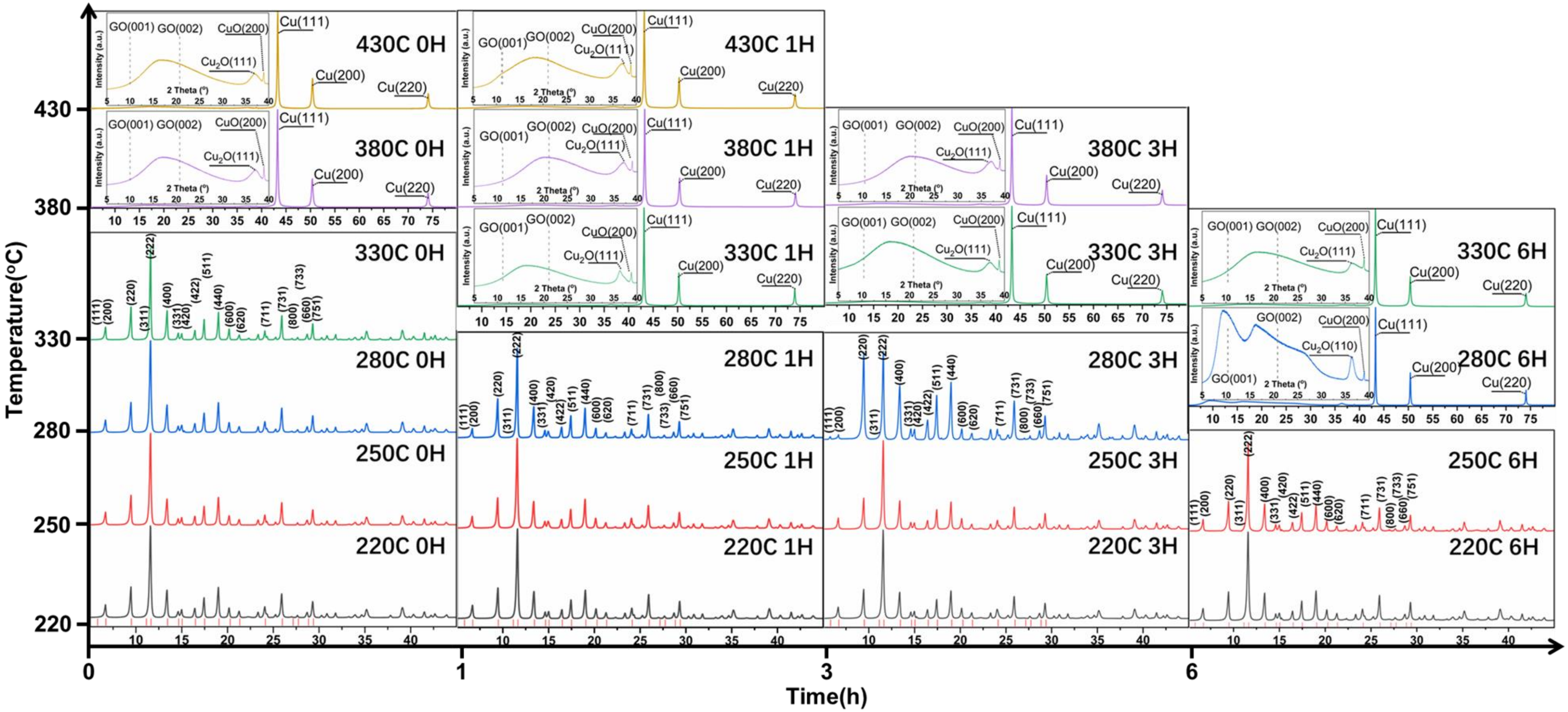

Figure 6-3 XRD patterns of thermal annealed HKUST-1 samples at the temperature range of 220-430 °C with different isotherm step maintained for 0 h, 1 h, 3 h and 6 h, respectively. the red bar is the simulated XRD patterns of HKUST-1. CuO, Cu_2O and Cu XRD pattern was matched up with PDF 80-1268, PDF 05-0667 and PDF 04-0836.

Table 6-1 The crystal parameters of different annealed HKUST-1 samples

Sample	Average Lattice Constant Å	Crystallite Size Å
220C 0H	26.42	45.100
220C 1H	26.41	46.380
220C 3H	26.46	47.600
220C 6H	26.43	48.280
250C 0H	26.42	47.410
250C 1H	26.46	47.682
250C 3H	26.45	51.070
250C 6H	26.44	54.760
280C 0H	26.41	47.518
280C 1H	26.44	55.200
280C 3H	26.44	48.240
280C 6H	3.95	52.300
330C 0H	26.39	61.790
330C 1H	3.95	37.700
330C 3H	3.93	31.500
330C 6H	3.95	33.000
380C 0H	3.93	29.770
380C 1H	3.95	29.900
380C 3H	3.94	30.233
430C 0H	3.93	29.167
430C 1H	3.95	29.300

6.2.4 Functional group identity

In agreement with the XRD data, the FTIR spectra of different HKUST-1 samples annealed by different temperature with various prolonged isothermal steps were given in Figure 6-4. In analogy with XRD pattern, the FTIR spectrum of HKUST-1 structure-like sample (220-250 °C for 0-6 h, 280 °C for 0-3 h, and 330 °C for 0 h) clearly evidenced an almost isobidentate behaviour of COO moiety since bands at 1718(vs(C=O)), 1445(vs(O-H)) and 1371(vs(O-H), 1273(vs(C-O)), 1107(vs(C-O)) cm^{-1} are characteristic of this coordination mode. The vibration range of 1500-1600 cm^{-1} and 950-1000 cm^{-1} was assigned to the C=C stretching and bending, respectively, of benzene ring that also exhibited vs(C-H) of 730-770 cm^{-1}. In addition of vs(Cu(II)-O) [321] assigned to the band of 592-430 cm^{-1}, the presence of monomeric clusters, iso- and aniso-bidentate dicopper(II) carboxylate, was the epitome of HKUST-1 [$Cu_3(BTC)_2$] frame, and revealed the parameter of temperature and isotherm step (220-250 °C for 0-6 h, 280 °C for 0-3 h, and 330 °C for 0 h) did not influence the complete structure of pristine HKUST-1. As only temperature increasing (220-430 °C for 0 h), the change of sample structure was in agreement with the suggestion of XRD patterns. From the beginning of 380 °C, two obvious bands of strong vs(C=O) and benzene derivatives were appearing at 1735 and 700 cm^{-1}, the band of vs(C=C) at 1500-1600 cm^{-1} were strengthened and vibration of O-H stretching at 1310-1440 cm^{-1} were weakened. Surprisingly, two bands of vs(C-O) at 1100-1300 cm^{-1} became stronger after a high-temperature annealing, and the carboxyl group of C-O gradually was evolved into vas(C-O-C) (strong, 1150-1085 cm^{-1}) and vs(C-O-C) (weak, 1075-100 cm^{-1}), where the spectrum corresponds to stretching vibrations of epoxide and ketonic functional groups. This change process directly referred to the formation of graphene oxide. Regarding the isotherm step, there was no spectra changes under 220-250 ^{o}C and 380-430 ^{o}C, still remaining HKUST-1 structure and CuNP/GO structure, respectively. Except for them, GO formation occurred in both samples annealed under 330 ^{o}C for 1h and 280 ^{o}C for 6 h. besides, the sample under 280 ^{o}C for 6 h was partially graphitized, evidenced by the weakened vs(C-H) at 760 cm^{-1} and little strengthened vs(C=O) at 1730 cm^{-1}, and still strong vs(O-H) at 1310-1440 cm^{-1}. Therefore, the HKUST-1 annealed under mild temperature 280 ^{o}C for a longer period can also be transformed into the complete structure of CuNP/GO. Note the broadened band of v(O-H) at 3050-3800 cm^{-1} was mainly characteristic of O-H bonds in water.

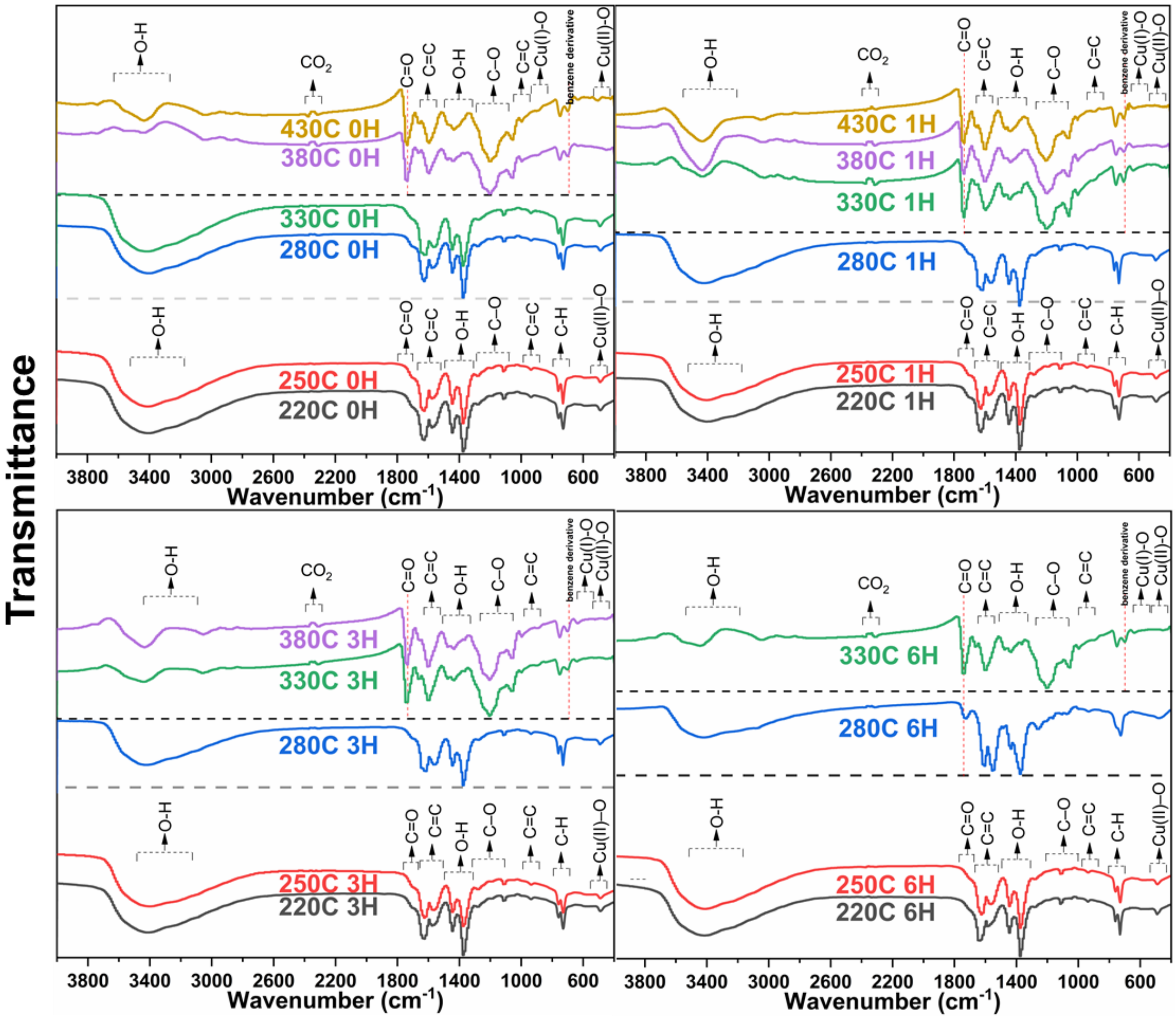

Figure 6-4 XRD patterns of thermal annealed HKUST-1 samples at the temperature range of 220-430 °C with different isotherm step maintained for 0 h, 1 h, 3 h and 6 h, respectively.

6.2.5 Chemical analyses

As shown in Figure 6-5, the XPS Cu2p, C1s and O1s level spectra of different annealed samples were resolved to analyse the surface composition. Importantly, the linker bond dissociation of Cu-O was observed by the low binding energy shifts of O1s and Cu2p peaks from remained HKUST-1 structure at a low temperature for short-range of the isotherm step. However, the increased temperature and prolonged isotherm step would induce the graphitization of the carbon-containing group in HKUST-1 and more Cu(II) ions were reduced into the state of Cu(I)/Cu(0) by C atoms. In the configuration of HKUST-1 (220-330 ^{o}C for 0 h and 220-250 ^{o}C for 3 h), a framework bridged oxygen of carboxylates showed a symmetric O1s peak resolved around 531 and 532 eV, and the Cu of monomeric clusters in HKUST-1 presented a Cu2p peak at 934.14 eV (2p3/2) and 954.27 eV (2p1/2). For the CuNP/GO structure (380-430 ^{o}C for 0h and 330-380 ^{o}C for 3h), the onset formation of Cu particle was evidenced by obvious disappearance of Cu2p satellite peaks and decreased intensity of O1s, also, the C1s compared with the assignment of HKUST-1 exhibited more graphene features corresponding to the appearance of C=C (around 285 eV). During the mild condition annealing (280 °C for 6 h), the direct indication for the dissociation of Cu-O on linker bond was observed through a shift of Cu2p binding energy with the weakened peak of Cu(II) and satellite and strengthen peak of Cu(I)/Cu(0). Further, the peaks of (C=O)-OH and C=C appeared in C1s, that indicated the structure of HKUST-1 started graphitization undergoing long-term isotherm. The O1s spectra also showed the intensity of C-O and C=O were weakened, which was corresponding to the appearance of CO, CO_2 and CH_4 in Figure 6-2.

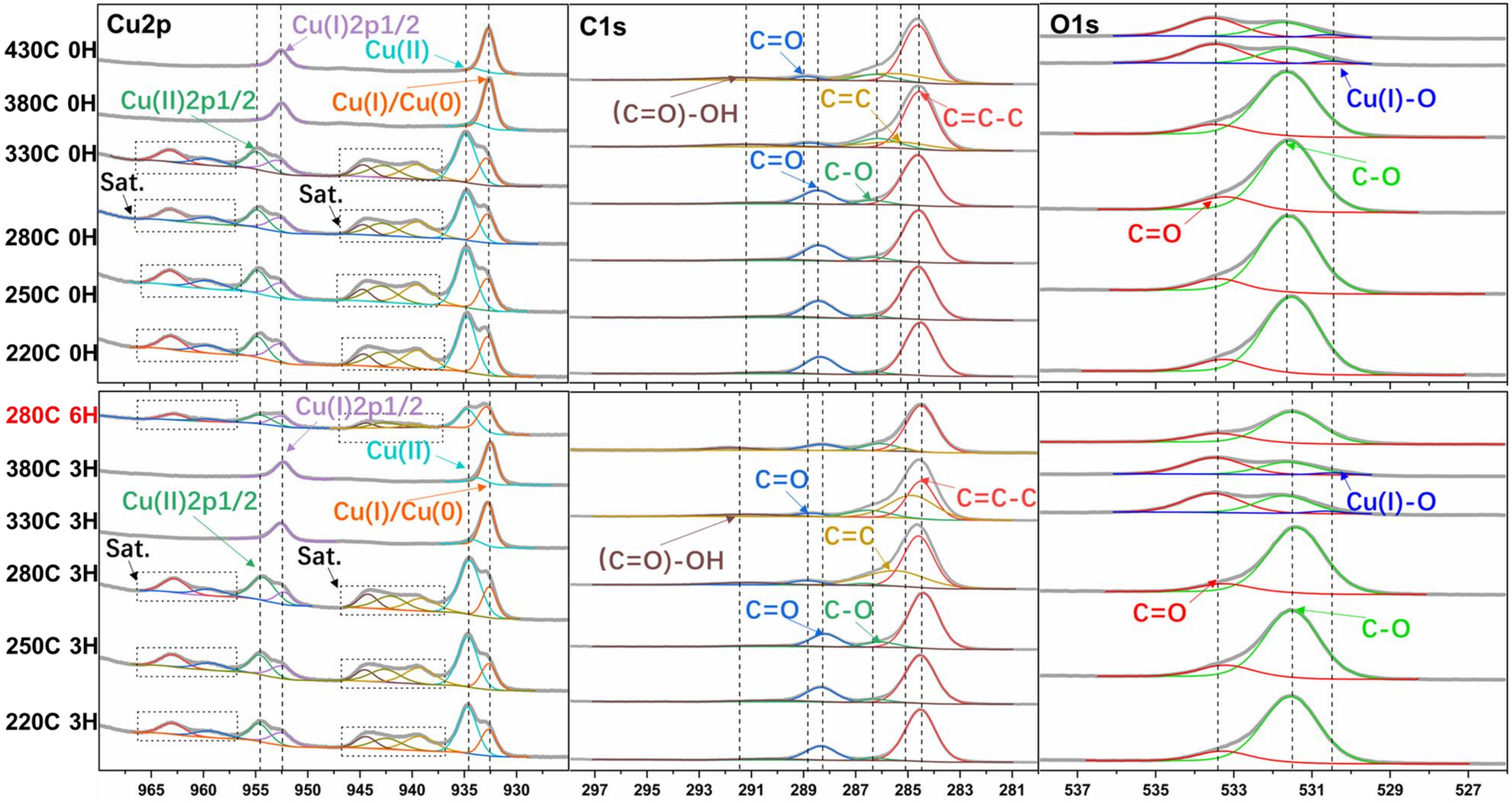

Figure 6-5 XPS spectra (C1s, Cu2p, O1s) of different annealed HKUST-1 sample. The XPS tested samples were extracted from 0 h and 3 h of all samples. the x coordination is binding energy (eV), the y coordination is intensity (a.u.).

6.2.6 Texture analyses

Figure 6-6 showed five representative images to illustrate the surface geometry and particle distribution of annealed HKUST-1 under mild temperature for a prolonged period and harsh condition as deduced by TEM. In the upper-right corner of each image, the Cu particles were dispersed onto the graphene oxide sheets. Counting around 200 particles of each TEM image by ImageJ, the particle size population was concluded in the upper left corner of each image, and all annealed samples contained Cu nanoparticles (<100 nm). It should be mentioned that mild condition would produce the smallest Cu nanoparticles, but harsh condition would induce Cu particle aggregation into larger particles, since high temperature could promote the Cu nanoparticles movement on the plane of graphene oxide and increase probability of their contact, so that, copper metal cluster grew up through metal bond on the plane of graphene oxide.

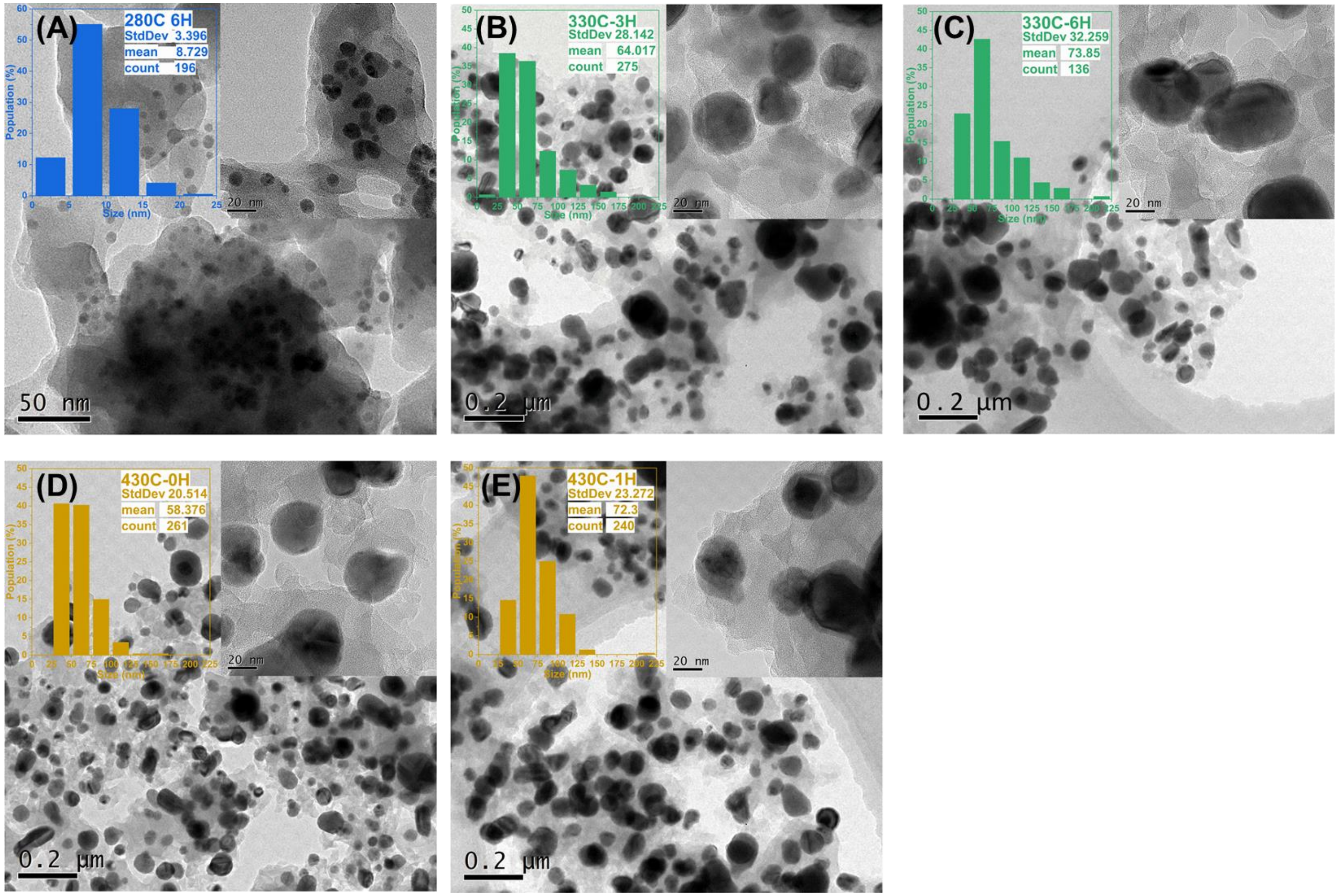

Figure 6-6 TEM images of HKUST-1 samples annealed under (A) 280 °C for 6 h, (B) 330 °C for 3 h, (C) 330 °C for 6 h, (D)430 °C for 0 h, (E) 430 °C for 1 h.

6.2.7 Surface property analyses

Table 6-2 Porosity characteristics parameter

Sample	BET (m^2/g)	Langmuir (m^2/g)	micropore (cm^3/g)	total pore	$P_{micropore}$(%)	pore width (Å)
220C 0H	1426.86	1632.42	0.55	0.72	0.77	9.73
220C 1H	1428.47	1663.00	0.56	0.75	0.74	8.75
220C 3H	1322.62	1525.82	0.52	0.68	0.76	8.21
220C 6H	1342.18	1600.65	0.55	0.72	0.76	6.57
250C 0H	1329.17	1615.31	0.52	0.74	0.70	9.89
250C 1H	1224.12	1556.40	0.53	0.74	0.71	9.15
250C 3H	1059.99	1462.53	0.50	0.67	0.75	6.75
250C 6H	947.62	1306.81	0.44	0.61	0.73	6.48
280C 0H	1042.21	1473.68	0.50	0.67	0.75	7.08
280C 1H	761.21	883.84	0.30	0.52	0.57	6.65
280C 3H	211.21	261.05	0.08	0.27	0.31	12.51
280C 6H	29.38	47.63	0.01	0.15	0.08	196.65
330C 0H	961.31	1144.03	0.38	0.58	0.67	6.88
330C 1H	26.03	42.46	0.01	0.14	0.07	260.84
330C 3H	29.03	44.58	0.01	0.13	0.09	173.10
330C 6H	30.26	46.55	0.01	0.13	0.09	195.35
380C 0H	27.79	44.31	0.01	0.14	0.08	229.79
380C 1H	39.11	59.72	0.02	0.15	0.11	145.04
380C 3H	35.17	55.24	0.01	0.14	0.11	192.87
430C 0H	37.88	59.57	0.02	0.18	0.09	168.81
430C 1H	50.47	74.38	0.02	0.13	0.17	118.44

Combined with XRD patterns of each sample, the pore properties in Table 6-2 and Figure 6-7, showed that the annealed samples treated in different temperature remained highly porous, but the over-temperature process would damage the pore structure and reduce surface areas. In Table 6-2, the porosity characteristic parameter derived from isotherm of each sample revealed notable retention of surface area and micropore volume percentage of over 70% at mild annealing conditions. When the temperature increased or the constant temperature increased, the structure of the pores will be affected, to some extent, which was observed by the decrease of the SSA and the decrease of the micro porosity, and even the increase of the pore size. Interestingly, all annealed samples followed the same rule due to the generation of mesopores and the generation of macropores with increased temperature. After 330 °C, there was almost no micropore structure in each annealed sample (330C-X, X=1-6H; 380C-X, X=0-3; 430C-X, X=0-1H), and main type of pores in those samples were in the presence of meso/macro pores. As N_2 isotherm suggested, according to the IUPAC classification, all the catalysts are considered as the combined characteristics of type-II and type-IV isotherms [322] (Figure 6-7), which was a typical feature of mesoporous materials containing micropore. In details, up to 30% porosity is still retained even at harsh annealing conditions, before complete framework decomposition at 330 °C for 1 h to yield Cu nanoparticle embedded on graphene oxide. The collapse of the framework structure produced a poor SSA (221 m^2/g, 280C-3H) sample and elucidated just 15% of the 1426 m^2/g of 220C 0H sample. Regarding the other obvious observation, that some annealed sample (220C 1H) showed a little higher total pore volume than that of 220C 0H sample. The retention or improvement in pore volume of HKUST-1 correlated to a vacancy defect-induced enhancement. Besides, the reduced specific surface area and the micropore volume indicated a partial collapse of the local pore structure due to decomposition of the carboxylate linker, which was also proven by the lattice constant change of Table 6-1. In harsh annealing condition, the surface area of annealed sample was increased with temperature increasing or retention increasing, but pore volume of harsh annealed sample had no significant change. Provided by the TGA result, the mass loss of harsh annealed sample is basically absent. That is, the increased surface area was because of the copper particle change under high temperature with a prolonged period. The high temperature or long-term isotherm would induce the accumulation of Cu nanoparticle on the surface of graphene oxide, also, the surface energy of graphene oxide itself was low. Therefore, the later accumulated Cu nano-clusters would no longer take up the previously occupied channel or pore.

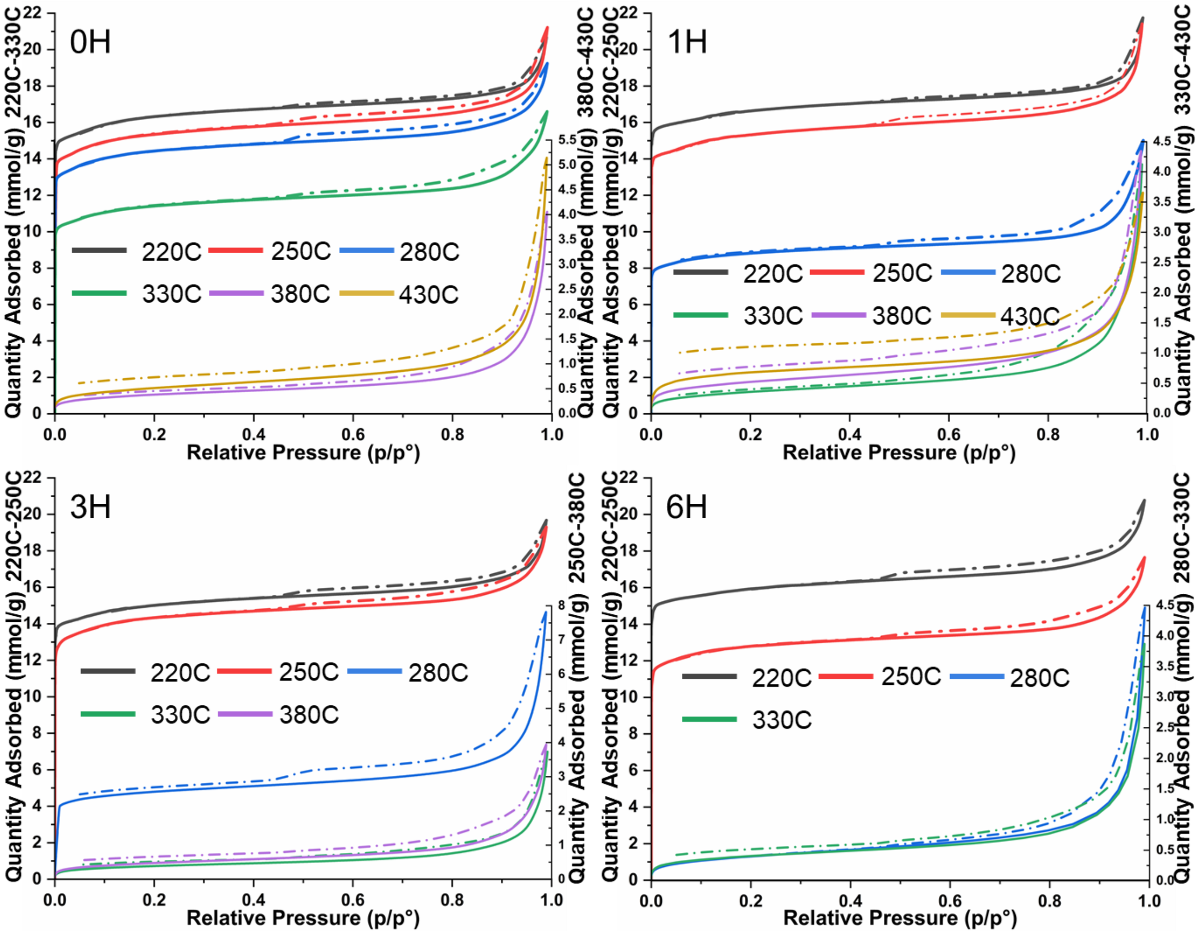

Figure 6-7 N_2 adsorption and desorption isotherms

6.2.8 In-situ DRIFT analyses

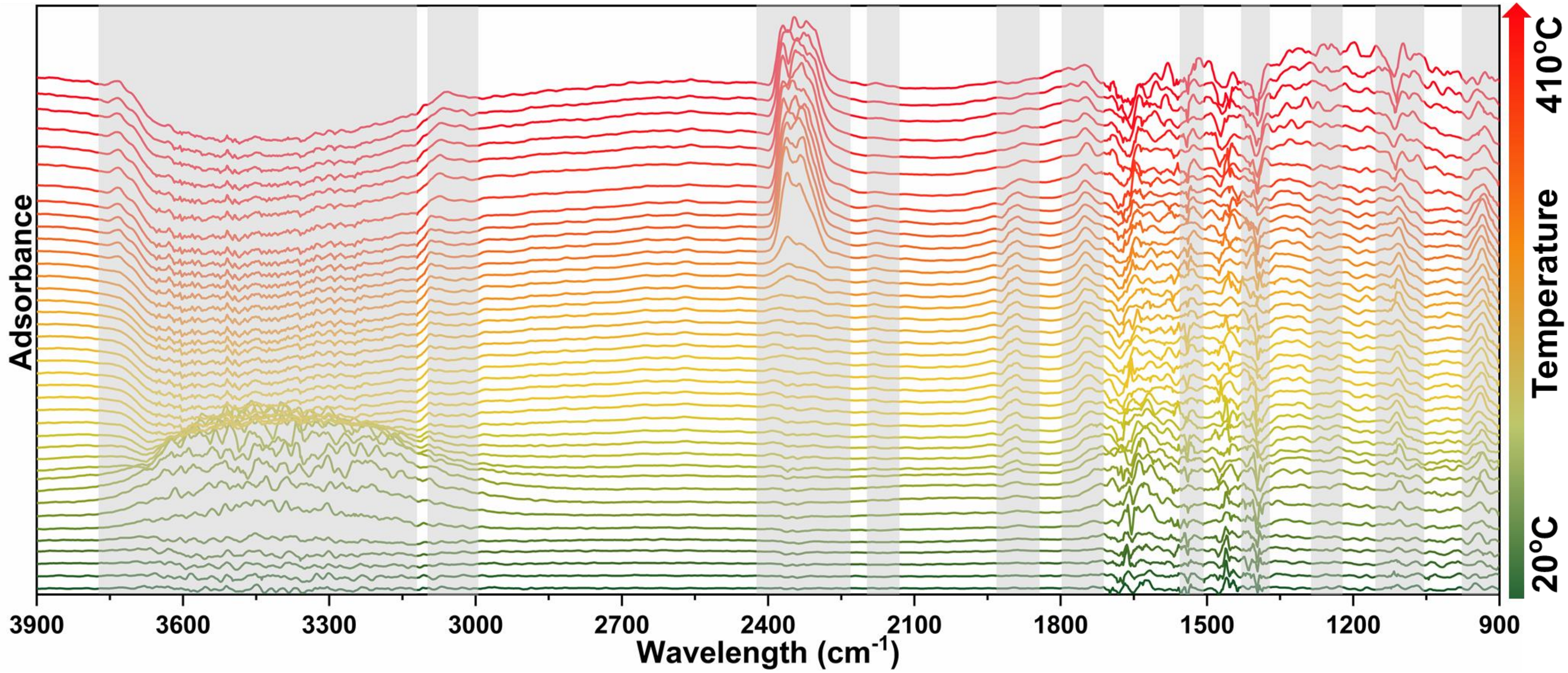

Figure 6-8 In-situ surface characterization of HKUST-1 sample via DRIFT spectroscopy in the IR range of 3000-900 cm^{-1}. The spectra were monitored per 10 ^{o}C. the significant changed areas were marked.

To reveal the insight of framework change in HKUST-1 in different temperature, the diffuse reflectance infrared Fourier transform (DRIFT) spectra of HKUST-1 thermal evolution was recorded in Figure 6-8. Spectra of HKUST-1 surface pointed out important bands change regarding hydroxyl(-OH)), CO_2, CO and carboxylic functional groups (-COOH). Stretching vibrations of O-H bonds appeared in the range of 3000-3800 cm^{-1} and v(O-H) bending was at 1400 cm^{-1}. Driven by temperature rising in the range of 3800-3000 cm^{-1}, H_2O molecules physisorbed through the transpiration would migrate from the pores of MOFs to the surface and aggregate, the positive peak of v(O-H) exhibited increased around 60 ^{o}C and maximum around 120 ^{o}C. As the temperature continued to rise, the water molecules collected on the surface will leave from the surface, which was corresponding to the smooth and broad peak in the range of 3800-3200 cm^{-1} around 180 ^{o}C. After that, negative peaks were remained and strengthened around 280 ^{o}C, which were attributed to v(OH) of isolated surface hydroxyl groups in carboxylic group (unreacted with Cu and individually exposed carboxyl groups). The free hydroxyl group would be liberated onto the isolated copper particles or onto the graphene to form the graphene oxide, and the correspondingly negative signals was related to the v(OH) bending around 1400 cm^{-1} from the decomposing carboxylic group (-C(O)-OH). About CO_2 (2400-2300 cm^{-1}) and CO (2180 cm^{-1}) [323], there were weak negative peaks of CO_2 coming out and no presence of CO before 120 ^{o}C, but when heating up to 280 ^{o}C, positive intensities of CO_2 and CO were observed, where both of gas were formed. As an intermediate of partial CO oxidized into CO_2, positive signals of formate can be detected, with a continuous intensity up to 410 °C. The related vibrations for the vas and the vs mode of the formate were at 1595 and 1375 cm^{-1}, and the related v(CH) vibrations were at 3060 and 1884 cm^{-1}. Besides, the decrease of surface hydroxyl groups (in Figure 6-4. 220 - 430 °C for 0 h) can be detected between 3800 and 3100 cm^{-1}, which illustrated the similarity to the mentioned evidence about CO_2 adsorption/carbonate formation. Above the temperature of 340 °C, the formate was rapidly decomposed corresponding to the v(C-H) shifted to the right and disappeared. The shift to lower wave numbers may indicate an interaction between the carboxylic group and Cu. Accompanied by the already mentioned formate signals, the combination mode, vas(CO_2 + δ(CH), at 2980 cm^{-1} was observed, where the observed formate species were considered as a bridged species [324, 325]. As observed at carboxylic group characteristic range of 1800-900 cm^{-1}, the vibration of C=O stretching appeared at 1751 cm^{-1}, as well as was strengthened after 120 °C. Because H_2O around the active site Cu (SBU, secondary building unit) was released, Cu-Cu and carboxylic groups linked with Cu all exposed, which corresponds to the intensity of v(C=O) increased. Observed bands in 1649 and 1460 cm^{-1} were attributed to asymmetric and symmetric stretching vibrations of the carboxylic group, respectively. The positive intensities at 1101 and 931 cm^{-1} were attributed to the C-O stretching vibration of the carboxylic group and the C-O stretching decreased with contributions from the deformation of C-OH after 350 °C.

6.2.9 HKUST-1 annealing mechanism

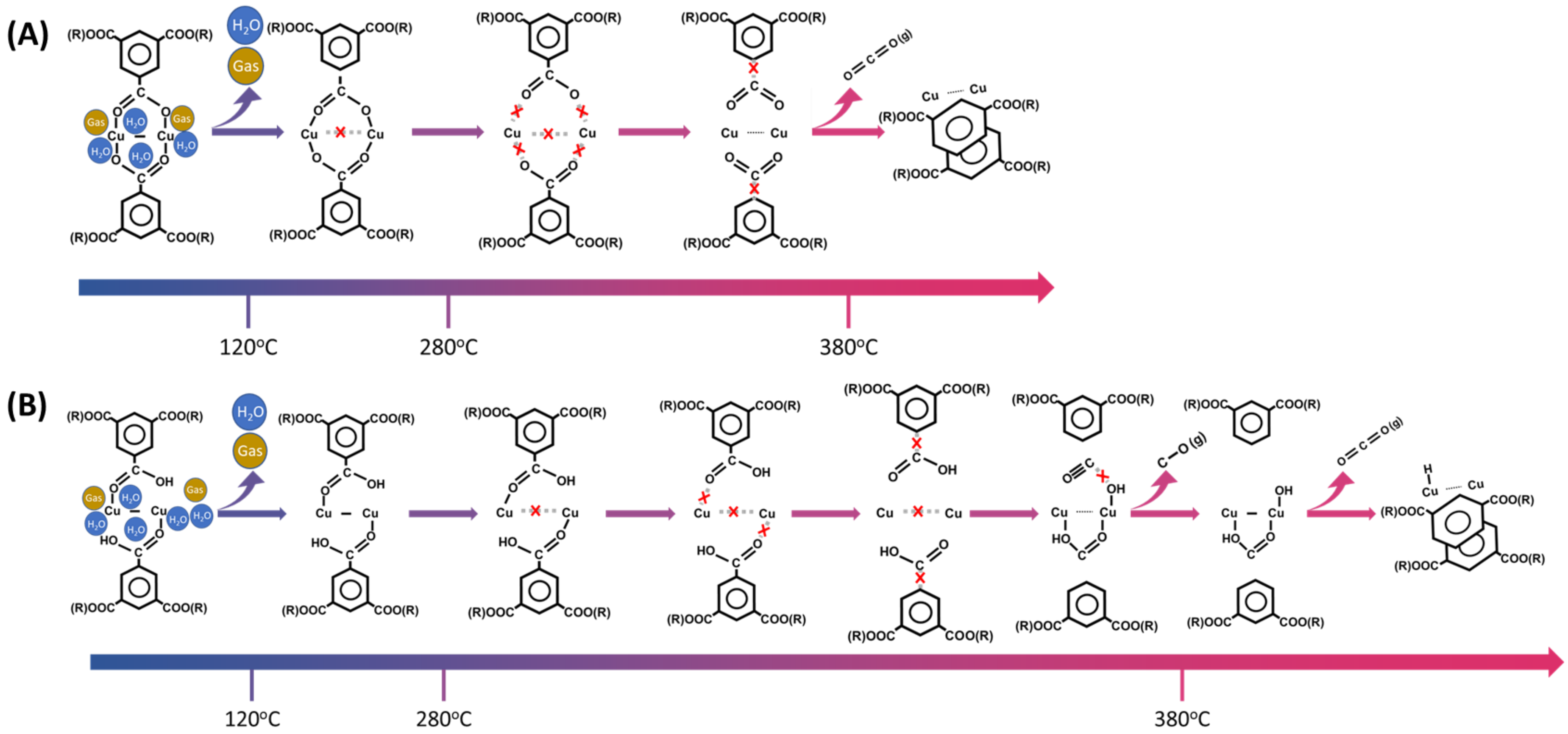

Figure 6-9 The conception of HKUST-1 decomposition process in annealing treatment. Here, the SBU of HKUST-1 MOFs represents the complete configuration of HKUST-1. A is complete configuration of HKUST-1 MOFs (defect-free HKUST-1). B is the incomplete configuration of HKUST-1 MOFs (defective HKUST-1). Here, the change of structural formula was depicted as the distortion, decomposition, and graphitization of HKUST-1.

Taken together with the all characteristic result of annealed HKUST-1 samples, the plotted conception process of HKUST-1 decomposition was based on experimental bond dissociation energy in Table 6-3, which made a convinced prediction. In accordance with the presence of CO and -OH during heating process, the incompletely reacted HKUST-1 was proven to exist within the structure of MOFs. Thus, two kinds of HKUST-1 configuration were displayed in Figure 6-9. In Table 6-3, each bond in HKUST-1 structure would break followed as the order of dissociation energy (Cu-Cu < Cu(II) < C-C < O-H < C-OH < C-H < C=C < C=O). Regarding the complete HKUST-1 structure (defect-free HKUST-1), the physisorbed gas and water would be removed after 120 °C, and individual frame of HKUST-1 was left. Continuous heat from increasing temperature drove the original bond of Cu-Cu elongated, where the linked Cu(II)-O bond could be influenced in this case. When temperature was heated around 280 °C, the bonds of Cu(II)-O (oxygen from C=O and C-O) broke due to the intolerance at this high temperature, and individual Cu atoms would be bound together into a larger block under the interaction of metal bond. Maybe, the bond of C-C broke at this time due to the catalysis of metal cluster and further heat, and a large number of individual benzene ring would be left behind. After 380 °C, yielded CO_2 would be released from the surface of residue. Those individual benzene rings, doped with the residual product of the carboxylic group, would be self-joined and form a parallel layered structure induced by sp^2 pi-pi interaction and Cu cluster would be bound to the coordinated oxygen group. In case of CO and formate intermediates observed, the incompletely reacted HKUST-1 (defective HKUST-1) was considered as the dominant factor to drive this reaction. In Figure 6-9(B), the incompletely reacted HKUST-1 contained a complete carboxylic group, that is, the other end of the oxygen from C-O was still attached to H atom. Such defective structure was easier destructed than complete one. On account of fewer Cu-O bonds, the bond of Cu-Cu in relatively instable structure would prefer to break at a slightly higher temperature, and the total bond dissociation of Cu-O consumed lower than that in complete structure in temperature range of 280-380 ^{o}C. These two accelerated steps directly would promote the fracture of C-C bond, and the formate intermediate appeared at the moment. As the temperature rose up to 380 ^{o}C, partial formate adsorbed on the surface of Cu clusters, would be decomposed into -OH free radicals and CO gas. Besides, not decomposed formate intermediates and hydroxyl free radicals could be detected via In-situ DRIFT. Meanwhile, another part of formate, bridged adsorbed on two Cu atoms, would be decomposed into CO_2 and H* free radicals, at the same time, more H* free radicals aggregated and spontaneously formed H_2 gas as this reaction proceeded in the forward direction. As the result, the Cu nanoparticle embedded on graphene oxide were formed.

Table 6-3 Bond dissociation energy of each bond in HKUST-1 MOFs

Bond Type		Bond Dissociation Energy (kJ/mol)
	Cu-Cu [326]	201
Cu(II)-O	Cu-O [326]	287 .4 ± 11 .6
C-C	C_6H_5-C(O)OH [326]	429 .7 ± 8 .4
O-H	$C_6H_5CH_2$O-H [326]	334 .1 ± 2 .6
	CH_3C(O)O-H [326]	442 .7 ± 8.8 1
C-OH	$C_6H_5CH_2$-OH [326]	459 .4 ± 4 .2 1
	CH_3C(O)-OH [326]	468 .6 ± 12 .6 1
C-H	H-C_6H_5 [326]	472 .2 ± 2 .2
	C=C [327]	602 ± 21
	C=O [327]	798.9 ± 0.4

6.3 Summary

a) The present work has shown simply annealing process of HKUST-1 under 220-430 °C for different prolonged isotherm steps.

b) Due to defects and unstable bond of compound at a high temperature, the structure of the MOFs would completely collapse after 330 °C. At this stage, the entire structure began graphitization accompanied by the occurrence of the metal cluster. Additionally, these periods would be followed with the formation of CO_2, CO, etc. At 430 °C, MOFs structure would finally become Cu NP embedded with GO.

c) A series of characterization techniques all supported the existence of CuNP/GO structure. Thus, the present approach of annealing under inert condition is very operative to prepare a functional CuNP/GO, and such the kind of product could enhance some certain catalysis reactions more effectively.

Chapter 7 Construction of CuNP/GO catalyst and its application in CO catalytic oxidation

7.1 Introduction

The design of economically viable and eco-benign catalytic processes is one of the foremost claiming for securing a sustainable future [328]. During the past decade, the excellent gas storage capacity of metal-organic frameworks (MOFs) at an ambient temperature has enabled themselves to grow rapidly, providing a new member for the family of recyclable adsorbents [329 330]. Meanwhile, MOFs, as the self-assembly of metal ions or clusters with organic ligands, become a highly versatile platform to immobilize molecular catalysts that are imparted through the field ligands under homogeneous conditions, thus supporting access to a new set of catalytic materials [329, 331]. Despite the fact, they have been convinced of taking a fabulous performance, there is one concern about their durability when they are exposed to ambient moisture [332]. To broaden cost-effective capacity of MOFs, considerable efforts have been devoted to recycling and reusing MOFs [333, 334]. Particularly, thermal treatment approach, one of the simple and effective methods, was broadly utilized to re-modify surface structures and obtain different properties of catalyst [335, 336].

The catalytic oxidation of carbon monoxide (CO) under a mild condition is still a technological challenge and fundamental interest in heterogeneous catalysis [337, 338]. The elimination of CO, sourced from fuel impurities on Polymer electrolyte membrane (PEM) fuel cells [339] and incomplete combustion of vehicle fuel [340], hunts for the application of novel materials in the CO catalytic oxidation at a low temperature. Traditionally, noble catalysts, such as Au [341], Pt [342] and Pd [343] based catalysts, are used for the high-efficiency oxidation of CO. However, several barriers of cost and limited amount in nature interfere with their wide application in the large-scale industrial process [344]. With the issue of dwindling precious metal supplies and stable demand of catalyst [345], it is highly important to replace precious metal catalyst by with earth-abundant non-precious metals. Thus, it is a further attempt and necessary to design a low-cost and high-efficiency non-precious metal-based catalyst for CO oxidation under ambient atmospheres from recycled and reused MOFs.

As a substitute noble-metal-free catalyst, Cu based catalyst shows excellent catalytic performance for CO oxidation [346-348]. Also, Cu have rich varieties of formations including Cu(0) and Cu(I) and Cu(II) [349], many encouraging results from catalytic oxidation reactions were promoted by different copper complexes and oxides [350]. Likewise, the substrate design must be dealt with. The main role of substrates should be enhancing the stabilities and the catalytic properties of nano catalysts [351, 352]. Graphite oxide possesses a similar layered structure [353] and anionic surface [354] with hydrophilicity [355], being a competitive substitute. Theoretically, the surface of

GO possesses rich oxygen containing group [356], which are the key to immobilize metal atoms and enhance the metal-GO binding to prevent metal agglomeration [357], GO can serve as the potential substrate to covalently anchor metal atoms. Besides, the design of Cu-embedded graphene shows an excellent catalytic behaviour [358] in CO catalytic oxidation.

In this chapter, we present a simple but prudent method for thermal annealing of MOF structures around the intermediate temperature window for complete framework decomposition/carbonization. Here, we try HKUST-1 MOFs [42], also referred to as $Cu_3(BTC)_2$, (BTC = 1,3,5-benzenetricarboxylate) here, which possess a simple pore structure and high porosity with high content of Cu. According to the suggestion of Chapter 6, a series of Cu nanoparticles (CuNPs) embedded on graphene oxide (GO) were obtained and applied in CO catalytic oxidation. During the CO oxidation process, the presence of formate intermediates was confirmed by the In-situ technique. Additionally, it is essential observation that Cu_4O_3 was detected from the surface of In-situ spent catalyst via XRD. As the most mysterious copper compound, there have been few reports about the performance of its catalytic field after the first mention [359] of Cu_4O_3 (paramelaconite). The reason not only includes the synthetic difficulty but also is involved in non-resistance in high temperature [360]. However, paramelaconite as a divalent state compound is necessary to demonstrate the CO oxidation process in this work. On a practical level, this is the first time that paramelaconite is applied into the CO catalytic oxidation.

7.2 Results and discussion

7.2.1 Physicochemical properties of Cu/graphene oxide catalysts

7.2.1.1 Crystallinity and Morphology analyses

The XRD patterns of different CuNP/GO catalysts were given in Figure 7-1. Importantly, the characteristic diffraction peak around 20.754° belonged to graphite structure [361], attributing to (002) GO. All the catalysts present the other five reflections at the peak of 37.009°, 38.957°, 43.297°, 50.433°, 74.130°, which were corresponding to the (111) Cu_2O, (200) CuO, (111) Cu, (200) Cu, and (220) Cu. The XRD patterns of CuO, Cu_2O and Cu were matched up with PDF#80-1268, PDF#05-0667 and PDF#04-0836. The copper oxide species were attributed to two planes of (111) 37.009° and (200) 38.957°, but the diffraction intensity of copper oxide species was weak, where almost CuO/Cu_2O transforming into metallic Cu was reduced by the presence of C atoms during the annealing process. In addition, TEM images of the CuNP/GO catalyst (305C-6H, 330C-3H, 360C-1H, 380C-0H, 430C-0H) indicated that the well-dispersed copper nanoparticles were embedded on the basal plane of GO sheet (Figure 7-2(a)). The observations proved that GO would immobilize CuNP with the size of 40-60 nm (Figure 7-2(b)) on the substrate as well as could prevent these nanoparticles into being larger agglomerates (inset Figure 7-2(a)). Therefore, the facile approach is also low-cost and accessible to synthesize in large quantities of CuNP/GO catalysts.

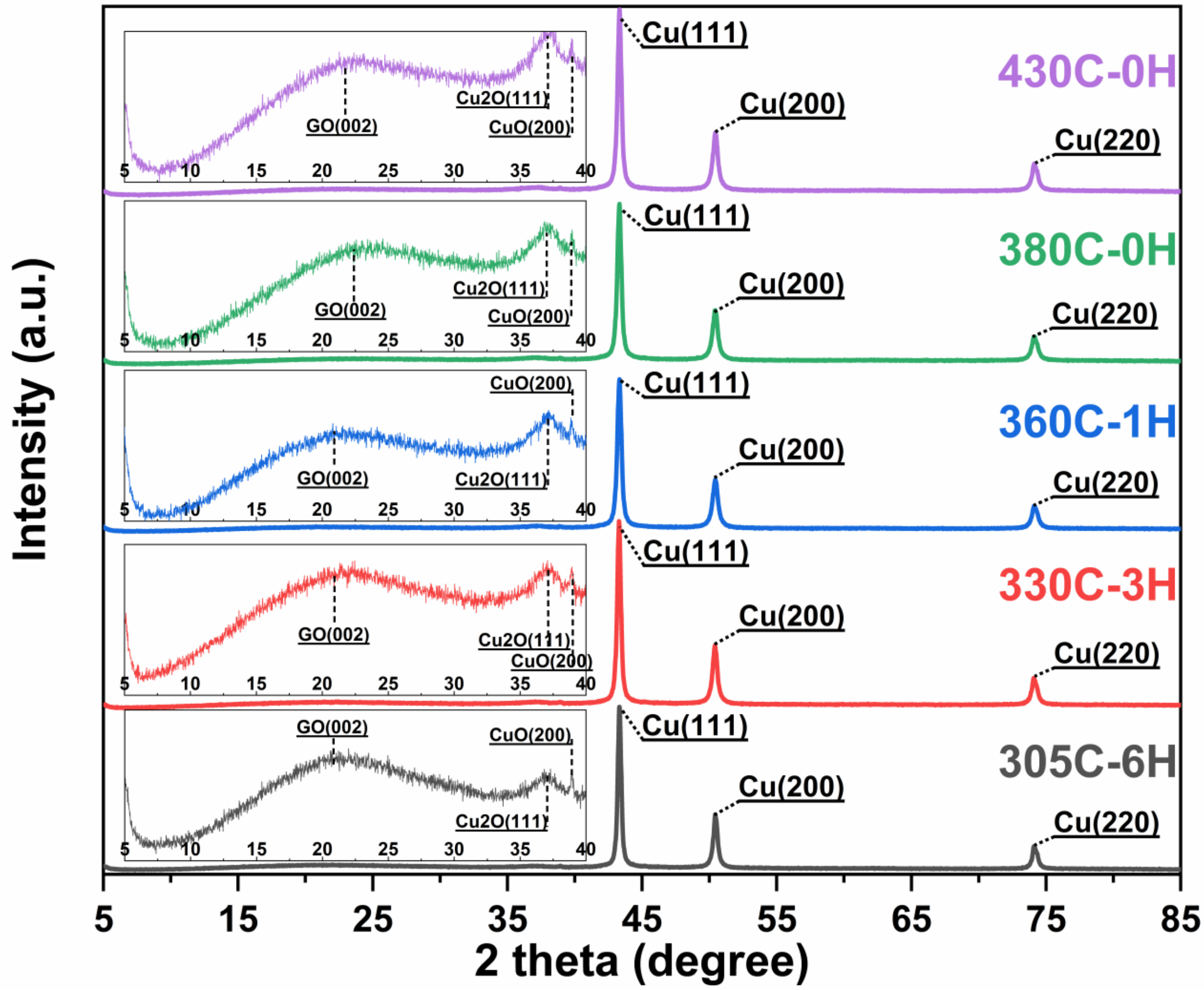

Figure 7-1 XRD patterns of different CuNP/GO catalysts, 305C-6H, 330C-3H, 360C-1H, 380C-0H, 430C-0H. Five inset graphs are their XRD patterns in the 2 theta range from 5-40° and the range of intensity axis are the same level. Cu XRD pattern was matched up with PDF 04-0836.

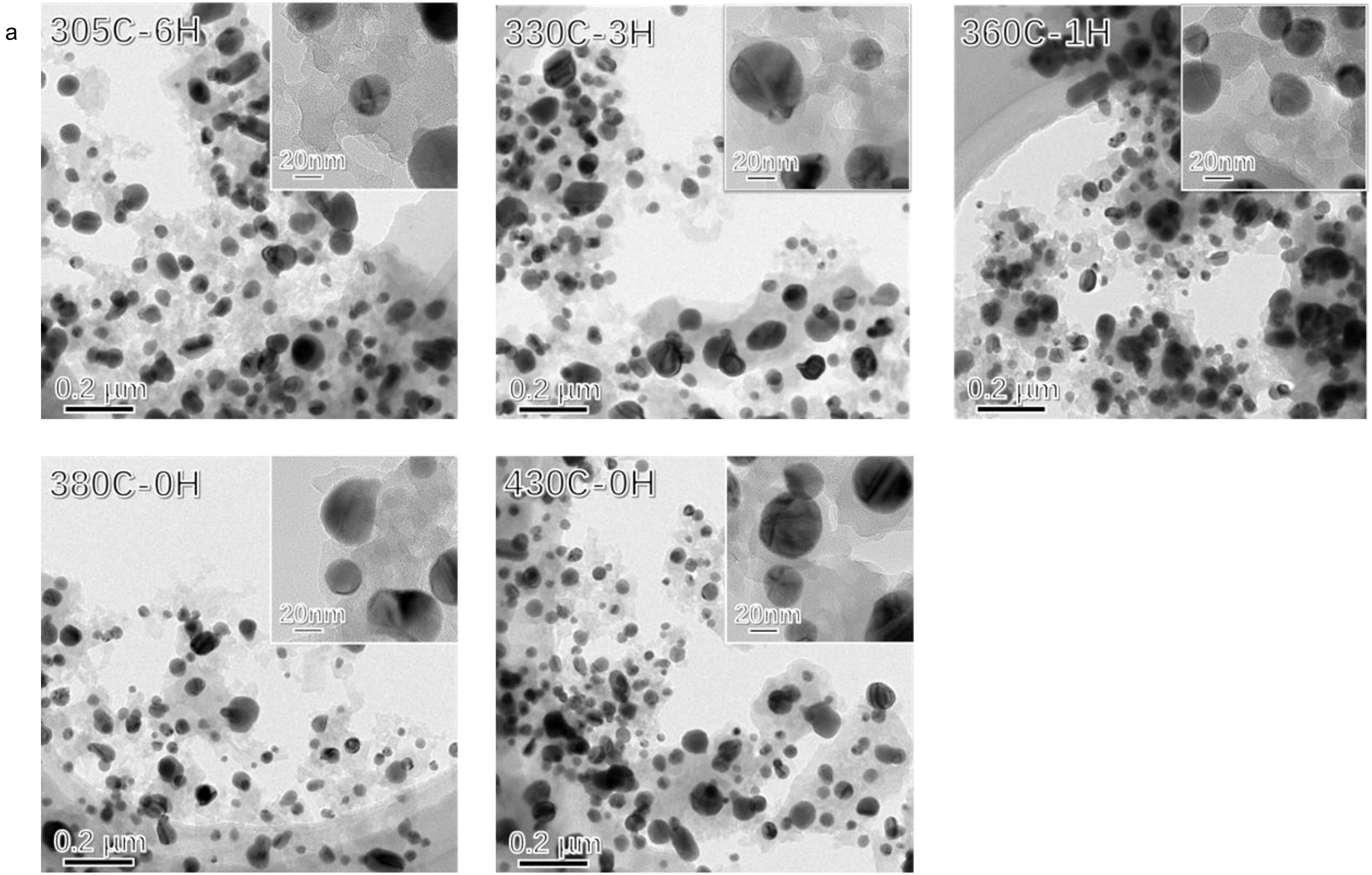
a
305C-6H
20nm
0.2 µm
330C-3H
20nm
0.2 µm
360C-1H
20nm
0.2 µm
380C-0H
20nm
0.2 µm
430C-0H
20nm
0.2 µm

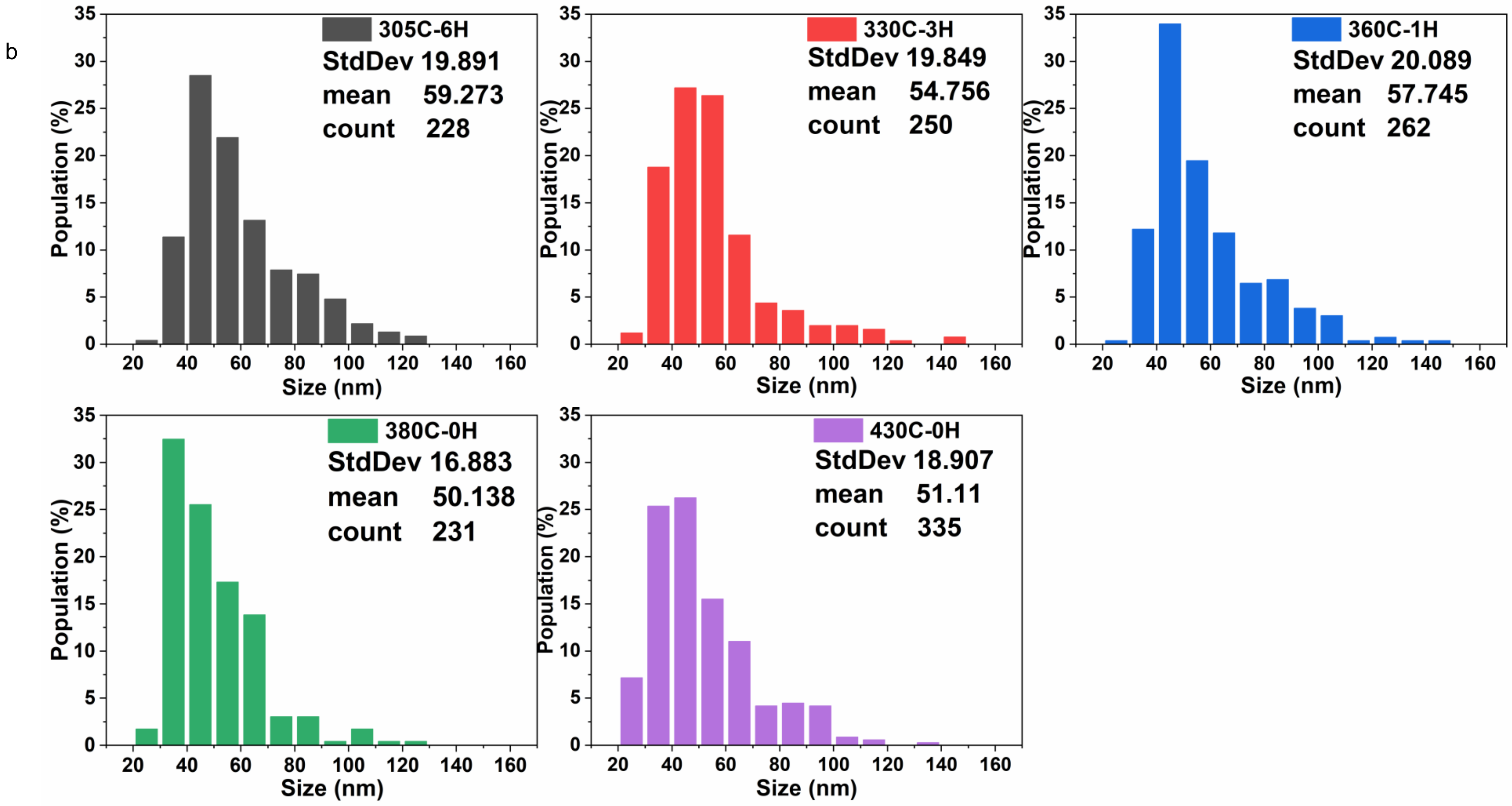

Figure 7-2 TEM image (a) and size distribution histogram (b) of CuNP on GO, 305C-6H, 330C-3H, 360C-1H, 380C-0H, 430C-0H. the sample number for different catalysts counts around 200 particles. the size unit was in nm (Feret’s diameter).

7.2.1.2 Functional group identity

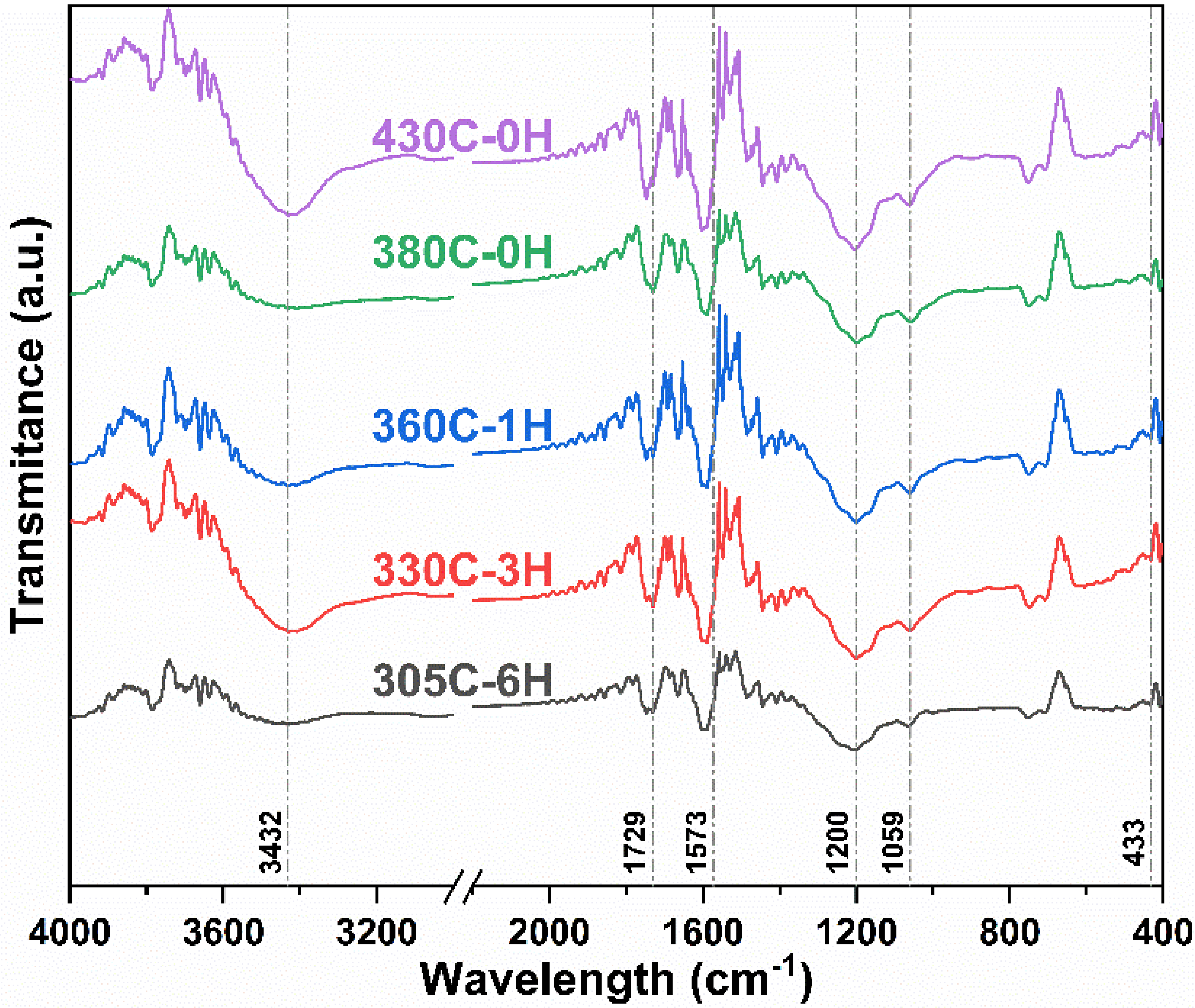

Figure 7-3 FTIR spectra of different CuNP/GO catalysts, 305C-6H, 330C-3H, 360C-1H, 380C-0H, 430C-0H.

Obviously in Figure 7-3, the stretching vibrations (vs) of hydroxyl (O-H) [356], C=O [356], C=C [356], C-O-C [356], C-O [356] and Cu(II)-O [362] were attributed to around 3432, 1729, 1573, 1200, 1059 and 433 cm^{-1}, respectively. First, the spectra of CuNP/GO catalyst revealed the appearance of oxygen-containing functional groups (hydroxyl, epoxide, carbonyl and carboxyl groups). The spectra between 1200 and 1330 cm^{-1} corresponded to stretching vibrations of epoxide and ketonic functional groups [356]. Besides, most characteristic band at 1200 cm^{-1} was emerging from the C-C stretch of epoxide bands [356] on GO surface. However, vibration modes in the 1500 - 1600 cm^{-1} range [356] were representatively assigned to the in-plane vibrations of sp^2-hybridized C=C within the GO basal plane, C=C aromatic stretch was still well-visible, which proves sp^2 graphene-like structure was remained after the thermal process. Furthermore, the presence of residual hydroxyl [356] (vs(C-OH), 3050 - 3800 cm^{-1} and 1070 cm^{-1}) was proven beneficial to the improvement of catalytic activity, and hydroxyl groups of GO nanosheets would decrease the interface energy between GO and CuNP, improving the metal anchoring.

7.2.1.3 Pore property analyses

The N_2 adsorption-desorption isotherms and pore size distribution of different CuNP/GO catalysts were presented in Figure 7-4 (a) and (b). Adsorption at a low relative pressure ($P/P_0 < 0.02$), a hysteresis at $0.1 < P/P_0 < 0.5$, and a sharp increase at $0.8 < P/P_0 < 1$ were attributed to the existence of micro-, meso-, and macro-pores, respectively. According to the IUPAC classification, all the catalysts were considered as the combined characteristics of type-II and type-IV isotherms [363] (Figure 7-4(a)), which was a typical feature of mesoporous materials containing micropore. Also, the pore volume distribution curves as a function of the pore size were calculated using the BJH method in Figure 7-4(b), that demonstrated the change of a mesoporous structure in CuNP/GO catalysts with the random distribution of micro-, meso-, and macro-pores. Apparently in Table 7-1, the 330C-3H catalyst possesses the largest SSA (specific surface area) with 42.21 m^2/g would increase the number of reaction active sites and enhance the catalytic activity. As increasing in the CuNP content, the SSA decreased gradually. This showed that the increased CuNP triggered the restacking overlays on those in-plane pores of graphene, and a higher CuNP content mean more copper oxide species and carbon atoms participating in redox reaction during the annealing process, which would cause a further decrease in the specific surface area and pore volume with consuming C atoms.

(a)

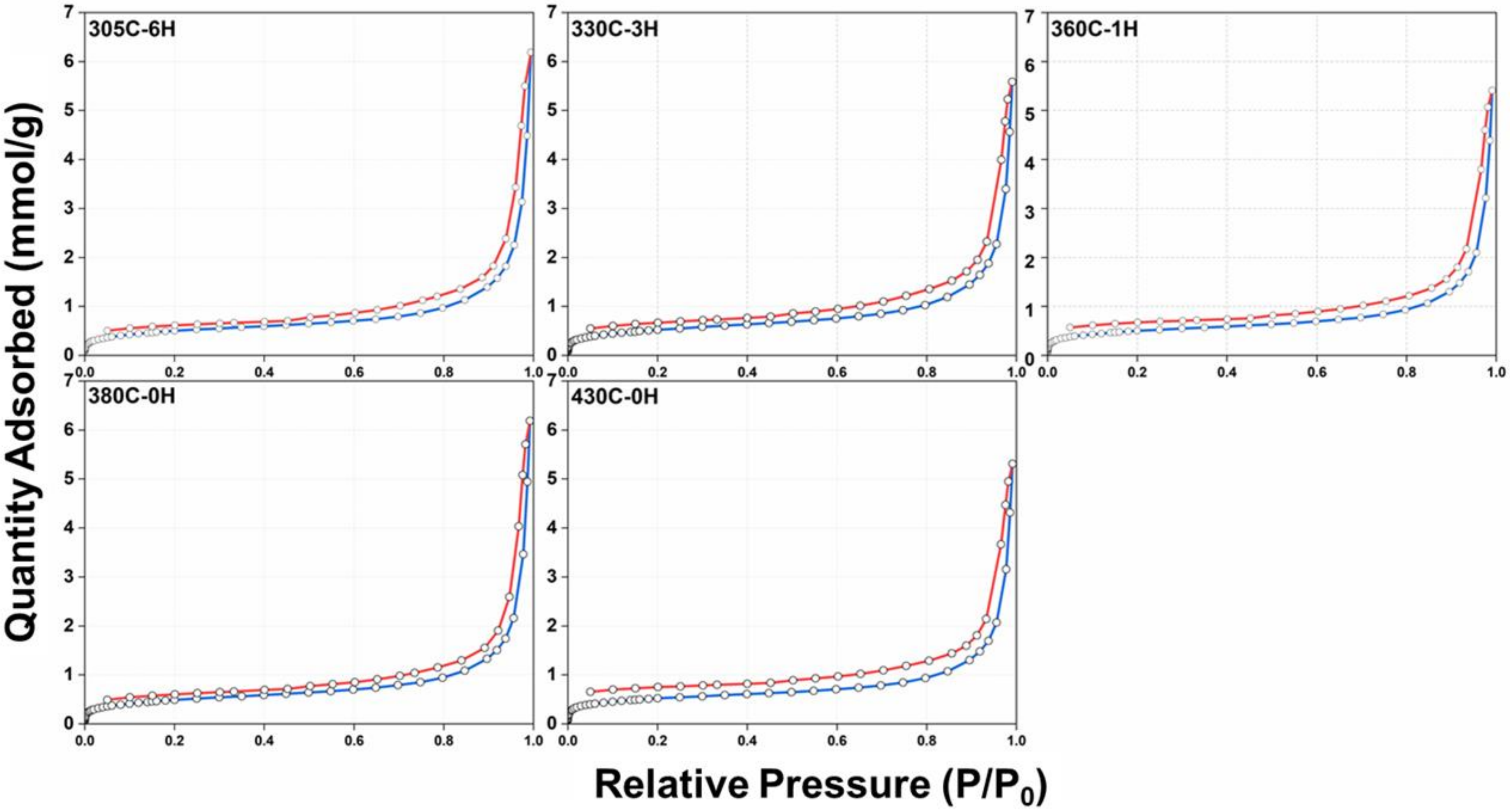
305C-6H
330C-3H
360C-1H
380C-0H
430C-0H
Quantity Adsorbed (mmol/g)
Relative Pressure (P/P0)
0
1
2
3
4
5
6
7
0.0
0.2
0.4
0.6
0.8
1.0

(b)

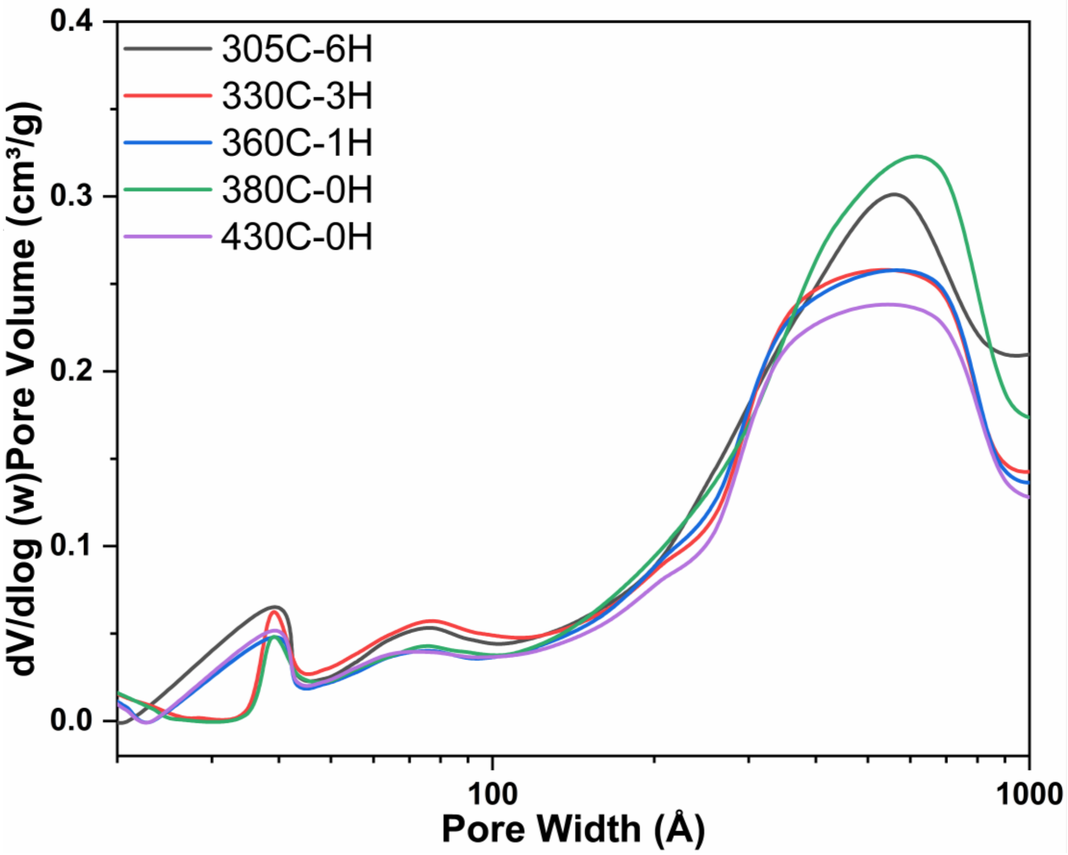

Figure 7-4 N_2 adsorption and desorption isotherms (a) and BJH desorption dV/dD pore volume: Halsey plot with FAAS correction (b) of different Cu/rGO catalysts, 305C-6H, 330C-3H, 360C-1H, 380C-0H, 430C-0H.

Table 7-1 Surface properties of CuNP/GO catalysts

Catalysts	S_{BET} (m^2/g)	$S_{Langmuir}$ (m^2/g)	V_P (cm^3/g)	Cu Content
305C-6H	40.64	57.93	0.21	46.41%
330C-3H	42.21	60.19	0.19	32.29%
360C-1H	40.56	56.91	0.19	48.02%
380C-0H	39.60	56.56	0.21	40.88%
430C-0H	42.10	58.38	0.18	33.17%

7.2.1.4 Chemical analyses

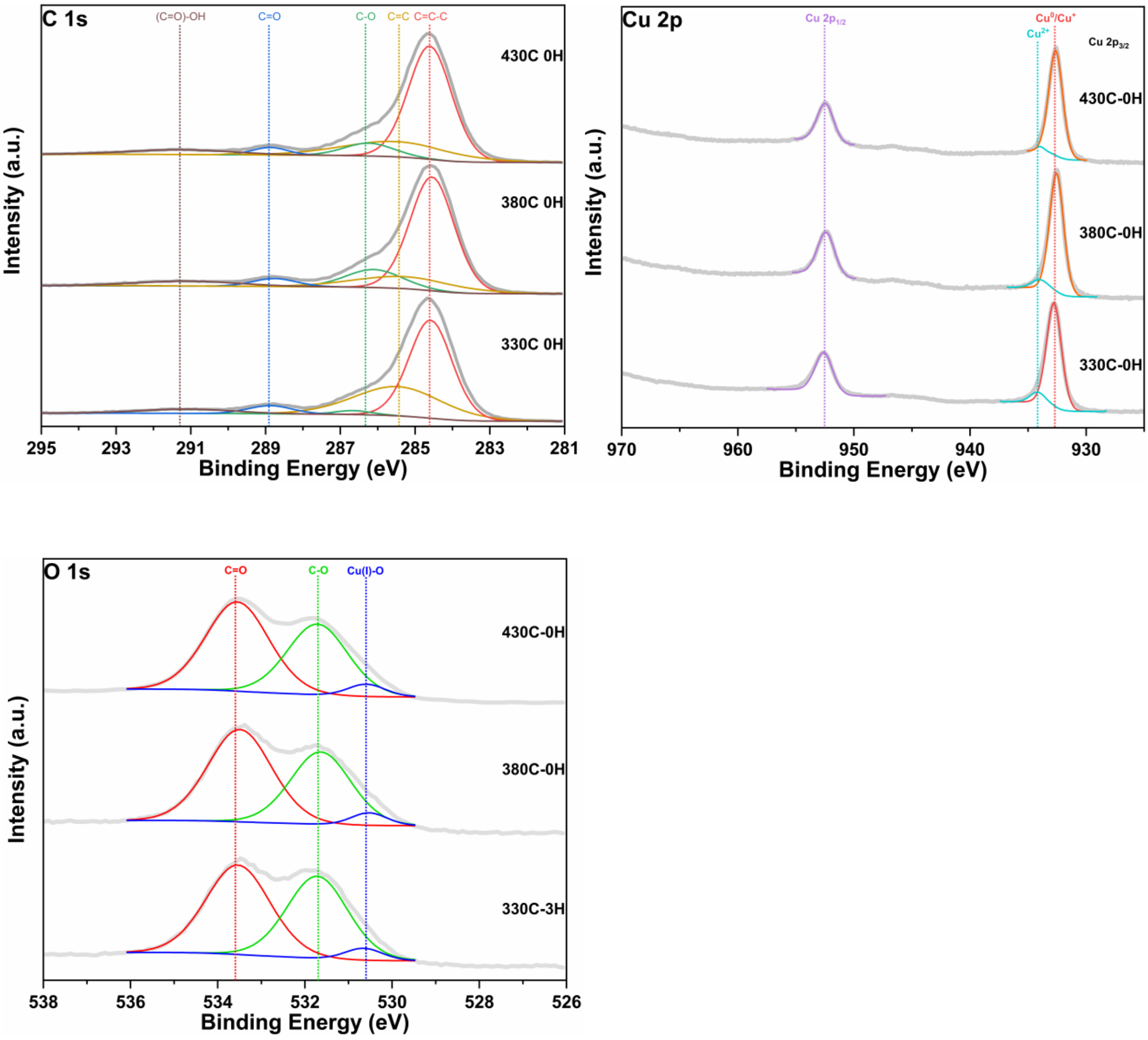

Figure 7-5 C1s, Cu2p and O1s XPS spectra of CuNPs/GO catalysts, 330C-3H, 380C-0H, 430C-0H.

More convincingly, XPS of C1s, Cu2p and O1s spectra was investigated to identify the configuration of CuNPs/GO catalyst in Figure 7-5. The signal of C1s XPS spectra was fitted with six peaks (C=C) at 284.6 eV, (C-C/C-H) at 285.2 eV, (C-OX) at 286.2 eV, (C=O/O-C-O) of epoxides at 288.9 eV, (C(=O)OX) of carboxylic acid at 290.9 eV and the satellite peak at 291.6 eV to pi-pi interactions. Peaks from Cu 2p3/2 and 2p1/2 can be identified at 932.8 and 952.6 eV, respectively. The fitting of the Cu peaks revealed a main signal at 932.8 eV that can be attributed to the Cu(0) or Cu(I) and smaller peaks at 934.2 eV that are due to the presence of Cu(II). The latter indicates a tiny portion of CuNP surface could be as the form of oxidized copper. Regarding O1s XPS spectra, it was resolved into three peaks attributed to (Cu(I)-O) of metal oxide at 530.7 eV [364], (C-O) of the carboxyl at 531.7 eV, and (C=O) of ketone or carbonyl at 533.5 eV. Accompanied with the aforementioned characterization result, the structure of CuNP embedded on graphene oxide was verified.

7.2.2 Catalytic oxidation of CO on CuNP/GO catalysts

The CuNPs/GO catalysts were tested in CO oxidation reaction illustrated in Figure 7-6. The result exhibited the catalytic performance for CO oxidation in the temperature range of 20-250 ^{o}C. Under the same reaction conditions, all the catalysts performed with analogous patterns that CO conversion increased with improving the reaction temperature. The results indicated CO conversion over the CuNP/GO catalysts at 132.9 ^{o}C (T_{50}, 305C-6H) and 199.3 ^{o}C (T_{93}, 305C-6H); 124.3^{o}C (T_{50}, 330C-3H) and 180.7 ^{o}C (T_{93}, 330C-3H); 131.6^{o}C (T_{50}, 360C-1H) and 189.2 ^{o}C (T_{93}, 360C-1H);

128.8 °C (T_{50}, 380C-0H) and 187.4 °C (T_{93}, 380C-0H); 128.6 °C (T_{50}, 430C-0H) and 182.5 °C (T_{93}, 430C-0H) as a function of reaction time, where the temperatures of 50% and 93% CO conversion were denoted as T_{50} and T_{93}. Notably, the maximum catalytic conversion of the CuNPs/GO catalysts was 93%, and the two catalysts of 380C-0H and 430C-0H have almost identical catalytic performance. Among all the catalyst, the catalysts of 330C-3H exhibited highest activity, also, its 50% conversion and 93% conversion both show a better performance in lower temperatures. As observed, these five catalysts exhibited different apparent activation energy. Based on the Arrhenius equation, the activation energy were calculated as follows: 86.14 kJ/mol (380C-0H) > 79.38 kJ/mol (305C-6H) ≈ 79.38 kJ/mol (360C-1H) > 68.16 kJ/mol (430C-0H) > 57.17 kJ/mol (330C-3H). The difference of activity could be ascribed to two factors. On the one hand, it was the crystalline size as literature suggested. Through the Debye-Scherrer's equation, the average calculated crystalline sizes of Cu were 29.5 nm, 24.3 nm, 27.3 nm, 24.7 nm, 25.7 nm for 305C-6H, 330C-3H, 360C-1H, 380C-0H, 430C-0H, respectively. Thus, the CuNP content of each catalyst was followed as the order of crystalline size, which showed the smaller crystalline size and lower CuNP content can distribute to the higher metal dispersion, that was the main reason for the 330C-3H as the best one in CO catalytic performance. On the other hand, there may be an interaction between CuNPs and the graphene oxide support, where the synergistic effect could affect their catalytic CO oxidation activities. The CuNP content of Table 7-1 also can be seen that the activity of the CuNPs/GO enhanced with the decrease of CuNP content, that is, low content of oxidized CuNP in catalysts can be more accessible and faster to be reduced by surrounding GO and reduced CuNP can instantly participate in the sequent catalytic oxidation.

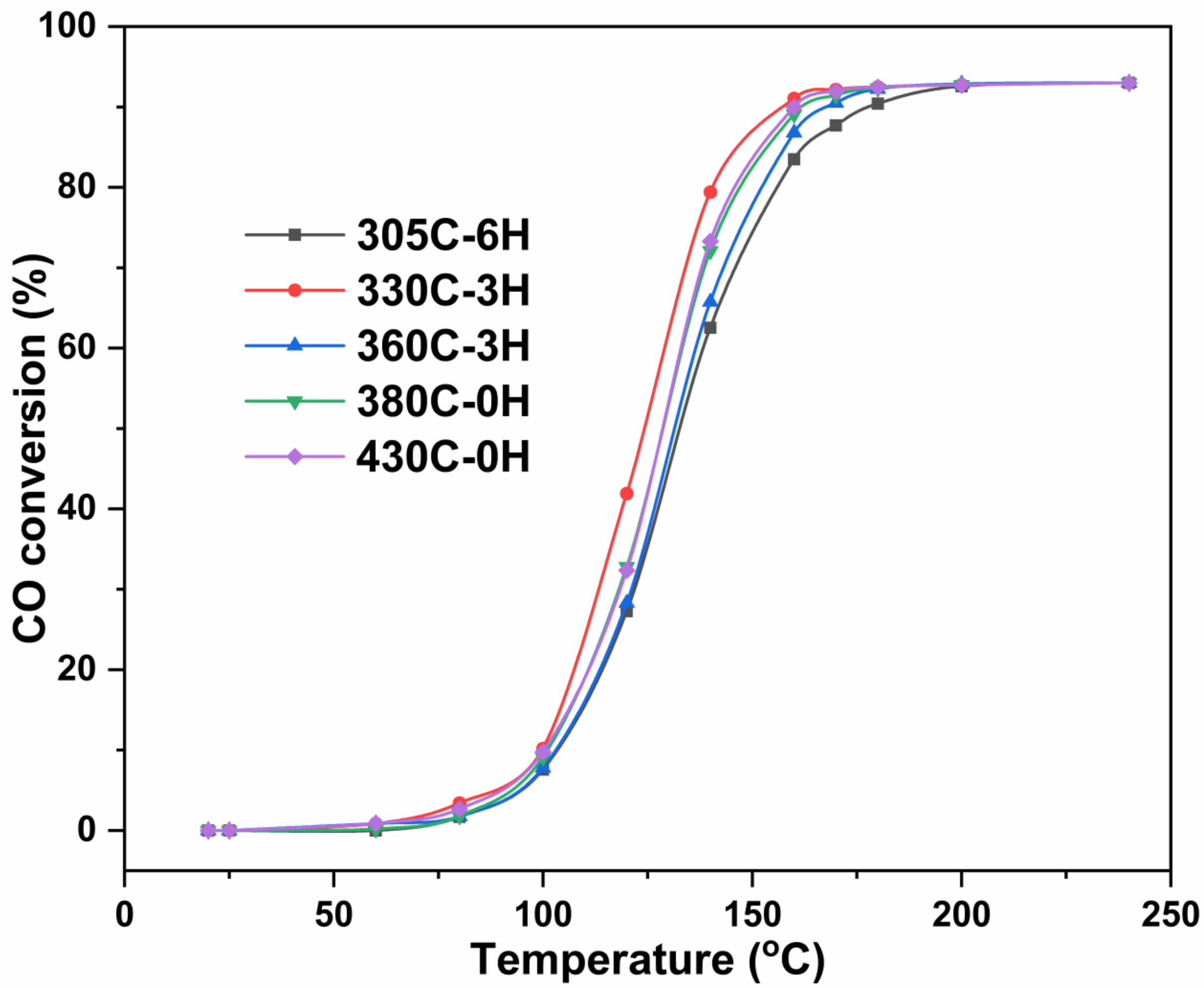

Figure 7-6 Catalytic activity of the CuNP/GO catalysts, 305C-6H, 330C-3H, 360C-1H, 380C-0H, 430C-0H for CO oxidation.

Furthermore, the long-term permanence of the CuNPs/GO catalyst (330C-3H) was shown in Figure 7-7. At the beginning, the CO conversion of catalyst (330C-3H) was 93%. When the reaction lasting for 12h, the CO conversion was almost stationary, and the conversion did not have some significant change after 12h. The FTIR spectra of fresh and spent CuNPs/GO catalyst (330C-3H) were shown in the inset graph of Figure 7-7. Obviously, the momentous change was the strengthened peak of 531.83 (Cu(II)-O) [358]. This was attributed to copper oxide appeared in the reaction environment with 20% O_2, the other characteristic peaks of GO were almost identical before and after reaction, that showed the kind of catalyst owns great thermal stability under 200 °C for long time with high CO conversion

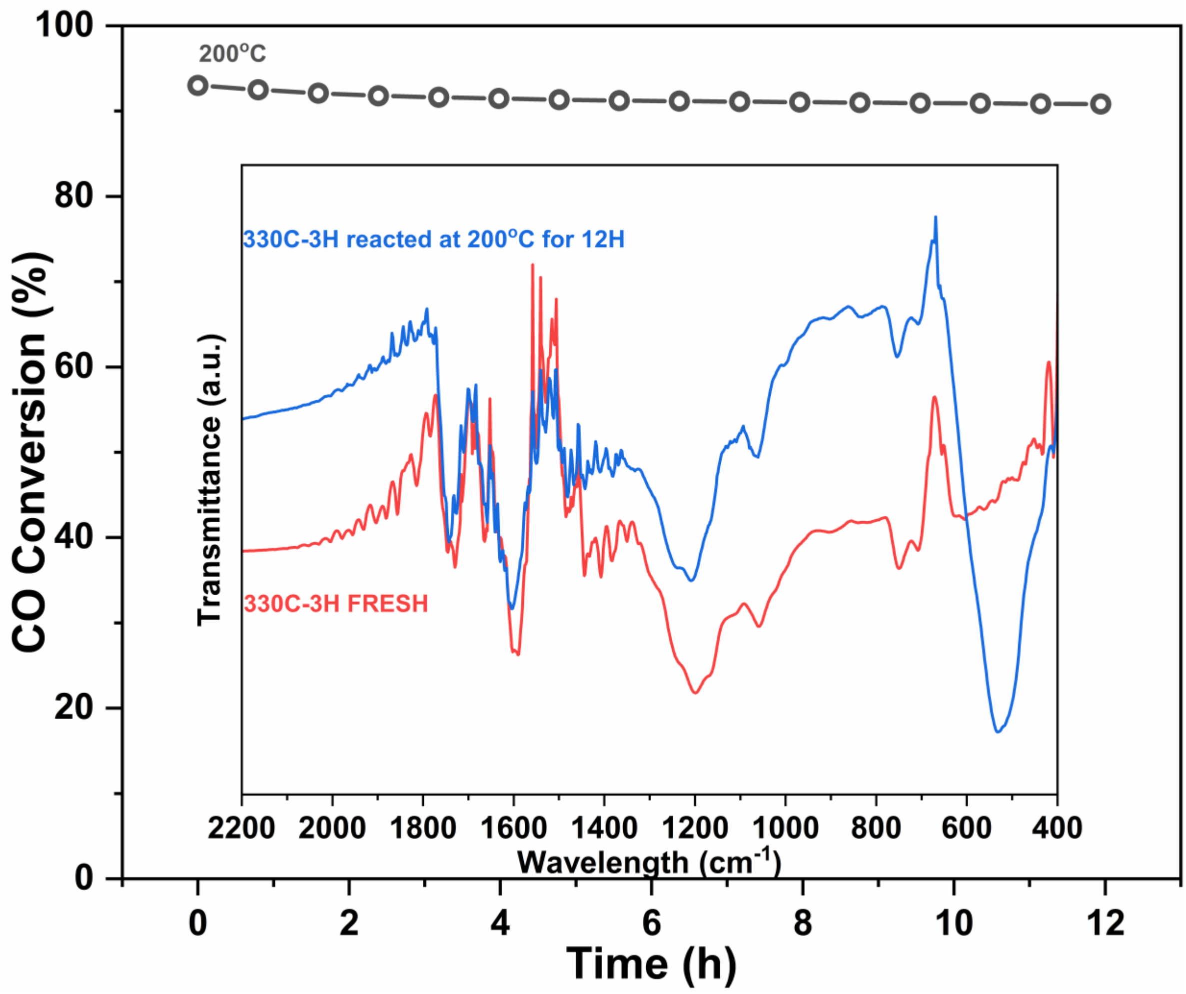

Figure 7-7 Long-term stability of CO oxidation over the CuNPs/GO catalyst (330C-3H) under 200 °C. inset graph is the FTIR spectra over the fresh catalyst and reacted catalyst after 12 h.

7.2.3 Reaction mechanism

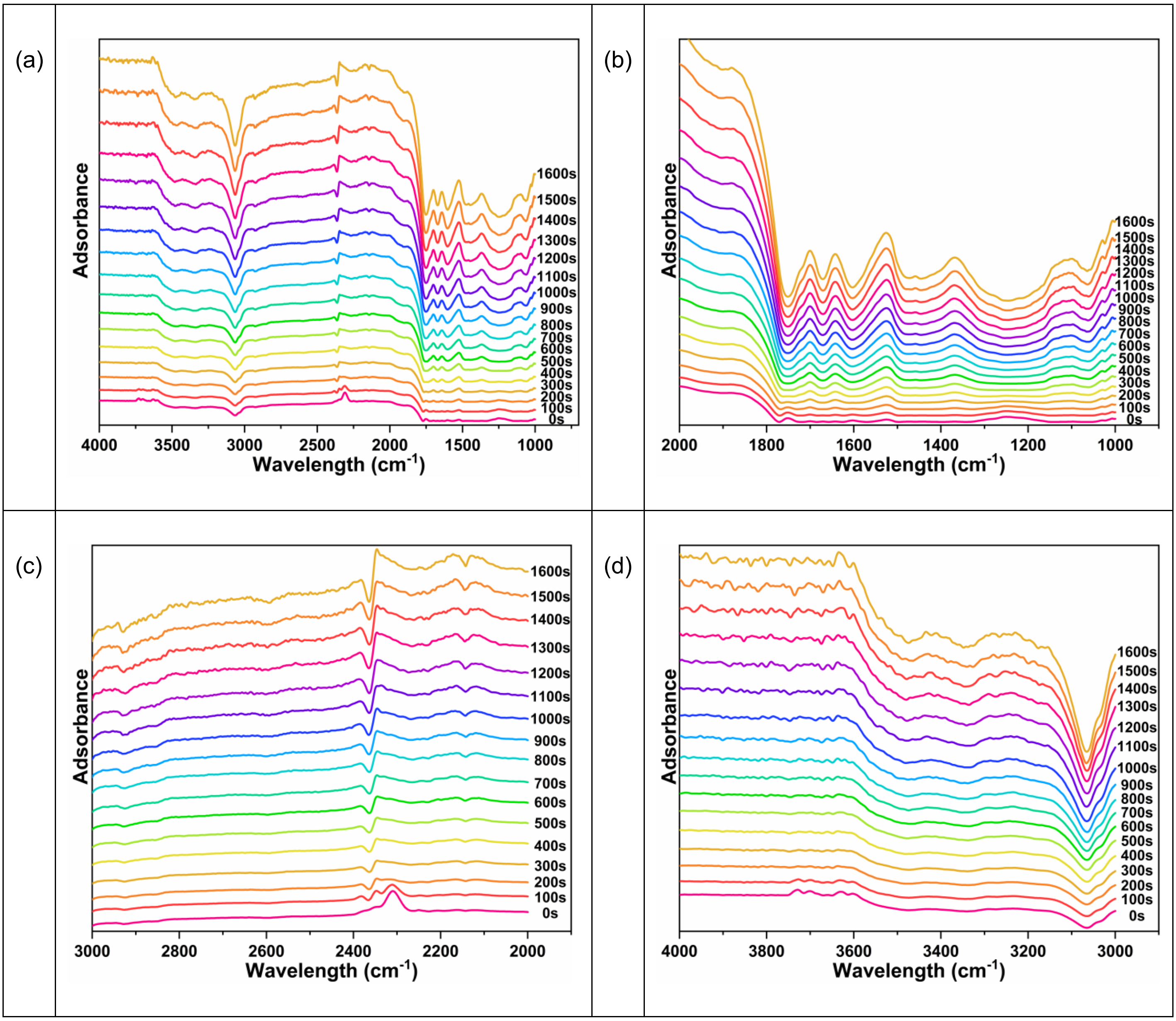

Figure 7-8 Probing surface intermediates on CuNP/GO (330C-3H) surfaces by In-situ DRIFTS under ambient pressure. Gas flow = 100 mL/min, CO 1%, O_2 20%, balance was Ar. Reaction temperature was 180 ^{o}C. a, the whole range of in situ DRIFTS (1000 - 4000 cm^{-1}). b, the details of the wavenumber region above 2000 cm^{-1}. c, the details of the wavenumber region between 2000-3000 cm^{-1}. d, the details of the wavenumber region above 3000 cm^{-1}.

DRIFT-Time measurement was obtained on CuNP/GO catalyst (330C-3H) under oxygen-containing CO catalytic oxidation (Figure 7-8) for 15 min. The original CuNP/GO catalyst (330C-3H) was pre-treated at 180 ^oC under Ar environment for 30min, and then the mixture of 1% CO, 20% O_2, and balanced Ar was injected into reaction chamber at 180 °C. These spectra owned several common features in the characteristic band of CO adsorption, oxidation, and CO_2 generation. Additional bands range between 2000 and 1000 cm^{-1}, were attributed to bicarbonate, carboxylate, and carbonate species. Early in the reaction, the CO and O_2 adsorption took place. The formation of CO_2 occurred initially, and signals of formats can be detected. Oxygen would be adsorbed much more strongly than CO on copper [365], and therefore, CO adsorption would not be a potential competitor and can be decreased on these Cu surfaces, where O_2 would prefer chemisorption bonding to these metallic Cu as the initial stage of reaction. The first adsorbed CO would be oxidized into CO_2 with the aid of lattice oxygen ions. Strongly bound carbonates appeared from the beginning and part of CO_2 would be bound with surface hydroxyl to from bicarbonates. The features assigned to CO_3^{2-} initially increased and HCO_3^- began to decrease in intensity, as time progresses. The obvious evidence of CO_3^{2-} species was assigned to the bands at 1526, 1368, and 1005 cm^{-1}. Also, the presence of HCO_3 was ascribed to 3606 cm^{-1} (vs(O-H), Figure 7-7(d)), 1701 cm^{-1} (vs(C=O)), 1602 cm^{-1} (vs(C-O)), 1220 cm^{-1} (C-O-H bending), and 1030 cm^{-1} (vs(O-C-O)) indicate that the surface of CuNP/GO catalyst (330C-3H) is partially hydroxylated. Collectively, these bands give an intuitive revelation of the interaction among CO, O_2, and CO_2 on CuNP/GO catalyst (330C-3H). For corresponding vibrations of the formate (HCO_2^-), related band of v(C-H) was positioned at 2864 cm^{-1} and vas of the formate was at 1595 cm^{-1} appeared. Besides, the decrease of surface hydroxyl groups (3000-4000 cm^{-1}) can be detected at 3065, 3475, 3340, and 3746 cm^{-1}, which was related to the observations of the CO adsorption/carbonate formation.

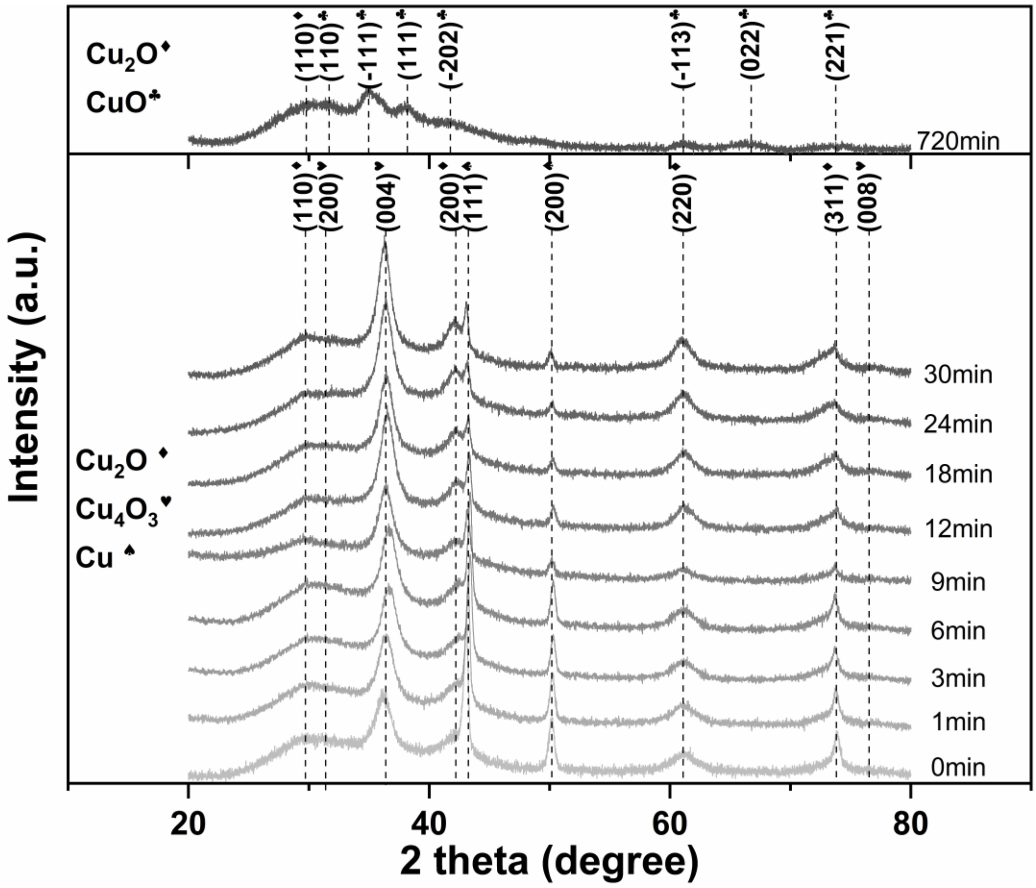

Figure 7-9 XRD pattern of In-situ spent catalyst CuNP/GO (330C-3H). Gas flow = 40 mL/min, CO 1%, O_2 20%, balance was Ar. Reaction temperature was 180 °C. The XRD patterns of Cu_3O_4, CuO, Cu_2O and Cu were matched up with PDF 49-1830, PDF 80-1268, PDF 05-0667 and PDF 04-0836.

XRD patterns in Figure 7-1 showed the presence of only primary metallic Cu with a small detectable amount of Cu_2O and CuO could be observed, besides, the XRD patterns of In-situ spent catalyst were characterized and shown in Figure 7-9. The catalyst exhibited the beginning of reaction produced the Cu_4O_3 and Cu_2O, where Cu_4O_3 (004) and Cu_2O (110) were attributed to the peak of 30.698° and 29.554°. As the time progressed, the intensity of Cu peak (43.297° and 50.433°) was falling, caused by O_2 environment and converted into Cu_3O_4 and Cu_2O. After 720 min, the catalyst was oxidized into CuO with little Cu_2O, which was corresponding to the peak (35.565°, CuO(-111)) and (29.554°, Cu_2O(110)). Consequently, one model of this system in the early reaction would suggest that the surface of these particles should be mainly in the form of Cu_3O_4, allowing CO adsorbed on exposed Cu(I) or Cu(II) sites. That is, O_2 would initially interact with metallic Cu surface to generate Cu_2O and Cu_3O_4 and then the adsorption of a CO molecule could follow the possible sequential reaction into CO_2 on an oxide surface (Cu(II) or Cu(I)). According to the In-situ DRIFT of Figure 8-7(c), It should be remarked that the band at 2119 and 2166 cm^{-1} (C-O stretch) increased with time going on, which is the evidence of CO adsorbed on Cu(I) (Cu^+-CO) and Cu(II) (Cu^{2+}-CO), respectively [366-368]. Meanwhile, asymmetric absorption peaks at 0 second appeared at 2320, 2351 and 2380 cm^{-1}, which is attributed to CO_2. After this peak almost saturated, there were ascended symmetric absorption peaks at 2345 cm^{-1} and 2383 cm^{-1}. Due to the CO_2 formation, vibration modes of the main species (carbonates) were observed in analogy to the formation of bridged carbonate when CO_2 adsorbed on the catalyst surface. Combined with the above-mentioned formate signals, the combination vibration of vas(CO_2 + δ(CH)) and vs(CO_2) + δ(CH)) was observed at 2942 and 2724 cm^{-1} in Figure 7-8(c). Thus, the observation of formate species was accordingly assigned to a bidentate or bridged species [369, 370].

7.4 Summary

a) The results of characterization confirmed that the Cu nanoparticles had a high crystalline and high dispersion on GO sheet. Obviously, the CuNP/GO catalyst (330C-3H) performed the highest activity for CO catalytic oxidation (T_{93} = 180 °C, T_{50} = 124 °C, E_a= 57.17 kJ/mol) with a long-term permanence of the CuNP/GO catalyst (330C-3H).

b) The DRIFT-time spectra and spent catalyst XRD pattern suggested the presence of surface Cu(I) or Cu(II) from Cu_4O_3 is the main active surface to drive the reaction to proceed.

c) About the CO oxidation, the formation of formate intermediates was observed through DRIFT test. The mechanism of CO chemisorption possibly proceeded via an insertion of the CO molecule onto a Cu(I) or Cu(II) surface bounded with O atom, and the intermediate was formed as the carbonate (CO_3^{2-}). As oxygen continuously adsorbed on the catalyst surface, the metallic Cu phase of catalytic surface would be, firstly, transformed into Cu_4O_3 and Cu_2O, and then was completely oxidized into CuO.

d) Taken together, the presence of Cu_4O_3 was beneficial for promoting the oxidation of CO, but Cu_4O_3 with prolonged exposure to O_2 environment, would be oxidized into CuO, which is the main caused for decreasing the CO oxidation conversion. Additional research would pay more attention to the stability of Cu_4O_3 phase.

Chapter 8 Conclusions and recommendations for future work

8.1 Conclusions

The thesis has discussed the MOFs preparation, MOFs modification and its applications in CO_2 capture and CO catalytic oxidation. It has explained the effect of MOFs synthesis condition and activation process on textural properties, morphology and size of MOFs crystals. The two different post-synthetic modification were attempted and produced different new functional material. The corresponding applications were further performed, and the insight of mechanism was revealed with the aid of In-situ techniques and simulation methods. Thus, the structure-function relationship between selected gas molecules (CO_2, CO, or O_2) and active sites (original HKUST-1, MoS_2/HKUST-1 hybrid or CuNP/GO) were verified and clearly clarified.

For the first contribution of this thesis, the optimized solvothermal approach developed in this research is a cheap and efficient method for the synthesis of nanoscale HKUST-1 MOFs with a BET surface area of 1542.4 m^2/g. The activation methods for HKUST-1 MOFs shows two different functions, i.e., the improvement of the specific surface area and the increased micropore volume and smaller mesopore size. Besides, the HKUST-1 prepared in this study showed a high CO_2 adsorption capacity with an uptake around 11% wt. (2.5mmol/g) at 27 ^{o}C and 1 bar.

For the second contribution of this thesis, the mechanisms of the growth of HKUST-1 and MoS_2/HKUST-1 composites were revealed via DFT modelling. It is found that the growth of the MoS_2/HKUST-1 composites of core-shell structure follows six steps. It is shown that MoS_2 not only is an integral part of the composites but also impels controllability in the size and crystallinity of the MOF crystals through the interactions between surface sulphur atoms and metal centres. The MoS_2/HKUST-1 composites exhibit a high efficiency for CO_2 capture and improve adsorption efficiency by 13% compared with HKUST-1. The enhanced CO_2 adsorption is attributed to the presence of a high specific surface area together with the strong electrostatic force induced by MoS_2 quantum dots.

For the third contribution of this thesis, the current work found the entire structure began graphitization at 330 ^{o}C due to the presence of defects in frameworks. The GO was gradually layered, and the copper particles progressively begin to be an aggregate into a metal cluster from size of 10 nm to size of 70 nm. Meanwhile, the formation of CO_2, CO, etc. is accompanied with. At 430 ^{o}C, MOFs structure would finally become Cu nanoparticle embedded with GO. Supposedly, this preferential growth is a result of defective structure in HKUST-1. The unsaturated Cu site or incomplete protonation of the carboxylic group would accelerate the decomposition process. Besides, the research of annealing under inert condition is a good reference and technical guidance to rapidly prepare a functional CuNP/GO.

For the fourth contribution of this thesis, the optimal CuNP/GO catalysts were conducted to CO catalytic oxidation. Obviously, the CuNP/GO catalyst (330C-3H) performed the highest activity for CO catalytic oxidation (T_{93} = 180 °C, T_{50} = 124 °C, Ea = 57.17 kJ/mol) with at least 12h long-term permanence of the CuNP/GO catalyst (330C-3H). The DRIFT-time spectra and spent catalyst XRD pattern suggested the presence of surface Cu(I) or Cu(II) from Cu_4O_3 is a fundamental factor of an active surface to drive reaction to proceed in a forward direction. The In-situ technique explains the mechanism of CO chemisorption possibly proceeds via an insertion of the CO molecule onto a Cu(I) or Cu(II) surface bounded with O atom, following formation of a carbonate (CO_3^{2-}). Despite that, the catalytic effect of the sample in the long-term oxygen exposure is lowered to 89% after 12 hours. Therefore, the long-term existence of Cu_4O_3 is essential for efficiently catalytic oxidation of CO. Further research would pay more attention to the stability of Cu_4O_3 existence.

Generally, suitably tuning the textural properties, introducing bi-functionalities, transforming original phase of MOFs during pre/post synthesis can significantly promote their adsorption capacity and activity for their intentional application.

8.2 Recommendations for future work

For the future work, a few aspects need to be figured out and developed further to serve MOFs for its potential adsorption and catalysis application. For this issue, the detailed recommendation has been provided as followed,

i) Further study on the CO_2 adsorption test of adsorption-desorption

performance and elevated pressure/temperature.

Currently, the research of CO2 adsorption test was conducted at the ambient temperature and pressure, which is similar to the condition of outlet of exhaust gas. For further storage and recovery of adsorbents, it is suggested to expand previous results to focus the other more practical issues, like the adsorption-desorption test and storage under elevated pressure/temperature.

ii) Further study on the new bi-metal organic frameworks against complex condition.

Currently, the metal precursor only attempts Cu ions. For further optimization of the structure and properties, the introduction of a second metal into the MOFs (i.e. bimetallic MOFs) has been researched lately [371]. The incorporation of a second metal prominently alters the intrinsic properties of the MOFs. Especially, the obtained bimetallic MOF-74 by adding various extra metal ions, possessed very different gas adsorption and catalytic activity compared with the monometallic MOF-74 [372-374]. For the other modification method, bimetallic MOFs can act as sacrificial templates to make hybrid nano-materials, which is widely used for catalysts, and energy storage and conversion applications. Huang et al. prepared porous $ZnO/ZnFe_2O_4/C$ hybrid by sacrificing bimetallic MOF-5 incorporated with Fe ions. The resulting material exhibits excellent lithium-storage performance [375].

iii) Further investigation of other 2D quantum material additives in the MOFs pre-synthesis process to broaden the application of bi-functional MOFs.

Quantum dots (QD) materials own a narrow and symmetrical emission, broad absorption band [376, 377], high surface energy and nano size [378], have advantaged predominance, including high stability, dispersibility and chemical activity, and hence attract more attention than coarse particles [379]. Besides, the superiorities of MOFs have tunable and ordered crystalline porous structure, as well as, attachability of multi-coordination sites. The combination of QD and MOFs can therefore improve the inherent functionality of MOFs and bring about additional features not observed in MOFs. Previously, an electrochemical method by Bishnu et al. was employed to synthesize graphene quantum dots, where graphene QDs was encapsulated and stabilized in a ZIF-8 network [380].

iv) Further exploring the transformation of CuNP/GO under oxidation conditions and controlling the presence of the Cu_4O_3 phase at the interface of copper oxides and hence applying the optimized CuNP/GO into CO catalytic oxidation.

Due to the difficulty in stabilizing both the Cu(II) and Cu(I) atom simultaneously via the conventional approaches, it is difficult for the pure phase of Cu_4O_3 to exist in the form of bulk or particle [381, 382]. Assuming that the Cu_4O_3 phase could achieve controllability, it would be a great chance to explore its possible catalytic activity and other applications.

Chapter 9 Appendix

Synthesis of MoS_2/HKUST-1 core-shell composite and its CO_2 capture via Theoretical and experimental study

9.1 Computational results

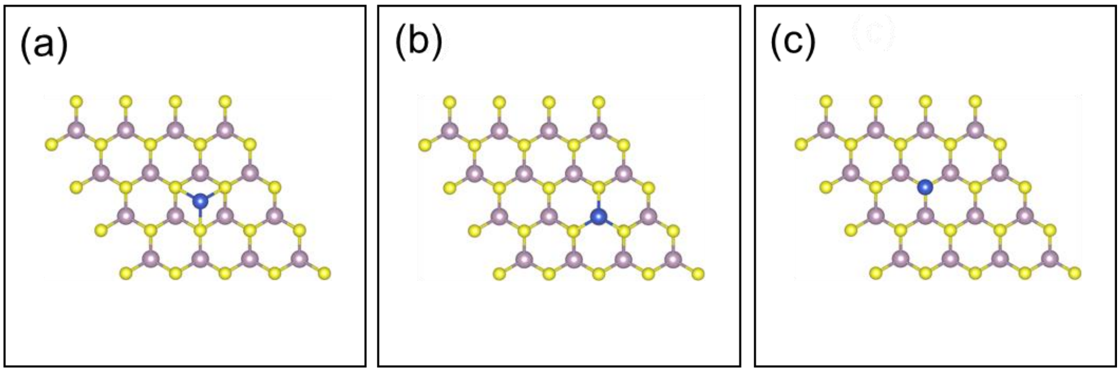

Figure 9S-1 Adsorption configurations of single Cu atom on MoS_2 nanosheet. Top views of the possible configurations for (a)Hollow site (H); (b) Top of Mo atom site(T_{Mo}); (c) Top of S atom site(T_S). The violet and yellow balls represent Mo and S atoms, whereas the blue balls represent Cu atoms.

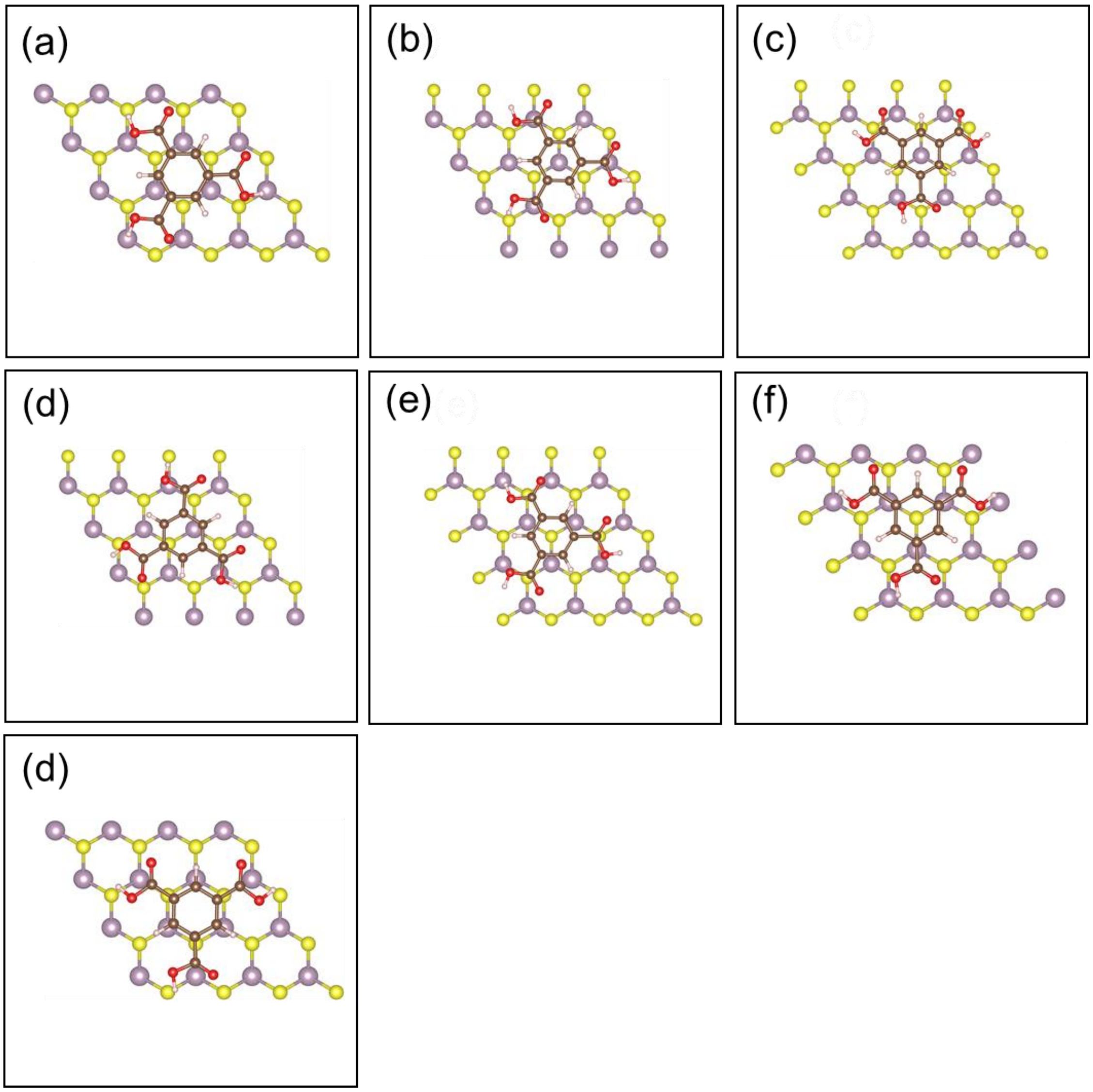

Figure 9S-3 Adsorption configurations of TMA on MoS_2 nanosheet. Top views of the possible configurations for (a) cross; (b) Mo-centre cross (center$_{Mo}$ cross); (c) Mo-centre (center$_{Mo}$); (d) Mo-S bridge (bridge); (e) S-centre cross (center$_S$ cross); (f) S-centre (center$_S$); (j) top. The violet and yellow balls represent Mo and S atoms, whereas the pink, red balls represent H, O atoms, respectively.

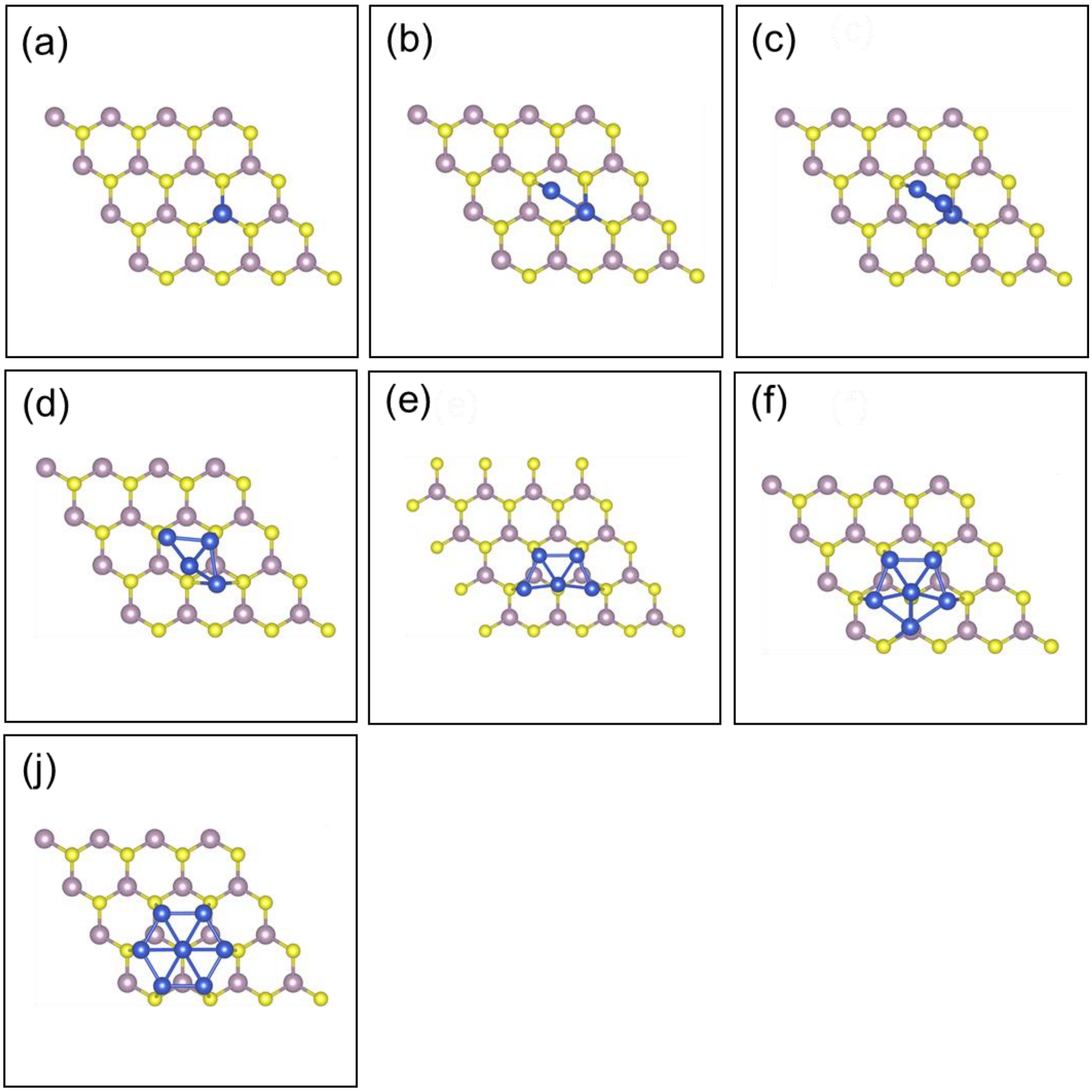

Figure 9S-4 Adsorption configurations of Cu$_n$ cluster on MoS$_2$ nanosheet. Top views of the most favourable configurations for (a) Cu; (b) Cu$_2$; (c) Cu$_3$; (d) Cu$_4$; (e) Cu$_5$; (f) Cu$_6$; (j) Cu$_7$. The violet and yellow balls represent Mo and S atoms, whereas the blue balls represent Cu atoms.

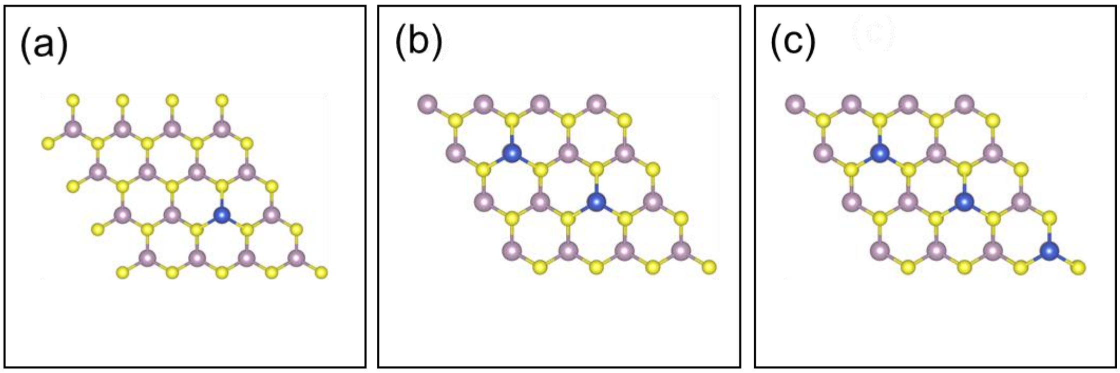

Figure 9S-5 Adsorption configurations of single Cu atoms on MoS_2 nanosheet. Top views of the possible configurations for (a) (MoS_2)-Cu; (b) (MoS_2)-Cu,Cu; (c) (MoS_2)-Cu,Cu,Cu. The violet and yellow balls represent Mo and S atoms, whereas the blue balls represent Cu atoms.

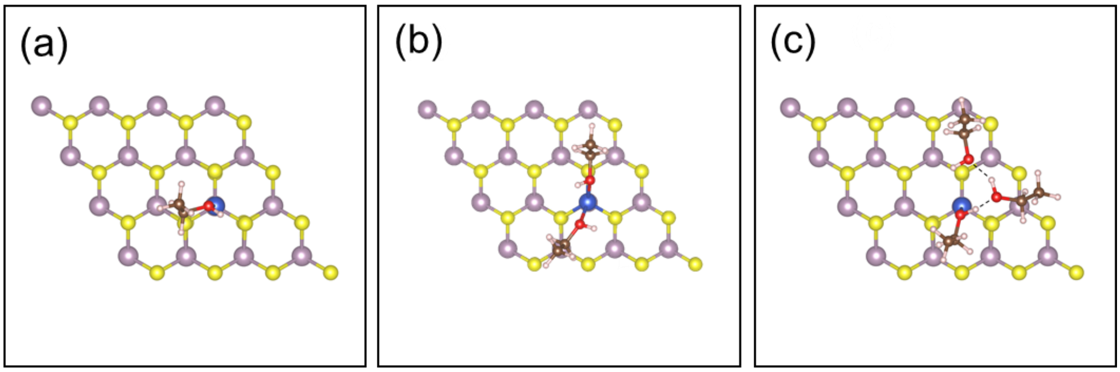

Figure 9S-6 Adsorption configurations of nEtOH on (MoS_2)-Cu system. Top views of the possible configurations for (a) EtOH; (b) 2EtOH; (c) 3EtOH. The violet and yellow balls represent Mo and S atoms, whereas the pink, red, brown, blue balls represent H, O, C, Cu atoms, respectively.

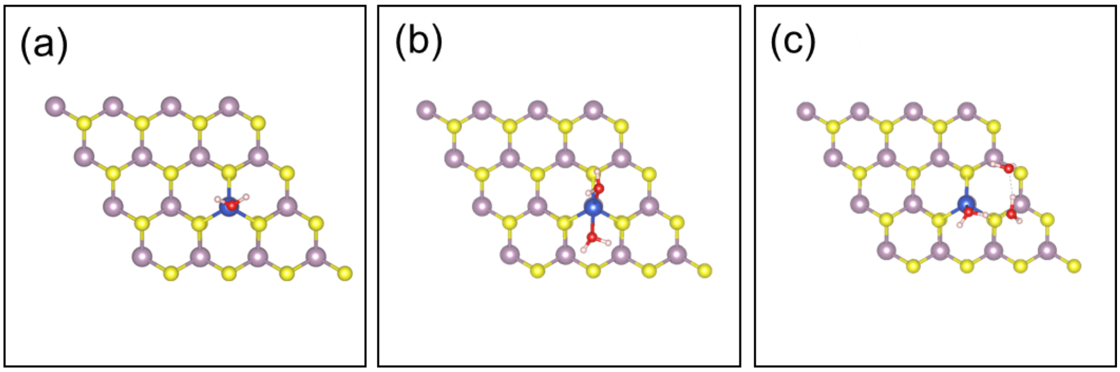

Figure 9S-7 Adsorption configurations of nH_2O on (MoS_2)-Cu system. Top views of the possible configurations for (a) H_2O; (b) 2H_2O; (c) 3H_2O. The violet and yellow balls represent Mo and S atoms, whereas the pink, red, blue balls represent H, O, Cu atoms, respectively.

9.2 Experimental results

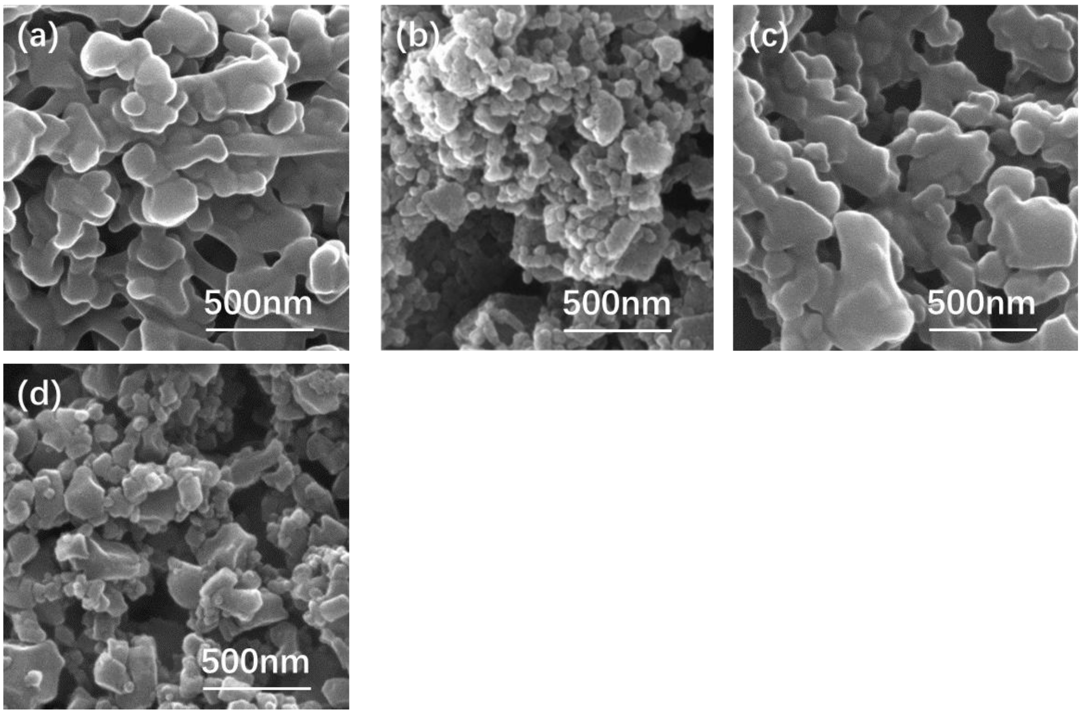

Figure 9S-8 (a) SEM images of original/modified HKUST-1. a, MH-0. b, MH-1. c, MH-2. d, MH-3.

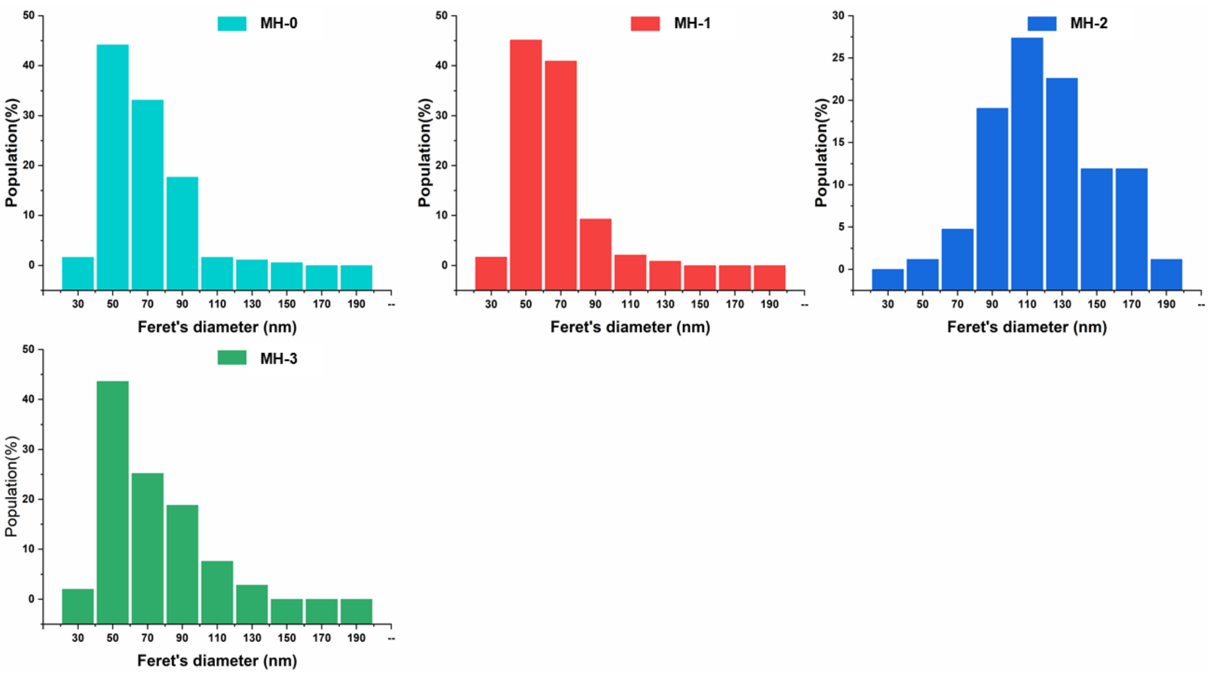

Figure 9S-8 (b) Particle size distribution (based on Feret’s diameter) of original/modified HKUST-1 (results obtained from ImageJ).

Morphologies and particle size of the original/modified HKUST-1 composites were determined by using a Scanning Electron Microscope (SEM, FEI Nova NanoSEM 450)

9.2.1 N_2 Isotherm

In Figure 9S-9, it is evident that N_2 adsorption rate increases rapidly in the relative pressure interval ($0.0 < P/P_0 < 0.1$) and the N_2 adsorption of HKUST-1 and MoS_2/HKUST-1 composite is the Type I isotherm [383, 384]. These samples are of microporous structure (< 2 nm) [385]. It can be seen in Figure 9S-8 that there are the hysteresis loops occurring at a higher relative pressure ($P/P_0 > 0.4$), which could be linked to the stacking combination of large particles [386] or the formation of defects [387] in HKUST-1 and MoS_2/HKUST-1 composite. As the particle distribution indicates in Figure 9S-8 (a) and (b), the particle distribution of all samples was within 100 nm, therefore, the occurrence of the hysteresis loop is unlikely linked to large particle accumulation but can be attributed to the formation of defects. Normally, hysteresis loops occurring at a higher relative pressure can be attributed to the cavitation phenomenon [388] that occurs when the pore size is less than 6 nm, which is the case for this study as the average pore size is around 6 nm as shown in Table 5-4.

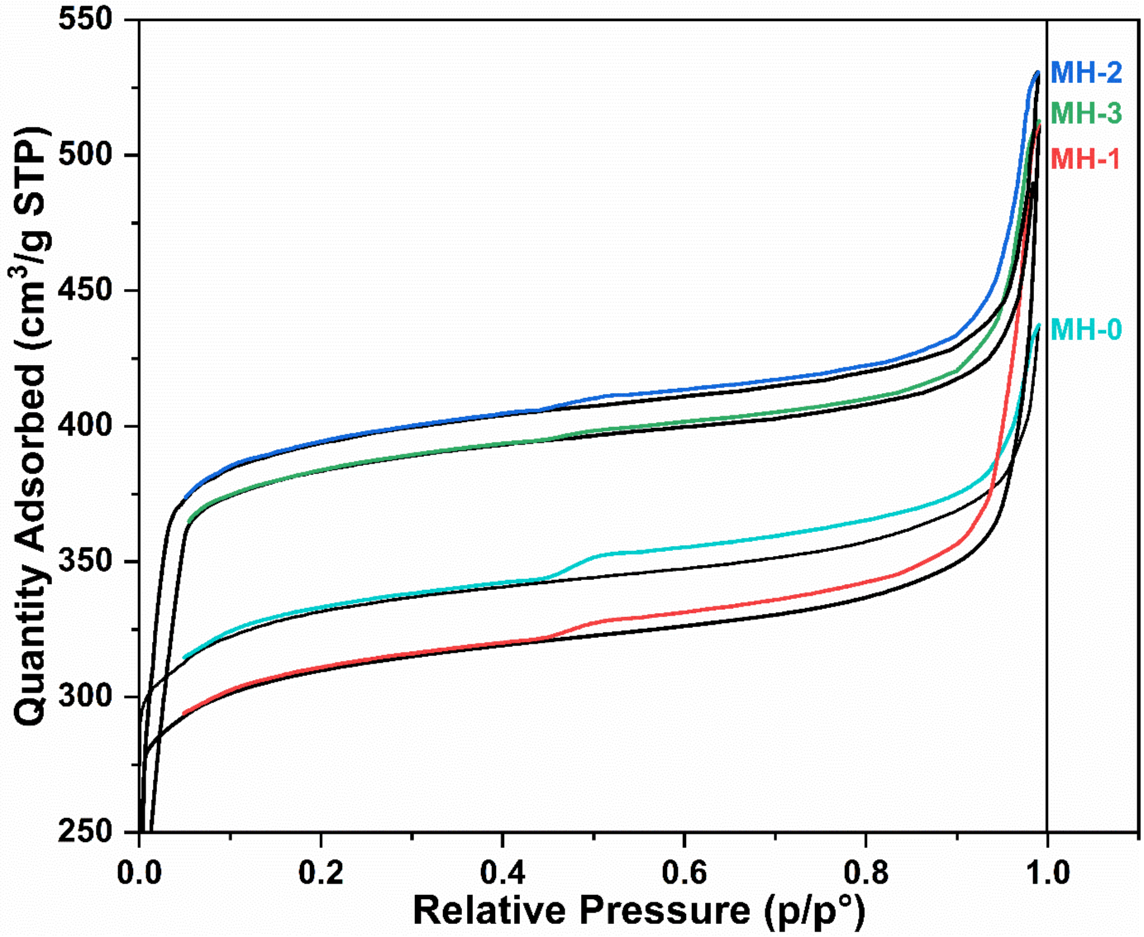

Figure 9S-9 N_2 isotherm of pristine HKUST-1 and MoS_2/HKUST-1 composite

9.2.2 Stability

9.2.2.1 Thermal stability

The thermal stability of HKUST-1 and MoS_2/HKUST-1 was examined using TGA as shown in Figure 9S-10(a). The HKUST-1 and MoS_2/HKUST-1 composites have shown a consecutive mass loss up to a temperature of 120 °C, which can be attributed to the desorption of physisorbed water and other gas, respectively. Between 120 and 180 °C, the mass loss is due to the release of combined crystal water. When the temperature is further raised to 320 °C, there is no significant weight loss, which confirms the outstanding thermal stability of the composites, as well as extremely low impurities trapped in these samples. It is also found that MH-X (X=1-3) has a smaller mass loss in the temperature range of 180-300 °C than original HKUST-1 (MH-0) (as illustrated by Table 9S-1), which elucidates that the proper addition of MoS_2 could improve the thermal stability of HKUST-1 structure. Moreover, the best thermal stability of MoS_2/HKUST-1 composite (MH-2) also demonstrates the highest crystallinity, which further confirms that MoS_2 quantum dots involved in the formation of chemical bonding of the HKUST-1. When the temperature was additionally raised to 300 °C and above HKUST-1 and MoS_2/HKUST-1 started to decompose and level off when temperature reached 475 °C. It is clear from Figure 8 that the mass-loss profile of MH-X is very much similar as that of MH-0, which suggests that the structure of HKUST-1 was not altered by the addition of MoS_2 quantum, but also the thermal stability of HKUST-1 has been improved. This is consistent with the prediction of calculation results on thermal stability of the hybrid.

Table 9S-1 The mass change of TGA curve in different temperature range

ID	ΔM (25-120^{o}C)	ΔM (180-300^{o}C)	ΔM (180-300^{o}C)	ΔM (300-420^{o}C)	ΔM (420-600^{o}C)	ΔM (25-600^{o}C)
MH-0	24.37%	5.90%	3.12%	25.35%	4.20%	62.94%
MH-1	26.17%	4.41%	2.72%	25.79%	4.01%	63.10%
MH-2	30.40%	3.98%	1.70%	23.78%	4.17%	64.03%
MH-3	27.96%	3.21%	2.22%	24.67%	4.03%	62.09%

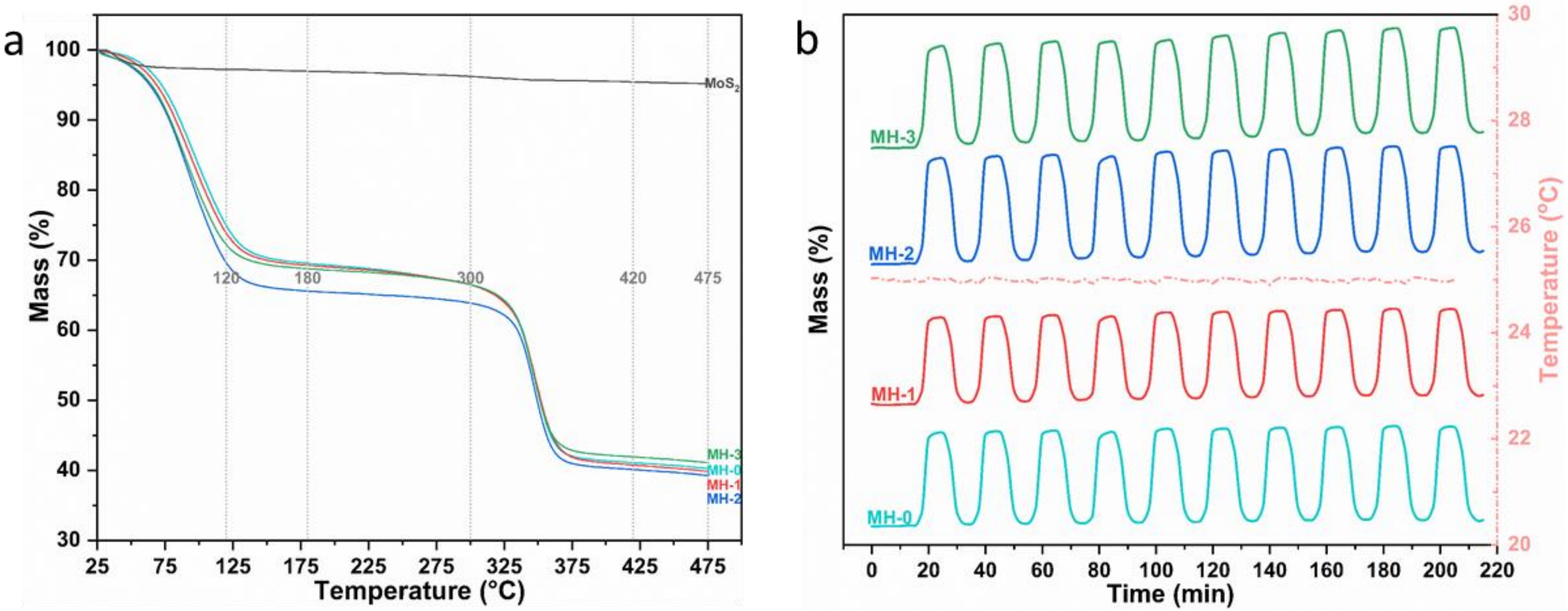

Figure 9S-10 (a) TGA of original & modified HKUST-1 under N_2 atmosphere and (b) Cyclic testing of the HKUST-1 and the MoS_2/HKUST-1 composites on CO_2 adsorption.

9.2.2.2 CO_2 regenerability

The CO_2 cyclic testing results of the HKUST-1 and the MoS_2/HKUST-1 hybrids are shown in Figure 9S-10(b). Clearly, the composites prepared in this study exhibit exceptional regenerability and recyclability properties in CO_2 multiple adsorption-desorption characteristics, which are critical attributes of solid sorbents. In the cycling experiments, the results illustrated that the desorption process finished rapidly by N_2 purging under a mild condition, and the adsorption capacity remains almost unchanged after ten adsorption/desorption cycles, which revealed the good stability of modified HKUST-1 adsorbents.

Reference

1. Bureau, P.R. Human Population: Lesson Plans. 2009 [May 25, 2019]; Available from: https://www.prb.org/humanpopulation.

2. Bongaarts, J., Human population growth and the demographic transition. Philosophical transactions of the Royal Society of London. Series B, Biological sciences, 2009. 364(1532): p. 2985-2990.

3. Knoema. "World GDP Ranking 2017 | GDP by country | Data and Charts. 2018 [May 25, 2019]; Available from: https://knoema.com/nwnfkne/world-gdp-ranking-2018-gdp-by-country-data-and-charts?origin=cn.knoema.com.

4. BP p.l.c., BP Energy Outlook: 2019 edition Demand and supply of fuels 2019; Available from: https://www.bp.com/en/global/corporate/energy-economics/energy-outlook/demand-by-fuel.html.

5. Khalid, T., Pre-service high school teachers' perceptions of three environmental phenomena. Environmental Education Research, 2010. 9(1): p. 35-50.

6. Reeve, P.J. and H.J. Fallowfield, Natural and surfactant modified zeolites: a review of their applications for water remediation with a focus on surfactant desorption and toxicity towards microorganisms. Journal of environmental management, 2018. 205: p. 253-261.

7. Zhang, Z., Z. Jiang, and W. Shangguan, Low-temperature catalysis for VOCs removal in technology and application: A state-of-the-art review. Catalysis Today, 2016. 264: p. 270-278.

8. Ferella, F., V. Innocenzi, and F. Maggiore, Oil refining spent catalysts: A review of possible recycling technologies. Resources, Conservation Recycling, 2016. 108: p. 10-20.

9. Yaghi, O.M., Crystalline metal-organic microporous materials. 1997, Google Patents.

10. Mueller, U., Schubert, M., Teich, F., Puetter, H., Schierle-Arndt, K., Pastre, J., Metal–organic frameworks—prospective industrial applications. Journal of Materials Chemistry, 2006. 16(7): p. 626-636.

11. Jhung, S.-H., Chang, J.-S., Hwang, Y.-K., Serre, C., Ferey, G., Preparation method of porous organic inorganic hybrid materials. 2010, Google Patents.

12. Son, W.-J., et al., Sonochemical synthesis of MOF-5. Chemical Communications, 2008(47): p. 6336-6338.

13. Stein, A., S.W. Keller, and T.E. Mallouk, Turning down the heat: design and mechanism in solid-state synthesis. Science, 1993. 259(5101): p. 1558.

14. Yaghi, O.M., O'Keeffe, M., Ockwig, N.-W., Chae, H.-K., Eddaoudi, M., Kim, J., Reticular synthesis and the design of new materials. Nature, 2003. 423: p. 705.

15. Kalmutzki, M.J., N. Hanikel, and O.M. Yaghi, Secondary building units as the turning point in the development of the reticular chemistry of MOFs. Science Advances, 2018. 4(10): p. eaat9180.

16. Na, K., Choi, K.-M., Yaghi, O.M., and Somorjai, G.A., Metal Nanocrystals embedded in single nanocrystals of MOFs give unusual selectivity as heterogeneous catalysts. Nano Letters, 2014. 14(10): p. 5979-5983.

17. Kuo, C.-H., Tang, Y., Chou, L.-Y., et al., Yolk–shell nanocrystal@ZIF-8 nanostructures for gas-phase heterogeneous catalysis with selectivity control. Journal of the American Chemical Society, 2012. 134(35): p. 14345-14348.

18. Xu, X., Cao, R., Jeong, S., and Cho, J., Spindle-like mesoporous α-Fe_2O_3 anode material prepared from MOF template for high-rate lithium batteries. Nano Letters, 2012. 12(9): p. 4988-4991.

19. Uemura, T., N. Yanai, and S. Kitagawa, Polymerization reactions in porous coordination polymers. Chemical Society Reviews, 2009. 38(5): p. 1228-1236.

20. O'Keeffe, M., Design of MOFs and intellectual content in reticular chemistry: a personal view. Chemical Society Reviews, 2009. 38(5): p. 1215-1217.

21. Kinoshita, Y., Ikuo, M., Taiichi, H., and Yoshihiko, S., The crystal structure of Bis(adiponitrilo)copper(I) Nitrate. Bulletin of the Chemical Society of Japan, 1959. 32(11): p. 1221-1226.

22. Abrahams, B.F., Hskin, B.F., Michail, D.M., and Robson, R., Assembly of porphyrin building blocks into network structures with large channels. Nature, 1994. 369(6483): p. 727-729.

23. Hoskins, B.F. and R. Robson, Design and construction of a new class of scaffolding-like materials comprising infinite polymeric frameworks of 3D-linked molecular rods. A reappraisal of the zinc cyanide and cadmium cyanide structures and the synthesis and structure of the diamond-related frameworks $[N(CH_3)_4][Cu^IZn^{II}(CN)_4]$ and Cu^I[4,4',4'',4'''-tetracyanotetraphenylmethane] $BF_4.xC_6H_5NO_2$. Journal of the American Chemical Society, 1990. 112(4): p. 1546-1554.

24. Yaghi, O.M. and H. Li, Hydrothermal synthesis of a metal-organic framework containing large rectangular channels. Journal of the American Chemical Society, 1995. 117(41): p. 10401-10402.

25. Subramanian, S. and M.J. Zaworotko, Porous solids by design: [Zn(4,4′-bpy)2(SiF6)]n·xDMF, a single framework octahedral coordination polymer with large square channels. Angewandte Chemie International Edition in English, 1995. 34(19): p. 2127-2129.

26. Li, H., Eddaoudi, M., Groy, T.L., and Yaghi, O.M., Establishing microporosity in open metal-organic frameworks: gas sorption isotherms for Zn(BDC) (BDC = 1,4-

Benzenedicarboxylate). Journal of the American Chemical Society, 1998. 120(33): p. 8571-8572.

27. Jiang, J., Y. Zhao, and O.M. Yaghi, Covalent Chemistry beyond Molecules. Journal of the American Chemical Society, 2016. 138(10): p. 3255-3265.

28. Ahmed, I. and S.H. Jhung, Composites of metal-organic frameworks: preparation and application in adsorption. Materials Today, 2014. 17(3): p. 136-146.

29. Wee, L.H., Meledina, M., Turner, S., et al., 1D-2D-3D Transformation synthesis of hierarchical metal-organic framework adsorbent for multicomponent alkane separation. Journal of the American Chemical Society, 2017. 139(2): p. 819-828.

30. Rowsell, J.L.C. and O.M. Yaghi, Metal-organic frameworks: a new class of porous materials. Microporous and Mesoporous Materials, 2004. 73(1): p. 3-14.

31. Rangnekar, N., Mittal, N., Elyassi, B., et al., Zeolite membranes - a review and comparison with MOFs. Chemical Society Reviews, 2015. 44(20): p. 7128-7154.

32. Kikhtyanin, O., D. Kubička, and J. Čejka, Toward understanding of the role of Lewis acidity in aldol condensation of acetone and furfural using MOF and zeolite catalysts. Catalysis Today, 2015. 243: p. 158-162.

33. De Toni, M., Jonchiere, R., Pullumbi, P., et al., How can a hydrophobic MOF be Water-Unstable? Insight into the hydration mechanism of IRMOFs. ChemPhysChem, 2012. 13(15): p. 3497-3503.

34. Park, K.S., Ni, Z., Cote, A.P., et al., Exceptional chemical and thermal stability of zeolitic imidazolate frameworks. Proceedings of the National Academy of Sciences, 2006. 103(27): p. 10186.

35. Eddaoudi, M., Sava, D.F., Eubank, J.F., et al., Zeolite-like metal-organic frameworks (ZMOFs): design, synthesis, and properties. Chemical Society Reviews, 2015. 44(1): p. 228-249.

36. Ding, S.Y. and W. Wang, Covalent organic frameworks (COFs): from design to applications. Chemical Society Reviews, 2013. 42(2): p. 548-568.

37. Kaur, P., J.T. Hupp, and S.T. Nguyen, Porous organic polymers in catalysis: opportunities and challenges. ACS Catalysis, 2011. 1(7): p. 819-835.

38. Getman, R.B., Bae, U.S., Wilmer, C.E., et al., Review and analysis of molecular simulations of methane, hydrogen, and acetylene storage in metal-organic frameworks. Chemical Reviews, 2012. 112(2): p. 703-723.

39. Vitillo, J.G., B. Smit, and L. Gagliardi, Introduction: carbon capture and separation. chemical reviews, 2017. 117(14): p. 9521-9523.

40. Khan, N.A., Z. Hasan, and S.H. Jhung, Adsorptive removal of hazardous materials using metal-organic frameworks (MOFs): A review. Journal of Hazardous Materials, 2013. 244-245: p. 444-456.

41. Lee, J., Farha, O.K., Roberts, J., et al., Metal-organic framework materials as catalysts. Chemical Society Reviews, 2009. 38(5): p. 1450-1459.

42. Chui, S.S.Y., Lo, S.M.F., Carmant, J.P., et al., A chemically functionalizable nanoporous material $[Cu_3(TMA)_2(H_2O)_3]_n$. Science, 1999. 283(5405): p. 1148.

43. Hendon, C.H. and A. Walsh, Chemical principles underpinning the performance of the metal-organic framework HKUST-1. Chemical Science, 2015. 6(7): p. 3674-3683.

44. Yaghi, O.M., Crystalline metal-organic microporous materials. 1997, Google Patents.

45. Yaghi, O.M., G. Li, and H. Li, Selective binding and removal of guests in a microporous metal-organic framework. Nature, 1995. 378(6558): p. 703-706.

46. Sun, Y. and H. C. Zhou, Recent progress in the synthesis of metal-organic frameworks. Science and Technology of Advanced Materials, 2015. 16(5): p. 054202.

47. Mueller U, P.H., Hesse M and Wessel H, Method for electrochemical production of a crystalline porous metal organic skeleton material. 2005.

48. Sabouni, R., H. Kazemian, and S. Rohani, Microwave Synthesis of the CPM-5 Metal Organic Framework. Chemical Engineering & Technology, 2012. 35(6): p. 1085-1092.

49. Son, W.J., Kim, J., Kim, J., and Ahn, W.S., Sonochemical synthesis of MOF-5. Chem Commun (Camb), 2008(47): p. 6336-8.

50. Pichon, A., A. Lazuen-Garay, and S.L. James, Solvent-free synthesis of a microporous metal-organic framework. CrystEngComm, 2006. 8(3): p. 211-214.

51. Liu, J., Culp, J.T., Natesakhawat, S., and et al., Experimental and theoretical studies of gas adsorption in $Cu_3(BTC)_2$: an effective activation procedure. The Journal of Physical Chemistry C, 2007. 111(26): p. 9305-9313.

52. Liu, J., Wang, U., Benin, A.I. et al., CO_2/H_2O adsorption equilibrium and rates on metal-organic frameworks: HKUST-1 and Ni/DOBDC. Langmuir, 2010. 26(17): p. 14301-14307.

53. Rowsell, J.L.C. and O.M. Yaghi, Effects of functionalization, catenation, and variation of the metal oxide and organic linking units on the low-pressure hydrogen adsorption properties of metal-organic frameworks. Journal of the American Chemical Society, 2006. 128(4): p. 1304-1315.

54. Sun, L.-B., Li, J.T., Park, J., et al., Cooperative template-directed assembly of mesoporous metal-organic frameworks. Journal of the American Chemical Society, 2012. 134(1): p. 126-129.

55. Chowdhury, P., Bikkina, C., Meister, D., et al., Comparison of adsorption isotherms on Cu-BTC metal organic frameworks synthesized from different routes. Microporous and Mesoporous Materials, 2009. 117(1): p. 406-413.

56. Hartmann, M., Kunz, S., Himsl, D., et al., Adsorptive Separation of Isobutene and Isobutane on $Cu_3(BTC)_2$. Langmuir, 2008. 24(16): p. 8634-8642.

57. Jiang, D., Mallt, T., Krumeich, F., et al., Polymer-assisted synthesis of nanocrystalline copper-based metal-organic framework for amine oxidation. Catalysis Communications, 2011. 12(7): p. 602-605.

58. Schlichte, K., T. Kratzke, and S. Kaskel, Improved synthesis, thermal stability and catalytic properties of the metal-organic framework compound $Cu_3(BTC)_2$. Microporous and Mesoporous Materials, 2004. 73(1): p. 81-88.

59. Krawiec, P., Kramer, M., Sabo, M., et al., Improved hydrogen storage in the metal-organic framework $Cu_3(BTC)_2$. Advanced Engineering Materials, 2006. 8(4): p. 293-296.

60. Meek, S.T., J.A. Greathouse, and M.D. Allendorf, Metal-organic frameworks: a rapidly growing class of versatile nanoporous materials. Advanced Materials, 2011. 23(2): p. 249-267.

61. Seo, Y.K., Hundal, G., Jang, I.T., et al., Microwave synthesis of hybrid inorganic-organic materials including porous $Cu_3(BTC)_2$ from Cu(II)-trimesate mixture. Microporous and Mesoporous Materials, 2009. 119(1): p. 331-337.

62. Mu, X., Chen, Y., and Lester, E., et al., Optimized synthesis of nano-scale high quality HKUST-1 under mild conditions and its application in CO_2 capture. Microporous and Mesoporous Materials, 2018. 270: p. 249-257.

63. Xu, Y.P., Tian, Z.J., Wang, S.J., et al., Microwave-Enhanced Ionothermal Synthesis of Aluminophosphate Molecular Sieves. Angewandte Chemie International Edition, 2006. 45(24): p. 3965-3970.

64. Yoon, J.W., Jnag, I.T., Lee, K.Y., et al., Adsorptive separation of propylene and propane on a porous metal-organic framework, copper trimesate. Bulletin of the Korean Chemical Society, 2010. 31(1): p. 220-223.

65. Diring, S., Furukawa, S., Takashima, Y., et al., Controlled Multiscale Synthesis of Porous Coordination Polymer in Nano/Micro Regimes. Chemistry of Materials, 2010. 22(16): p. 4531-4538.

66. Blanita, G., Borodi, G., Lazar, M.D., et al., Microwave assisted non-solvothermal synthesis of metal-organic frameworks. RSC Advances, 2016. 6(31): p. 25967-25974.

67. Suslick, K.S., Choe, S.B., Cichowlas, A.A., et al., Sonochemical synthesis of amorphous iron. Nature, 1991. 353(6343): p. 414-416.

68. Gedanken, A., Using sonochemistry for the fabrication of nanomaterials. Ultrasonics Sonochemistry, 2004. 11(2): p. 47-55.

69. Suslick, K.S., D.A. Hammerton, and R.E. Cline, Sonochemical hot spot. Journal of the American Chemical Society, 1986. 108(18): p. 5641-5642.

70. Li, Z.Q., Qiu, L.G., Xu, T., et al., Ultrasonic synthesis of the microporous metal-organic framework $Cu_3(BTC)_2$ at ambient temperature and pressure: an efficient and environmentally friendly method. Materials Letters, 2009. 63(1): p. 78-80.

71. Kim, S.H., Yang, S.T., Kim, J., et al., Sonochemical synthesis of $Cu_3(BTC)_2$ in a deep eutectic mixture of choline chloride/dimethylurea. Bulletin of the Korean Chemical Society, 2011. 32(8): p. 2783-2786.

72. Yuan, W., Garay, A.L., Pichon, A., et al., Study of the mechanochemical formation and resulting properties of an archetypal MOF: $Cu_3(BTC)_2$ (BTC = 1,3,5-benzenetricarboxylate). CrystEngComm, 2010. 12(12): p. 4063-4065.

73. Klimakow, M., Klobes, P., Thunemann, A.F., et al., Mechanochemical synthesis of metal-organic frameworks: a fast and facile approach toward quantitative yields and high specific surface areas. Chemistry of Materials, 2010. 22(18): p. 5216-5221.

74. Lien Nguyen, K., Friscic, T., Day, G.M., et al., Terahertz time-domain spectroscopy and the quantitative monitoring of mechanochemical cocrystal formation. Nature Materials, 2007. 6: p. 206.

75. Stolar, T., Batzdorf, L., Lukin, S., et al., In situ monitoring of the mechanosynthesis of the archetypal metal-organic framework HKUST-1: effect of liquid additives on the milling reactivity. Inorganic Chemistry, 2017. 56(11): p. 6599-6608.

76. Tanaka, K. and F. Toda, Solvent-free organic synthesis. Chemical Reviews, 2000. 100(3): p. 1025-1074.

77. Garay, A.L., A. Pichon, and S.L. James, Solvent-free synthesis of metal complexes. Chemical Society Reviews, 2007. 36(6): p. 846-855.

78. Zhang, Z. and M.J. Zaworotko, Template-directed synthesis of metal-organic materials. Chemical Society Reviews, 2014. 43(16): p. 5444-5455.

79. Zhang, B., Zhang, J., Liu, C., et al., Solvent determines the formation and properties of metal-organic frameworks. RSC Advances, 2015. 5(47): p. 37691-37696.

80. Lestari, W.W., Nugraha, R.E., Winarni, I.D., et al., Optimization on electrochemical synthesis of HKUST-1 as candidate catalytic material for Green diesel production. AIP Conference Proceedings. Vol. 1725, No. 1. AIP PUBLISHING, 2016.

81. Ameloot, R., Stappers, L., Feansaer, J., et al., Patterned Growth of Metal-Organic Framework Coatings by Electrochemical Synthesis. Chemistry of Materials, 2009. 21(13): p. 2580-2582.

82. Van Assche, T.R.C., Desmet, G., Ameloot, R., et al., Electrochemical synthesis of thin HKUST-1 layers on copper mesh. Microporous and Mesoporous Materials, 2012. 158: p. 209-213.

83. Gascon, J., S. Aguado, and F. Kapteijn, Manufacture of dense coatings of $Cu_3(BTC)_2$ (HKUST-1) on α-alumina. Microporous and Mesoporous Materials, 2008. 113(1): p. 132-138.

84. Van Assche, T.R.C., Campagnol, N., Muselle, T., et al., On controlling the anodic electrochemical film deposition of HKUST-1 metal-organic frameworks. Microporous and Mesoporous Materials, 2016. 224: p. 302-310.

85. Xu, X., Controllable synthesis of ultra-small metal-organic framework nanocrystals composed of copper(ii) carboxylates. Nanoscale, 2016. 8(37): p. 16725-16732.

86. Wang, X. G., Cheng, Q., Yu, U., et al., Controlled Nucleation and Controlled Growth for Size Predicable Synthesis of Nanoscale Metal-Organic Frameworks (MOFs): A General and Scalable Approach. Angewandte Chemie International Edition, 2018. 57(26): p. 7836-7840.

87. Wang, F., Guo, H., Chai, Y., et al., The controlled regulation of morphology and size of HKUST-1 by “coordination modulation method”. Microporous and Mesoporous Materials, 2013. 173: p. 181-188.

88. Safarifard, V. and A. Morsali, Applications of ultrasound to the synthesis of nanoscale metal-organic coordination polymers. Coordination Chemistry Reviews, 2015. 292: p. 1-14.

89. Xin, C., Zhan, H., Huang, X., et al., Effect of various alkaline agents on the size and morphology of nano-sized HKUST-1 for CO_2 adsorption. RSC Advances, 2015. 5(35): p. 27901-27911.

90. Wahiduzzaman, Stone, J., Harp, S., et al., Synthesis and electrospraying of nanoscale MOF (metal organic framework) for high-performance CO_2 adsorption membrane. Nanoscale research letters, 2017. 12(1): p. 6-6.

91. Seoane, B., Dikhtiarenko, A., Mayoral, A., et al., Metal organic framework synthesis in the presence of surfactants: towards hierarchical MOFs. CrystEngComm, 2015. 17(7): p. 1693-1700.

92. Taylor, K.M.L., A. Jin, and W. Lin, Surfactant-Assisted Synthesis of Nanoscale Gadolinium Metal-Organic Frameworks for Potential Multimodal Imaging. Angewandte Chemie, 2008. 120(40): p. 7836-7839.

93. Bradshaw, D., S. El-Hankari, and L. Lupica-Spagnolo, Supramolecular templating of hierarchically porous metal-organic frameworks. Chem Soc Rev, 2014. 43(16): p. 5431-43.

94. Zhao, Y., Zhang, Q., Li, Y., et al., Large-scale synthesis of monodisperse UiO-66 crystals with tunable sizes and missing linker defects via acid/base co-modulation. ACS Appl Mater Interfaces, 2017. 9(17): p. 15079-15085.

95. Qiu, L.-G., Xu, T., Li, Z.Q., et al., Hierarchically micro- and mesoporous metal-organic frameworks with tunable porosity. Angewandte Chemie International Edition, 2008. 47(49): p. 9487-9491.

96. Biemmi, E., Christian, S., Stock, N., et al., High-throughput screening of synthesis parameters in the formation of the metal-organic frameworks MOF-5 and HKUST-1. Microporous and Mesoporous Materials, 2009. 117(1-2): p. 111-117.

97. Sahiner, N., Sel, K., Ozturkm O.F., et al., Facile synthesis and characterization of trimesic acid-Cu based metal organic frameworks. Applied Surface Science, 2014. 314: p. 663-669.

98. Huo, J., Brightwell, M., El Hankari, S., et al., A versatile, industrially relevant, aqueous room temperature synthesis of HKUST-1 with high space-time yield. Journal of Materials Chemistry A, 2013. 1(48).

99. Shekhah, O., Wang, H., Zacher, D., et al., Growth mechanism of metal-organic frameworks: insights into the nucleation by employing a step-by-step route. Angewandte Chemie International Edition, 2009. 48(27): p. 5038-5041.

100. Eddaoudi, M., Kim, J., Rosi, N., et al., Systematic design of pore size and functionality in isoreticular MOFs and their application in methane storage. Science, 2002. 295(5554): p. 469.

101. Wong-Foy, A.G., A.J. Matzger, and O.M. Yaghi, Exceptional H2 Saturation Uptake in Microporous Metal-Organic Frameworks. Journal of the American Chemical Society, 2006. 128(11): p. 3494-3495.

102. Yang, Y., Shukla, P., Wang , S., et al., Significant improvement of surface area and CO_2 adsorption of Cu-BTC via solvent exchange activation. RSC Advances, 2013. 3(38): p. 17065-17072.

103. Liu, B., A.G. Wong-Foy, and A.J. Matzger, Rapid and enhanced activation of microporous coordination polymers by flowing supercritical CO_2. Chemical Communications, 2013. 49(14): p. 1419-1421.

104. Li, B., Zhang, Y., Ma, D., et al., A strategy toward constructing a bifunctionalized MOF catalyst: post-synthetic modification of MOFs on organic ligands and coordinatively unsaturated metal sites. Chemical Communications, 2012. 48(49): p. 6151-6153.

105. Zhu, C., Zhang, Z., Wang, B., et al., Synthesis of HKUST-1#MCF compositing materials for CO_2 adsorption. Microporous and Mesoporous Materials, 2016. 226: p. 476-481.

106. Chen, C., Wu, Z., Que, Y., et al., Immobilization of a thiol-functionalized ionic liquid onto HKUST-1 through thiol compounds as the chemical bridge. RSC Advances, 2016. 6(59): p. 54119-54128.

107. Zhu, Q.L. and Q. Xu, Metal-organic framework composites. Chemical Society Reviews, 2014. 43(16): p. 5468-5512.

108. Alfè, M., Gargiulo, V., Lisi, L., et al., Synthesis and characterization of conductive copper-based metal-organic framework/graphene-like composites. Materials Chemistry and Physics, 2014. 147(3): p. 744-750.

109. Petit, C. and T.J. Bandosz, Enhanced Adsorption of Ammonia on Metal-Organic Framework/Graphite Oxide Composites: Analysis of Surface Interactions. Advanced Functional Materials, 2010. 20(1): p. 111-118.

110. Mao, Y., Li, G., Guo, Y., et al., Foldable interpenetrated metal-organic frameworks/carbon nanotubes thin film for lithium-sulfur batteries. Nature Communications, 2017. 8: p. 14628.

111. Kobayashi, H., Y. Mitsuka, and H. Kitagawa, Metal Nanoparticles Covered with a Metal-Organic Framework: From One-Pot Synthetic Methods to Synergistic Energy Storage and Conversion Functions. Inorganic Chemistry, 2016. 55(15): p. 7301-7310.

112. Cai, G., Zhang, W., Jiao, L., et al., Template-Directed Growth of Well-Aligned MOF Arrays and Derived Self-Supporting Electrodes for Water Splitting. Chem, 2017. 2(6): p. 791-802.

113. Ke, F., Qiu, L.G., Yuan, Y.P., et al., Fe_3O_4@MOF core-shell magnetic microspheres with a designable metal-organic framework shell. Journal of Materials Chemistry, 2012. 22(19): p. 9497-9500.

114. Song, X., Jeong, S., Kim, D., et al., Transmetalations in two metal-organic frameworks with different framework flexibilities: Kinetics and core-shell heterostructure. CrystEngComm, 2012. 14(18): p. 5753-5756.

115. Sun, J.-K. and Q. Xu, Functional materials derived from open framework templates/precursors: synthesis and applications. Energy & Environmental Science, 2014. 7(7): p. 2071-2100.

116. Liu, B., Shioyama, H., Akita, T., et al., Metal-organic framework as a template for porous carbon synthesis. Journal of the American Chemical Society, 2008. 130(16): p. 5390-5391.

117. Liu, B., Shioyama, H., Akita, T., et al., Metal-organic framework (MOF) as a template for syntheses of nanoporous carbons as electrode materials for supercapacitor. Carbon, 2010. 48(2): p. 456-463.

118. Jiang, H.-L., Liu, B., Lan, Y.Q., et al., From metal-organic framework to nanoporous carbon: toward a very high surface area and hydrogen uptake. Journal of the American Chemical Society, 2011. 133(31): p. 11854-11857.

119. Yang, S.J., Kim, T., Im, J. H., et al., MOF-derived hierarchically porous carbon with exceptional porosity and hydrogen storage capacity. Chemistry of Materials, 2012. 24(3): p. 464-470.

120. Tang, J., Salunkhe, R.R., Liu, J., et al., Thermal conversion of core-shell metal-organic frameworks: a new method for selectively functionalized nanoporous hybrid carbon. Journal of the American Chemical Society, 2015. 137(4): p. 1572-1580.

121. Yan, X., Li, X., Yan, Z., et al., Porous carbons prepared by direct carbonization of MOFs for supercapacitors. Applied Surface Science, 2014. 308: p. 306-310.

122. Song, Y., Cho, D., Venkateswarlu, S., et al., Systematic study on preparation of copper nanoparticle embedded porous carbon by carbonization of metal-organic framework for enzymatic glucose sensor. RSC Advances, 2017. 7(17): p. 10592-10600.

123. Zhao, K., Liu, U., Quan, X., et al., CO_2 electroreduction at low overpotential on oxide-derived Cu/carbons fabricated from metal organic framework. ACS Applied Materials & Interfaces, 2017. 9(6): p. 5302-5311.

124. Kim, A.Y., Kim, M.K., Cho, K., et al., One-step catalytic synthesis of CuO/Cu_2O in a graphitized porous c matrix derived from the Cu-based metal-organic framework for Li- and Na-ion batteries. ACS Applied Materials & Interfaces, 2016. 8(30): p. 19514-19523.

125. Schlapbach, L. and A. Züttel, Hydrogen-storage materials for mobile applications. Nature, 2001. 414: p. 353.

126. van den Berg, A.W.C. and C.O. Areán, Materials for hydrogen storage: current research trends and perspectives. Chemical Communications, 2008(6): p. 668-681.

127. Wang, X., S. Fordham, and H.-C. Zhou, Metal-organic frameworks for methane storage, in Nanomaterials for Sustainable Energy. 2015, American Chemical Society. p. 173-191.

128. Rosi, N.L., Eckert, J., Eddaoudi, M., et al., Hydrogen storage in microporous metal-organic frameworks. Science, 2003. 300(5622): p. 1127.

129. Grzech, A., Yang, J., Dingemans, T.J., et al., Irreversible High-Temperature Hydrogen Interaction with the Metal Organic Framework $Cu_3(BTC)_2$. The Journal of Physical Chemistry C, 2011. 115(43): p. 21521-21525.

130. Rowsell, J.L.C. and O.M. Yaghi, Strategies for Hydrogen Storage in Metal-Organic Frameworks. Angewandte Chemie International Edition, 2005. 44(30): p. 4670-4679.

131. Panella, B., Hirscher, M., Putter, H., et al., Hydrogen Adsorption in Metal-Organic Frameworks: Cu-MOFs and Zn-MOFs Compared. Advanced Functional Materials, 2006. 16(4): p. 520-524.

132. Houston Frost, T.D., and Randall Q. Snurr, Effects of surface area, free volume, and heat of adsorption on hydrogen uptake in metal-organic frameworks. J. Phys. Chem. B, 2006. 110(19): p. 9565-9570.

133. Guo, H., Zhu, G., Hewitt, I.J., et al., “Twin Copper source” growth of metal-organic framework membrane: $Cu_3(BTC)_2$ with high permeability and selectivity

for recycling H_2. Journal of the American Chemical Society, 2009. 131(5): p. 1646-1647.

134. Wu, H., Simmons, J.M., Liu, Y., et al., Metal-organic frameworks with exceptionally high methane uptake: where and how is methane stored? Chemistry - A European Journal, 2010. 16(17): p. 5205-5214.

135. Cavenati, S., Grande, C.A., Rodrifues, et al., Metal Organic Framework Adsorbent for Biogas Upgrading. Industrial & Engineering Chemistry Research, 2008. 47(16): p. 6333-6335.

136. Pachauri, R.K. and A. Reisinger, IPCC Fourth Assessment Report Intergovernmental Panel on Climate Change. 2007. 2007.

137. Haszeldine, R.S., Carbon Capture and Storage: How Green Can Black Be? Science, 2009. 325(5948): p. 1647.

138. Grajciar, L., Wiersum, A.D., Llewellyn, P.L., et al., Understanding CO_2 Adsorption in CuBTC MOF: Comparing Combined DFT-ab Initio Calculations with Microcalorimetry Experiments. The Journal of Physical Chemistry C, 2011. 115(36): p. 17925-17933.

139. Karra, J.R. and K.S. Walton, Molecular Simulations and Experimental Studies of CO_2, CO, and N_2 Adsorption in Metal-Organic Frameworks. The Journal of Physical Chemistry C, 2010. 114(37): p. 15735-15740.

140. Yazaydın, A.Ö., Benin, A.I., Faheem, S.A., et al., Enhanced CO_2 Adsorption in Metal-Organic Frameworks via Occupation of Open-Metal Sites by Coordinated Water Molecules. Chemistry of Materials, 2009. 21(8): p. 1425-1430.

141. Lan, J., Cao, D., Wang, W., et al., Doping of Alkali, Alkaline-Earth, and transition metals in covalent-organic frameworks for enhancing CO_2 capture by first-principles calculations and molecular simulations. ACS Nano, 2010. 4(7): p. 4225-4237.

142. Yu, J., Y. Ma, and P.B. Balbuena, Evaluation of the Impact of H_2O, O_2, and SO_2 on postcombustion CO_2 capture in metal-organic frameworks. Langmuir, 2012. 28(21): p. 8064-8071.

143. Dasgupta, S., Biswas, N., Gode, N.G., et al., CO_2 recovery from mixtures with nitrogen in a vacuum swing adsorber using metal organic framework adsorbent: A comparative study. International Journal of Greenhouse Gas Control, 2012. 7: p. 225-229.

144. Millward, A.R. and O.M. Yaghi, Metal-Organic Frameworks with Exceptionally High Capacity for Storage of Carbon Dioxide at Room Temperature. Journal of the American Chemical Society, 2005. 127(51): p. 17998-17999.

145. Wang, S., Sun, H., Ang, H.M., et al., Adsorptive remediation of environmental pollutants using novel graphene-based nanomaterials. Chemical Engineering Journal, 2013. 226: p. 336-347.

146. Borfecchia, E., M aurelli, S., Fianolio, D., et al., Insights into Adsorption of NH_3 on HKUST-1 Metal-Organic Framework: A Multitechnique Approach. The Journal of Physical Chemistry C, 2012. 116(37): p. 19839-19850.

147. Petit, C., B. Mendoza, and T.J. Bandosz, Reactive adsorption of ammonia on Cu-based MOF/graphene composites. Langmuir, 2010. 26(19): p. 15302-9.

148. Dathe, H., Peringer, E., Roberts, V.,et al., Metal organic frameworks based on Cu^{2+} and benzene-1,3,5-tricarboxylate as host for SO_2 trapping agents. Comptes Rendus Chimie, 2005. 8(3): p. 753-763.

149. Petit, C., Levasseur, B., Mendoza, B.,et al., Reactive adsorption of acidic gases on MOF/graphite oxide composites. Microporous and Mesoporous Materials, 2012. 154: p. 107-112.

150. Hinks, N.J., McKinlay, A.C., Xiao, B.,et al., Metal organic frameworks as NO delivery materials for biological applications. Microporous and Mesoporous Materials, 2010. 129(3): p. 330-334.

151. DeCoste, J.B., Weston, M.H., Fuller, P.E.,et al., Metal-organic frameworks for oxygen storage. Angewandte Chemie International Edition, 2014. 53(51): p. 14092-14095.

152. Münch, A.S. and F.O.R.L. Mertens, HKUST-1 as an open metal site gas chromatographic stationary phase—capillary preparation, separation of small hydrocarbons and electron donating compounds, determination of thermodynamic data. Journal of Materials Chemistry, 2012. 22(20): p. 10228-10234.

153. Min Wang, Q., Shen, D., Bulow, M.,et al., Metallo-organic molecular sieve for gas separation and purification. Microporous and Mesoporous Materials, 2002. 55(2): p. 217-230.

154. Yang, Q. and C. Zhong, Electrostatic-Field-Induced enhancement of gas mixture separation in Metal-Organic Frameworks: A Computational Study. ChemPhysChem, 2006. 7(7): p. 1417-1421.

155. Martín-Calvo, A., Garcia-Perez, E., Castillo, J.M.,et al., Molecular simulations for adsorption and separation of natural gas in IRMOF-1 and Cu-BTC metal-organic frameworks. Physical Chemistry Chemical Physics, 2008. 10(47): p. 7085-7091.

156. Chmelik, C., Karger, J., Wiebcke, M.,et al., Adsorption and diffusion of alkanes in CuBTC crystals investigated using infra-red microscopy and molecular simulations. Microporous and Mesoporous Materials, 2009. 117(1): p. 22-32.

157. Mueller, U., Schubert, M., Teich, F.,et al., Metal-organic frameworks—prospective industrial applications. Journal of Materials Chemistry, 2006. 16(7): p. 626-636.

158. Ke, F., Qiu, L.G., Yuan, Y.P.,et al., Thiol-functionalization of metal-organic framework by a facile coordination-based postsynthetic strategy and enhanced removal of Hg^{2+} from water. Journal of Hazardous Materials, 2011. 196: p. 36-43.

159. Huang, Y.-B., Liang, J., Wang , X.S.,et al., Multifunctional metal-organic framework catalysts: synergistic catalysis and tandem reactions. Chemical Society Reviews, 2017. 46(1): p. 126-157.

160. Moreno, J.M., et al., Synthesis of 2D and 3D MOFs with tuneable Lewis acidity from preformed 1D hybrid sub-domains. Chemical Science, 2019. 10(7): p. 2053-2066.

161. Janiak, C., Engineering coordination polymers towards applications. Dalton Transactions, 2003(14): p. 2781-2804.

162. Huang, L., Wang, H., Chen, J.,et al., Synthesis, morphology control, and properties of porous metal-organic coordination polymers. Microporous and Mesoporous Materials, 2003. 58(2): p. 105-114.

163. Reineke, T.M., Eddaoudi, M., O’keeffe, M., et al., A microporous lanthanide-organic framework. Angewandte Chemie International Edition, 1999. 38(17): p. 2590-2594.

164. Hu, Z., ePeng, Y., tan, K.M., et al., Enhanced catalytic activity of a hierarchical porous metal-organic framework CuBTC. CrystEngComm, 2015. 17(37): p. 7124-7129.

165. Hori, Y., K. Kikuchi, and S. Suzuki, Production of CO and CH_4 in electrochemical reduction of CO_2 at metal electrodes in aqueous hydrogencarbonate solution. Chemistry Letters, 1985. 14(11): p. 1695-1698.

166. Qiu, Y.-L., Zhong, H.X., Zhang, T.T., et al., Selective electrochemical reduction of carbon dioxide using cu based metal organic framework for CO_2 capture. ACS Applied Materials & Interfaces, 2018. 10(3): p. 2480-2489.

167. Genovino, J., Lutz, S., Sames, D., et al., Complementation of biotransformations with chemical C-H oxidation: copper-catalyzed oxidation of tertiary amines in complex pharmaceuticals. Journal of the American Chemical Society, 2013. 135(33): p. 12346-12352.

168. Chen, Y., Huang, X., Feng, X., et al., Facile fabrication of magnetically recyclable metal-organic framework nanocomposites for highly efficient and selective catalytic oxidation of benzylic C-H bonds. Chem Commun (Camb), 2014. 50(61): p. 8374-7.

169. Li, P.Z., Wang, X.J., Liu, J., et al., A triazole-containing metal-organic framework as a highly effective and substrate size-dependent catalyst for CO_2 conversion. Journal of the American Chemical Society, 2016. 138(7): p. 2142-2145.

170. Nguyen, H.T.D., Nguyen, T.T., Nguyen, P.T., et al., A highly active copper-based metal-organic framework catalyst for a friedel-crafts alkylation in the synthesis of bis(indolyl)methanes under ultrasound irradiation. Arabian Journal of Chemistry, 2017.

171. Appel, A.M., Bercaw, J.E., Bocarsly, A.B., et al., Frontiers, Opportunities, and Challenges in biochemical and chemical catalysis of CO_2 fixation. Chemical Reviews, 2013. 113(8): p. 6621-6658.

172. Surface coordinative unsaturation, in Studies in Surface Science and Catalysis, H.H. Kung, Editor. 1989, Elsevier. p. 53-71.

173. Toyao, T., Styles, M.J., Yago, T., et al., Fe_3O_4@HKUST-1 and Pd/Fe_3O_4@HKUST-1 as magnetically recyclable catalysts prepared via

conversion from a Cu-based ceramic. CrystEngComm, 2017. 19(29): p. 4201-4210.

174. Coleman, J.N., Lotya, M., O'Neill, A., et al., Two-dimensional nanosheets produced by liquid exfoliation of layered materials. Science, 2011. 331(6017): p. 568-71.

175. Majchrzak-Kucęba, I. and D. Bukalak-Gaik, Regeneration performance of metal-organic frameworks. Journal of Thermal Analysis and Calorimetry, 2016. 125(3): p. 1461-1466.

176. Chui, S.S.Y., Lo, S.M.F., Charmant, J.P., et al., A chemically functionalizable nanoporous material [$Cu_3(TMA)_2(H2O)_3$]. Science, 1999. 283: p. 1148-1150.

177. Blöchl, P.E., Projector augmented-wave method. Physical review B, 1994. 50(24): p. 17953.

178. Perdew, J.P., K. Burke, and M. Ernzerhof, Generalized gradient approximation made simple. Physical review letters, 1996. 77(18): p. 3865.

179. Perdew, J.P.a.B., Kieron and Ernzerhof, Matthias, Generalized Gradient Approximation made simple [Phys. Rev. Lett. 77, 3865 (1996)]. Phys. Rev. Lett., 1997. 78(7): p. 1396--1396.

180. Grimme, S., Antony, J., Ehrlich, S., et al., A consistent and accurate ab initio parametrization of density functional dispersion correction (DFT-D) for the 94 elements H-Pu. The Journal of chemical physics, 2010. 132(15): p. 154104.

181. Joo, J., H. Kim, and S.S. Han, Volume shrinkage of a metal-organic framework host induced by the dispersive attraction of guest gas molecules. Physical Chemistry Chemical Physics, 2013. 15(43): p. 18822-18826.

182. Gee, J.A. and D.S. Sholl, Effect of Framework Flexibility on C_8 Aromatic Adsorption at High Loadings in Metal-Organic Frameworks. The Journal of Physical Chemistry C, 2015. 120(1): p. 370-376.

183. Chang, B.K., Bristowe, N.C., Bristowe, P.D., et al., Van der Waals forces in the perfluorinated metal-organic framework zinc 1, 2-bis (4-pyridyl) ethane tetrafluoroterephthalate. Physical Chemistry Chemical Physics, 2012. 14(19): p. 7059-7064.

184. Lee, K., Howe, J.D., Lin, L.C., et al., Small-molecule adsorption in open-site metal-organic frameworks: a systematic density functional theory study for rational design. Chemistry of Materials, 2015. 27(3): p. 668-678.

185. Henkelman, G., A. Arnaldsson, and H. Jónsson, A fast and robust algorithm for Bader decomposition of charge density. Computational Materials Science, 2006. 36(3): p. 354-360.

186. Kresse, G. and J. Hafner, Ab initio molecular dynamics for open-shell transition metals. Physical Review B, 1993. 48(17): p. 13115.

187. Gross, E. and R. Dreizler, Density functional theory: an approach to the quantum many-body problem. 1990, Springer, Berlin.

188. Parr, R.G., Density functional theory of atoms and molecules, in Horizons of Quantum Chemistry. 1980, Springer. p. 5-15.

189. Fulde, P., Electron correlations in molecules and solids. Vol. 100. 2012: Springer Science & Business Media.

190. Martin, R.M., Electronic structure: basic theory and practical methods. 2004: Cambridge university press.

191. Mahan, G.D., Many-particle physics. 2013: Springer Science & Business Media.

192. Hohenberg, P. and W. Kohn, Inhomogeneous Electron Gas. Physical Review, 1964. 136(3B): p. B864-B871.

193. Dreizler, R.M. and E.K. Gross, Density functional theory: an approach to the quantum many-body problem. 2012: Springer Science & Business Media.

194. Kohn, W. and L.J. Sham, Self-consistent equations including exchange and correlation effects. Physical Review, 1965. 140(4A): p. A1133-A1138.

195. Jones, R.O. and O.J.R.o.M.P. Gunnarsson, The density functional formalism, its applications and prospects. 1989. 61(3): p. 689.

196. Lundqvist, S. and N.H. March, Theory of the inhomogeneous electron gas. 2013: Springer Science & Business Media.

197. Perdew, J.P.J.P.R.B., Density-functional approximation for the correlation energy of the inhomogeneous electron gas. 1986. 33(12): p. 8822.

198. Kohn, W.J.R.o.M.P., Nobel Lecture: Electronic structure of matter—wave functions and density functionals. 1999. 71(5): p. 1253.

199. Farrusseng, D., Metal-organic frameworks: applications from catalysis to gas storage. 2011: John Wiley & Sons.

200. Wee, L.H., Bajpe, S.R., Janssens, N., et al., Convenient synthesis of $Cu_3(BTC)_2$ encapsulated Keggin heteropolyacid nanomaterial for application in catalysis. Chem Commun (Camb), 2010. 46(43): p. 8186-8.

201. Jiang, D., Mallat, T., Krumeich, F., et al., Polymer-assisted synthesis of nanocrystalline copper-based metal-organic framework for amine oxidation. Catalysis Communications, 2011. 12(7): p. 602-605.

202. Tanaka, D., Henke, A., Albrecht, K., et al., Rapid preparation of flexible porous coordination polymer nanocrystals with accelerated guest adsorption kinetics. Nat Chem, 2010. 2(5): p. 410-416.

203. Beg, S., Rahman, M., Jain, A., et al., Nanoporous metal organic frameworks as hybrid polymer-metal composites for drug delivery and biomedical applications. Drug Discov Today, 2017. 22(4): p. 625-637.

204. Vishnyakov, A., Ravikovitch, P.I., Neimark, A.V., et al., Nanopore structure and sorption properties of Cu-BTC metal-organic framework. Nano Letters, 2003. 3(6): p. 713-718.

205. Chui, S.S.-Y., Lo, S.M., Charmant, J.P., et al., A chemically functionalizable nanoporous material $[Cu_3 (TMA)_2(H_2O)_3]_n$. Science, 1999. 283(5405): p. 1148-1150.

206. Biemmi, E., Christian, S., Stock, N., et al., High-throughput screening of synthesis parameters in the formation of the metal-organic frameworks MOF-5 and HKUST-1. Microporous and Mesoporous Materials, 2009. 117(1-2): p. 111-117.

207. Yaghi, O.M., O'Keeffe, M., Ockwig, M.W., et al., Reticular synthesis and the design of new materials. Nature, 2003. 423(6941): p. 705-714.

208. Férey, G., Mellot-Draznieks, C., Serre, C., et al., Crystallized frameworks with giant pores: are there limits to the possible? Accounts of Chemical Research, 2005. 38(4): p. 217-225.

209. Kitagawa, S., R. Kitaura, and S. Noro, Functional porous coordination polymers. Angew Chem Int Ed Engl, 2004. 43(18): p. 2334-75.

210. Ferey, G., Hybrid porous solids: past, present, future. Chem Soc Rev, 2008. 37(1): p. 191-214.

211. Stock, N. and S. Biswas, Synthesis of metal-organic frameworks (MOFs): routes to various MOF topologies, morphologies, and composites. Chem Rev, 2012. 112(2): p. 933-69.

212. Chaturvedi, S., P.N. Dave, and N.K. Shah, Applications of nano-catalyst in new era. Journal of Saudi Chemical Society, 2012. 16(3): p. 307-325.

213. Yang, Q. and C. Li, Catalysis in porous-material-based nanoreactors: a bridge between homogeneous and heterogeneous catalysis. Bridging Heterogeneous And Homogeneous Catalysis: Concepts, Strategies, And Applications: p. 351-396.

214. Lestari, W.W., Arvinawati, M., Martien, R., et al., Green and facile synthesis of MOF and nano MOF containing zinc(II) and benzen 1,3,5-tri carboxylate and its study in ibuprofen slow-release. Materials Chemistry and Physics, 2018. 204: p. 141-146.

215. Allmod, K., Stone, J., Harp, S., et al., Synthesis and electrospraying of nanoscale MOF (metal organic framework) for high-performance CO_2 adsorption membrane. Nanoscale Research Letters, 2017. 12(1): p. 6.

216. Li, P., Klet, R.C., Moon, S.Y., et al., Synthesis of nanocrystals of Zr-based metal-organic frameworks with csq-net: significant enhancement in the degradation of a nerve agent simulant. Chem Commun (Camb), 2015. 51(54): p. 10925-8.

217. Khan, N.A. and S.-H. Jhung, Facile Syntheses of Metal-organic Framework $Cu_3(BTC)_2(H_2O)_3$ under Ultrasound. Bulletin of the Korean Chemical Society, 2009. 30(12): p. 2921-2926.

218. Schlesinger, M., Schulze, S., Hietschold, M., et al., Evaluation of synthetic methods for microporous metal-organic frameworks exemplified by the competitive formation of $[Cu_2(btc)_3(H_2O)_3]$ and $[Cu_2(btc)(OH)(H_2O)]$. Microporous and Mesoporous Materials, 2010. 132(1-2): p. 121-127.

219. Kim, J., Kim, S.H., Yang, S.T., et al., Bench-scale preparation of $Cu_3(BTC)_2$ by ethanol reflux: Synthesis optimization and adsorption/catalytic applications. Microporous and Mesoporous Materials, 2012. 161: p. 48-55.

220. Lee, Y.-R., J. Kim, and W.-S. Ahn, Synthesis of metal-organic frameworks: A mini review. Korean Journal of Chemical Engineering, 2013. 30(9): p. 1667-1680.

221. Majchrzak-Kucęba, I. and D. Bukalak-Gaik, Regeneration performance of metal-organic frameworks. Journal of Thermal Analysis and Calorimetry, 2016. 125(3): p. 1461-1466.

222. Xin, C., Zhan, H., Huang, X., et al., Effect of various alkaline agents on the size and morphology of nano-sized HKUST-1 for CO_2 adsorption. RSC Adv., 2015. 5(35): p. 27901-27911.

223. Ye, S., Jiang, X., Ruan, L.W., et al., Post-combustion CO_2 capture with the HKUST-1 and MIL-101 (Cr) metal-organic frameworks: adsorption, separation and regeneration investigations. Microporous and Mesoporous Materials, 2013. 179: p. 191-197.

224. Klimakow, M., Klobes, P., Thunemann, A.F., et al., Mechanochemical synthesis of metal-organic frameworks: a fast and facile approach toward quantitative yields and high specific surface areas. Chemistry of Materials, 2010. 22(18): p. 5216-5221.

225. Li, L., Liu, X.L., Gao, M., et al., The adsorption on magnetic hybrid Fe3O4/HKUST-1/GO of methylene blue from water solution. J. Mater. Chem. A, 2014. 2(6): p. 1795-1801.

226. Fang, Z., Durholt, J.P., Kauer, M., et al., Structural complexity in metal-organic frameworks: simultaneous modification of open metal sites and hierarchical porosity by systematic doping with defective linkers. Journal of the American Chemical Society, 2014. 136(27): p. 9627-9636.

227. Thommes, M., Physical adsorption characterization of nanoporous materials. Chemie Ingenieur Technik, 2010. 82(7): p. 1059-1073.

228. Jang, H.R., Oh, H.H., Kim, J.H., et al., Synthesis of mesoporous spherical silica via spray pyrolysis: Pore size control and evaluation of performance in paclitaxel pre-purification. Microporous and Mesoporous Materials, 2013. 165: p. 219-227.

229. Park, J.T., Roh, D.K., Patel, R., et al., Preparation of TiO_2 spheres with hierarchical pores via grafting polymerization and sol-gel process for dye-sensitized solar cells. Journal of Materials Chemistry, 2010. 20(39): p. 8521.

230. Diring, S., Furukawa, S., Takashima, Y., et al., Controlled multiscale synthesis of porous coordination polymer in nano/micro regimes. Chemistry of Materials, 2010. 22(16): p. 4531-4538.

231. Ameloot, R., Gobechiya, E., Uji-i, H., et al., Direct patterning of oriented metal-organic framework crystals via control over crystallization kinetics in clear precursor solutions. Advanced materials, 2010. 22(24): p. 2685-2688.

232. Schlesinger, M., Schulze, S., Hietschold, M., et al., Evaluation of synthetic methods for microporous metal-organic frameworks exemplified by the competitive formation of $[Cu_2(btc)_3(H_2O)_3]$ and $[Cu_2(btc)(OH)(H_2O)]$. Microporous and Mesoporous Materials, 2010. 132(1): p. 121-127.

233. Liu, J., Culp, J.T., Natesakhawat, S., et al., Experimental and theoretical studies of gas adsorption in $Cu_3(BTC)_2$: an effective activation procedure. The Journal of Physical Chemistry C, 2007. 111(26): p. 9305-9313.

234. Yakovenko, A.A., Reibenspies, J.H., Bhuvanesh, N., et al., Generation and applications of structure envelopes for porous metal-organic frameworks. Journal of Applied Crystallography, 2013. 46(2): p. 346-353.

235. He, X., and Gan, Z., Gisenko, S., et al., Rapid formation of metal-organic frameworks (MOFs) based nanocomposites in microdroplets and their applications for CO_2 photoreduction. ACS Appl Mater Interfaces, 2017. 9(11): p. 9688-9698.

236. Huang, L., Joshi, K.L, Van Dui, A.C., et al., ReaxFF molecular dynamics simulation of thermal stability of a $Cu_3(BTC)_2$ metal-organic framework. Physical Chemistry Chemical Physics, 2012. 14(32): p. 11327-11332.

237. Dauth, A. and J.A. Love, Synthesis and reactivity of 2-azametallacyclobutanes. Dalton Trans, 2012. 41(26): p. 7782-91.

238. Liu, S.H., Lin, Y.C., Chien, Y.C., et al., Adsorption of CO_2 from Flue Gas Streams by a Highly Efficient and Stable Aminosilica Adsorbent. Journal of the Air & Waste Management Association, 2011. 61(2): p. 226-233.

239. Ye, S., Jiang, X., Ruan, L.W. and et al., Post-combustion CO_2 capture with the HKUST-1 and MIL-101(Cr) metal-organic frameworks: adsorption, separation and regeneration investigations. Microporous and Mesoporous Materials, 2013. 179: p. 191-197.

240. Chugh, R., P. Bajpai, and H. Bhunia, Carbon dioxide adsorption on metal organic framework Basolite C300. 2015.

241. Aprea, P., Caputo, D., Gargiulo, N., et al., Modeling carbon dioxide adsorption on microporous substrates: comparison between Cu-BTC metal-organic framework and 13X zeolitic molecular sieve. Journal of Chemical & Engineering Data, 2010. 55(9): p. 3655-3661.

242. Zhao, Y., Y. Cao, and Q. Zhong, CO_2 capture on metal-organic framework and graphene oxide composite using a high-pressure static adsorption Apparatus. Journal of Clean Energy Technologies, 2014: p. 34-37.

243. Majano, G. and J. Pérez-Ramírez, Scalable room-temperature conversion of copper(ii) hydroxide into HKUST-1 ($Cu_3(BTC)_2$). Advanced Materials, 2013. 25(7): p. 1052-1057.

244. Heinke, L. and C. Wöll, Surface-mounted metal-organic frameworks: crystalline and porous molecular assemblies for fundamental insights and advanced applications. Advanced Materials, 2019. 0(0): p. 1806324.

245. Jiao, L., Wang Y., Jiang, H.L. and et al., Metal-organic frameworks as platforms for catalytic applications. Advanced Materials, 2018. 30(37): p. 1703663.

246. Pirngruber, G.D., Hamon, L., Bourelly, S., et al., A method for screening the potential of mofs as CO_2 adsorbents in pressure swing adsorption processes. ChemSusChem, 2012. 5(4): p. 762-776.

247. Kondo, A., Noguchi, H., Ohnishi, S., et al., Novel expansion/shrinkage modulation of 2D layered MOF triggered by clathrate formation with CO_2 molecules. Nano Letters, 2006. 6(11): p. 2581-2584.

248. Planas, N., Dzubak, A.L., Poloni, R., et al., The mechanism of carbon dioxide adsorption in an alkylamine-functionalized metal-organic framework. J Am Chem Soc, 2013. 135(20): p. 7402-5.

249. Hu, Y., Verdegaal, W.M., Yu, S.H., et al., Alkylamine-tethered stable metal-organic framework for CO_2 capture from flue gas. ChemSusChem, 2014. 7(3): p. 734-7.

250. Du, D.Y., Qin, J.S., Li, S.L., et al., Recent advances in porous polyoxometalate-based metal-organic framework materials. Chem Soc Rev, 2014. 43(13): p. 4615-32.

251. Lin, R., Ge, l., Liu, S., et al., Mixed-matrix membranes with metal-organic framework-decorated cnt fillers for efficient CO_2 separation. ACS Appl Mater Interfaces, 2015. 7(27): p. 14750-7.

252. Chen, Y., Lv, D., Wu, J., et al., A new MOF-505@GO composite with high selectivity for CO_2/CH_4 and CO_2/N_2 separation. Chemical Engineering Journal, 2017. 308: p. 1065-1072.

253. Rodenas, T., Luz, I., Prieto, G., et al., Metal-organic framework nanosheets in polymer composite materials for gas separation. Nat Mater, 2015. 14(1): p. 48-55.

254. Falcaro, P., Ricco, R., Yazdi, A., et al., Application of metal and metal oxide nanoparticles@MOFs. Coordination Chemistry Reviews, 2016. 307: p. 237-254.

255. Li, Z. and H.C. Zeng, Armored MOFs: enforcing soft microporous MOF nanocrystals with hard mesoporous silica. J Am Chem Soc, 2014. 136(15): p. 5631-9.

256. Jin, P., Tan, W., Huo, J., et al., Hierarchically porous MOF/polymer composites via interfacial nanoassembly and emulsion polymerization. Journal of Materials Chemistry A, 2018. 6(41): p. 20473-20479.

257. Yin, Z., Li, H., Li, H., et al., Single-Layer MoS_2 Phototransistors. ACS Nano, 2011. 6(1): p. 74-80.

258. Xie, J., Zhang, H., Li, S., et al., Defect-rich MoS_2 ultrathin nanosheets with additional active edge sites for enhanced electrocatalytic hydrogen evolution. Advanced Materials, 2013. 25(40): p. 5807-5813.

259. Yang, T., Liang, J., Sultana, I., et al., Formation of hollow MoS_2/carbon microspheres for high capacity and high rate reversible alkali-ion storage. Journal of Materials Chemistry A, 2018. 6(18): p. 8280-8288.

260. Shinde, P.S., Fontenot, P.R., Donahue, J.P., et al., Synthesis of MoS_2 from $[Mo_3S_7(S_2CNEt_2)_3]I$ for enhancing photoelectrochemical performance and stability of Cu_2O photocathode toward efficient solar water splitting. Journal of Materials Chemistry A, 2018. 6(20): p. 9569-9582.

261. Shen, Y., Wang, H., Zhang, X., et al., MoS_2 Nanosheets Functionalized Composite Mixed Matrix Membrane for Enhanced CO_2 Capture via Surface Drop-Coating Method. ACS Appl Mater Interfaces, 2016. 8(35): p. 23371-8.

262. Wang, T., Chen, S., Pang, H., et al., MoS_2-based nanocomposites for electrochemical energy storage. Advanced Science, 2017. 4(2): p. 1600289.

263. Lukowski, M.A., Daniel, A.S., Meng, F., et al., Enhanced hydrogen evolution catalysis from chemically exfoliated metallic MoS_2 nanosheets. Journal of the American Chemical Society, 2013. 135(28): p. 10274-10277.

264. Li, Y., Wu, D., Zhou, Z., et al., Enhanced Li adsorption and diffusion on MoS_2 zigzag nanoribbons by edge effects: a computational study. The Journal of Physical Chemistry Letters, 2012. 3(16): p. 2221-2227.

265. Hendon, C.H. and A. Walsh, Chemical principles underpinning the performance of the metal-organic framework HKUST-1. Chem Sci, 2015. 6(7): p. 3674-3683.

266. Peng, Y., Krungleviciute, V., Eryazici, I., et al., Methane storage in metal-organic frameworks: current records, surprise findings, and challenges. J Am Chem Soc, 2013. 135(32): p. 11887-94.

267. Mao, Y., Huang, H., Cao, W., et al., Room temperature synthesis of free-standing HKUST-1 membranes from copper hydroxide nanostrands for gas separation. Chem Commun (Camb), 2013. 49(50): p. 5666-8.

268. Kumar, R., Raut, D., Ramamurty, U., et al., Remarkable Improvement in the Mechanical Properties and CO_2 Uptake of MOFs Brought About by Covalent Linking to Graphene. Angew Chem Int Ed Engl, 2016. 55(27): p. 7857-61.

269. Garcia-Gallastegui, A., Iruretagoyena, D., Gouvea, V., et al., Graphene oxide as support for layered double hydroxides: enhancing the CO_2 adsorption capacity. Chemistry of Materials, 2012. 24(23): p. 4531-4539.

270. Beyzavi, M.H., Stephenson, C.J., Liu, Y., et al., Metal-organic framework-based catalysts: chemical fixation of CO_2 with epoxides leading to cyclic organic carbonates. Frontiers in Energy Research, 2015. 2.

271. Shekhah, O., Wang, H., Zacher, D., et al., Growth mechanism of metal-organic frameworks: insights into the nucleation by employing a step-by-step route. Angew Chem Int Ed Engl, 2009. 48(27): p. 5038-41.

272. Walker, A.M. and B. Slater, Comment upon the screw dislocation structure on HKUST-1 (111) surfaces. CrystEngComm, 2008. 10(6): p. 790.

273. Chui, S.S.Y., Lo, S.M., Charmant, J.P., et al., A Chemically functionalizable nanoporous material $[Cu_3(TMA)_2(H_2O)_3]_n$. Science, 1999. 283(5405): p. 1148.

274. Chan, W.C.W. and S. Nie, Quantum dot bioconjugates for ultrasensitive nonisotopic detection. Science, 1998. 281(5385): p. 2016.

275. Gopalakrishnan, D., D. Damien, M.M. Shaijumon, MoS_2 Quantum Dot-Interspersed Exfoliated MoS_2 Nanosheets. ACS Nano, 2014. 8(5): p. 5297-5303.

276. Loera-Serna, S., Oliver-Tolentino, M.A., de Lourdes Lopez-Nunez, M., et al., Electrochemical behavior of $[Cu_3(BTC)_2]$ metal-organic framework: The effect of the method of synthesis. Journal of Alloys and Compounds, 2012. 540: p. 113-120.

277. Nagaraju, G., Tharamani, C.N., Chandrappa, G.T., et al., Hydrothermal synthesis of amorphous MoS_2 nanofiber bundles via acidification of ammonium heptamolybdate tetrahydrate. Nanoscale research letters, 2007. 2(9): p. 461.

278. Dutta, S., Ray, C., Mallick, S., et al., A gel-based approach to design hierarchical CuS decorated reduced graphene oxide nanosheets for enhanced peroxidase-like activity leading to colorimetric detection of dopamine. The Journal of Physical Chemistry C, 2015. 119(41): p. 23790-23800.

279. Paschoal, V.H., L.F.O. Faria, and M.C.C. Ribeiro, Vibrational spectroscopy of ionic liquids. Chemical Reviews, 2017. 117(10): p. 7053-7112.

280. Chen, Y., Mu, X., Lester, E., et al., High efficiency synthesis of HKUST-1 under mild conditions with high BET surface area and CO_2 uptake capacity. Progress in Natural Science: Materials International, 2018. 28(5): p. 584-589.

281. Mu, X., Chen, Y., Lester, E., et al., Optimized synthesis of nano-scale high quality HKUST-1 under mild conditions and its application in CO_2 capture. Microporous and Mesoporous Materials, 2018. 270: p. 249-257.

282. Bian, Z., Xu, J., Zhang, S., et al., Interfacial growth of metal organic framework/graphite oxide composites through pickering emulsion and their CO_2 capture performance in the presence of humidity. Langmuir, 2015. 31(26): p. 7410-7417.

283. Yazaydın, A.Ö., Benin, A.I., Faheem, S.A., et al., Enhanced CO_2 adsorption in metal-organic frameworks via occupation of open-metal sites by coordinated water molecules. Chemistry of Materials, 2009. 21(8): p. 1425-1430.

284. Qian, D., Lei, C., Hao, G.P., et al., Synthesis of hierarchical porous carbon monoliths with incorporated metal-organic frameworks for enhancing volumetric based CO_2 capture capability. ACS Appl Mater Interfaces, 2012. 4(11): p. 6125-32.

285. Zhang, Z., Wang, H., Chen, X., et al., Chromium-based metal-organic framework/mesoporous carbon composite: synthesis, characterization and CO_2 adsorption. Adsorption, 2015. 21(1-2): p. 77-86.

286. Cao, Y., Zhao, Y., Lv, Z., et al., Preparation and enhanced CO_2 adsorption capacity of UiO-66/graphene oxide composites. Journal of Industrial and Engineering Chemistry, 2015. 27: p. 102-107.

287. Yu, N., Wang, L., Li, M., et al., Molybdenum disulfide as a highly efficient adsorbent for non-polar gases. Phys Chem Chem Phys, 2015. 17(17): p. 11700-4.

288. Grajciar, L., Wiersum, A.D., Llewellyn, P.L., et al., Understanding CO_2 adsorption in CuBTC MOF: comparing combined DFT-ab initio calculations with microcalorimetry experiments. The Journal of Physical Chemistry C, 2011. 115(36): p. 17925-17933.

289. Zhou, H.C.J. and S. Kitagawa, Metal-organic frameworks (MOFs). Chemical Society reviews, 2014. 43(16): p. 5415-5418.

290. Shekhah, O., Liu, J., Fischer, R.A., et al., MOF thin films: existing and future applications. Chemical Society Reviews, 2011. 40(2): p. 1081-1106.

291. Liu, Y., Eubank, J.F., Cairns, A.J., et al., Assembly of metal-organic frameworks (MOFs) based on Indium-trimer building blocks: a porous MOF with soc topology and high hydrogen storage. Angewandte Chemie, 2007. 119(18): p. 3342-3347.

292. Zhang, Z., Zhao, Y., Gong, Q., et al., MOFs for CO_2 capture and separation from flue gas mixtures: the effect of multifunctional sites on their adsorption capacity and selectivity. Chemical Communications, 2013. 49(7): p. 653-661.

293. i Xamena, F.X.L., Abad, A., Corma, A., et al., MOFs as catalysts: activity, reusability and shape-selectivity of a Pd-containing MOF. Journal of Catalysis, 2007. 250(2): p. 294-298.

294. Kind, M. and C. Wöll, Organic surfaces exposed by self-assembled organothiol monolayers: Preparation, characterization, and application. Progress in Surface Science, 2009. 84(7): p. 230-278.

295. Feng, P.L., Perry IV, J.J., Nikodemski, S., et al., Assessing the purity of metal-organic frameworks using photoluminescence: MOF-5, zno quantum dots, and

framework decomposition. Journal of the American Chemical Society, 2010. 132(44): p. 15487-15489.

296. Chen, Y., Hna, S., Li, X., et al., Why does enzyme not leach from metal-organic frameworks (MOFS)? unveiling the interactions between an enzyme molecule and a MOF. Inorganic Chemistry, 2014. 53(19): p. 10006-10008.

297. Zhao, T.-M., Chen, S., Shang, R., et al., Perovskite-like polar lanthanide formate frameworks of $[NH_2NH_3][Ln(HCOO)_4]$ (Ln = Tb-Lu and Y): synthesis, structures, magnetism, and anisotropic thermal expansion. Inorganic Chemistry, 2016. 55(20): p. 10075-10082.

298. Wang, C., X. Qian, and X. An, In situ green preparation and antibacterial activity of copper-based metal-organic frameworks/cellulose fibers (HKUST-1/CF) composite. Cellulose, 2015. 22(6): p. 3789-3797.

299. Petit, C. and T.J. Bandosz, Exploring the coordination chemistry of MOF-graphite oxide composites and their applications as adsorbents. Dalton Transactions, 2012. 41(14): p. 4027-4035.

300. Ma, S. and H.-C. Zhou, Gas storage in porous metal-organic frameworks for clean energy applications. Chemical Communications, 2010. 46(1): p. 44-53.

301. Maina, J.W., Pozo-Gonzalo, C., Kong, L., et al., Metal organic framework based catalysts for CO_2 conversion. Materials Horizons, 2017. 4(3): p. 345-361.

302. Granato, T., F. Testa, and R. Olivo, Catalytic activity of HKUST-1 coated on ceramic foam. Microporous and Mesoporous Materials, 2012. 153: p. 236-246.

303. Coudert, F.X., Boutin, A., Jeffroy, M., et al., Thermodynamic methods and models to study flexible metal-organic frameworks. ChemPhysChem, 2011. 12(2): p. 247-258.

304. Ethiraj, J., Bonino, F., Lamberti, C., et al., H_2S interaction with HKUST-1 and ZIF-8 MOFs: A multitechnique study. Microporous and Mesoporous Materials, 2015. 207: p. 90-94.

305. Al-Janabi, N., Hill, P., Torrente-Murciano, L., et al., Mapping the Cu-BTC metal-organic framework (HKUST-1) stability envelope in the presence of water vapour for CO_2 adsorption from flue gases. Chemical Engineering Journal, 2015. 281: p. 669-677.

306. Gul-E-Noor, F., Jee, B., Poppl, A., et al., Effects of varying water adsorption on a $Cu_3(BTC)_2$ metal-organic framework (MOF) as studied by ^1H and ^{13}C solid-state NMR spectroscopy. Physical Chemistry Chemical Physics, 2011. 13(17): p. 7783-7788.

307. Allendorf, M.D., Houk, R.J., Andruszkiewicz, L., et al., Stress-induced chemical detection using flexible metal-organic frameworks. Journal of the American Chemical Society, 2008. 130(44): p. 14404-14405.

308. Petit, C., B. Mendoza, and T.J. Bandosz, Hydrogen sulfide adsorption on MOFs and MOF/Graphite oxide composites. ChemPhysChem, 2010. 11(17): p. 3678-3684.

309. Alhamami, M., H. Doan, and C.H. Cheng, A review on breathing behaviors of Metal-Organic-Frameworks (MOFs) for gas adsorption. Materials, 2014. 7(4).

310. An, J. and N.L. Rosi, Tuning MOF CO_2 adsorption properties via cation exchange. Journal of the American Chemical Society, 2010. 132(16): p. 5578-5579.

311. Botas, J.A., Mavrandonakis, A., Tylianakis, E., et al., Cobalt doping of the MOF-5 framework and its effect on gas-adsorption properties. Langmuir, 2010. 26(8): p. 5300-5303.

312. Klontzas, E., Mavrandonakis, A., Tylianakis, E., et al., Improving hydrogen storage capacity of MOF by functionalization of the organic linker with lithium atoms. Nano Letters, 2008. 8(6): p. 1572-1576.

313. Hwang, Y.K., Hong, D.Y., Cahng, J.S., et al., Amine grafting on coordinatively unsaturated metal centers of MOFs: consequences for catalysis and metal encapsulation. Angewandte Chemie, 2008. 120(22): p. 4212-4216.

314. Xu, S.J., Wang, X.C., Wang C.H.， et al., Effects of rapid thermal annealing on structure and luminescence of self-assembled InAs/GaAs quantum dots. Applied Physics Letters, 1998. 72(25): p. 3335-3337.

315. Singh, J., Sahu, K., Singh, R., et al., Thermal annealing induced strong photoluminescence enhancement in Ag-TiO_2 plasmonic nanocomposite thin films. Journal of Alloys and Compounds, 2019. 786: p. 750-757.

316. Faraz, A., Mahmood, K., Ali, A., et al., Enhancement of Al-N co-dopant solubility in ZnO by high temperature thermal annealing. Ceramics International, 2019. 45(3): p. 2948-2952.

317. Park, S.M. and S.F. Kim, Synergistic effects of processing additives and thermal annealing on nanomorphology and hole mobility of Poly(3-hexylthiophene) thin films. Polymers, 2019. 11(1).

318. Mu, X., Chen, Y., and Lester, E., et al., Optimized synthesis of nano-scale high quality HKUST-1 under mild conditions and its application in CO_2 capture. Microporous and Mesoporous Materials, 2018. 270: p. 249-257.

319. Chen, Y., Mu, X., Lester, E., et al., High efficiency synthesis of HKUST-1 under mild conditions with high BET surface area and CO_2 uptake capacity. Progress in Natural Science: Materials International, 2018. 28(5): p. 584-589.

320. Mu, S.-J., Su, Y., Xiao, L., et al., X-ray diffraction pattern of graphite oxide. Chinese Physics Letters, 2013. 30(9): p. 096101.

321. Amelkovich, Y.A., Nazarenko, O.B., Sechin, A.I., et al., Characterization of copper nanopowders after natural aging. IOP Conference Series: Materials Science and Engineering, 2015. 81: p. 012072.

322. Sing, K.S.W., The use of gas adsorption for the characterization of porous solids. Colloids and Surfaces, 1989. 38(1): p. 113-124.

323. Hadjiivanov, K. and H. Knözinger, Low-Temperature CO Adsorption on Ag^+/SiO_2 and Ag-ZSM-5: An FTIR Study. The Journal of Physical Chemistry B, 1998. 102(52): p. 10936-10940.

324. Calatayud, M., Collins, S.E., and Baltanas, M.A., et al., Stability of formate species on β-Ga_2O_3. Physical Chemistry Chemical Physics, 2009. 11(9): p. 1397-1405.

325. Haghofer, A., Ferri, D., Fottinger, K., et al., Who is doing the job? Unraveling the role of Ga_2O_3 in methanol steam reforming on Pd_2Ga/Ga_2O_3. ACS Catalysis, 2012. 2(11): p. 2305-2315.

326. Luo, Y.-R., Comprehensive handbook of chemical bond energies. 2007: CRC press.

327. Bond Energies, in Encyclopedia of Inorganic Chemistry, R.H.C. R. B. King, C. M. Lukehart, D. A. Atwood and R. A. Scott, Editor. 2006, John Wiley & Sons, Ltd.

328. Agency, U.S.E.P. Green Chemistry. Basics of green chemistry 2017 [cited 2019 Feb., 24th]; Available from: https://www.epa.gov/greenchemistry/basics-green-chemistry.

329. Brotchie, A., Porous materials: MOFs go fungal. Nature Reviews Materials, 2016. 1: p. 15015.

330. Kumar, A., Madden, D.G., Lusi, M., et al., Direct air capture of CO_2 by physisorbent materials. Angewandte Chemie International Edition, 2015. 54(48): p. 14372-14377.

331. Liu, H., et al., Controllable encapsulation of “clean” metal clusters within MOFs through kinetic modulation: towards advanced heterogeneous nanocatalysts. Angewandte Chemie International Edition, 2016. 55(16): p. 5019-5023.

332. Yang, S.J. and C.R. Park, Preparation of highly moisture-resistant black-colored metal organic frameworks. Advanced Materials, 2012. 24(29): p. 4010-4013.

333. Shultz, A.M., Farha, O.K., Hupp, J.T., et al., A catalytically active, permanently microporous mof with metalloporphyrin struts. Journal of the American Chemical Society, 2009. 131(12): p. 4204-4205.

334. Fajula, F., A. Galarneau, and F.D. Renzo, Advanced porous materials: New developments and emerging trends. Microporous and Mesoporous Materials, 2005. 82(3): p. 227-239.

335. Zhou, W., Zou, B., Zhang, W., et al., Synthesis of stable heterogeneous catalysts by supporting carbon-stabilized palladium nanoparticles on MOFs. Nanoscale, 2015. 7(19): p. 8720-4.

336. Yilmaz, G., Yam, K.M., Zhang, C., et al., In situ transformation of MOFs into layered double hydroxide embedded metal sulfides for improved electrocatalytic and supercapacitive performance. Advanced Materials, 2017. 29(26): p. 1606814.

337. Royer, S. and D. Duprez, Catalytic oxidation of carbon monoxide over transition metal oxides. ChemCatChem, 2011. 3(1): p. 24-65.

338. Rola Mohammad Al Soubaihi , K.M.S., and Joydeep Dutta, Critical review of low-temperature CO oxidation and hysteresis phenomenon on heterogeneous catalysts. Catalysts, 2018. 8(12): p. 660.

339. Nachiappan, N., G. Paruthimal Kalaignan, and G. Sasikumar, Effect of nitrogen and carbon dioxide as fuel impurities on PEM fuel cell performances. Vol. 19. 2013. 351-354.

340. Thomsen, A.H. and M. Gregersen, Suicide by carbon monoxide from car exhaust-gas in Denmark 1995-1999. Forensic Science International, 2006. 161(1): p. 41-46.

341. Xu, C., Su, J., Xu, X., et al., Low temperature CO oxidation over unsupported nanoporous gold. Journal of the American Chemical Society, 2007. 129(1): p. 42-43.

342. Newton, M.A., Ferri, D., Smolentsev, G., et al., Room-temperature carbon monoxide oxidation by oxygen over Pt/Al_2O_3 mediated by reactive platinum carbonates. Nature Communications, 2015. 6: p. 8675.

343. Liang, Q., Liu, J., Wei, Y., Zhao, Z., et al., Palladium nanoparticles supported on a triptycene-based microporous polymer: highly active catalysts for CO oxidation. Chemical Communications, 2013. 49(79): p. 8928-8930.

344. Yang, C.-J., An impending platinum crisis and its implications for the future of the automobile. Energy Policy, 2009. 37(5): p. 1805-1808.

345. Naumov, A.V., Review of the world market of rare-earth metals. Russian Journal of Non-Ferrous Metals, 2008. 49(1): p. 14-22.

346. Ye, J.Y. and Liu, C.J., $Cu_3(BTC)_2$: CO oxidation over MOF based catalysts. J Chemical Communications, 2011. 47(7): p. 2167-2169.

347. Kandoi, S., Gokhale, A.A., Grabow, L.C., et al., Why Au and Cu are more selective than Pt for preferential oxidation of CO at low temperature. Catalysis Letters, 2004. 93(1): p. 93-100.

348. Tu, C.-H., Wang, A.Q., Zheng, M.Y., et al., Factors influencing the catalytic activity of SBA-15-supported copper nanoparticles in CO oxidation. Applied Catalysis A: General, 2006. 297(1): p. 40-47.

349. Sambiagio, C., Marsden, SP., Blacker, A.J., et al., Copper catalysed Ullmann type chemistry: from mechanistic aspects to modern development. Chemical Society Reviews, 2014. 43(10): p. 3525-3550.

350. Gawande, M.B., Goswami, A., Felpin, F.X., et al., Cu and Cu-based nanoparticles: synthesis and applications in catalysis. Chemical Reviews, 2016. 116(6): p. 3722-3811.

351. Yim, C.M., Pang, C.L., Hermoso, D.R., et al., Influence of support morphology on the bonding of molecules to nanoparticles. Proceedings of the National Academy of Sciences, 2015. 112(26): p. 7903.

352. Glaspell, G., Hassan, H.M., Elzatahry, A., et al., Nanocatalysis on tailored shape supports: Au and Pd nanoparticles supported on MgO nanocubes and ZnO nanobelts. The Journal of Physical Chemistry B, 2006. 110(43): p. 21387-21393.

353. Szabó, T., Berkesi, O., Forgo, P., et al., Evolution of surface functional groups in a series of progressively oxidized graphite oxides. Chemistry of Materials, 2006. 18(11): p. 2740-2749.

354. Kovtyukhova, N.I., Ollivier, P.J., Martin, B.R., et al., Layer-by-layer assembly of ultrathin composite films from micron-sized graphite oxide sheets and polycations. Chemistry of Materials, 1999. 11(3): p. 771-778.

355. Marcano, D.C., Kosynkin, D.V., Berlin , J.M., et al., Improved synthesis of graphene oxide. ACS Nano, 2010. 4(8): p. 4806-4814.

356. Acik, M., Lee, G., Mattevi, C., et al., Unusual infrared-absorption mechanism in thermally reduced graphene oxide. Nat Mater, 2010. 9(10): p. 840-5.

357. Zhang, D., Wei, S., Kaila, C., et al., Carbon-stabilized iron nanoparticles for environmental remediation. Nanoscale, 2010. 2(6): p. 917-919.

358. Song, E.H., Z. Wen, and Q. Jiang, CO catalytic oxidation on copper-embedded graphene. The Journal of Physical Chemistry C, 2011. 115(9): p. 3678-3683.

359. Koenig, G.A., On paramelaconite, and the associated minerals. Proc. Acad. Nat. Sci. Philadelphia, 1891. 284.

360. Morgan, P.E.D., Partin, D.E., Chamberland, B.L., et al., Synthesis of Paramelaconite: Cu_4O_3. Journal of Solid State Chemistry, 1996. 121(1): p. 33-37.

361. Mu, S.-J., Su, Y., Xiao, L., et al., X-ray difraction pattern of graphite oxide. Chinese Physics Letters, 2013. 30(9): p. 096101.

362. Malek, K., Vla, M., Swiatek-Kozlowska, J., et al., Solid state study of the copper(ii) complex of 2-hydroxyiminopropanoic acid. New J. Chem., 2004. 28(4): p. 477-483.

363. Sing, K.S.W., The use of gas adsorption for the characterization of porous solids. Colloids and Surfaces, 1989. 38(1): p. 113-124.

364. Bukhtiyarov, V.I., Prosvirin, I.P., Tikhomirov, E.P., et al., In situ study of selective oxidation of methanol to formaldehyde over copper. Reaction Kinetics and Catalysis Letters, 2003. 79(1): p. 181-188.

365. Thurston, E., Adsorption and interaction of oxygen, carbon monoxide and certain inert gases on copper at 77 K. Transactions of the Faraday Society, 1968. 64: p. 2181-2189.

366. Bera, P., Camara, A.L., Hornes, A., et al., Comparative in situ drifts-ms study of ^{12}CO- and ^{13}CO-TPR on CuO/CeO$_2$ catalyst. The Journal of Physical Chemistry C, 2009. 113(24): p. 10689-10695.

367. Padley, M.B., Rochester, C.H., Hutchings, G.J., et al., FTIR Spectroscopic Study of Thiophene, SO$_2$, and CO Adsorption on Cu/Al$_2$O$_3$ Catalysts. Journal of Catalysis, 1994. 148(2): p. 438-452.

368. Busca, G., FT-IR study of the surface of copper oxide. Journal of Molecular Catalysis, 1987. 43(2): p. 225-236.

369. Calatayud, M., Collins, S.E., Baltanas, M.A., et al., Stability of formate species on β-Ga_2O_3. Physical Chemistry Chemical Physics, 2009. 11(9): p. 1397-1405.

370. Haghofer, A., Ferri, D., Fottinger, K., et al., Who is doing the job? Unraveling the role of Ga_2O_3 in methanol steam reforming on Pd_2Ga/Ga_2O_3. ACS Catalysis, 2012. 2(11): p. 2305-2315.

371. Yang, X. and Q. Xu, Bimetallic metal-organic frameworks for gas storage and separation. Crystal Growth & Design, 2017. 17(4): p. 1450-1455.

372. Kim, D. and A. Coskun, Template-directed approach towards the realization of ordered heterogeneity in bimetallic metal-organic frameworks. Angewandte Chemie International Edition, 2017. 56(18): p. 5071-5076.

373. Sun, D., Sun, G., Deng, X., et al., Mixed-metal strategy on metal-organic frameworks (MOFs) for functionalities expansion: Co substitution induces aerobic oxidation of cyclohexene over inactive Ni-MOF-74. Inorganic Chemistry, 2015. 54(17): p. 8639-8643.

374. Villajos, J.A., Orcajo, G., Martos, C., et al., Co/Ni mixed-metal sited MOF-74 material as hydrogen adsorbent. International Journal of Hydrogen Energy, 2015. 40(15): p. 5346-5352.

375. Zou, F., Hu, X., Li, Z., et al., MOF-derived porous ZnO/$ZnFe_2O_4$/C octahedra with hollow interiors for high-rate lithium-ion batteries. Advanced Materials, 2014. 26(38): p. 6622-6628.

376. Aguilera-Sigalat, J. and D. Bradshaw, Synthesis and applications of metal-organic framework-quantum dot (QD@MOF) composites. Coordination Chemistry Reviews, 2016. 307: p. 267-291.

377. Resch-Genger, U., Grabolle, M., agAVALIERE-Jaricot, S., et al., Quantum dots versus organic dyes as fluorescent labels. Nature Methods, 2008. 5: p. 763.

378. Liu, Y. and Z. Tang, Multifunctional nanoparticle@MOF core-shell nanostructures. Advanced Materials, 2013. 25(40): p. 5819-5825.

379. Aijaz, A., Karkamkar, A., Choi, Y.J., et al., Immobilizing highly catalytically active Pt nanoparticles inside the pores of metal-organic framework: a double solvents approach. Journal of the American Chemical Society, 2012. 134(34): p. 13926-13929.

380. Shinde, D.B. and V.K. Pillai, Electrochemical preparation of luminescent graphene quantum dots from multiwalled carbon nanotubes. Chemistry - A European Journal, 2012. 18(39): p. 12522-12528.

381. Pierson, J.F., E. Duverger, and O. Banakh, Experimental and theoretical contributions to the determination of optical properties of synthetic paramelaconite. Journal of Solid State Chemistry, 2007. 180(3): p. 968-973.

382. Pierson, J.F., Wiederkehr, D., Chappe, J.M., et al., Reactive sputtering: A method to modify the metallic ratio in the novel silver-copper oxides. Applied Surface Science, 2006. 253(3): p. 1484-1488.

383. Ye, S., et al., Post-combustion CO 2 capture with the HKUST-1 and MIL-101 (Cr) metal–organic frameworks: adsorption, separation and regeneration investigations. Microporous and Mesoporous Materials, 2013. 179: p. 191-197.

384. Majchrzak-Kucęba, I. and D. Bukalak-Gaik, Regeneration performance of metal–organic frameworks. Journal of Thermal Analysis and Calorimetry, 2016. 125(3): p. 1461-1466.

385. Klimakow, M., et al., Mechanochemical Synthesis of Metal−Organic Frameworks: A Fast and Facile Approach toward Quantitative Yields and High Specific Surface Areas. Chemistry of Materials, 2010. 22(18): p. 5216-5221.

386. Li, L., et al., The adsorption on magnetic hybrid Fe3O4/HKUST-1/GO of methylene blue from water solution. J. Mater. Chem. A, 2014. 2(6): p. 1795-1801.

387. Fang, Z., et al., Structural Complexity in Metal–Organic Frameworks: Simultaneous Modification of Open Metal Sites and Hierarchical Porosity by

Systematic Doping with Defective Linkers. Journal of the American Chemical Society, 2014. 136(27): p. 9627-9636.

388. Thommes, M., Physical Adsorption Characterization of Nanoporous Materials. Chemie Ingenieur Technik, 2010. 82(7): p. 1059-1073.